Linking Pattern and Process in the Disturbance Ecology of Sierra Nevada Mixed Conifer Forests

By

Daniel Everett Foster

A dissertation submitted in partial satisfaction of the requirements for the degree of
Doctor of Philosophy
in
Environmental Science, Policy, and Management
in the
Graduate Division
of the
University of California, Berkeley

Committee in charge:
Professor John Battles, Chair
Professor Scott Stephens
Professor Perry de Valpine

Fall 2022

1 ABSTRACT

Linking Pattern and Process in the Disturbance Ecology of Sierra Nevada Mixed Conifer Forests

by

Daniel Everett Foster

Doctor of Philosophy in Environmental Science, Policy, and Management

University of California, Berkeley

Professor John Battles, Chair

Disturbance ecology is central to the understanding and management of Sierra Nevada mixed conifer forests (MCF). Three studies relying on field data and hierarchical statistical regression models illuminate relationships between pattern and process in this important forest type.

In the first chapter, a suite of hierarchical spatial statistical models using Gaussian process spatial random effects is proposed to quantify fine-scale spatial patterns in the fuel load (biomass per unit area) of several wildland fuel components (duff, litter, fine woody debris, coarse woody debris, understory vegetation, trees, and saplings). A sampling protocol that generates spatially explicit fuel load information at a fine scale (sub-meter to tens of meters) is described and implemented in a Sierra Nevada mixed conifer forest affected by extensive mortality in the 2012-2016 drought. The statistical models are described, validated, and applied to test whether Sierra Nevada mixed conifer forests experiencing varying levels of drought mortality exhibit different fine-scale spatial patterns of wildland fuels. Model validation reveals varying performance in three tasks: 1) Making pointwise predictions of training or validation data, 2) reproducing the distribution of fine-scale (sub-meter to meter) fuel load observations, and 3) reproducing the distribution of coarse-scale (sub-hectare to hectare) mean fuel loads of the various fuel components. Models for the depth of duff, depth of litter, count of fine woody debris particles, and the size of coarse woody debris particles generally perform well in all three tasks and parameter estimates are well informed by the data. However, models for infrequent events such as the meter-scale presence of coarse woody debris, trees, or saplings do not perform well in terms of making pointwise predictions or learning from the data. There are mixed results from the models for the size of fine woody debris particles and the presence of understory vegetation. In general, forests experiencing different levels of drought mortality do not exhibit different fine-scale spatial patterns, with two exceptions. First, in the litter depths model the Gaussian process magnitude, controlling the relative strength of the spatial pattern, is greater on the low mortality plots than on the high mortality plots. Second, the Gaussian process length scale parameter for understory vegetation presence, controlling the distance at which spatial autocorrelation occurs, is higher in high mortality plots than in medium mortality plots. The sampling protocol and statistical analysis described in this chapter enable quantitative description and reproduction of the fine-scale spatial patterns of fuel loads, a prerequisite to predicting how fires will behave in fuel beds with varying fine-scale spatial properties. These models also facilitate study of the relationships between pattern and process by illuminating how parameters describing fine-scale spatial pattern vary in different contexts.

In the second study, I apply similar hierarchical spatial models with Gaussian process spatial random effects to describe the spatial pattern of litter, duff, and fine woody debris both before and after

three replicate prescribed fires in a Sierra Nevada mixed conifer forest. The analysis reveals that prescribed fire alters not only mean fuel loads, but also the fine-scale spatial pattern of biomass. Prescribed fire increased the relative strength of the fine-scale spatial pattern for litter and duff, 1-hour fine woody debris, and 10-hour fine woody debris. The burns decreased the length scale of the spatial pattern (the distance over which autocorrelation occurs) for litter and duff, increased it for 1-hour fuels, and did not change it for 10-hour fuels. Finally, the Gaussian process noise parameter describing very fine-scale autocorrelation increased for 1-hour fuels as a result of the prescribed burns. Changes to the fine-scale spatial pattern of litter, duff, and fine woody debris are likely to impact the behavior of future fires and the ecological function of these forests. As such, information about the effects of prescribed fire on the fine-scale spatial pattern of fuel loads is important to have a complete understanding of this crucial management practice.

Finally, for my third chapter I assess how numerous stressors shape the vital rates (survival, growth, and fecundity) of sugar pine across the vast majority of its range. Sugar pine (*Pinus lambertiana*) is the largest Pinus species, an important timber species, and a component of several dry conifer forest types of western North America, in particular the extensive Sierra Nevada mixed conifer forest. The species faces several challenges in the Anthropocene, including a disrupted fire regime, an invasive pathogen, forest structure changes, and drought with ensuing bark beetle epidemics. Managers are concerned about the conservation outlook for sugar pine, but it is unclear where and how to best invest conservation resources. Using data from the US Forest Service's Forest Inventory and Analysis program, I synthesize the vital rate functions by constructing an integral projection model which predicts the effects of various stressors on the asymptotic population growth rate. The asymptotic population growth rate is near or slightly below one even under undisturbed conditions, and the actual abundance (in terms of both stem density and basal area) slightly declined over the duration of the study (2001-2019). The analysis reveals that wildfire, white pine blister rust, and forest density are key drivers of the demographic rates of sugar pine across its range. Drought and site dryness had lesser, but still meaningful, effects. Fire has strong negative effects on survival, resulting in a strongly negative population trajectory on burned sites. Conversely, lower than average forest density (neighborhood basal area) results in a positive population growth rate via beneficial effects on individual growth. These results highlight the value of fire hazard mitigation, particularly where it also reduces forest density, in the conservation of this important species.

This work is dedicated to Everett.

2 ACKNOWLEDGEMENTS

First and foremost, this work would not have been possible without the support and love of my best friend and wife, Caity. Thank you for sharing this journey with me. Thank you to Everett for bringing so much joy and meaning into our lives.

Thank you to my advisors John Battles and Scott Stephens. John has provided thoughtful advice and guidance at every step of the process and provided an immense amount of support in making the fieldwork happen. Scott has fostered an amazing community and provided important guidance on my dissertation and career. Most importantly, you have both supported me not only as a scientist but as a whole person with your kindness, patience, and friendship.

Thank you to Perry de Valpine, Ian Wang, and Rob York for serving on my qualifying exam committee and to Perry for also serving on my dissertation committee. You have been generous with your time and attention, and your efforts have dramatically improved the quality of this work.

I have learned a great deal about science and life from my other mentors. Thank you to Carmen Tubbesing, Kristen Shive, Zack Steel, and Brandon Collins for your guidance and encouragement.

Thank you to the many other people who have contributed valuable feedback and supported the implementation of these research projects. Hudson Northrup, Ian Moore, Angie Notari, and Gavin Williams collected all of the field data used in the first two chapters, counting more than 40,000 sticks in the process. Lisa Rosenthal made major contributions to the development of the statistical models at the heart of the first two chapters. Ariel Roughton, Kestrel Grevatt, and the rest of the Blodgett Forest staff and volunteers made the prescribed fires happen and contributed some emergency data collection. Thank you also to Dave Saah, Carrie Levine, Mark Finney, Adrian Das, Johnny Nesmith, and the members of the Pyregence Consortium for providing valuable feedback that improved the early versions of this work.

I have learned from, been inspired by, and enjoyed the friendship of the Stephens and Battles Labs during my time as a PhD student. Thank you to Andrew Johnson, Stacey Frederick, Linnea Hardlund, Alexis Bernal, Hannah Fertel, Tara Seely, Marianne Cowherd, John Sanders, Elliot Kuskulis, Claudia Herbert, Katie Low, Julia Murphy, Ian Moore, Rachelle Hedges, Lauren Cox, Clarke Knight, Yihong Zhu, Corrie Munger, Taj Katuna, Spike Campbell, Lindsey Jasperse, Nat Macmillan, Rachel Pekelney, Jameson Christianson, and Gracie Williams.

My other friends and family have also made life joyful over the last several years despite some real challenges. Thank you to Mom, Kelly, Kevin, Lance, Scott, Josh, Desirée, Kai, Youri, Ryan, Kim, and everyone else.

Thank you to John, Scott, Perry, Hannah, Mom, and Caity for your helpful comments and edits which dramatically improved this dissertation.

Last but definitely not least, this research would not have been possible without financial support from the California Energy Commission via the Pyregence consortium, the California Air Resources Board, and the National Park Service.

3 TABLE OF CONTENTS

4 INTRODUCTION

Disturbance ecology - the study of disturbances, their causes, and their effects - is central to the management and conservation of forests in the Anthropocene (Newman, 2019). A disturbance is a "discrete event in time that disrupts ecosystem, community, or population structure and changes resources, substrate availability, or the physical environment" (White and Pickett, 1985). Of particular importance due to their role in patch dynamics are disturbances that lead to the mortality of trees, such as fire, herbivory, outbreaks of native or invasive pathogens, and timber harvests (White, 1979; Stephens and Moghaddas, 2005b; Das *et al.*, 2008; Collins and Roller, 2013; Stephenson *et al.*, 2019; Dudney *et al.*, 2020). During the Anthropocene, many disturbance regimes (characteristic patterns and features of disturbance processes in an ecosystem) have been radically altered, with far reaching effects. Logging for timber harvests or land-use conversion is a novel type of disturbance (Dolanc *et al.*, 2014; Tsujino *et al.*, 2016). Droughts have become warmer and killed more trees (Allen *et al.*, 2015; Anderegg *et al.*, 2015) and invasive pathogens threaten entire species (Tomback and Achuff, 2010).

Shifts in the fire regime are of particular importance to the Sierra Nevada mixed conifer forests, which occupy more than 3 million hectares of California's Sierra Nevada range (Hessburg *et al.*, 2016; Safford and Stevens, 2017). Fire suppression has shifted species composition and increased fuel loads (Stephens *et al.*, 2015; Levine *et al.*, 2016; Safford and Stevens, 2017). As a result of these changes and a warming climate, wildfires have increased in prevalence and patterns of fire severity have shifted (Steel *et al.*, 2015; Parks and Abatzoglou, 2020; Ellis *et al.*, 2021). These changes potentially threaten the ability of Sierra Nevada mixed conifer forests to persist (Shive *et al.*, 2018; Coop *et al.*, 2020). In this context, an applied understanding of disturbance processes and their effects is crucial for land managers seeking to restore or conserve Sierra Nevada mixed conifer forests (North, 2012; Nagel *et al.*, 2017; Newman, 2019; York *et al.*, 2021).

This dissertation makes three contributions to the study of disturbance ecology in Sierra Nevada mixed conifer forests by illuminating relationships between process and pattern. In the first chapter, I propose a novel application of hierarchical spatial statistical models (Diggle and Ribiero, 2007) to quantify fine-scale spatial patterns of forest biomass. These patterns are both a cause and an effect of disturbances such as fire (Thaxton and Platt, 2006; Vakili *et al.*, 2016a; Atchley *et al.*, 2021), and their quantification is an essential first step in facilitating study and informed decision-making. In the second chapter, I apply these hierarchical spatial models to explore the under-studied effects of prescribed fire on spatial pattern in a Sierra Nevada mixed conifer forest. Finally, in the third chapter, I use a range-wide demographic analysis to prioritize among stressors and inform management for an important tree species, *Pinus lambertiana*. Throughout, I rely on the powerful combination of sub-hectare scale field observations and hierarchical statistical regression models to improve our understanding of these forests and how they are shaped by disturbances. This work will aid forest managers and scientists alike by clarifying the ways in which forest patterns and disturbance processes influence each other.

5 QUANTIFYING FINE-SCALE SPATIAL HETEROGENEITY IN WILDLAND FUELS

5.1 INTRODUCTION

Wildland fuels are the live and dead vegetation whose biomass is combusted during wildland fire events. Conceptually, these fuels are often separated into distinct strata (canopy fuels > 2m above the ground, surface fuels < 2m above the ground, and ground fuels i.e. duff) and these strata are separated into distinct fuel components (e.g. duff, litter, fine woody debris, coarse woody debris, understory vegetation, saplings, and trees) (Sandberg *et al.*, 2001; Keane, 2015). These fuel components, considered together, form a fuel bed: The complex array of biomass in a given area. Multiple characteristics of these fuel components are important for predicting how they will combust, such as the fuel moisture, mineral content, and particle size (Burgan and Rothermel, 1984). However, fuel load (biomass per unit area) is the single most important characteristic of wildland fuels for determining fire behavior (Burgan and Rothermel, 1984; Finney, 1998; Linn *et al.*, 2002; Sandberg *et al.*, 2007) and emissions (Weise and Wright, 2014; Keane and Lutes, 2016). This is why fire hazard reduction treatments are often focused on reducing fuel loads (Agee and Skinner, 2005; Stephens and Moghaddas, 2005a). Describing fuel loads is also important to quantify carbon stocks (Hurteau *et al.*, 2008; Eskelson *et al.*, 2016; Eskelson and Monleon, 2018; Foster *et al.*, 2020) and to understand how fuel loads affect other ecosystem processes such as tree reproduction (Lanini and Radosevich, 1986) and wildlife movement (Ucitel *et al.*, 2003). Given the importance of fuel loads, it is crucial to quantify them accurately and precisely.

Most existing fuel classification systems describe fuel abundance in terms of mean fuel load for the various fuel components (Anderson, 1982; Sandberg *et al.*, 2001; Scott and Burgan, 2005; Ottmar *et al.*, 2007). This practice is largely driven by the Rothermel fire behavior model (Rothermel, 1972), which is the backbone of many tools used to predict wildfire behavior and effects in the United States (Burgan and Rothermel, 1984; Finney, 1998, 2006; Sandberg *et al.*, 2007). The Rothermel model assumes that fuel loads are uniformly distributed across the modeled spatial domain, which in many applications is a square 900 m^2 area. In reality, fuel loads are highly variable at fine scales (sub-meter to tens of meters) for most fuel components (Keane *et al.*, 2012a, 2013; Kreye *et al.*, 2014; Vakili *et al.*, 2016a). Furthermore, research has shown that fine-scale heterogeneity in fuel characteristics impacts fire behavior and effects. For example, different leaf morphologies cause the physical properties of the litter layer to vary under the crowns of different tree species, creating fine-scale variation in maximum air temperature during prescribed fires (Williamson and Black, 1981). In multiple ecosystems, experimental manipulations of fuel loads at fine scales have altered the composition of the post-fire community by changing rates of mortality and germination (Thaxton and Platt, 2006; Rocca, 2009; Wiggers *et al.*, 2013). Varying patterns of meter-scale tree crowns and gaps has altered hectare-scale fire behavior in a simulation study (Atchley *et al.*, 2021) and meter to meter variation in surface fuels has led to fine-scale variation in fire behavior in real fires (Loudermilk *et al.*, 2012, 2014). During the 2013 Rim Fire, small shrub patches (mean size 30 m^2) moderated fire behavior and reduced tree mortality within the patches (Lutz *et al.*, 2017).

Given the importance of fine-scale spatial heterogeneity in fuel component loads, it is important to quantify this heterogeneity and to understand its impact on fire behavior. Despite progress, initial efforts suffer from important limitations. Researchers have combined terrestrial laser scan data with classified high resolution photographs to develop fine-scale fuel bed maps that are subsequently linked to fine-scale observations of fire behavior (Hiers *et al.*, 2009, 2021; Loudermilk *et al.*, 2009, 2012, 2014; O'Brien *et al.*, 2016b; Hawley *et al.*, 2018). However, the linkage between fuels and fire in this approach is statistical, rather than mechanistic. That is, predictions of fire behavior are based on the empirical correlation between fuels and fire behavior, rather than on the underlying physical process of combustion. Such empirically based statistical models are unable to predict fire behavior outside the narrow context in which the models were fit (i.e., frequently-burned pine savannahs in the southern US). Another approach has been to use variogram analysis to describe the structure of spatial autocorrelation within various fuel components across different ecosystem types and disturbance histories (Keane *et al.*, 2012a, 2012b; Bivand *et al.*, 2013; Vakili *et al.*, 2016a). However, this variogram approach is purely descriptive and provides a spatially sparse set of observed loads. Without the ability to produce a continuous map of fuel loads, study of the connection between the spatial properties of fuel beds and fire behavior is impossible without physically burning the sampled fuel beds.

A third line of research has focused on coupled fire-atmosphere models. These models are capable of predicting wildfire behavior in forests with spatially heterogeneous fuel beds (Linn *et al.*, 2005; Ziegler *et al.*, 2017; Atchley *et al.*, 2021; Mueller *et al.*, 2021). The main drawback is that resolving the underlying fluid dynamics is too computationally intensive to be helpful for predicting fire behavior in real time. Moreover, applications of these models, sometimes known as computational fluid dynamic (CFD) models, have been primarily focused on canopy fuels. They either assume that surface fuels are homogeneously distributed or that their distribution mirrors the distribution of the canopy fuels. Neither assumption reflects reality. Surface fuels are rarely distributed homogeneously (Keane *et al.*, 2012a) and the canopy is often a poor predictor of surface fuels (Lydersen *et al.*, 2015; Leite *et al.*, 2022).

In this study, I develop and test novel methods for sampling and quantifying the spatial heterogeneity of wildland fuels. These methods are designed to provide added reality to existing CFD models and to meet the demands of next-generation empirical models. These are in development and will be able to incorporate information on fine-scale heterogeneity of fuel loads into predictions of wildfire behavior (Finney 2020, *pers. comm.*). Specifically, I propose to collect extensive and spatially explicit field data describing fuel loads. I will then use these data to build hierarchical spatial models using Gaussian process spatial random effects to describe fine-scale spatial patterns in the fuel load of a comprehensive suite of fuel components. Of particular importance are the surface and ground fuels, which cannot be accurately measured using remote sensing (Jakubowksi *et al.*, 2013) but which are crucial drivers of fire behavior (Rothermel, 1972; Burgan and Rothermel, 1984; Agee and Skinner, 2005).

Hierarchical spatial models have proven to be an effective tool for 1) quantifying fine-scale spatial pattern, 2) controlling for the effects of fine-scale spatial autocorrelation when estimating other model parameters, and 3) making predictions that incorporate information about the spatial pattern (Diggle and Ribiero, 2007). They are particularly well suited in cases where the response variable is non-normally distributed, unlike the related approach of kriging. Like variogram analysis, these models are capable of quantifying spatial patterns in fuel loads, facilitating study on the causes and effects of such patterns. However, once model parameters have been estimated, these models can also be used to simulate new data with realistic spatial properties. In this way, sparse observations can be interpolated to continuous fuel beds, and a limited number of observed locations can be extrapolated to an infinite array of realizations with realistic spatial properties. The effects of these spatial properties on fire behavior could be studied using a CFD fire model. Such extrapolation beyond the observed locations would provide two benefits: First, parameter uncertainty could be propagated through the simulations, ensuring that the modeled fire behavior reflects the uncertainty about the spatial pattern of fuel loads. Second, and more importantly, ensembles of simulated fuel beds are necessary to predict fire behavior across the ensembles of unsampled real fuel beds existing on the landscape because the modeled fire behavior is dependent upon the specific realized arrangement of fuel biomass (Atchley *et al.*, 2021). Without these ensembles of simulated fuel beds, predictions of fire behavior would likely be overfit to the specific realized arrangements in the few sampled fuel beds.

However, there are numerous challenges in attempting to apply these hierarchical spatial models to the study of wildland fuels. First and foremost, these models require many replicate observations with explicit spatial information. Measuring fuel load requires costly and time-intensive labor in the field, especially for ground and surface fuels. At the same time, the computational requirements for parameter estimation scale exponentially with the number of observations, imposing a major hurdle to estimating the model parameters even when there are sufficient data (Heaton *et al.*, 2019). Finally, because realistic simulations are a core goal of this work, models must strike a balance between being complex and flexible enough to capture the real patterns of spatial correlation within fuel components and cross correlation between components on one hand, and on the other hand avoiding overfitting or issues with identifiability.

An important and understudied type of real fuel bed is that of a Sierra Nevada mixed conifer forest which has suffered from extensive tree mortality. These conditions have become widespread, especially in the southern Sierra Nevada, in the wake of California's 2012-2015 drought (Asner *et al.*, 2015; Fettig *et al.*, 2019; Stephenson *et al.*, 2019). It is well documented that tree mortality alters the fuel bed as biomass falls from standing snags to the surface (Hoffman *et al.*, 2012b; Donato *et al.*, 2013; Stephens *et al.*, 2018). These changes potentially alter the behavior of wildfires (Wayman and Safford, 2021). It is likely that the same processes driving change in coarse-scale (sub-hectare scale) mean fuel loads change also alter the fine-scale spatial patterns of fuel loads. Given the importance of the fine-scale spatial pattern of fuel loads for determining wildfire behavior and effects and the extensive areas in which mass tree mortality has occurred in the Sierra Nevada, it is crucial to quantify the fine-scale spatial pattern of fuel loads in this context so that we can predict wildfire behavior. However, not all parts of the landscape experience drought mortality equally (Baguskas *et al.*, 2014). Therefore, quantification of the spatial pattern of fuel loads is necessary across varying levels of drought mortality. Furthermore, linking the fine-scale spatial patterns to drought mortality would enable us to apply fine-scale models to predict fuel bed characteristics across entire landscapes because the severity of drought mortality can be measured using cheap and widely available remote sensing.

I demonstrate the use of this sampling protocol and statistical approach in the context of a Sierra Nevada mixed conifer forest which experienced extensive mortality during California's 2012-2015 drought (Asner *et al.*, 2015; Stephens *et al.*, 2018; Fettig *et al.*, 2019; Stephenson *et al.*, 2019). To that end, this study focuses on two questions:

1) Can hierarchical spatial statistical models simulate realistic fuel beds with continuous fine-grain information on fuel loads for a suite of wildland fuel components?
2) Do the parameters of these statistical models vary across different levels of drought mortality severity?

5.2 METHODS

5.2.1 Site description

The area of interest (AOI) for this study is a 17 km^2 site dominated by Sierra Nevada mixed conifer forest. The AOI is located in the Kaweah River watershed in Sequoia National Park (approximately 36.76° N by 118.80° W) between 1,500 m and 1,850 m elevation (Stephenson *et al.*, 2019; Figure 1). The climate is Mediterranean, with mean annual temperature approximately 10° C and annual precipitation of 110-140 cm falling approximately half as snow (Stephenson *et al.*, 2019). Based on the CALVEG classification system (*Vegetation Classification and Mapping*, 2022), the AOI is dominated by the following vegetation alliances: "Mixed Conifer – Pine" (1,160 ha, 68% of the AOI), "Black Oak" (224 ha, 13%), and "Canyon Oak" (130 ha, 8%). For this study, I restricted sampling to the "Mixed Conifer – Pine" alliance, the most widespread conifer alliance in the southern Sierra Nevada. Constituent species of this alliance are ponderosa pine (*Pinus ponderosa*) and sugar pine (*Pinus lambertiana*), alongside white fir (*Abies concolor*), incense-cedar (*Calocedrus decurrens*), knobcone pine (*Pinus attenuata*), and various hardwoods such as black oak (*Quercus kelloggii*). Mountain misery (*Chamaebatia foliosa*), whitethorn ceanothus (*Ceanaothus cordulatus*), whiteleaf manzanita (*Arctostaphylos viscida* ssp. *mariposa*), and greenleaf manzanita (*Arctostaphylos patula*) are important understory shrub species (USDA Forest Service, 2009). Mixed conifer forests across the southern Sierra Nevada experienced extensive tree mortality following a severe drought from 2012-2015 (Asner *et al.*, 2015; Stephens *et al.*, 2018; Fettig *et al.*, 2019; Stephenson *et al.*, 2019).

5.2.2 Drought mortality classification and plot network

Geospatial analysis of remote sensing data was used to randomly place twenty-one inventory plots across three levels of drought mortality severity within the AOI using a random stratified sampling design. Drought mortality severity was assessed using the magnitude of mortality index (MMI) data product from the Ecosystem Disturbance and Recovery Tracker (eDaRT) system. eDaRT uses a time series of LANDSAT data to detect and quantify mortality events of overstory vegetation (Koltunov *et al.*, 2020). MMI provides an estimate of cumulative overstory percent-cover mortality at a 30 m resolution for a specific 5-year period. Given the importance of drought-induced mortality, I used the 5-year period that bracketed the start and end of the historic hotter drought in California, namely 2012-2016 (Stephenson *et al.*, 2018). The MMI raster was smoothed by taking the mean over a 90 m by 90 m window and clipped to just the Mixed Conifer – Pine vegetation alliance. Continuous MMI values were binned into low (<25th percentile, 0-7% cumulative mortality), medium (25-75th percentile, 7-18% cumulative mortality), and high (>75th percentile, 18-100% cumulative mortality) categories (Figure 1). Finally, pixels of the same category were aggregated into polygons and a 30 m inward buffer on each polygon was used to identify core zones of each mortality class.

To ensure safe and efficient access to remote field sites, plot placement was restricted to these core mortality zones with slopes less than 25° and at a distance of 50-600 m from a road or trail. I determined that this restricted accessible area was representative of the wider area of interest (Mixed Conifer – Pine vegetation alliance from 1,500-1,850 m elevation) based on a comparison of the topographic makeup (slope, elevation, aspect) of the full AOI and the accessible area. The accessible area had slightly lower slopes on average but was generally representative of the full AOI (Supplementary Figure 1). Seven plots per mortality class, for a total of twenty-one inventory plots, were randomly placed using a geographic information system within the accessible area of the core mortality zones in a stratified random research design.

5.2.3 Data collection

On each inventory plot, data were collected describing seven fuel components: Duff, litter, fine woody debris (FWD; woody particles < 7.6 cm diameter), coarse woody debris (CWD; woody particles ≥ 7.6 cm diameter), understory vegetation (forbs, graminoids, shrubs, and trees less than 1.37 m height), trees, and saplings (trees Figure 2 and Figure 3). Plots were sampled in the summer of 2021, approximately five years after the main pulse of drought mortality. The core approach for data collection was to modify a standard forest inventory protocol. The line-intercept method (Brown, 1974) was used to observe the fuel load of duff, litter, fine woody debris, and coarse woody debris. The line intersection method was used to sample understory vegetation (Lutes *et al.*, 2006). Finally, fixed area plots were used to inventory trees and saplings. These inventory methods all provide the information necessary to estimate fuel loads when combined with allometric equations (van Wagtendonk *et al.*, 1996, 1998; Jenkins *et al.*, 2013; McGinnis *et al.*, 2010). For duff, litter, and fine woody debris tallies, the standard protocol was modified to include a dense set of subsamples within each plot. For coarse woody debris, understory vegetation, trees, and saplings, the standard protocol was modified so that information about the location of each occurrence (either along the transect or within the fixed area plot) was included. Thus, the protocol for these components provided continuous information about the fuel load along the transects or within the plot.

The placement of samples for duff, litter, and fine woody debris were arranged such that the distribution of pairwise distances between samples within a plot spanned the range 0-60 m, with the bulk of pairwise distances being between 0 and 10 meters. This was done in order to maximize the ability of the data to capture a full gradient of spatial autocorrelation between observations. Previous work in other ecosystems using variogram analysis found that most of the autocorrelation in duff, litter, and fine woody debris samples occurs at distances less than 10 meters (Keane *et al.*, 2012a). Therefore, the depth of duff and litter was recorded to the nearest 0.5 cm at subsamples located at 2.0, 2.1, 2.2, 2.3, 2.4, 2.5, 3.0, 3.5, 4.0, 4.5, 5.5, 7.0, 7.5, 9.5, 19.5, and 29.5 meters along each of four transects arranged at cardinal directions from plot center (Figure 2 and Figure 3b).

Tallies of fine woody debris particles intersecting 1-meter subtransects were recorded by time lag classification (particle size classes defined using the time required for a particle's moisture content to reach equilibrium with the atmosphere; 1-hour: 0-0.6 cm; 10-hour: 0.6-2.5 cm; 100-hour: 2.5-7.6 cm). Sixteen 1-meter subtransects were observed on each transect, eight of which lay along the transect from 2-3, 3-4, 4-5, 5-6, 7-8, 9-10, 19-20, and 29-30 m from plot center, and eight of which lay orthogonal to the main transect at 2.5, 3.5, 4.5, 5.5, 7.5, 9.5, 19.5, and 29.5 m along the main transect (Figure 2 and Figure 3d). The standard time lag classes are coarse, and future fire models may require more fine-resolution definition of particle sizes (Finney 2020, *pers. comm.*). To supply that data, individual diameters of fine woody debris particles crossing the main transect 9-10 m from plot center were measured with calipers to the nearest millimeter and recorded (Figure 3c).

Coarse woody debris particles crossing the main transect anywhere from 0-30 m from plot center were inventoried with diameter at intersection, Forest Inventory and Analysis decay class (Woodall and Monleon, 2008), and location along the transect (Figure 2 and Figure 3f).

Understory vegetation (including seedlings, shrubs, forbs, and graminoids) was observed along the transects 0-15 m from plot center using the line-intercept method. For each continuous patch of cover along the transect crews recorded the dominant understory species, the average height, and the along-transect beginning and end points of the patch (Figure 2 and Figure 3e). Tree species were included in the understory sampling if they were shorter than breast height (1.37 m) for conifers, or for hardwoods, if there was no clear central stem.

Trees (stems with diameter at breast height, DBH ≥ 11.3 cm) were inventoried (species, live/dead status, height, DBH, height to live crown, and decay class for snags) and mapped within a cross-shaped fixed area plot extending out to 15 m from plot center at cardinal directions and in belts extending 5 m on either side of the main transects, for a total plot area of 500 m^2 (Figure 2 and Figure 3a).

Likewise, saplings with a clear central stem and a DBH < 11.3 cm and height > 1.37 m were inventoried and mapped within a cross-shaped fixed area plot extending out to 15 m from plot center at cardinal directions and out one meter from the transects on either side, for a total fixed area plot of 116 m^2 (Figure 2 and Figure 3a).

For analysis of the fine-scale spatial patterns within each plot, every observation was assigned easting / northing coordinates relative to plot center. For the duff and litter depths, these coordinates were simply the location of the subsamples, with sixteen subsamples per transect and four transects per plot giving sixty-four unique locations within each plot. For the fine woody debris tallies, each 1-meter subtransect was assigned the coordinates of the center of the subtransect, with sixteen subtransects per transect and four transects per plot giving thirty-two unique locations within each plot (because the along-transect and orthogonal-to-transect subtransects share the same center point). In other words, fine woody debris was observed on thirty-two 1 m^2 quadrats on each plot, and each quadrat was sampled by two orthogonal 1-meter subtransects along with fine woody debris was tallied. For the coarse woody debris, the continuous locations of particles were converted into a 1-meter resolution grid along each transect, yielding thirty subsamples per transect on four transects for a total of 120 unique locations on each plot. Likewise, the continuous locations of understory vegetation were converted into a 1-meter resolution grid, yielding thirty subsamples (each recording the presence or absence of understory vegetation at a location) on four transects for a total of 120 unique locations on each plot. The stem maps of trees and saplings were converted in a two-dimensional grid of 1 m^2 quadrats, yielding 500 unique locations for trees and 116 unique locations for saplings and a count of stems on each location (1 m^2 quadrat). For each fuel component, the individual observations were randomly assigned to one of two datasets. 90% of observations from each drought mortality class were assigned to the training dataset and used to estimate model parameters. The remaining 10% of observations from each drought mortality class were assigned to the validation dataset and used only to test model performance.

5.2.4 Exploratory analysis

If there is spatial autocorrelation not only within the fuel loads of each component, but between the different components, the hierarchical spatial statistical models must capture this behavior in order to reproduce it in simulations. To better understand the relationships between fuel components (e.g., between duff and litter, or between 1-hour fuels and understory vegetation) I created empirical variograms (Diggle and Ribiero, 2007). I also (for co-located observations) calculated the coefficient of correlation between observations from different components. The variograms were visually inspected for signs of spatially structured autocorrelation (between observations of the same fuel component) and spatially structured cross-correlation (between observations of different fuel components). Variograms were constructed separately for each drought severity class in case the relationships between components varied across the drought severity classes.

Most fuel components show strong evidence of spatial autocorrelation, with semi-variance values being lower at shorter distances and increasing with distance before reaching the sill and levelling off. The exceptions, for which variograms are ambiguous or reveal a lack of spatial autocorrelation for at least one drought mortality level, are litter depth, vegetation presence, tree counts, and sapling counts. Only a few pairs of components show any evidence of cross-correlation. There is some evidence of cross-correlation between duff and litter, between 1-hour and 10-hour fine woody debris, between 1-hour and 100-hour fine woody debris, between 1-hour fine woody debris and the presence of understory vegetation, between the presence of understory vegetation and the count of trees, and between the presence of understory vegetation and the count of saplings (Supplementary Figure 2, Supplementary Figure 3, and Supplementary Figure 4).

Across the entire dataset, the correlation coefficient between duff and litter is fairly weak at 0.19. The correlation between 1-hour and 10-hour fine woody debris tallies is stronger, at 0.50. Correlation between 1-hour and 100-hour fuels is weaker (0.10), as is correlation between 10-hour and 100-hour fuels (0.30). Direct correlation coefficients were not available for other pairs of components because the observations were not co-located.

Litter and duff depths were analyzed separately for two reasons. First, a model for the joint distribution of litter and duff depths, including both autocorrelation and cross-correlation, performed poorly in the parameter estimation diagnostics described below. Second, the cross-correlation between duff and litter was relatively weak. By contrast, the cross-correlation and direct correlation among 1-hour, 10-hour, and 100-hour fine woody debris tallies demands that the model incorporate some correlation among these components. Therefore, analysis of 1-hour, 10-hour, and 100-hour fuel loads is distributed across two models. The first model is for the total tally of fine woody debris particles (including 1-hour, 10-hour, and 100-hour fuels) at different spatial locations and the second model is for the size distribution of the individual particles without explicit consideration of space. Coarse woody debris is analyzed in a similar two-part fashion, with one model describing the distribution of CWD tallies across space and the second model describing the size of the individual CWD particles without explicit consideration of space. I analyze the spatial distribution of understory vegetation presence or absence using a binomial model. The quadrat tallies for saplings and trees are analyzed identically but separately in spatially explicit models. I do not attempt to jointly analyze 1-hour fine woody debris and understory vegetation height, despite the apparent cross-correlation between these fuel components, because of the difficulty of constructing a single hierarchical spatial model with multiple different response distributions for the observed data. Other fuel components are likewise modeled separately because of the weakness of the cross-correlation among them.

5.2.5 Duff and litter depths

Duff and litter are analyzed separately, though the structure of each model is identical. Each plot is assigned to a drought severity group $g \in (1, 2, \ldots, G)$. All observations within a plot share the same group, and all model parameters are specific to each group. This approach allows researchers to flexibly define and compare statistical models for various ecological contexts. In this study, there are three groups ($G = 3$) for the three levels of drought severity. I emphasize that, in general, the approach is agnostic as to how groups are defined. For example, a landscape could be stratified into groups based on vegetation type, disturbance history, or edaphic setting. Because the parameters for each group are independent (and the model likewise assumes that the data from different groups are independent), simultaneous estimation of all groups is equivalent to fitting a separate model for each group. I describe and perform simultaneous estimation of parameters for different groups to facilitate cross-group comparisons, which may provide useful insight to how the patterns of fine-scale heterogeneity vary across contexts.

The hierarchical spatial model for the depth of litter or duff is:

Equation 1

$$Y_i \sim \text{Neg.Binomial}(\mu_i, \kappa_{g[i]})$$

where Y_i is the observed depth of duff (or litter) at observation i (rounded to the nearest whole cm), μ_i is the unobserved mean depth of duff or litter at observation i, and $\kappa_{g[i]}$ is the dispersion parameter for the negative binomial distribution for group $g[i]$, the group containing observation i.

The choice of a discrete distribution often used for count data to model a continuous quantity (the depth of duff or litter) bears some explanation. A normal distribution was clearly inappropriate for the observed depths, whose empirical distribution is non-negative, skewed, and with a probability mass at 0. Neither a Gaussian response for log(depths) nor a distribution with positive-continuous support (such as the gamma, inverse gamma, or lognormal) were appropriate because none of these distributions are capable of generating simulated realizations with a depth of 0 cm (lack of litter or duff) at some locations. Such bare patches are present and ecologically important in the real data. A positive-continuous distribution with a mixture model allowing for zero inflation would likewise have been a poor choice because such a model would separate the spatial pattern of zeroes from the spatial pattern of the nonzero depths. In reality the zeros occur adjacent to areas of low depth, and this feature of the real data is an important characteristic to reproduce in simulations. The negative binomial distribution, by contrast, allows a probability mass at zero and non-negative values resulting from the same underlying spatial random effect. A compound Poisson-gamma distribution, which models the sum of gamma-distributed particle sizes for a Poisson-distributed count of particles (Dunn and Smyth, 2005, 2008; Zhang, 2013) would have been a reasonable candidate for analyzing fuel loads, but I was unable to successfully implement a compound Poisson-gamma distribution with a Gaussian process spatial random effect in Stan (see parameter estimation details below), with all attempts failing to converge on simulated data. (Because the distribution does not have a closed-form analytic expression for the probability density, statistical software is forced to approximate the density using Fourier inversion and/or series evaluation when calculating the likelihood; it is likely that minor discontinuities in the densities given by these approximations frustrated the Hamiltonian Monte Carlo algorithm described below.) The conversion of the observed depths (at 0.5 cm resolution) to the depths used for the negative binomial distribution (0, 1, 2, … cm) introduces relatively little error in the modeling of fuel load (van Wagtendonk *et al.*, 1998).

The mean μ_i is log-linked to a linear predictor:

Equation 2

$$\log \mu_i = \beta_{g[i]} + z_{p[i]} + S_{l[i],p[i]}$$

where $\beta_{g[i]}$ is the overall intercept for group $g[i]$. $\boldsymbol{z}$ is a $1 \times P$ vector of normally distributed random plot intercepts for each of the $P = 21$ plots with $z_p \sim \text{Normal}(0, \sigma_{g[p]})$ so that the standard deviation of the plot random effect for plot p depends on which group p is in ($g[p]$). $\boldsymbol{S}$ is an $L \times P$ matrix of realized Gaussian process spatial random effects with a row for each of the $L = 64$ within-plot spatial locations and a column for each of the P plots. $l[i]$ is the index for the location containing observation i and $p[i]$ is the index for the plot containing observation i. The Gaussian process spatial random effect $S_{l[i],p[i]}$ models fine-scale spatial autocorrelation within a plot, while coarse-scale variation between plots within a group is modeled by the plot random effect $z_{p[i]}$.

The vector of Gaussian process realizations for all the locations within a plot, $\boldsymbol{S}_{*,p}$, is the result of a Gaussian process modeling fine-scale spatial autocorrelation:

Equation 3

$$\boldsymbol{S}_{*,p} \sim \text{MVN}(\boldsymbol{0}, \boldsymbol{\Sigma}_{g[p]})$$

where $\boldsymbol{\Sigma}_g$ is the $L \times L$ covariance matrix for the L spatial locations within each plot belonging to group g, and $g[p]$ is the index for the group containing plot p. The Gaussian process parameters, and thus the covariance matrix, are identical across plots within a group, but vary between groups. Each plot gets a separate draw from the multivariate normal distribution (MVN). Thus, the observations from within the same plot are spatially autocorrelated, but observations from separate plots are independent. This assumption (proposed and first implemented by Rosenthal 2021, *pers. comm.*) greatly eases the computational burden of estimating parameters for the Gaussian process (Heaton *et al.*, 2019) by enabling likelihood calculations to work with $G = 3$ $L \times L$ covariance matrices rather than a single $N \times N$ covariance matrix with all the observations and $N \gg L$ (where N is the number of observations, e.g. $N =$ 1,107 observations for the duff training dataset). This assumption is sound given the distances between plots (ranging from 150 – 3,700 meters; Figure 1), which are substantially greater than the plausible range of spatial autocorrelation between observations of litter or duff depths (Keane *et al.*, 2012a, 2012b).

The covariance matrix for each group g is constructed using an exponentiated quadratic kernel:

Equation 4

$$\boldsymbol{\Sigma}_g = \alpha_g^2 \times \exp(\frac{-\boldsymbol{D}^2}{2\nu_g^2})$$

where α_g is the magnitude of the Gaussian process spatial random effect for group g, $\boldsymbol{D}$ is the $L \times L$ matrix of pairwise distances between observations within a plot, and ν_g is the length scale parameter of the Gaussian process spatial random effect for group g, which controls the rate at which the autocorrelation between observations decays as the distance between them increases (higher values of ν_g lead to autocorrelation at longer distances).

5.2.6 Fine woody debris tallies

The model for fine woody debris tallies follows the model for duff and litter depths, with two exceptions. First, there are only thirty-two unique locations observed on each plot, so $L = 32$. Second, because there are multiple observations per spatial location in the fine woody debris tallies sampling design, there is an additional parameter used to construct the between-locations covariance matrix:

Equation 5

$$\boldsymbol{\Sigma}_g = \alpha_g^2 \times \exp(\frac{-\boldsymbol{D}^2}{2\nu_g^2}) + (\boldsymbol{I} \times \tau_g)$$

where $\boldsymbol{\Sigma}_g$, α_g, $\boldsymbol{D}$, and ν_g are as defined for the duff and litter depths model (Equation 4). $\boldsymbol{I}$ is an $L \times L$ matrix whose entries are 1 on the diagonal and 0 otherwise. The new parameter τ_g is the Gaussian process nugget parameter for group g describing additional covariance between samples from the same location beyond that which would be expected between samples separated by a distance of 0 m. Estimation of τ_g was not possible for other fuel components because there is only a single observation per spatial location in those data. Without replicate observations at each spatial location, it is not possible to distinguish between variation explained by τ_g and residual variation.

5.2.7 Fine woody debris diameters

The diameters of individual particles of fine woody debris are modeled using an inverse gamma distribution truncated at the upper end at 7.6 (T[,7.6]):

Equation 6

$$Y_i \sim \text{Inv-gamma}(\gamma_i, \delta_i)\text{T}[,7.6]$$

where Y_i is the diameter (in centimeters) of particle i (with $Y_i < 7.6$ cm per the definition of fine woody debris), γ_i is the shape parameter and δ_i is the rate parameter for the inverse gamma distribution for observation i. Initial attempts to fit a model using the standard rate/shape parameterization failed model diagnostic tests (described below), so instead I use the mean/precision parameterization for the inverse gamma (Bourguignon and Gallardo, 2020), which gives a mean parameter μ and a precision parameter ϕ. These are related to γ and δ by the equations

Equation 7

$$\gamma_i = \phi_{g[i]} + 2$$

and

Equation 8

$$\delta_i = \mu_i(1 + \phi_{g[i]})$$

where $\phi_{g[i]}$ is the precision for group $g[i]$, the group containing observation i, and μ_i is the mean of the inverse gamma distribution for observation i. The precision for observation i simply varies according to the group $g[i]$ containing observation i: $\phi_i = \phi_{g[i]}$. $\mathrm{E}[Y] = \mu$ and $\mathrm{Var}[Y] = \frac{\mu^2}{\phi}$.

The mean for observation i is given by a linear function with a log link:

Equation 9

$$\log(\mu_i) = \beta_{g[i]} + z_{p[i]} + b_{u[i]}$$

where $\beta_{g[i]}$ is the intercept for group $g[i]$, $z_{p[i]}$ is a normally distributed plot random effect for plot $p[i]$, and $b_{u[i]}$ is a normally distributed random effect for subtransect $u[i]$. $z_p \sim \mathrm{Normal}(0, \sigma_{g[p]}^{PLOT})$ and $b_u \sim \mathrm{Normal}(0, \sigma_{g[t]}^{SUBTRANSECT})$. Thus, this model does incorporate fine-scale variation within a plot, but without an explicit consideration of space. It was not feasible to collect individual particle diameters on enough 1-meter subtransects within each plot to estimate the parameters for an explicitly spatial gaussian process random effect, which is why the fine woody debris diameters model does not include an explicit consideration of space.

5.2.8 Coarse woody debris tallies

Existing literature describing the spatial pattern of coarse woody debris loads both assumes (by the sampling design) and finds a coarser scale of spatial autocorrelation for this fuel component, with range values from 22-157 m (Keane *et al.*, 2012a). The objective for this study is to understand fine-scale autocorrelation, so both the sampling design and the statistical analysis were built to detect spatial autocorrelation in the number of coarse woody debris particles at ranges from 1-60 m. Coarser scale heterogeneity within a drought mortality level is captured by a plot random effect, which is not explicitly spatial. The sampling design used here (with only seven plots per group and no explicit spatial consideration in the location of plots on the landscape) is not conducive to analysis of coarse (between-plot; 150-3,700 m) spatial variation, though this is an important topic for future research.

The model for coarse woody debris tallies is similar to the model for duff or litter depths, with three exceptions. First, there are $L = 120$ distinct spatial locations observed on each plot. Second, the response variable is Poisson distributed:

Equation 10

$$Y_i \sim \mathrm{Poisson}(\mu_i)$$

where Y_i is the count of coarse woody debris particles on the ith 1-meter subtransect and μ_i is the mean density of coarse woody debris particles for that observation. The Poisson distribution is selected as the response distribution because a negative binomial distribution consistently resulted in parameter estimation failing diagnostic tests (described below).

The third difference is the inclusion of a transect random effect in the linear predictor:

Equation 11

$$\log \mu_i = \beta_{g[i]} + z_{p[i]} + S_{l[i],p[i]} + b_{a[i]}$$

where μ_i is the mean density of coarse woody debris particles on observation i, $\beta_{g[i]}$ is the intercept for group $g[i]$, $z_{p[i]}$ is a plot random effect with $z_p \sim \text{Normal}(0, \sigma_{g[p]}^{PLOT})$, and $S_{l[i],p[i]}$ is a Gaussian process spatial random effect, all as defined for the litter and duff models. The new term, $b_{a[i]}$, is a normally distributed random effect for observations from the same azimuth (i.e., observations are either from a transect running North/South or one running East/West), with $b_a \sim \text{Normal}(0, \sigma_{g[t]}^{AZIMUTH})$. I include the transect random effect to capture the potential effect of non-random orientation of CWD particles (e.g., due to slope). Such non-random orientation could induce correlation between observations (1-meter subtransects) which share the same orientation (either North/South or East/West). For example, if most particles are oriented on an East/West axis then a transect also running East/West will give counts biased downward because the sampling transect will likely lie parallel to the particles, while a transect running North/South will give counts biased upwards. An azimuth effect was not necessary with the FWD tallies model because the two orthogonal subsamples at each spatial location give an unbiased estimate of the particle density at that location, even if the particles are nonrandomly oriented (van Wagner, 1982).

5.2.9 Coarse woody debris diameters

Initial testing showed that a unified model for the diameters of both fine and coarse woody debris performed poorly in capturing the frequency and size of coarse woody debris particles, which occur as rare tail events in a shared diameter distribution. Instead, fine woody debris diameters and coarse woody debris diameters are analyzed separately, though with similar model structure. The first difference is that the truncation for the coarse woody debris diameters is different:

Equation 12

$$Y_i \sim \text{Inv-gamma}(\gamma_i, \delta_i)\text{T}[7.6, 110.1]$$

with $Y_i > 7.6$ cm per the definition of coarse woody debris and $Y_i < 110.1$. The upper limit is based on the maximum diameter observed in the data (110.0 cm) to prevent simulation of unrealistically large diameter particles when constructing simulated fuel beds. As with the fine woody debris diameters model, the inverse gamma is parameterized to use a distinct mean $\mu_{g[i]}$ and precision $\phi_{g[i]}$ for each group. However, for the coarse woody debris model $\mu_{g[i]}$ is used directly, without random effects, and with the constraint that $7.6 < \mu_{g[i]} < 110.1$. This approach was adopted because a more flexible model, with an unconstrained (log-scale) intercept and plot-level random effect, resulted in occasional problematic posterior samples with $\mu_{g[i]} \ll 7.6$, which meant that particles meeting the definition of coarse woody debris ($Y_i > 7.6$ cm) were extremely implausible (and thus difficult to simulate).

5.2.10 Understory vegetation presences

The model for understory vegetation presences is similar to the model used for duff and litter depths, though with a Bernoulli response because the observations are for presence/absence data:

Equation 13

$$Y_i \sim \text{Bernoulli}(\mu_i)$$

where Y_i is the presence (1) or absence (0) of understory vegetation at observation i and μ_i is the probability of presence at location i. There are $L = 120$ unique spatial locations observed on each plot. μ_i is linked to a linear predictor by a logit link:

Equation 14

$$\operatorname{logit} \mu_i = \beta_{g[i]} + z_{p[i]} + S_{l[i],p[i]}$$

where $\beta_{g[i]}$ is the intercept for group $g[i]$, $z_{p[i]}$ is the normally distributed plot random effect for plot $p[i]$, and $S_{l[i],p[i]}$ is a Gaussian process spatial random effect for location $l[i]$ on plot $p[i]$, all as defined for the duff and litter depths model above.

5.2.11 Tree and sapling stem counts

The densities of trees and of saplings are modeled identically but separately in a model similar to the model for duff and litter depths, though with a Poisson response:

Equation 15

$$Y_i \sim \text{Poisson}(\mu_i)$$

where Y_i is the number of trees (or saplings) in the ith 1 m^2 quadrat and μ_i is the latent intensity of the inhomogeneous Poisson point process at location i. μ_i is linked to a linear predictor by a log link:

Equation 16

$$\log \mu_i = \beta_{g[i]} + z_{p[i]} + S_{l[i],p[i]}$$

where $\beta_{g[i]}$ is the intercept for group $g[i]$, $z_{p[i]}$ is the normally distributed plot random effect for plot $p[i]$, and $S_{l[i],p[i]}$ is a Gaussian process spatial random effect for location $l[i]$ on plot $p[i]$, all as defined for the duff and litter depths model above. This model can represent the spatial pattern of trees (or saplings) as the result of a latent field of stem density. This latent field gives rise to clumps (areas with more than the average density of stems) and gaps (areas with less than the average density of stems). However, it is not capable of modeling true inter-stem interactions such as dispersal and competition. I opt to include this simple model for tree and sapling spatial patterns to maintain consistency with the framework for modelling surface and ground fuels, which are the primary focus of this study.

5.2.12 Parameter estimation and model validation

Priors were defined for each parameter in each fuel component model using prior predictive sampling to define plausible prior distributions (Betancourt, 2020b). Priors were the same across the drought mortality levels (groups). For all models including a Gaussian process, the prior for the length scale parameters was $\text{Inv-Gamma}(5,40)$, giving a prior probability distribution whose bulk lay in the interval 0.1 – 60.0 m, the range of within-plot pairwise distances sampled according to our study design (Betancourt, 2020a). Posterior parameter values were estimated using Hamiltonian Monte Carlo as implemented in the Stan software language version 2.30.1 (Gabry *et al.*, 2022; Stan Development Team, 2022b). Bayesian parameter estimation software such as Stan provides the flexibility needed to describe models with per-plot Gaussian processes, which is rare in the current R package ecosystem. All models were run with four chains, each running for 2,000 samples and discarding the first 1,000 samples as a warmup. Data preparation, statistical analysis, and processing of results were performed in R version

4.1.1 (R Core Team, 2021) using the packages bayesplot (Gabry and Mahr, 2021), bayestestR (Makowski *et al.*, 2019), cmdstanr (Gabry *et al.*, 2022), cowplot (Wilke, 2020), elevatr (Hollister, 2021), ggspatial (Dunnington, 2021), gstat (Pebesma, 2004), here (Müller, 2020), posterior (Bürkner *et al.*, 2021), raster (Hijmans, 2021), sf (Pebesma, 2018), tidyverse (Wickham *et al.*, 2019), tmap (Tennekes, 2018), and USAboundaries (Mullen and Bratt, 2018).

For each model, performance of the Hamiltonian Monte Carlo algorithm in estimating the model parameters was assessed by inspecting standard diagnostics (divergences, R-hat values, effective sample sizes) for signs of poor performance using the cmdstanr package (Gabry *et al.*, 2022). Specifically, a feature of Hamiltonian Monte Carlo is that where the sampler has difficulty capturing regions of high curvature in parameter space the sampler registers divergences, which indicate that there is likely a problem with biased parameter estimation (Stan Development Team, 2022a). R-hat indicates whether the multiple MCMC chains have converged to the same posterior distribution, while effective sample size estimates the number of effectively independent samples for each parameter in the posterior (Gelman *et al.*, 2021). For this study I relied on the built in diagnostics for the cmdstanr package, which throw warnings if the split R-hat (Gelman *et al.*, 2021) is greater than 1.05. These diagnostics are different from the more robust split-folded R-hat (Vehtari *et al.*, 2021), for which the authors recommend rejecting models with R-hat greater than 1.01. To evaluate the extent to which the posterior distributions were informed by the data rather than the prior assumptions, I plotted posterior parameter distributions against the prior probability density for each parameter.

Models were evaluated on their ability to: 1) Make pointwise predictions of both training and validation data, 2) produce response distributions similar to those observed in the training and validation data, and/or 3) produce realistic plot-scale (i.e., sub hectare scale, the standard scale to describe fuel loads) simulated fuel beds to assess the realism of the emergent plot-scale behaviors implied by the fine-scale models. To accomplish these validations, I used three sets of posterior predictions (datasets simulated using each draw of the posterior samples). First, new simulated responses were drawn for the training data. For the negative binomial and Poisson models (duff and litter depths, fine woody debris tallies, coarse woody debris tallies, tree tallies and sapling tallies) I compared the observed data and the mean simulated value for each observation and calculated the mean absolute error (MAE) and weighted mean absolute percentage error (wMAPE; MAE divided by the mean) for predictions. wMAPE and MAE were not calculated for either the fine woody debris diameters or the coarse woody debris diameters, because making pointwise predictions of individual diameters is not a goal for these models. wMAPE values below 0.5 were considered acceptable. Visual comparisons between the observed and simulated data used a simple linear fit between the mean simulated values and the observed values to assess model bias in making pointwise predictions. To assess models' ability to generate realistic response histograms, empirical density functions, and/or cumulative density functions for both observed and simulated data were compared. Second, the validation observations for each model were randomly held out from the training dataset and only used to validate model performance using the same techniques, again using fitted estimates for the random effect realizations. Finally, I simulated new datasets of twenty-one plots using posterior parameter values but drawing new random effect realizations, converted simulated values to biomass estimates using the methods described in Foster *et al.* (2020), and aggregated the observations to the plot level mean. This final validation is an important check that the fuel beds simulated by the models are realistic. To evaluate whether model parameters varied according to drought mortality severity, 89% shortest probability interval (Liu *et al.*, 2015) credible intervals (CIs) were calculated for each parameter and CIs compared across groups; where the CIs do not overlap I interpret this as a strong effect of drought mortality severity on the parameters describing the fine-scale spatial distribution of fuel loads. 89% credible intervals were selected based on the recommendation of McElreath (2016), with the understanding that any specific threshold is somewhat arbitrary.

5.3 RESULTS

5.3.1 Duff depths

R-hat values, lack of divergences, and effective sample sizes indicate satisfactory performance of the Hamiltonian Monte Carlo algorithm in estimating the parameters for the duff model. Posterior predictions indicate good model performance in predicting both the training data and the validation data, with wMAPE of 0.33 (MAE 1.5 cm and mean 4.6 cm) for the training data and 0.47 (MAE 2.2 cm and mean 4.6 cm) for the validation data (Supplementary Figure 5 and Supplementary Figure 8). Comparisons between the histogram of training observations and the distribution of simulated depths reveal that the model-predicted behavior is broadly consistent with the observed data. However, the model tends to under-predict the number of 0 cm duff depths, over-predict the number of 1 cm duff depths, and under-predict the number of 3 cm duff depths, suggesting zero inflation (Supplementary Figure 6). The validation data histogram was consistent with the simulated distributions for the validation sample (Supplementary Figure 9). The cumulative density function of the observed duff depths in both the training and the validation data falls within the range of cumulative density functions generated from simulated observations, indicating consistency between the model and reality (Supplementary Figure 7 and Supplementary Figure 10). When simulating plot-level fuel loads using posterior parameter values and drawing new random effect realizations, the observed distribution of plot-level fuel loads is within the range of behaviors predicted by the model (Supplementary Figure 11). However, the model simulations include rare outcomes with extreme plot-level duff loads greater than 1,000 Mg/ha or less than 1 Mg/ha which are ecologically implausible.

Comparison between the posterior distributions and the prior distribution for each model parameter indicate that the posterior distributions for all parameters are strongly informed by the data, rather than the prior (Figure 4a-e). However, the 89% credible intervals for each parameter overlap among the drought mortality classes (Figure 4a-e and Table 1). These results suggest that there are weak or no effects of the different drought mortality levels on the spatial pattern of duff depths, including on the overall mean depth.

5.3.2 Litter depths

Diagnostics for parameter estimation indicate good convergence of the Hamiltonian Monte Carlo algorithm for the litter model, though a high setting of the *adapt_delta* algorithm tuning parameter of 0.99 was required to avoid divergent transitions. There is a positive correlation between the posterior mean predicted values and the observed values for the training dataset, though with a bias towards under-prediction of depths greater than approximately 5 cm in the posterior predictions for the training dataset (Supplementary Figure 12). This bias is not evident in predictions for the validation dataset (Supplementary Figure 15). wMAPE for the posterior predictions from the training dataset was 0.36 (MAE 1.71 cm, mean 4.8 cm) and wMAPE for the predictions from the validation dataset was 0.38 (MAE 1.8 cm, mean 4.7 cm). There is generally good agreement between the depth distribution of observations from the training dataset and validation datasets and the depth distribution of simulated datasets. Again, however, the model tends to overpredict the proportion of 1 cm depths while slightly underpredicting the proportion of 2 cm depths (Supplementary Figure 13 and Supplementary Figure 16). However, the observed cumulative density function for training data depths is within the envelope of cumulative density functions found in the posterior predictions, indicating that the true behavior is within the range of possibilities predicted by the model (Supplementary Figure 14 and Supplementary Figure 17). The observed cumulative density function of plot-level fuel loads falls within the range of behaviors simulated using posterior parameter values and drawing new random effects realizations, though again the model occasionally simulates plot-level fuel loads with extremely high or extremely low fuel loads (Supplementary Figure 18).

The posterior distributions for the group intercept, the Gaussian process magnitude, the plot random effect standard deviation, and the negative binomial dispersion are all very constrained relative to the prior distribution, indicating that the posterior estimates for these parameters are well informed by the data rather than the prior (Figure 5a, Figure 5b, Figure 5d, and Figure 5e). By contrast, the data are less informative about the length scale parameters. There is extensive overlap between the posterior and prior distributions for the length scale parameters for the medium and high drought mortality sub models and between the posterior and prior distributions (Figure 5c). The posterior distributions suggest that increasing levels of drought mortality may result in increased values for the group-level intercept and decreased values for the Gaussian process magnitude (Figure 5a, Figure 5b, and Table 2). The 89% credible intervals for the Gaussian process magnitude do not overlap between the low and high levels of drought mortality. This indicates that the relative strength of the fine-scale spatial random effect was higher for areas with low levels of drought mortality than it was for areas experiencing high levels of drought mortality. For the group-level intercept parameter, representing (log) average litter depths within a drought mortality class, uncertainty is wide relative to any differences and the 89% credible intervals across the different levels of drought mortality overlap (Figure 5, Table 2).

5.3.3 Fine woody debris tallies

Hamiltonian Monte Carlo diagnostics for the fine woody debris tallies model indicate good convergence, again requiring an *adapt_delta* of 0.99. Posterior predictions generated using the training data show that the model is adepts at predicting individual observations (Supplementary Figure 19), with wMAPE of 0.19 (MAE 3.8 particles/m and mean 19.7 particles/m). Posterior predictions generated using the validation dataset tend to overpredict observed tallies for counts above approximately 25 for both medium and high drought mortality sub-models (Supplementary Figure 22), with wMAPE of 0.38 (MAE 8.0 particles and mean 21.2 particles). The model did a good job reproducing the overall distribution of observations in both the training and validation datasets (Supplementary Figure 20, Supplementary Figure 21, Supplementary Figure 23, and Supplementary Figure 24).

Comparison of posterior distributions for each model parameter with the prior distributions indicate that posterior estimates for most parameters are strongly informed by the data, rather than the prior distribution (Figure 6a and Figure 6c-f). The exceptions are the Gaussian process length scale parameters for the low and medium drought mortality classes, which are only moderately well informed by the data (Figure 6b). Varying levels of drought mortality do not have strong effects on the parameters describing the fine-scale distribution of fine woody debris tallies relative to the uncertainty in those parameters: 89% credible intervals overlap among all levels of drought mortality for all parameters (Table 3).

5.3.4 Fine woody debris diameters

As with fine woody debris tallies, model diagnostics for the fine woody debris diameters model are satisfactory, but only after setting *adapt_delta* to 0.99. Posterior predictive plots generated using the training data show broad agreement between the model predictions and the observed data (Supplementary Figure 25). However, the observed cumulative density function for the training data exhibits a stepwise pattern (corresponding to the rounding of diameters to the nearest 0.1 cm) which pushes the empirical cumulative density function to the edges of the envelope of cumulative density functions generated using model predictions (which include truly continuous diameters; Supplementary Figure 26). This is a minor issue because the rounding of diameters to the nearest 0.1 cm was a result of the sampling protocol; in this case, the model predictions are likely closer to the underlying physical reality (diameters are continuously distributed) than the observed data are.

The probability density function and cumulative density function constructed from the validation data fall within the envelope of posterior predictions for those observations (Supplementary Figure 27 and Supplementary Figure 28), with the exception that there is a smaller proportion of 0.1 cm diameters in the observed data than the model predicts. Again, this is likely an artifact of the way physically continuous diameters were rounded to the nearest 0.1 cm in the validation data. When combining simulations from the fine woody debris tallies model and the fine woody debris diameters model (both with new realizations of random effects) to simulate plot-level mean fuel loads, the observed data fall within the range of cumulative density functions for simulated plots. However, the observed spread of plot-level means is very tight relative to model predictions (Supplementary Figure 29).

Comparison of the posterior probability density functions with the prior probability density functions indicates that the intercept and the precision parameter are strongly informed by the data (Figure 7a and Figure 7d). For the plot random effect standard deviation, the high drought mortality parameter is well informed by the data, but for the low and medium levels of drought mortality the posterior is very similar to the prior (Figure 7b). For the subtransect random effect standard deviation, results are moderately well informed by the data, with the model ruling out values less than approximately 0.1 for all three levels of drought mortality (Figure 7c). The 89% credible intervals for the three levels of drought mortality overlap for all parameters except the plot random effect standard deviation, which should not be interpreted because the posteriors for the low and medium levels of drought mortality are so similar to the prior (Table 4). Median posterior values for the standard deviations of the plot random effect and the subtransect random effect are comparable to the differences in median intercept values across the three levels of drought mortality, indicating that there is as much variation in the mean fine woody debris particle diameter between different locations within a level of drought mortality as there is between levels of drought mortality.

5.3.5 Coarse woody debris tallies

After setting the *adapt_delta* to 0.99, the coarse woody debris tallies model estimated parameters without divergent transitions, and with good convergence shown by R-hat and effective sample size. Posterior predictions for both the training data and validation data show that for any specific location the mean simulated values tend to overpredict (for observed 0s) or underpredict (for counts above 0) the observed count (Supplementary Figure 30 and Supplementary Figure 33). However, interpretation of the posterior prediction plots is complicated by the very low mean tallies in both the training and validation datasets. The wMAPEs for coarse woody debris tallies are poor, at 1.6 (MAE 0.3 particles/m and mean 0.2 particles/m) for the training dataset and 1.6 (MAE 0.3 particles and mean 0.2 particles) for the validation dataset. By contrast, the overall distribution of observed coarse woody debris tallies is consistent with model predictions (i.e., the observed distributions lie within the envelope of simulated distributions; Supplementary Figure 31, Supplementary Figure 32, Supplementary Figure 34, and Supplementary Figure 35).

Comparison of the posterior probability densities with the prior probability densities indicates that only the intercept and the Gaussian process magnitude estimates are well informed by the data (Figure 8a and Figure 8b). For the other parameters, (the Gaussian process length scale, the plot random effect standard deviation, and the transect random effect standard deviation), the posterior strongly resembles the prior, indicating that the posterior estimates are not informed by the data (Figure 8c-e). There is substantial overlap across the 89% credible intervals of all three drought mortality levels for all model parameters: Any effects of the severity of drought mortality on the model parameters are minor relative to the uncertainty in those parameters (Table 5).

5.3.6 Coarse woody debris diameters

Model diagnostics indicate that Hamiltonian Monte Carlo algorithm performed well in estimating the parameters for the coarse woody debris diameters model. Posterior predictions generated using the training data indicate that the distribution of coarse woody debris diameters observed in the training data is consistent with model predictions (Supplementary Figure 36 and Supplementary Figure 37). Posterior predictions generated using the validation data likewise show generally good agreement between model predictions and observed data, though the dearth of coarse woody debris particles between 5 and 25 cm in diameter in the medium drought mortality group is on the edge of the model-simulated envelope (Supplementary Figure 38 and Supplementary Figure 39).

Posterior distributions for both the mean and precision parameters are distinctly different from the prior distributions for all three sub models, indicating that the posterior estimates are well informed by the data (Figure 9a and Figure 9b). The 89% credible intervals for all three classes overlap for both the mean and the precision parameters (Table 6). When simulating new plot-level fuel loads using new draws for the random effects, the coarse woody debris tallies and diameters models produce a simulation envelope which contains the observed behavior. This indicates that model predictions are broadly consistent with reality (Supplementary Figure 40). However, the highest simulated plot mean fuel loads are generally higher than the highest observed loads.

5.3.7 Understory vegetation presences

Model diagnostics for the understory vegetation presences model indicate good performance of the Hamiltonian Monte Carlo algorithm in estimating parameter values. Both posterior predictions generated using the training data and posterior predictions generated using validation data show good agreement between the predicted presence probabilities and the observed presence probabilities for binned groups of observations (Supplementary Figure 41 and Supplementary Figure 42). Posterior distributions are sharply different from the prior distributions for the Gaussian process magnitude and Gaussian process length scale parameters for all three groups (Figure 10b and Figure 10c), but posterior distributions are similar to the prior distributions for both the intercept and the standard deviation of the plot random effect (Figure 10a and Figure 10d). This indicates that the posterior estimates for those parameters are primarily informed by the prior, rather than by the data. The 89% credible intervals for the posterior distributions of the three groups overlap for all parameters except the Gaussian process length scale (Table 7). The high mortality class has longer length scales than the medium severity class.

5.3.8 Tree tallies

Model diagnostics for the tree tallies model indicate that the Hamiltonian Monte Carlo algorithm successfully estimated parameter values. The very high proportion of zeros in the training dataset (95% of quadrats had zero stems) makes evaluating the ability of the model to predict individual observations from either the training or validation datasets difficult. However, the model appears to perform reasonably well on the training data (with a positive relationship near the 1:1 line between mean predicted tallies and observed tallies, Supplementary Figure 44), but poorly on the validation data (with no or even a negative relationship between mean predicted tallies and observed tallies, Supplementary Figure 46). The wMAPEs for the tree tallies are poor, at 1.9 (MAE 0.10 stems/m^2 and mean 0.05 stems/m^2) for the training data and 2.1 (MAE 0.09 stems/m^2 and mean 0.04 stems/m^2) for the validation data. The observed distribution of plot-level mean stem densities is consistent with the envelope of distributions for plot-level mean stem densities generated using new draws for the random effects, but barely so (Supplementary Figure 47). In particular, the model appears to mildly overpredict the frequency of plots with more than 600 stems per hectare.

Comparison of the posterior and prior distributions for the tree tallies model reveals that the posterior estimates for the Gaussian process magnitudes, Gaussian process length scales, and plot random intercept standard deviations are all primarily informed by the prior, rather than the data (Figure 11b-d). Only the intercept estimates appear to be well informed by the data (Figure 11a), and for the intercepts there are no clear differences across the levels of drought mortality, with all 89% CIs overlapping (Table 8).

5.3.9 Sapling tallies

The Hamiltonian Monte Carlo algorithm performed well in estimating the parameters for the sapling tallies model, as indicated by model diagnostics. The saplings model performs similarly to the trees model in its ability to predict the counts of training and validation quadrats Supplementary Figure 48 and Supplementary Figure 50). wMAPEs of the sapling tallies model are again poor, at 1.8 (MAE 0.11 stems/m^2 and mean 0.06 stems/m^2) for the training data and 2.5 (MAE 0.10 stems/m^2 and mean 0.04 stems/m^2) for the validation data. The saplings model performs well in predicting the frequency of 0-count quadrats (Supplementary Figure 49) and in simulating realistic distributions of plot-level mean stem densities using new draws for the random effects (Supplementary Figure 51). As with the trees model, only the estimates for the intercept terms appear to be well informed by the data (Figure 12a-d), and there are no clear differences across the levels of drought mortality in the intercept parameter (Table 9).

5.4 DISCUSSION

In this study, my primary question is whether hierarchical spatial statistical models can simulate realistic fuel beds with continuous fine-grain information on fuel loads for a suite of wildland fuel components. The key features of these simulations are realistic fine-scale (sub-meter to tens of meters) autocorrelation and realistic coarse-scale (hundreds of meters to hectares) bulk properties. The answer is a qualified yes (Table 10). The models' ability to make predictions for fuel loads at specific spatial locations ranges from good (fine woody debris tallies) to moderate (duff and litter depths, vegetation presences) to poor (coarse woody debris tallies, tree tallies, and sapling tallies). However, the purpose of these models is not to make precise or accurate predictions for individual locations, but to generate fuel beds with realistic spatial patterns and bulk properties. All models performed reasonably well in reproducing the overall response distributions of depths, tallies, and particle sizes. The main weakness here was with the duff model, where missing zero inflation seems to play a minor role.

In terms of simulating bulk properties (plot-level means), i.e., those properties which are usually used to characterize the load of fuel components in fuel description systems (Anderson, 1982; Scott and Burgan, 2005; Ottmar *et al.*, 2007; Keane, 2013), all component models in this study perform well overall, showing consistency between the observed cumulative density function of plot-level means and the cumulative density functions of simulated plot-level means. However, most of the models tend to overestimate the frequency of extreme plot-level fuel loads with very low or very high loads relative to both the observed plots and the literature (Vilanova *et al.*, in review; Keane *et al.*, 2013).

Models also vary in their ability to quantify the parameters describing both fine-scale (Gaussian process magnitude and length scale) and coarse-scale (plot random effect standard deviation and group-level intercept) variation in fuel loads. Posterior estimates for all parameters are at least moderately well informed by the data for the duff depths, fine woody debris tallies, and coarse woody debris diameters models (Figure 4, Figure 6, and Figure 9). Results are mixed for the litter depths model (Figure 5), the fine woody debris tallies model (Figure 7), and the vegetation presences model (Figure 10). The models for coarse woody debris tallies, tree tallies, and sapling tallies all fail to glean much information from the data, with most parameters other than the intercept showing little difference between prior and posterior distributions (Figure 8, Figure 11, and Figure 12). It is possible that the distribution of these components is not spatially autocorrelated at fine-scales or not well captured by a simple Gaussian process (Das *et al.*, 2008; Keane *et al.*, 2012a). It is likely that the rarity of coarse woody debris, trees, and saplings at the meter or square-meter scale is frustrating parameter estimation. It is difficult to detect the underlying spatial pattern in intensity when most observations are zeros. This difficulty highlights an important trade-off: Increasing the spatial resolution of sampling for rare events also increases the proportion of zeros and the difficulty of modeling the spatial pattern.

Overall, the duff depths, litter depths, and fine woody debris tallies hierarchical spatial models appear fit for further use in generating realistic fuel beds or exploring ecological questions related to fine-scale spatial pattern. The aspatial models for fine woody debris diameters and coarse woody debris diameters also perform well, and the vegetation presences model performs adequately. However, the spatial models for coarse woody debris tallies, tree tallies, and sapling tallies all perform poorly and require either more data, a new modelling approach, or the use of continuous observations to produce fuel beds with realistic fine-scale spatial patterns. Fortunately, the rarity of these fuel components at a fine scale makes collecting continuous spatially explicit fuel load data via field methods (Brown, 1974; Woodall and Graham, 2004; Lutes *et al.*, 2006; Pawlikowski *et al.*, 2019) or (for trees and saplings) remote sensing (Li *et al.*, 2013; Lydersen *et al.*, 2013; Jeronimo *et al.*, 2018) a viable solution. That is, using a hierarchical spatial statistical model to simulate fine-scale distributions of fuel loads is unnecessary if real-world observations are available in sufficient quantities.

The secondary question for this study is whether the various parameters of the models for fuel loads of different fuel components vary across different levels of drought mortality severity. The answer is that they generally do not (or at least, parameter uncertainty is large relative to any differences across the levels of drought mortality). There are two exceptions with clear differences across drought mortality classes (i.e., the 89% credible intervals do not overlap, and all posterior estimates are well informed by the data).

First, for litter depths, it is clear that the Gaussian process magnitude (which describes the relative strength of the spatial pattern) is greater on the low mortality plots than on the high mortality plots. This means that high levels of drought severity appear to weaken the influence of fine-scale spatial pattern on litter depth, resulting in a more spatially homogeneous fuel bed (Figure 5). There are also differences in the intercept which were not strong enough to result in distinct CIs, with high mortality plots generally having deeper litter beds than medium plots, which have deeper litter beds than low mortality plots. Fresh foliage biomass, or litter, is the first fuel to move from the canopy to the surface in the wake of drought- or beetle-related mortality (Stephens *et al.*, 2018; Gray *et al.*, 2021), which likely explains why one of the few clear signals of drought mortality in the data appears in litter depths. The fine-scale spatial pattern of litter is the result of an array of spatially heterogeneous processes such as primary productivity in the canopy, abscission of foliage from live trees, loss of foliage from newly-dead trees, wind dispersal of foliage between the canopy and the surface, and decomposition of litter into duff (Ferrari, 1999; Keane, 2008; Vanderwel *et al.*, 2016; Schaedel *et al.*, 2017; DiMario *et al.*, 2018; Fry *et al.*, 2018). Varying levels of drought mortality could be causally or correlatively connected to several of these processes. For example, the decreased spatial heterogeneity evident on high drought mortality plots could be the result of the relatively high numbers of recently killed trees creating a spatially homogeneous pulse of litter deposition (Stephens *et al.*, 2018).

Second, the Gaussian process length scale parameter for understory vegetation presence, controlling the distance at which autocorrelation occurs, is higher in high mortality plots than in medium mortality plots (Figure 10). This indicates that the patches and gaps in understory vegetation cover are spatially larger on high mortality plots than medium mortality ones. In addition to this clear finding, the posterior suggests that the high mortality plots have larger length scales than the low mortality plots, which have larger length scales than the medium mortality plots. Again, the fine-scale spatial pattern of understory vegetation is linked to the canopy. These links are both causal via spatially heterogeneous competition for light and water resources (Das *et al.*, 2008; York *et al.*, 2012; Krebs *et al.*, 2019) and correlative via spatial variation in microsite influencing both the presence of understory vegetation and vulnerability to drought (Raaflaub *et al.*, 2012; North *et al.*, 2019; Werner *et al.*, 2021). Further research is necessary to better understand the mechanisms by which drought mortality is connected to the fine-scale spatial pattern of litter and of understory vegetation. However, this study makes important strides towards that goal by providing methods to quantify the spatial pattern of fuel loads.

It is interesting that this study generally finds minimal effects of drought mortality level on fuels, given the clear mechanistic ties between tree mortality and fuels and existing research linking changes in fuels to drought mortality (Stephens *et al.*, 2018; Gray *et al.*, 2021). Several explanations are plausible. First, it is possible that for some fuel components this study simply did not sample enough data, and that more plots would allow the models to detect relatively subtle differences between the drought mortality classes. It is also possible that the eDaRT MMI data product does a poor job capturing mortality. However, this seems unlikely, because exploratory analysis for this study revealed a positive correlation between dead basal area at the plot level and the MMI detected on the plot. Another explanation is that the low/medium/high bins used for this study do not reflect an ecologically meaningful variation in drought mortality levels. Finally, it is clear that time-since-death is an important factor in the relationship between canopy mortality and fuels (Keane, 2008; Hicke *et al.*, 2012; Eskelson and Monleon, 2018; Stephens *et al.*, 2018; Lydersen *et al.*, 2019) and this study only examines fuels at a single snapshot in time. The stands studied here are still in the grey stage of mortality: Foliage has fallen to the surface, but most of the woody material in dead trees is still standing. With the litter models showing some of the greatest differences among drought mortality classes, it is very plausible that the approximately five years between mortality pulse and fuels observation was enough time for litter deposition to vary with the level of drought mortality, but not enough time for that pulse to decompose into duff, or for substantial amounts of woody material to have fallen.

The data collection and statistical approach proposed here has both advantages and disadvantages in meeting the goal of generating high resolution fuel loads data for input into a CFD fire model. The results of this study highlight some of the disadvantages. First, a common problem is that the models described here tend to overpredict the abundance of (still quite rare) instances of extreme emergent behaviors which do not appear in the real data. Second, the models proposed here are very flexible, and some parameter values may be very difficult to estimate. Several models failed to learn much about the Gaussian process length scale or the plot random effect standard deviation from the data. Third, subtle or complex relationships may exist in reality while being difficult or impossible to represent in a statistical model. For example, the cross correlation between litter and duff depths, which is relatively weak but present in the observed data, was excluded from statistical modelling in favor of split models that passed diagnostic tests.

Despite these disadvantages, the methods described here offer important benefits. First, the quantification of a continuous distribution of particle sizes for fine woody debris and coarse woody debris is an important step towards providing high resolution information about particle sizes to combustion models (Vakili *et al.*, 2016b). Second, and more importantly, the fitted hierarchical spatial statistical models are capable generating simulated data with realistic spatial properties. These simulations could be used to interpolate between sparse measurements to continuous high-resolution data (and unlike kriging, they can do so in a context where the response variable is not normally distributed; Bivand *et al.*, 2013). Alternatively, simulations from the fitted models could be used to extrapolate into an infinite number of hypothetical fuel beds, each having realistic spatial properties, which would enable realistic predictions of fire behavior incorporating fire-atmosphere feedbacks from a CFD fire model. Such ensembles of fuel beds are necessary to study the effects of spatial pattern on fire behavior because generalized spatial patterns are realized in a diverse array of specific realizations on the landscape. The hierarchical spatial models used here are flexible and could be modified to incorporate covariates if variables relevant to fuel loads are identified.

One challenge in applying these models to generate high-resolution simulated fuel beds is that the per-plot Gaussian process approach used here may not scale well to simulating larger areas in two dimensions (e.g., 1 ha) at high resolution. Doing so would require performing a Cholesky factorization of an $L \times L$ covariance matrix, for which the computational requirements increase exponentially with L, making large L impractical to simulate (Heaton *et al.*, 2019). One solution would be to fit the models using a nearest neighbor Gaussian process (Datta *et al.*, 2016; Finley *et al.*, 2020) rather than estimating a full Gaussian process for each plot. This solution is not a drastic departure from the models described here, which are effectively nearest neighbor Gaussian processes where neighbors are observations from the same plot. Another solution to this problem would be to use a fire model which operates in one dimension, as some in-development spatially explicit models do (Finney 2020, *pers. comm.*).

The results of this study enable me to make some recommendations for generating continuous high resolution fuel loads data to feed into CFD fire models. First, the poor performance of models for low-information responses (rare events like coarse woody debris, trees, or saplings, or binomial responses like understory vegetation presence) indicate that whenever possible researchers should collect and rely on continuous observations of these fuel components, rather than attempt to interpolate or extrapolate using statistical models. I anticipated this problem, and the sampling protocol used for this study is explicitly designed to feed into a continuous one-dimensional transect describing fuel conditions for understory vegetation and coarse woody debris, reducing the need to model these components statistically. Likewise, continuous information on the presence of biomass in trees and saplings is widely available either from inventory data or remote sensing (Lydersen *et al.*, 2013; Jeronimo *et al.*, 2018). Fortunately, for fuel components where continuous high-resolution sampling would be prohibitively time intensive (duff, litter, fine woody debris) the models perform relatively well and could be effectively used to interpolate between sparse observations or simulate new fuel beds. When using this statistical approach, I advise including some filtering of the simulated fuel beds to constrain use to realistic fuel beds. For example, simulations with plot-level fuel loads greater than 1,000 Mg/ha of duff or less than 1 Mg/ha of duff should probably be excluded as ecologically unrealistic in the context of unburned mixed conifer forests.

Feeding data generated from these hierarchical spatial models (using either parameters estimated from real data or parameters chosen to explore their effects) into a CFD fire model is an important next step for research. Such a study would increase our fundamental understanding of how and when fire behavior changes as a result of different fuel spatial patterns. This is a clear knowledge gap when it comes to surface and ground fuels (Hoffman *et al.*, 2012a; Ziegler *et al.*, 2017; Atchley *et al.*, 2021). An additional avenue for further study is that other fuel bed properties (e.g. moisture) also exhibit spatial patterns and will likely also be important data for realistic predictions from a fire model (Raaflaub *et al.*, 2012; Kreye *et al.*, 2014; Rakhmatulina *et al.*, 2021).

A final benefit of the methods described in the first chapter is that these hierarchical spatial models offer a more robust framework for testing hypotheses about the ecology of fine-scale spatial patterns than do the variogram or classification analyses often applied in the literature (Hiers *et al.*, 2009; Keane *et al.*, 2012a; Loudermilk *et al.*, 2014; Vakili *et al.*, 2016a). They accomplish this by providing uncertainty intervals for random effects parameters from either Bayesian parameter estimation or profile likelihood testing. In this framework random effects are not nuisances but themselves important objects of study (Ives, 2022).

5.5 TABLES

Parameter	Low drought mortality	Medium drought mortality	High drought mortality
Intercept (β)	1.33 (0.98, 1.69)	1.22 (0.81, 1.61)	1.31 (1.11, 1.51)
GP magnitude (α)	0.62 (0.52, 0.76)	0.74 (0.6, 0.88)	0.57 (0.48, 0.67)
GP length scale (ν)	2.86 (2.2, 3.48)	3.39 (2.39, 4.7)	2.16 (1.77, 2.61)
Plot effect SD (σ)	0.47 (0.18, 0.86)	0.54 (0.2, 0.97)	0.22 (0, 0.44)
NB Dispersion (κ)	7.22 (5.56, 8.88)	7.05 (5.36, 8.8)	8.1 (6.36, 9.88)

Table 1: Posterior parameter values for duff depths model. Posterior median values for each parameter are given alongside an 89% credible interval in parentheses.

Parameter	Low drought mortality	Medium drought mortality	High drought mortality
Intercept (β)	1.31 (1.11, 1.53)	1.42 (1.2, 1.65)	1.61 (1.4, 1.83)
GP magnitude (α)	0.51 (0.41, 0.62)	0.44 (0.32, 0.57)	0.23 (0.11, 0.35)
GP length scale (ν)	2.38 (1.88, 2.95)	7.47 (3.91, 12.85)	6.37 (2.88, 11.2)
Plot effect SD (σ)	0.22 (0, 0.41)	0.2 (0, 0.42)	0.29 (0.1, 0.53)
NB Dispersion (κ)	7.26 (5.6, 8.87)	7.99 (6.36, 9.69)	7.57 (6.04, 9.17)

Table 2: Posterior parameter values for the litter depths model. Posterior median values for each parameter are given alongside an 89% credible interval in parentheses.

Parameter	Low drought mortality	Medium drought mortality	High drought mortality
Intercept (β)	2.61 (2.29, 2.93)	2.87 (2.57, 3.13)	2.34 (1.77, 2.91)
GP magnitude (α)	0.63 (0.48, 0.76)	0.56 (0.46, 0.68)	0.69 (0.58, 0.81)
GP length scale (ν)	4.46 (2.62, 7.45)	4.64 (2.58, 6.47)	3.78 (2.96, 4.61)
GP nugget (τ)	0.15 (0.07, 0.25)	0.11 (0.05, 0.18)	0.11 (0.06, 0.17)
Plot effect SD (σ)	0.41 (0.14, 0.75)	0.36 (0.07, 0.68)	0.84 (0.47, 1.4)
NB Dispersion (κ)	9.18 (7.39, 11.03)	8.99 (7.23, 10.84)	9.32 (7.44, 11.11)

Table 3: Posterior parameter values for the fine woody debris tallies model. Posterior median values for each parameter are given alongside an 89% credible interval in parentheses.

Parameter	Low drought mortality	Medium drought mortality	High drought mortality
Intercept (β)	-0.49 (-0.65, -0.28)	-0.41 (-0.55, -0.29)	-0.21 (-0.53, 0.08)
Plot effect SD (σ^{PLOT})	0.14 (0, 0.28)	0.1 (0, 0.21)	0.48 (0.32, 0.67)
Subtransect effect SD ($\sigma^{SUBTRANSECT}$)	0.33 (0.22, 0.45)	0.28 (0.19, 0.36)	0.23 (0.11, 0.33)
Precision (φ)	0.15 (0, 0.32)	0.04 (0, 0.12)	0.05 (0, 0.14)

Table 4: Posterior parameter values for the fine woody debris diameters model. Posterior median values for each parameter are given alongside an 89% credible interval in parentheses.

Parameter	Low drought mortality	Medium drought mortality	High drought mortality
Intercept (β)	-1.76 (-2.12, -1.4)	-1.71 (-2.04, -1.37)	-1.57 (-2.08, -1.01)
GP magnitude (α)	0.6 (0.35, 0.88)	0.64 (0.43, 0.85)	0.96 (0.65, 1.29)
GP length scale (ν)	7.48 (3.52, 12.37)	6.19 (3.26, 10.75)	13.19 (7.54, 20.95)
Plot effect SD (σ^{PLOT})	0.26 (0, 0.62)	0.24 (0, 0.59)	0.43 (0, 0.89)

Azimuth effect SD ($\sigma^{AZIMUTH}$)	0.26 (0, 0.53)	0.18 (0, 0.4)	0.16 (0, 0.42)

Table 5: Posterior parameter values for the coarse woody debris tallies model. Posterior median values for each parameter are given alongside an 89% credible interval in parentheses.

Parameter	**Low drought mortality**	**Medium drought mortality**	**High drought mortality**
Mean (μ)	24.58 (20.44, 28.62)	18.51 (14.82, 22.32)	19.19 (16.11, 22.6)
Precision (φ)	0.16 (0, 0.45)	0.11 (0, 0.31)	0.46 (0, 1.04)

Table 6: Posterior parameter values for the coarse woody debris diameters model. Posterior median values for each parameter are given alongside an 89% credible interval in parentheses.

Parameter	**Low drought mortality**	**Medium drought mortality**	**High drought mortality**
Intercept (β)	0.81 (-0.28, 1.91)	-0.52 (-1.95, 0.89)	-0.94 (-2.16, 0.48)
GP magnitude (α)	2.82 (2.15, 3.37)	3.18 (2.44, 3.91)	3.15 (2.38, 3.96)
GP length scale (ν)	3.41 (2.59, 4.28)	2.2 (1.78, 2.69)	5.27 (4.24, 6.42)
Plot effect SD (σ)	1.65 (0.65, 2.78)	2.6 (1.57, 3.61)	2 (0.68, 3.16)

Table 7: Posterior parameter values for the vegetation presence model. Posterior median values for each parameter are given alongside an 89% credible interval in parentheses.

Parameter	**Low drought mortality**	**Medium drought mortality**	**High drought mortality**
Intercept (β)	-2.96 (-3.11, -2.78)	-2.81 (-3.18, -2.38)	-2.83 (-3.16, -2.42)
GP magnitude (α)	0.12 (0, 0.29)	0.43 (0.12, 0.72)	0.22 (0, 0.45)
GP length scale (ν)	8.05 (3.01, 15.12)	6.92 (2.77, 12.73)	8 (2.89, 17.67)
Plot effect SD (σ^{PLOT})	0.08 (0, 0.24)	0.41 (0, 0.77)	0.38 (0.01, 0.74)

Table 8: Posterior parameter values for the trees count model. Posterior median values for each parameter are given alongside an 89% credible interval in parentheses.

Parameter	**Low drought mortality**	**Medium drought mortality**	**High drought mortality**
Intercept (β)	-2.27 (-2.75, -1.79)	-2.61 (-3.01, -2.07)	-2.61 (-3.41, -1.86)
GP magnitude (α)	0.95 (0.63, 1.31)	0.31 (0, 0.63)	0.36 (0, 0.84)
GP length scale (ν)	5.51 (2.5, 10.99)	8.2 (3.01, 16.04)	9.25 (3.32, 18.83)
Plot effect SD (σ^{PLOT})	0.43 (0, 0.84)	0.43 (0, 0.88)	1.19 (0.51, 1.85)

Table 9: Posterior parameter values for the saplings count model. Posterior median values for each parameter are given alongside an 89% credible interval in parentheses.

Model	Model diagnostics satisfactory	wMAPE training data	wMAPE validation data	Bias in pointwise predictions	Distribution of simulated samples consistent with the observed data	Distribution of simulated plot-level means consistent with observed data	Parameters poorly informed by the data
Duff depths (cm)	Yes	0.33	0.47	No	Missing zero inflation	Simulated extremes are implausibly low or high	None
Litter depths	Yes	0.36	0.38	Yes (training only)	Yes	Simulated extremes are implausibly low or high	GP length scales
FWD tallies	Yes	0.19	0.38	No	Yes	Simulated extremes are implausibly low or high	None
FWD diameters	Yes	NA	NA	NA	Yes		Plot effect SD
CWD tallies	Yes	1.6	1.6	Yes	Yes	Simulated extremes are implausibly low or high	GP length scale, plot effect SD, azimuth effect SD
CWD diameters	Yes	NA	NA	NA	Yes		None
Understory veg. pres./abs.	Yes	NA	NA	No	Yes	Yes	Intercept
Tree tallies	Yes	1.9	2.1	Yes	Yes	Simulated extremes are implausibly low or high	GP magnitude, GP length scale, plot effect SD
Sapling tallies	Yes	1.8	2.5	Yes	Yes	Yes	GP magnitude, GP length scale, plot effect SD

Table 10: Model diagnostics and validation summary.

5.6 FIGURES

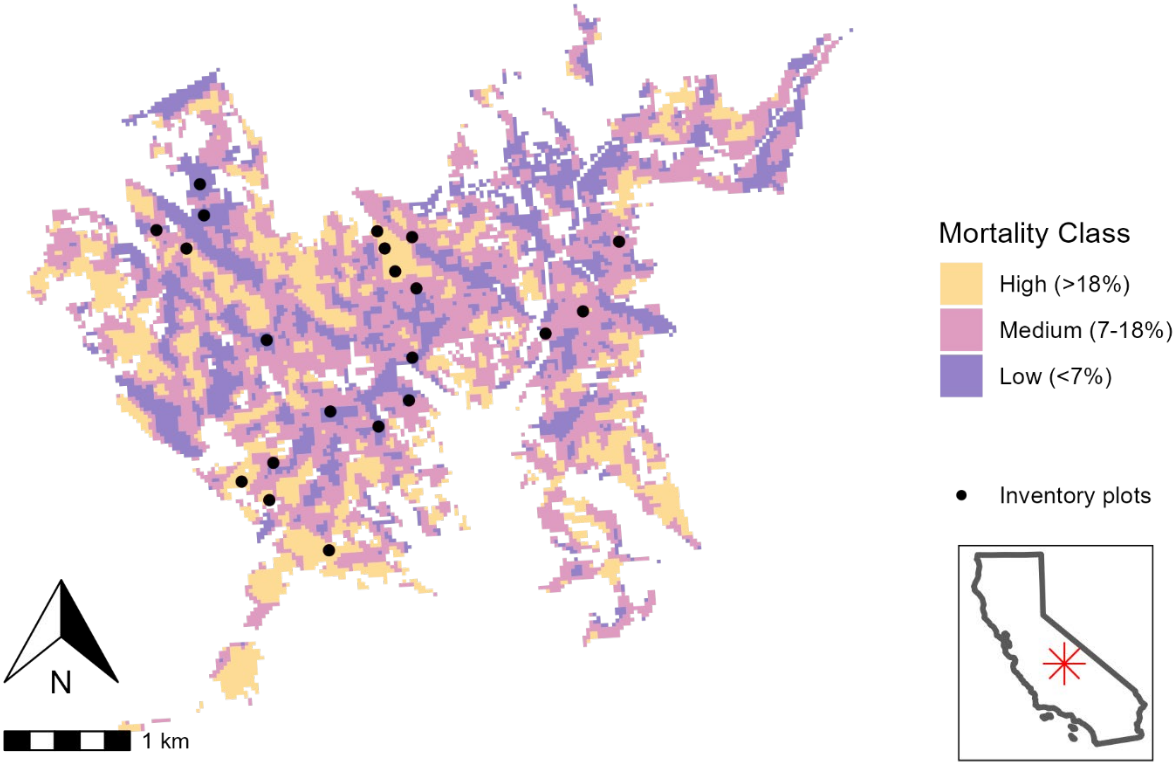

Figure 1: Area of interest, drought mortality classes, and plot locations. Area of interest (CALVEG-mapped mixed conifer forest - pine from 1,500-1,850 m elevation) shown with colors indicating the level of cumulative drought mortality from 2012-2016 as mapped by the (smoothed) eDaRT data product. Plot locations shown as black points. Plots were randomly located within the core area of each zone of drought mortality and limited to locations 50-600m from a road or trail. Inset shows position of the study site within California state boundaries.

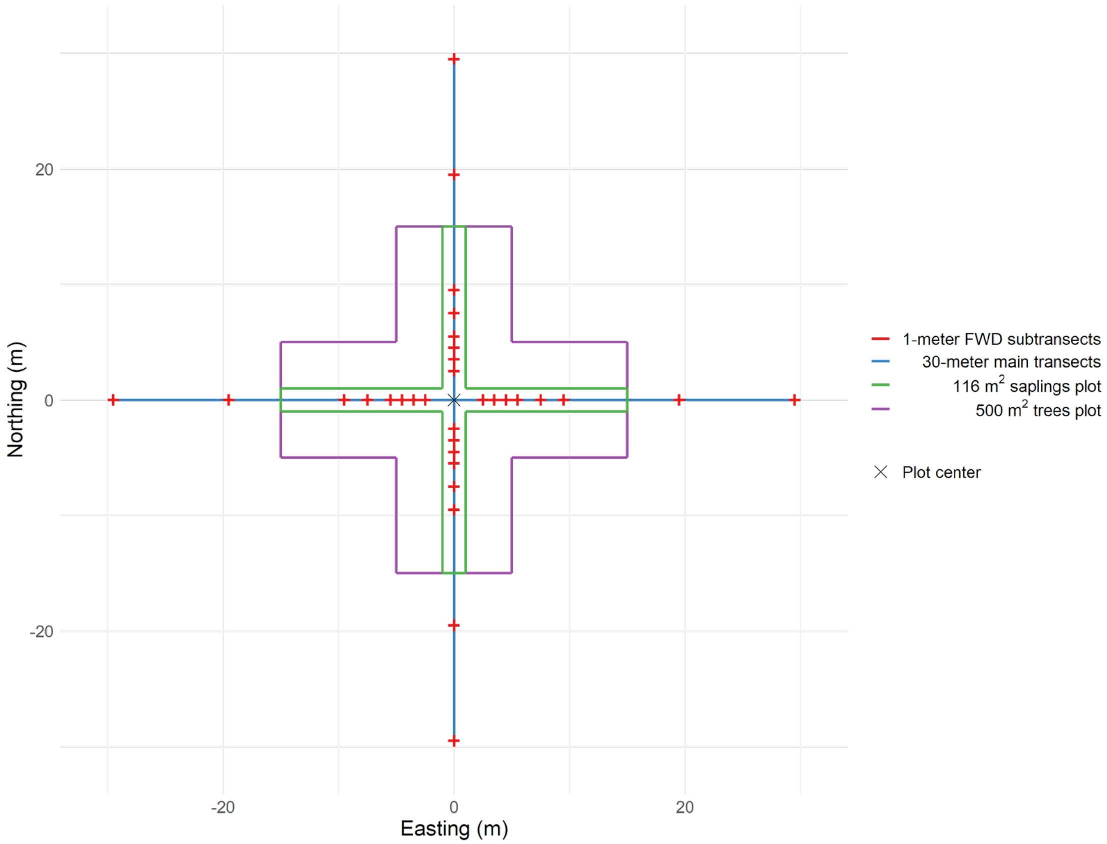

Figure 2. Plot layout. There are four 30-meter main transects (blue) extending from plot center at cardinal directions. Depths of duff and of litter were sampled at locations 2.0, 2.1, 2.2, 2.3, 2.4, 2.5, 3.0, 3.5, 4.0, 4.5, 5.5, 7.0, 7.5, 9.5, 19.5, and 29.5 meters from plot center along each of the four main transects. 1-hour, 10-hour, and 100-hour fine woody debris particles were tallied on 1-meter subtransects located along each main transect from 2-3, 3-4, 4-5, 7-8, 9-10, 19-20, and 29-30 meters along each main transect and orthogonal to (bisected by) the main transect and intersecting it at 2.5, 3.5, 4.5, 5.5, 7.5, 9.5, 19.5, and 29.5 meters (red). On one of these subtransects per transect, individual diameters of fine woody debris particles were recorded. Coarse woody debris particles were inventoried (diameter, location, decay class) from 0-30 meters along each main transect, and understory vegetation intersecting the main transect from 0-15 meters was recorded using line intercept sampling. Trees ≥ 11.4 cm DBH and saplings ≥ 1.37 m height were inventoried (species, DBH, height, height to live crown, live/dead status, and spatial location) within a 500 m² fixed area plot (trees; purple) or a 116 m² fixed area plot (saplings; green).

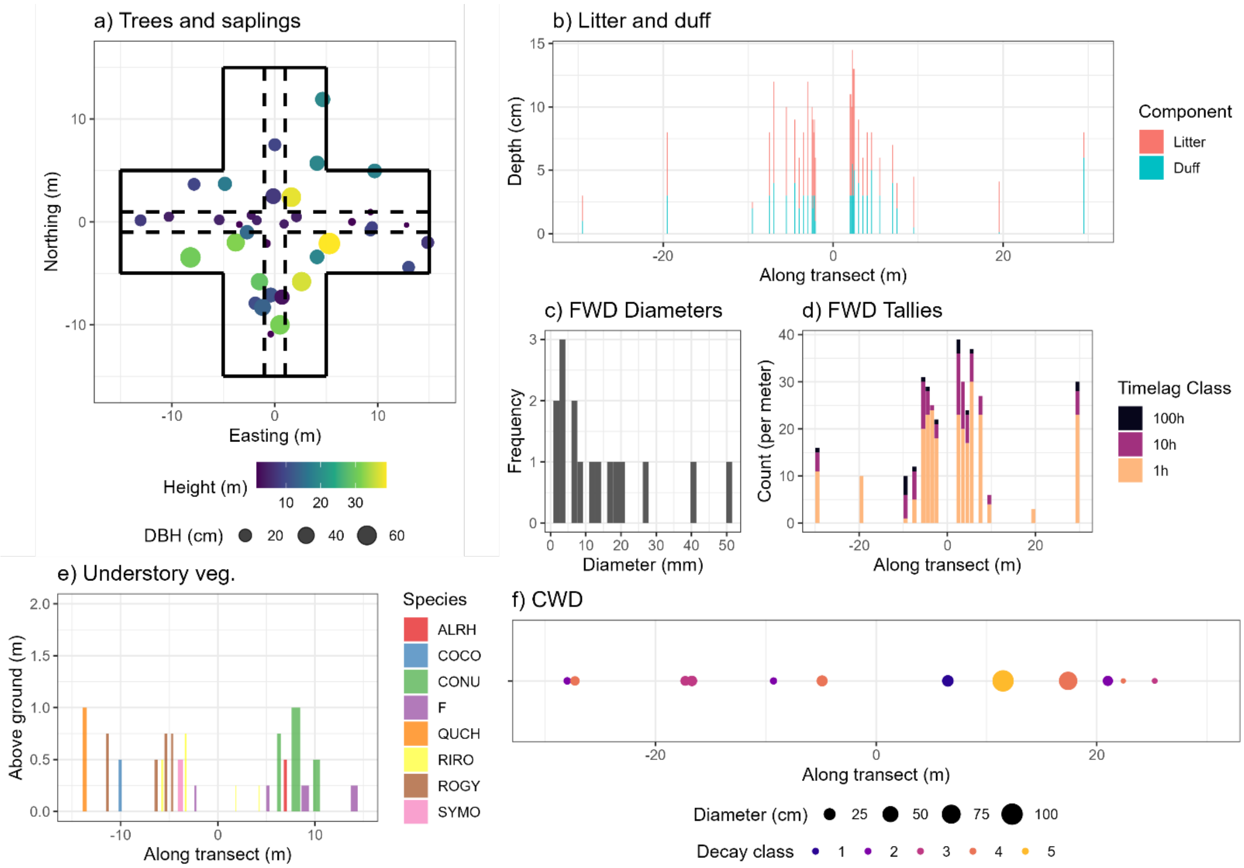

Figure 3: Sample of observations from a single inventory plot. Panel a: Data on trees >= 11.4 cm DBH and saplings >= 1.37 m height include species, DBH, height, height to live crown, live/dead status, and spatial location within a 500 m^2 fixed area plot (trees) or a 116 m^2 fixed area plot (saplings). b: Depth of duff and litter was sampled at locations 2.0, 2.1, 2.2, 2.3, 2.4, 2.5, 3.0, 3.5, 4.0, 4.5, 5.5, 7.0, 7.5, 9.5, 19.5, and 29.5 m along each of four transects arranged at cardinal directions from plot center (data from East and West transects shown). c: From 9.0-10.0 m along each transect, diameter (mm) of each individual particle of fine woody debris intersecting the transect was recorded. d: Tally of 1-hour, 10-hour, and 100-hour fine woody debris particles intersecting two 1 m subtransects located at 2.5, 3.5, 4.5, 5.5, 7.5, 9.5, 19.5, and 29.5 m along each transect (data from East and West transects shown). e: Location, height, and species of dominant vegetation was recorded along four 15 m transects arranged at cardinal directions from plot center (data from East and West transects shown). f: Location, diameter, and decay class of coarse woody debris particles intersecting four 30 m transects arranged at cardinal directions from plot center were recorded (data from East and West transects shown).

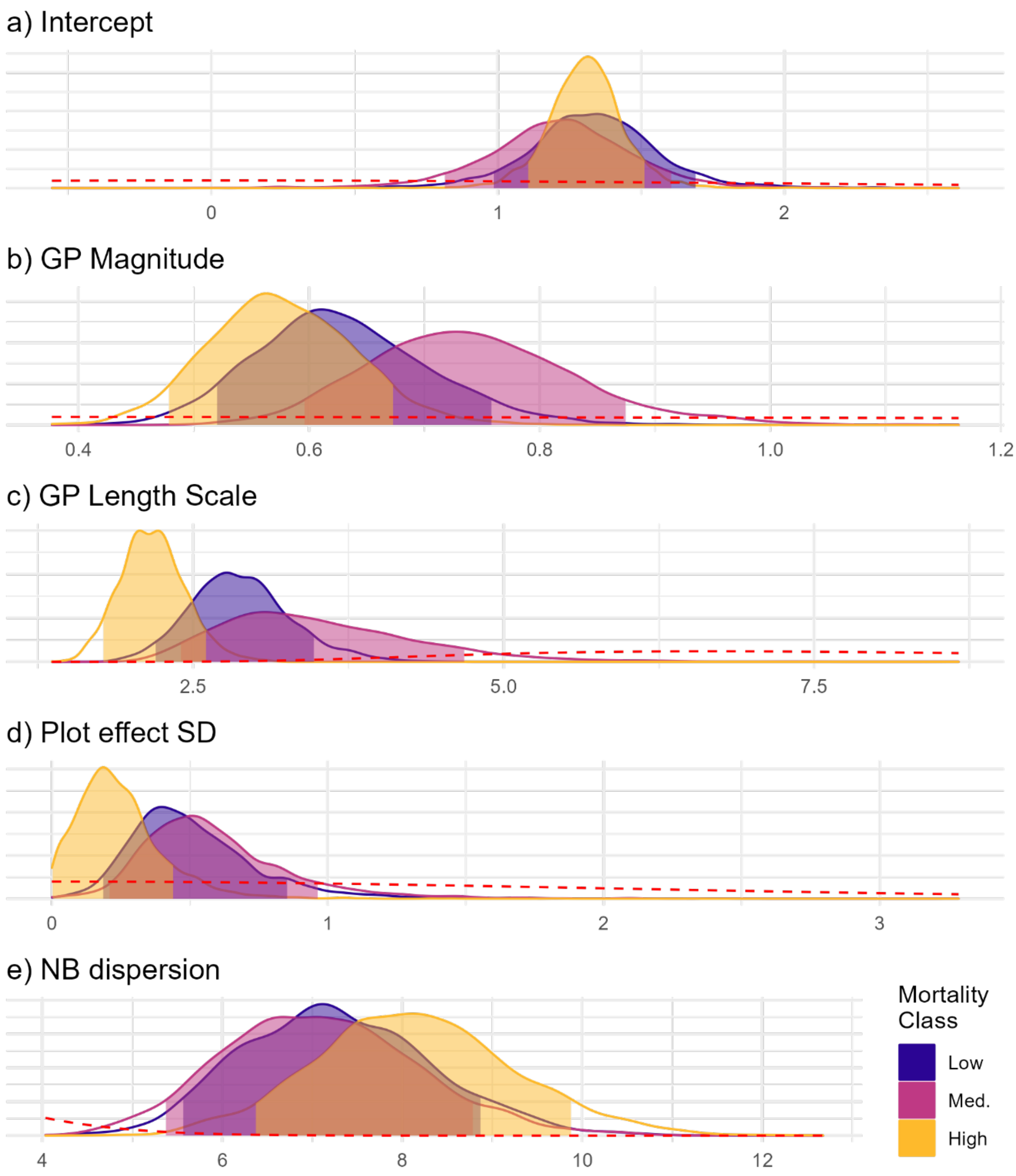

Figure 4: Posterior probability distributions for parameters of the duff depths model. Colors indicate the group (drought mortality class). Each panel is for a model parameter, with the parameter value on the x-axis and the posterior probability density on the y-axis. The shaded portion of each posterior probability density curve shows an 89% credible interval for each parameter. The prior probability density for each parameter is shown as the red dashed lines. For all parameters, the posterior values for each group are sharply different from the relatively broad prior distribution, indicating that the posteriors are well informed by the data rather than the prior distribution for each parameter. There is extensive overlap in the posterior distribution across the drought mortality classes for all parameters, indicating that any differences in the parameters describing the pattern of duff depth across drought mortality classes are small relative to the uncertainty in parameter values.

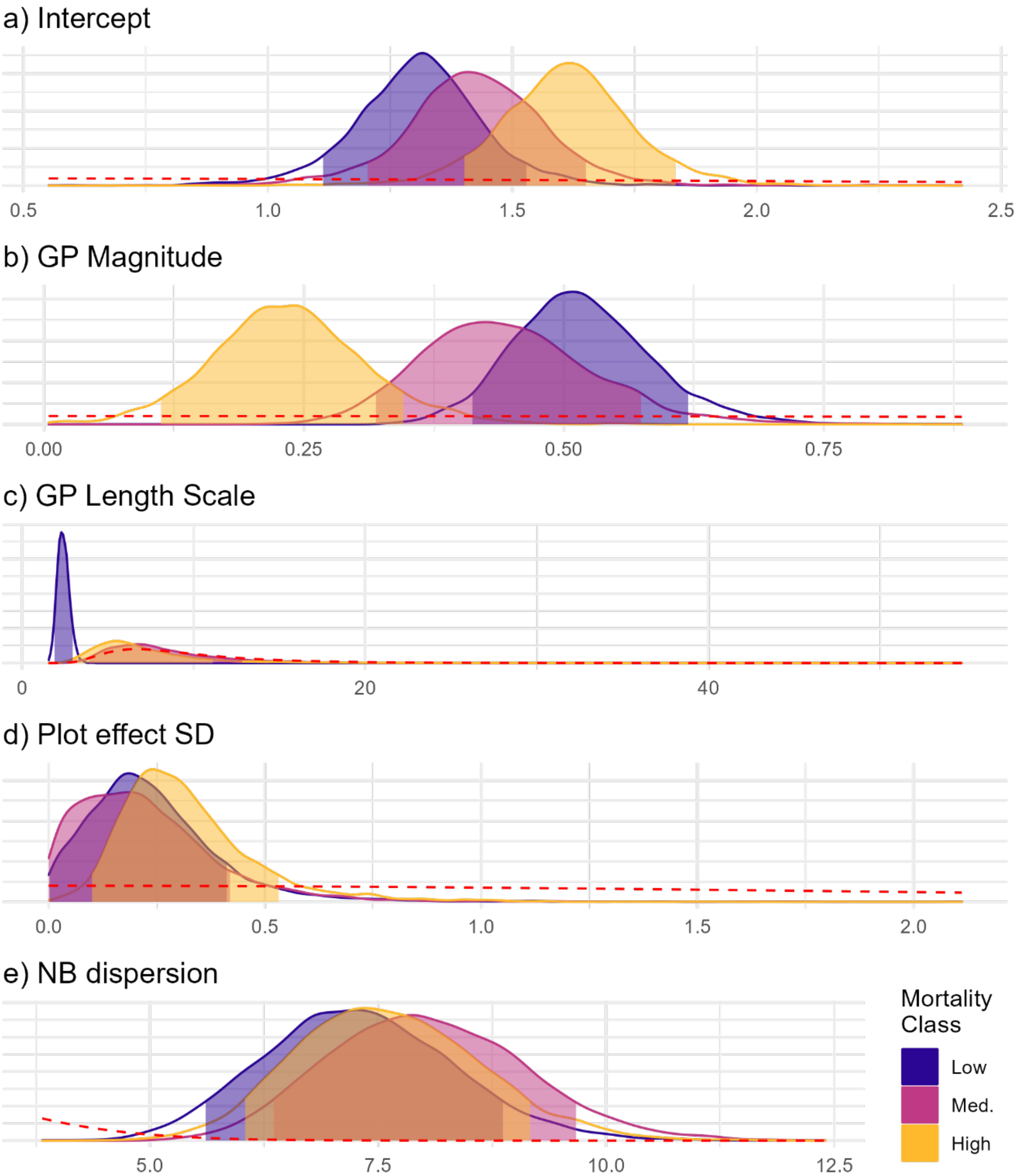

Figure 5: Posterior probability distributions for parameters of the litter depths model. Fill colors indicate the group (drought mortality class). Each panel is for a model parameter, with the parameter value on the x-axis and the posterior probability density on the y-axis. The shaded portion of each posterior probability density curve shows an 89% credible interval for each parameter. Prior distributions for each parameter are shown as the red dashed lines. The posterior distributions suggest that high drought mortality plots may have had a higher mean, lower Gaussian process magnitude, and greater Gaussian process length scale than did plots with low levels of drought mortality. However, the differences are small relative to the parameter uncertainty and the 95% credible intervals of the drought mortality classes overlap for all parameters except the GP magnitudes for low and high drought mortality. Furthermore, the posterior distributions for the length scale of the Gaussian process effect for medium and high drought mortality classes substantially overlap with the prior distribution, suggesting that the posterior distributions for those parameters are only weakly informed by the data, rather than the prior.

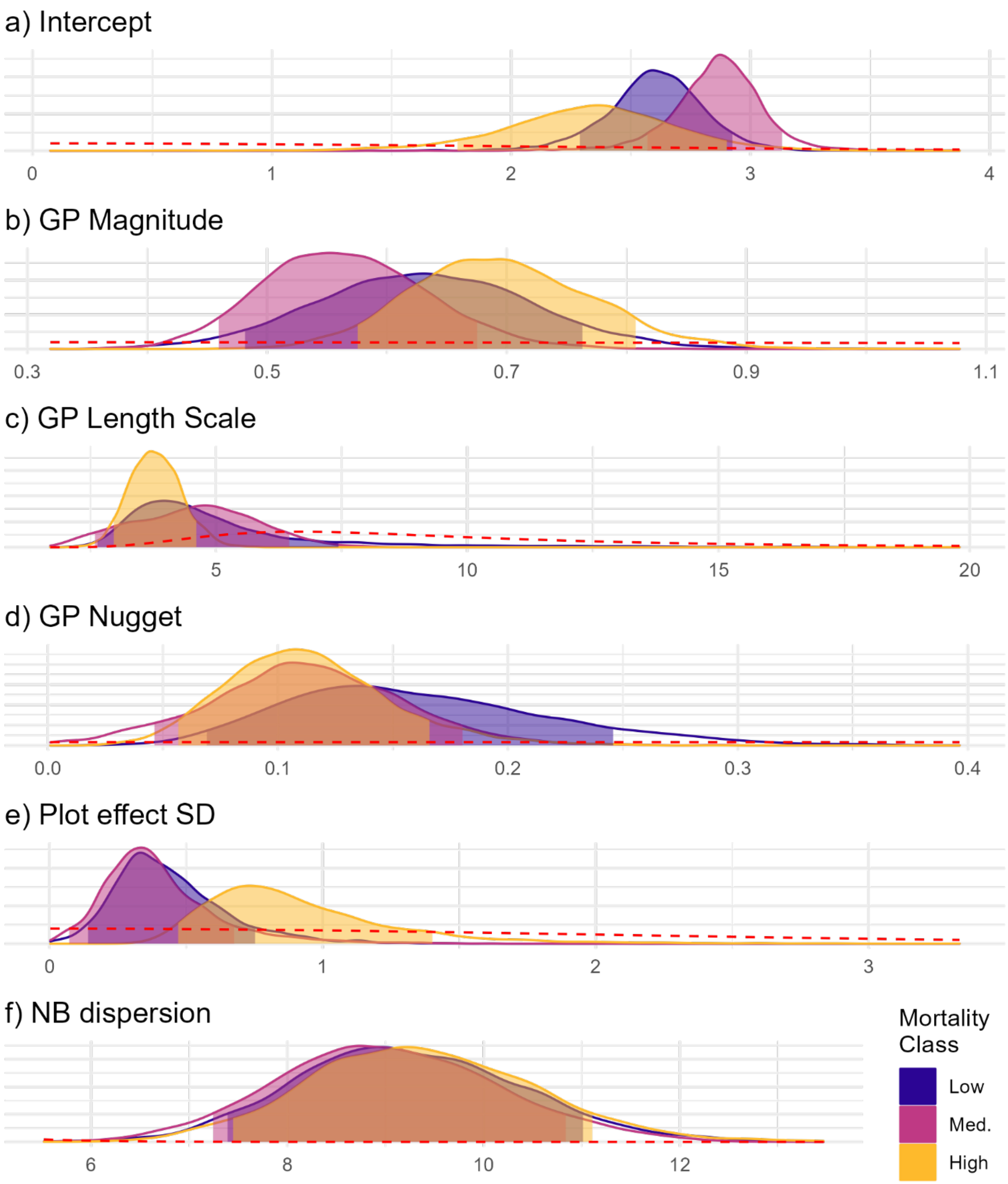

Figure 6: Posterior probability distributions for parameters of the fine woody debris tallies model. Fill colors indicate the group (drought mortality class). Each panel is for a model parameter, with the parameter value on the x-axis and the posterior probability density on the y-axis. The shaded portion of each posterior probability density curve shows an 89% credible interval for each parameter. Prior distributions for each parameter are shown as red dashed lines. All parameters appear well informed by the data except the Gaussian process length scales for the low and medium levels of drought mortality, which are only moderately well informed by the data. However, any differences between drought mortality classes are small relative to the parameter uncertainty and the 95% credible intervals of the drought mortality classes overlap for all parameters.

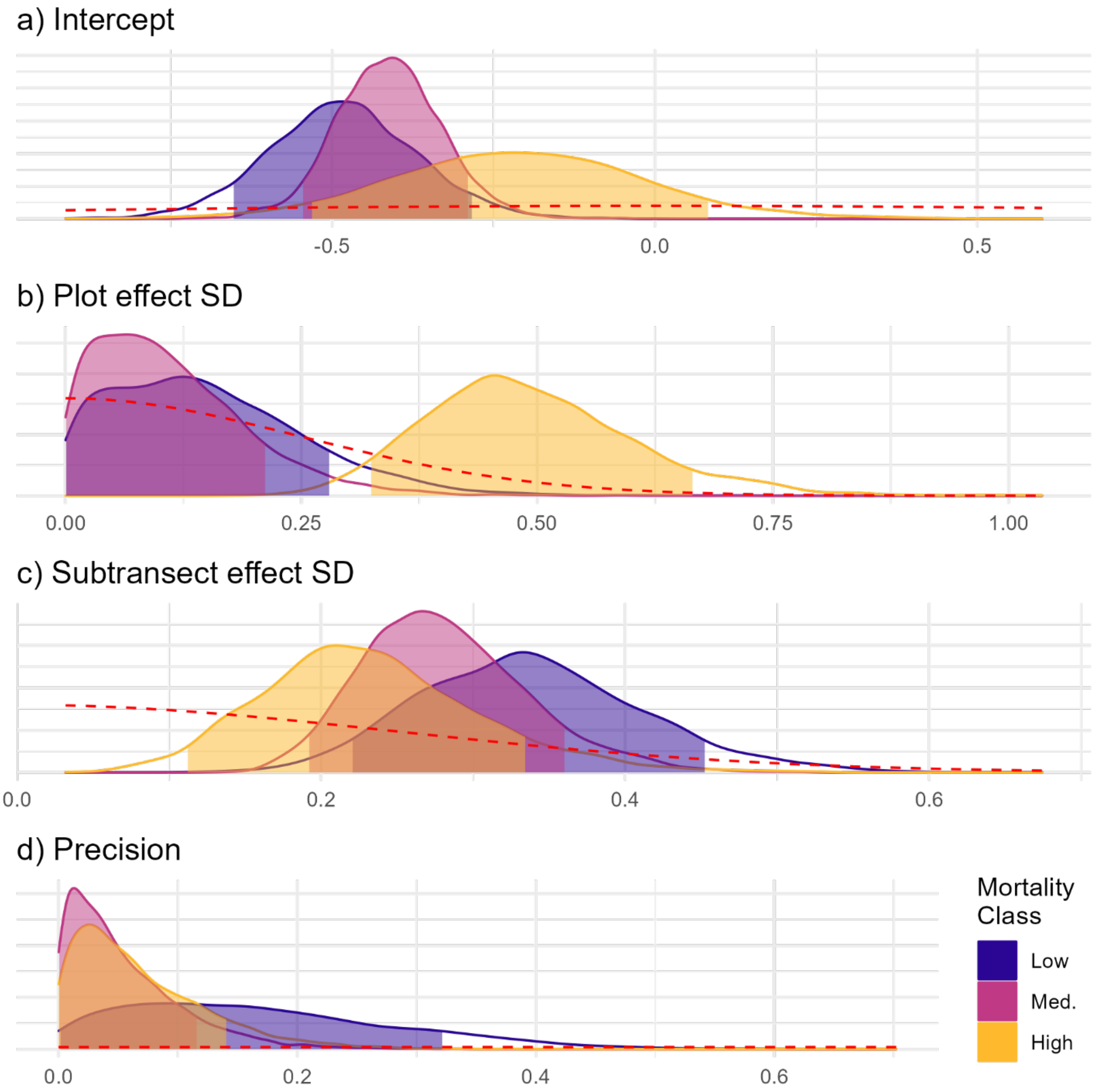

Figure 7: Posterior probability distributions for parameters of the fine woody debris diameters model. Fill colors indicate the group (drought mortality class). Each panel is for a model parameter, with the parameter value on the x-axis and the posterior probability density on the y-axis. The shaded portion of each posterior probability density curve shows an 89% credible interval for each parameter. Prior distributions for each parameter are shown as the red dashed lines. For the intercept and the precision parameter, the posterior values for each group are sharply different from the relatively broad prior distribution, indicating that the posteriors are well informed by the data rather than the prior distribution. For the standard deviation of the transect random effect, the posterior distributions for all three groups are fairly similar to the prior distribution, with the posterior only excluding values less than approximately 0.15. This suggests that the data are only weakly informing the posterior distribution for this parameter in all three sub models. For the standard deviation of the plot random effect, only the posterior for the high drought mortality group is different from the prior, indicating that for the low and medium levels of drought mortality the data were not informative about the standard deviation of the plot effect.

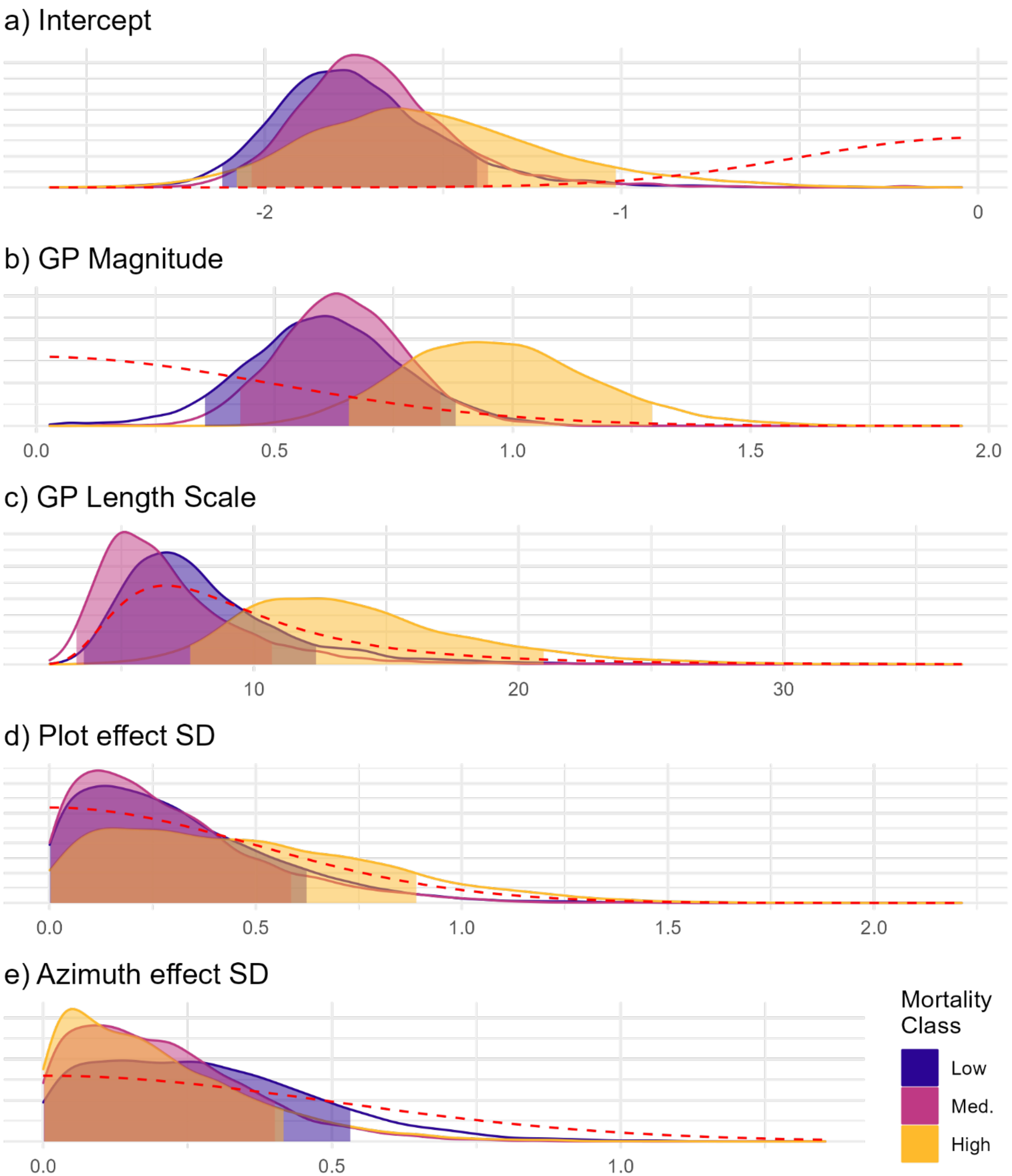

Figure 8: Posterior probability distributions for parameters of the coarse woody debris tallies model. Fill colors indicate the group (drought mortality class). Each panel is for a model parameter, with the parameter value on the x-axis and the posterior probability density on the y-axis. The shaded portion of each posterior probability density curve shows an 89% credible interval for each parameter. Prior distributions for each parameter are shown as the red dashed lines. The 89% credible intervals of the drought mortality classes overlap for all parameters. For the intercept and Gaussian process magnitude, the posterior values for each group are clearly distinct from the prior distributions. The posterior distributions for the other parameters appear strongly influenced by their respective priors.

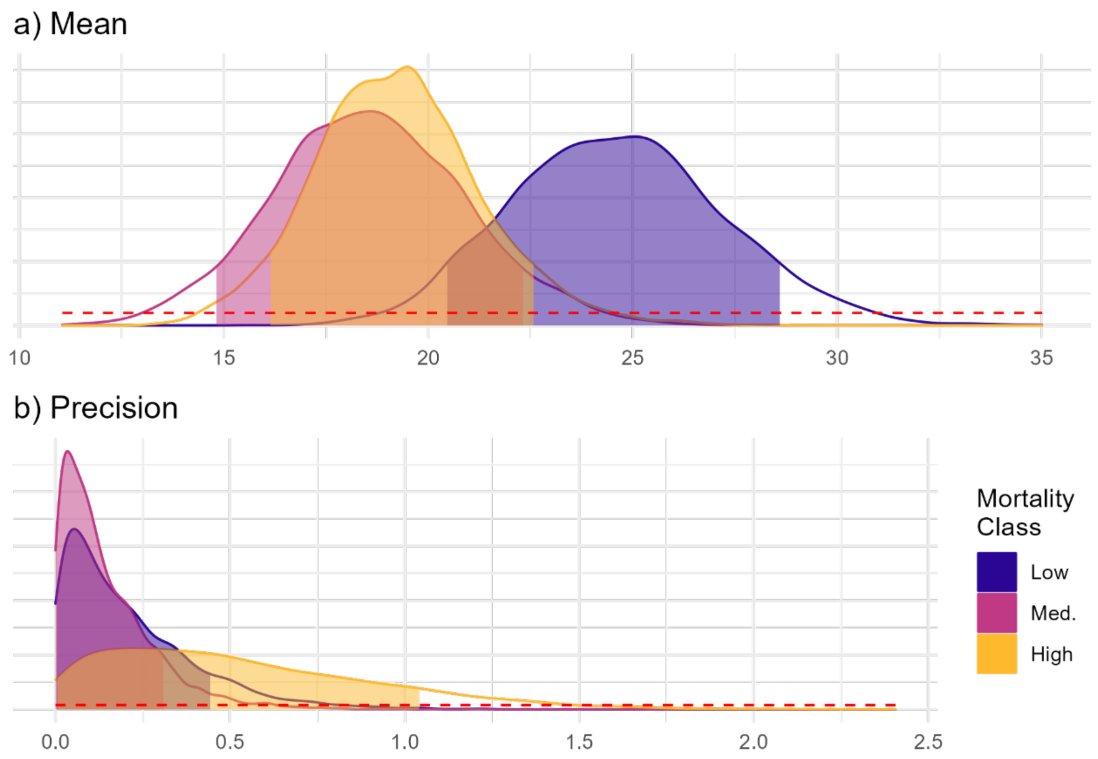

Figure 9: Posterior probability distributions for parameters of the coarse woody debris diameters model. Fill colors indicate the group (drought mortality class). Each panel is for a model parameter, with the parameter value on the x-axis and the posterior probability density on the y-axis. The shaded portion of each posterior probability density curve shows an 89% credible interval for each parameter. Prior probability densities for each parameter are shown as the red dashed lines. The posterior distributions are sharply distinct from the prior distribution for both parameters, but the differences between drought mortality classes are small relative to the parameter uncertainty and the 89% credible intervals of the drought mortality classes overlap for all parameters.

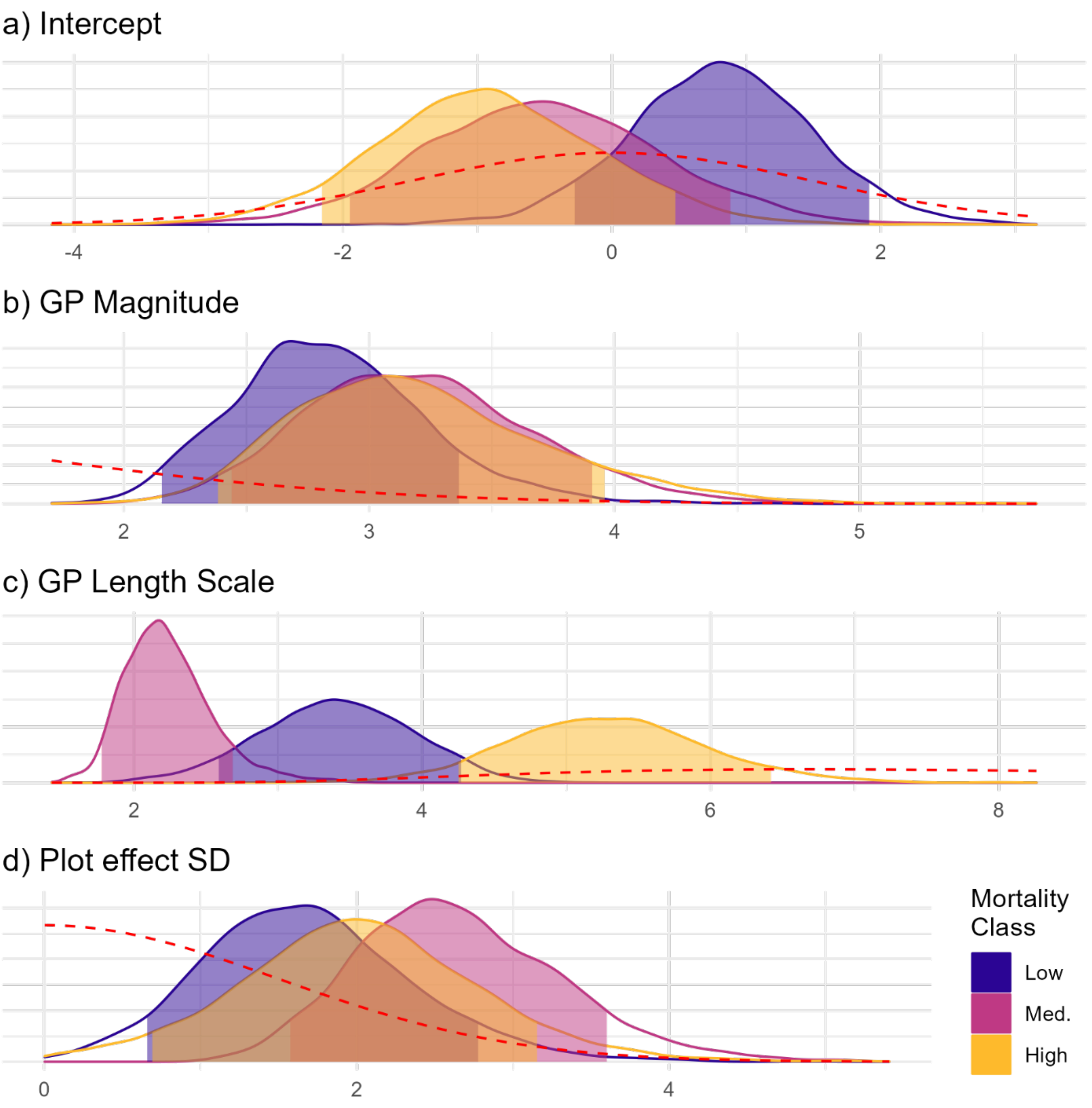

Figure 10: Posterior probability distributions for parameters of the vegetation presences model. Fill colors indicate the group (drought mortality class). Each panel is for a model parameter, with the parameter value on the x-axis and the posterior probability density on the y-axis. The shaded portion of each posterior probability density curve shows an 89% credible interval for each parameter. The prior distributions for each parameter are shown as the red dashed lines. There is extensive overlap in the posterior distribution across the drought mortality classes for the intercept, GP magnitude, and the standard deviation of the plot random effect, indicating that any differences in the parameters describing the pattern of vegetation presence across drought mortality classes are small relative to the uncertainty in parameter values for these parameters. The figure is suggestive of a difference in the GP length scale parameter across the three groups, and the 89% credible intervals of the medium and high drought mortality groups do not overlap. The data were informative for the Gaussian process magnitude and Gaussian process length scale parameters, but not for the intercept and only marginally for the plot random effect standard deviation.

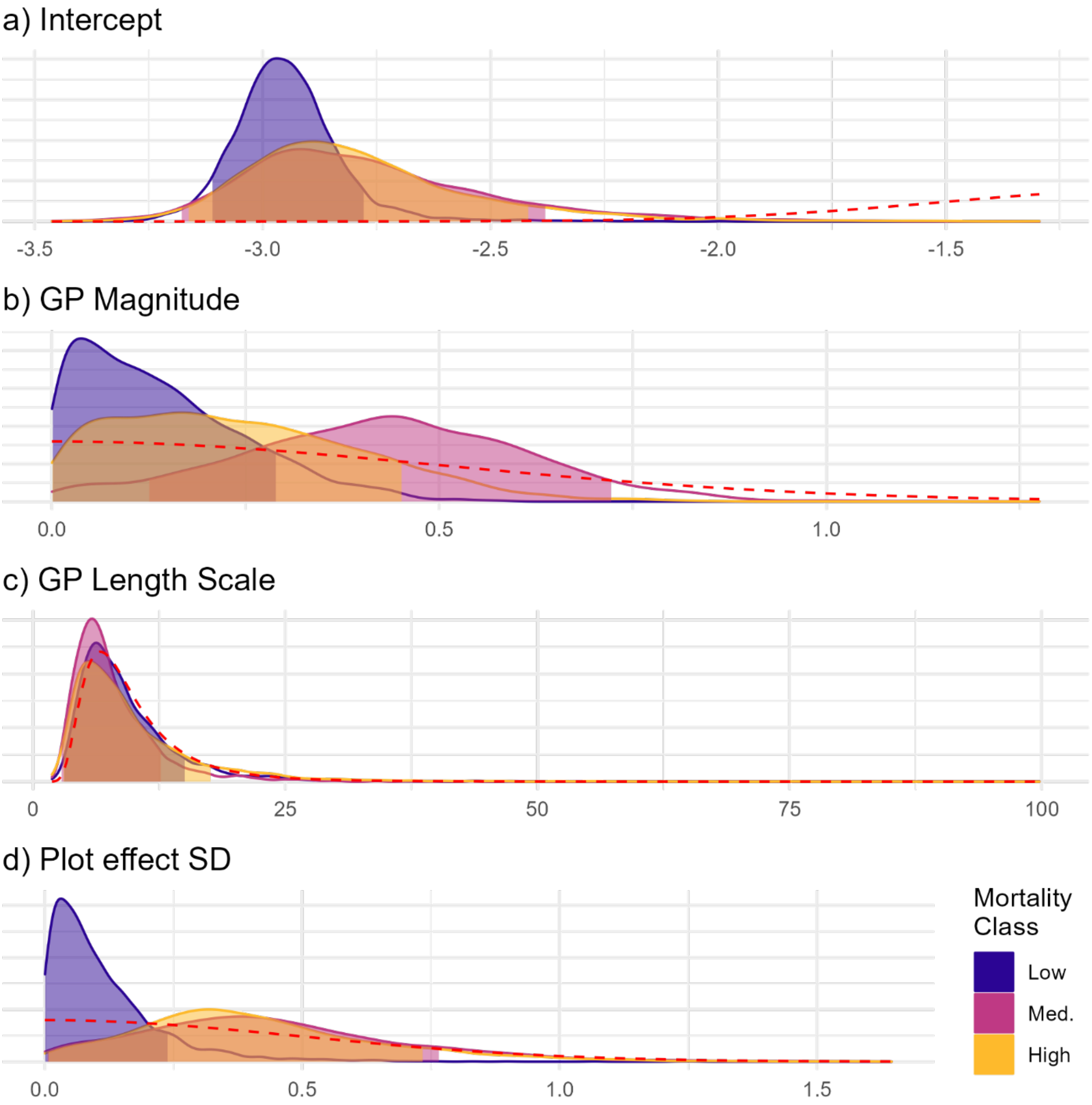

Figure 11: Posterior probability distributions for parameters of the trees quadrat-count model. Fill colors indicate the group (drought mortality class). Each panel is for a model parameter, with the parameter value on the x-axis and the posterior probability density on the y-axis. The shaded portion of each posterior probability density curve shows an 89% credible interval for each parameter. The prior distributions for each parameter are shown as the red dashed lines. For all parameters except the intercept, the posterior distributions strongly overlap the prior distribution, indicating that the model estimates are not well informed by the data. Unsurprisingly, there is extensive overlap in the posterior distribution across the drought mortality classes for all parameters, indicating that any differences in the parameters describing the pattern of tree density across drought mortality classes are small relative to the uncertainty in parameter values for these parameters.

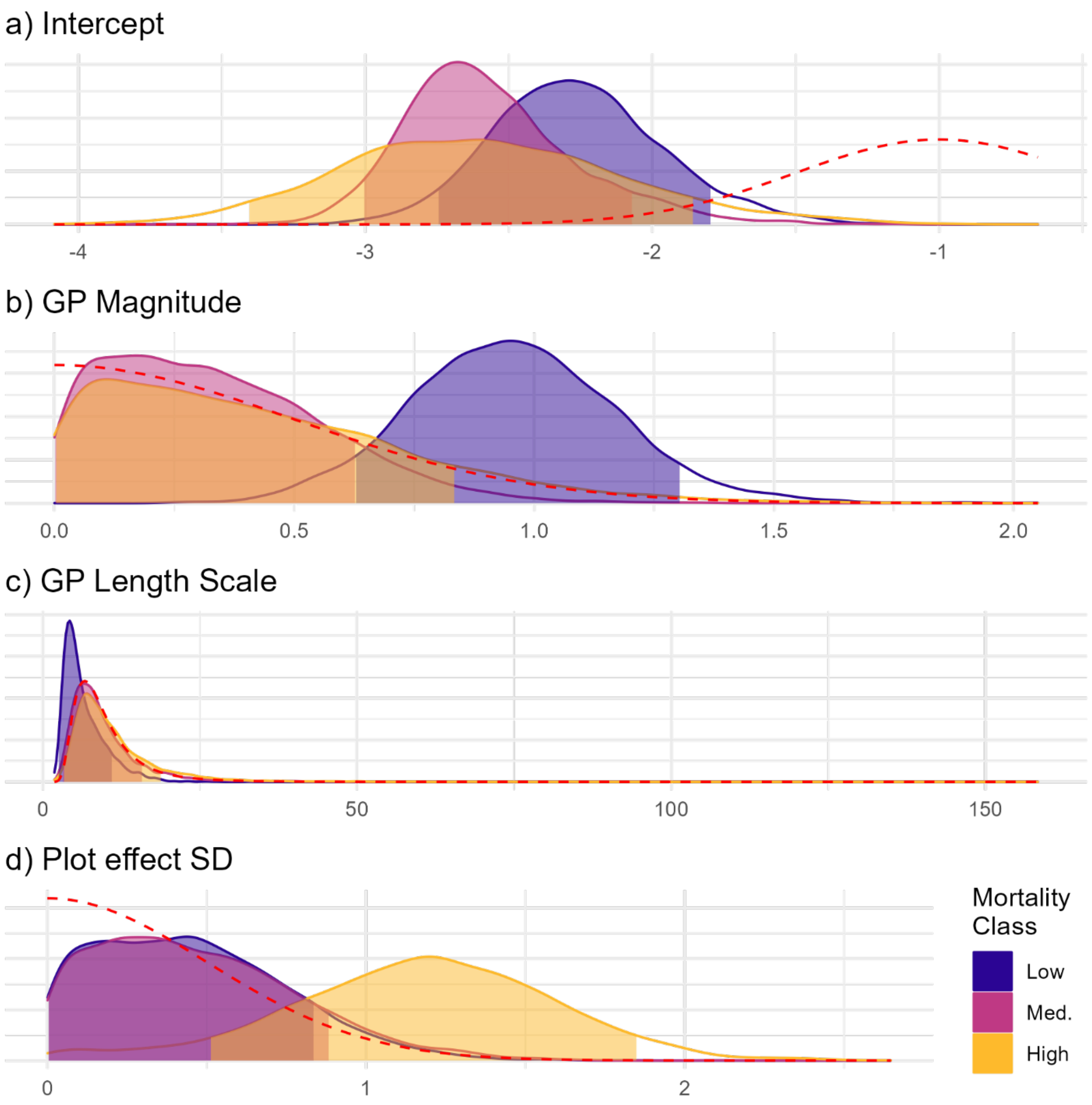

Figure 12: Posterior probability distributions for parameters of the saplings quadrat-count model. Fill colors indicate the group (drought mortality class). Each panel is for a model parameter, with the parameter value on the x-axis and the posterior probability density on the y-axis. The shaded portion of each posterior probability density curve shows a 95% credible interval for each parameter. The prior distributions for each parameter are shown as the red dashed lines. For all parameters except the intercept, the Gaussian process magnitude for the low mortality group, and the plot effect standard deviation for the high mortality group, the posterior distributions strongly overlap the prior distribution, indicating that the model estimates are not well informed by the data. Unsurprisingly, there is extensive overlap in the posterior distribution across the drought mortality classes for all parameters except the Gaussian process magnitude, for which the data were only informative for the low mortality group.

6 TRANSITION

In the first chapter, I proposed the use of hierarchical spatial statistical models to describe fine-scale heterogeneity in the fuel loads of several fuel components. Though the primary benefit of this approach is to generate data for spatially explicit fire behavior models, an ancillary benefit is that the models facilitate quantification of the spatial pattern into the parameters controlling a Gaussian process spatial random effect. By making these parameters the objects of hypothesis tests, using either a Bayesian or frequentist framework, researchers can address ecological questions about the causes and effects of different spatial patterns. In the next chapter, I demonstrate an application of these models to explore the effects of prescribed fire on the fine-scale spatial distribution of duff, litter, and fine woody debris.

7 BEYOND FUEL REDUCTION: PRESCRIBED FIRES ALTER SPATIAL PATTERN OF WILDLAND FUELS

7.1 INTRODUCTION

Mixed-severity fire regime forests across much of the western United States are facing challenges associated with a disrupted disturbance regime (Perry *et al.*, 2011; Hessburg *et al.*, 2016). In this context, a warming climate has combined with structural changes associated with a century of fire suppression to disrupt the disturbance regime that historically maintained these forests (Westerling *et al.*, 2006, 2011; Liang *et al.*, 2017; Alizadeh *et al.*, 2021). Mixed conifer forests (MCF), which occupy more than 3 million hectares throughout the Sierra Nevada, Klamath, and Cascades mountain ranges, were historically maintained by a regime of high frequency and mixed severity wildfires (Hessburg *et al.*, 2016; Safford and Stevens, 2017). Today, that regime has been replaced by one of infrequent high severity wildfires (North *et al.*, 2009; Taylor *et al.*, 2014; Steel *et al.*, 2015; Stephens *et al.*, 2015; Stevens *et al.*, 2017). This change threatens the ability of mixed conifer forests to persist throughout much of their range (Airey Lauvaux *et al.*, 2016; Coppoletta *et al.*, 2016; Coop *et al.*, 2020; Steel *et al.*, 2021b).

Amid these macro-scale concerns, there is evidence for the importance of fine-scale (submeter to tens of meters) spatial distribution of the fuel loads (biomass per unit area) of forest fuels in shaping combustion processes that drive fire behavior and effects (Hiers *et al.*, 2009; Wiggers *et al.*, 2013; Loudermilk *et al.*, 2014; Lutz *et al.*, 2017). Forest fuels are the live and dead biomass which is combusted during fire events, and fuel load is one of the most important characteristics of a fuel bed, the complex realized arrangement of fuels in some area (Keane, 2015). Features of the fine-scale pattern of fuel loads affect combustion processes. For example, submeter scale gaps in fuel can be sufficient to stop forward progress of a flaming front (Finney *et al.*, 2010). Meter-scale manipulation of surface fuels can significantly alter prescribed fire behavior and effects (Thaxton and Platt, 2006). Likewise, local (within 10m) density of trees can affect the presence of small (1-900m2) patches of unburned refugia within a wildfire, with higher tree survival in refugia (Blomdahl *et al.*, 2019). Multiple studies have revealed the importance of fine-scale canopy fuel patterns in shaping fire behavior. For example, the different stem patterns resulting from varying silvicultural prescriptions have been shown to significantly affect modeled wildfire behavior (Ziegler *et al.*, 2017) and the scale and strength of patchiness in canopy fuels can significantly affect the spread rate of simulated wildfires (Atchley *et al.*, 2021).

Fire and other ecological processes likewise shape the fine-scale spatial pattern of fuels, completing a pattern-process feedback loop between fire and fuels. Different disturbance regimes produce characteristic patterns of individual trees, clumps, and openings (Lydersen *et al.*, 2013; Jeronimo *et al.*, 2019; Pawlikowski *et al.*, 2019). The strength and scale of spatial autocorrelation of various surface and ground fuels (duff, litter, fine woody debris, coarse woody debris, and understory vegetation) has been found to vary across ecosystems (Keane *et al.*, 2012a) and with disturbance history (Vakili *et al.*, 2016a). The surface and ground fuels under individual trees vary according to the characteristics of those trees, including their size, crown condition, and whether they have been killed by bark beetles (Hille and Stephens, 2005; Gray *et al.*, 2021). Germination rates of different species can be altered by fine-scale variation in fuels and fire behavior, shaping the distribution and composition of post-fire vegetation (Wiggers *et al.*, 2013).

Given the importance of fine-scale heterogeneity in pattern-process feedbacks shaping the role of wildfire, an understanding of fine-scale spatial patterns and how they interact with disturbances is essential for management of MCF (Hiers *et al.*, 2020). A management practice of particular importance in MCF is prescribed fire, which restores several important ecosystem processes and is a cost-effective way to reduce fuel loads and thereby reduce wildfire hazard (Moghaddas and Stephens, 2007; Hartsough *et al.*, 2008; Schwilk *et al.*, 2009; Stephens *et al.*, 2012; Hessburg *et al.*, 2016; McCaskill, 2018; Foster *et al.*, 2020; York *et al.*, 2021). However, because spatially explicit data describing surface and ground fuels are costly to collect, there are important gaps in our knowledge. This study applies the best models from the previous chapter (those for fuel loads of duff, litter, and fine woody debris) to better understand the effects of prescribed fire on the fine-scale spatial pattern of fuel loads for these fuel components. These components are those whose fuel loads are most strongly affected by prescribed fire (Levine *et al.*, 2020; Foster *et al.*, 2020) and their fuel loads likewise shape fire behavior and effects (Thaxton and Platt, 2006; Keane, 2015; O'Brien *et al.*, 2016a). This study addresses two outstanding questions:

1) What are the characteristics of the fine-scale spatial patterns of fuel loads for duff, litter, and fine woody debris in the Sierra Nevada mixed conifer forest ecosystem?
2) What effects does prescribed fire have on the fine-scale spatial pattern of duff, litter, and fine woody debris loads?

7.2 METHODS

7.2.1 Study site

The study site is located at Blodgett Forest Research Station, located near Georgetown, California, USA (38°54'45" N; 120°39'27" W) at approximately 1300 m elevation. Soils range in depth from 85 to 115 cm and are composed of well-developed and drained sandy loam Ultic Haploxeralfs (Alfisols), with mean slopes generally <30%. The climate is Mediterranean: A long dry-warm season with temperatures from 10-29° C is followed by a cool-wet winter with temperatures 0-8° C and approximately 160 cm per year of precipitation falling mostly in the winter and spring (Hart *et al.*, 1992; Stephens and Collins, 2004; Stephens *et al.*, 2009). The site is a mixed conifer forest with *Abies concolor*, *Calocedrus decurrens*, *Pinus lambertiana*, *Pinus ponderosa*, *Pseudotsuga menziesii*, and *Quercus kellogii* as the dominant tree species. Similar to many MCF, the area historically experienced a regime of frequent low- to moderate-severity fires, with fire return intervals ranging from 8 to 15 years at most (Stephens and Collins, 2004). Forest structure has been altered from historical norms by intensive logging in the early 20th century and effective fire suppression in the decades since. The stands included in this study have experienced single tree selection harvests using conventional methods on approximately a 10-year interval. In recent years efforts were made during harvests to avoid depositing substantial leaf and branch biomass into the litter and fine woody debris components of the fuel bed (York 2021, *pers. comm.*). This disturbance history has created stands typical of second-growth MCF with high tree density, high surface fuel loads, and high wildfire hazard (Stephens *et al.*, 2009; York *et al.*, 2012).

7.2.2 Prescribed fire

In the spring of 2021, a series of prescribed fires were implemented on the three experimental units included in this study. The objective of each burn was to reduce surface fuel loads by 50% (primarily through the consumption of litter and fine woody debris) while limiting crown scorch of canopy trees to less than 50% on average and limiting post-burn mortality of trees greater than 50.8 cm diameter at breast height (DBH) to less than 10%. The three units are contiguous but were separated by containment lines and burned on separate days. Unit A (9.8 ha) was burned on April 20 and 21 of 2021, Unit B (7.5 ha) was burned on April 22, 2021, and Unit C (6.6 ha) was burned on April 23, 2021. Unit A was burned over the course of two days because poor weather conditions (high winds and low relative humidity) created control difficulties on the first day. Active ignitions occurred between 10:30 and 16:00 each day using strip head fires. Dry bulb temperature during active ignitions ranged from 14-18 °C, relative humidity ranged from 33-53%, average midflame windspeeds ranged from 1.0-2.0 kph, and 10-hour fuel moisture at 10:00 hours ranged from 11-15% (Grevatt 2021, *pers. comm.*). Fuels were sampled as described below both before (July 2020) and after (July 2021) the prescribed burns.

7.2.3 Data collection and processing

Data describing the overstory, shrub cover, surface fuels, and duff were collected at 19 pre-existing permanent inventory plots. This study focuses on the litter, duff, and fine woody debris observations. Surface and ground fuels were inventoried using Brown's transects (Brown, 1974), with four transects per plot established at cardinal directions from plot center. Litter and duff depths were sampled to the nearest 0.5 cm at points 2.0, 2.1, 2.2, 2.3, 2.4, 2.5, 3.0, 3.5, 4.0, 4.5, 5.5, 7.0, 7.5, 9.5, 19.5, and 29.5 m along each transect. Fine woody debris (FWD; woody particles < 7.62 cm diameter) was tallied by time lag class (1-hour: 0-0.64 cm; 10-hour: 0.64-2.54 cm; 100-hour: 2.54-7.62 cm) along a series of 1-meter subtransects located from 2-3 m, 3-4 m, 4-5 m, 5-6 m, 7-8 m, 9-10 m, 19-20 m, and 29-30 m along each transect and a series of 1m subtransects placed orthogonal to the main transect and crossing at 2.5, 2.5, 4.5, 5.5, 7.6, 9.5, 19.5, and 29.5 m. This arrangement of subsamples was selected to provide a range of between-subsample distances on each plot from 1-60 m for FWD and from 0.1-60 m for litter and duff with a large number of pairwise distances observed in the 1-10 m range. Previous studies have found that most of the spatial autocorrelation in duff, litter, and fine woody debris occurs within 10 meters (Keane *et al.*, 2012a), and this sampling arrangement was designed to maximize ability to detect changes in the spatial pattern.

Forest structure metrics for ground fuels, surface fuels, and trees were calculated using the plot data alongside allometric equations as described in Foster *et al.* (2020) to produce across-plot means and standard deviations at both the pre-burn and post-burn times for tree density (trees/ha), basal area (m^2/ha), duff and litter depths (cm) and loads (Mg/ha), fine woody debris densities (particles/m) and loads (Mg/ha), coarse woody debris loads (Mg/ha) and shrub loads (Mg/ha; Table 11). For statistical analysis, I combine the depth of duff and of litter at each sampling location and model the combined depth. Litter and duff, when considered separately, each exhibited a pattern of zero inflation which is difficult to capture with hierarchical spatial statistical models for reasons described in the previous chapter. By contrast, the different time lag classes of FWD are modeled separately because it is plausible that the effects of prescribed fire on spatial pattern are contingent on the particle size. The unit of observation for duff and litter depths is a single depth sample, and the unit of observation for fine woody debris tallies is a single 1-meter subtransect. As in the previous chapter, the within-plot relative easting and northing coordinates of each observation were calculated using the geometry of the sampling scheme, and these coordinates were used in constructing the covariance matrix during parameter estimation (details below).

7.2.4 Statistical analysis

To quantify the effects of prescribed fire on the fine-scale spatial patterns of duff, litter, and fine woody debris I apply hierarchical spatial statistical models (Diggle and Ribiero, 2007) similar to those used in the previous chapter. The model for depth of litter and duff is:

Equation 17

$$Y_i \sim \text{NegBinomial}(\mu_i, \kappa)$$

where Y_i is the observed depth of litter and duff (combined and rounded to the nearest centimeter) at observation i, μ_i is the unobserved mean depth at observation i, and κ is the dispersion parameter controlling the overdispersion in the negative binomial distribution, which is here assumed constant across all observations.

The mean depth of litter and duff is predicted (with a log link) by a hierarchical (generalized) linear model:

Equation 18

$$\log \mu_i = \boldsymbol{X}_i \boldsymbol{\beta} + \left(GPPRE_{l[i],p[i]} \times PRE_i\right) + \left(GPPOST_{l[i],p[i]} \times POST_i\right) + PLOT_{p[i]}$$

where $\boldsymbol{X}_i$ is the 1×6 row-vector of fixed effect covariates for observation i, $\boldsymbol{\beta}$ is the 6×1 column vector of fixed effect coefficients. The fixed effects for this study are the experimental unit (Unit A, Unit B, or Unit C) crossed with the time (pre-burn or post-burn). $\boldsymbol{GPPRE}$ is an $L \times P$ matrix of realized Gaussian process spatial random effects for pre-burn observations with a row for each of the $L = 64$ within-plot spatial locations and a column for each of the $P = 19$ plots. PRE_i is a dummy variable whose value is 1 if observation i is a pre-burn sample and 0 otherwise. $\boldsymbol{GPPOST}$ is an $L \times P$ matrix of realized Gaussian process spatial random effects for post-burn observations. $POST_i$ is a dummy variable whose value is 1 if observation i is a post-burn sample and 0 otherwise, and $\boldsymbol{PLOT}$ is a $1 \times P$ vector of normally distributed random plot intercepts, $\boldsymbol{PLOT} \sim \text{Normal}(0, \sigma)$. $l[i]$ is the index of the within-plot spatial locations for observation i, and $p[i]$ is the index for the plot containing observation i. Thus, the mean depth for observation i is the sum of the fixed effects, the Gaussian process spatial random effect for either the pre-burn or post-burn time, and the random intercept for the plot containing the observation.

The realized Gaussian process spatial random effects within each plot for the pre-burn time are drawn from a multivariate normal distribution:

Equation 19

$$\boldsymbol{GPPRE}_{1:L,p[i]} \sim \text{MVN}(\boldsymbol{0}, \boldsymbol{\Sigma}_{pre})$$

where $\boldsymbol{GPPRE}_{1:L,p[i]}$ is the L-length vector of realized Gaussian process spatial random effects for all L unique locations within plot $p[i]$, the plot containing observation i. $\boldsymbol{\Sigma}_{pre}$ is an $L \times L$ covariance matrix for the L spatial locations within a plot. The Gaussian process parameters, and thus the covariance matrix, are constant across plots. However, each plot gets a separate draw from the multivariate normal distribution (MVN). Thus, the observations from within the same plot are spatially autocorrelated, but observations from separate plots do not share any spatial autocorrelation. This assumption is sound given the distances between plots (56-1,234 m), which are substantially greater than the plausible range of spatial autocorrelation between samples (0.5-15.0 m; Keane *et al.*, 2012a; Keane *et al.*, 2012b).

Finally, the primary parameters of interest for this study are those controlling the structure of the fine-scale spatial autocorrelation:

Equation 20

$$\boldsymbol{\Sigma}_{pre} = \alpha_{pre}^2 \times \exp\left(\frac{-\boldsymbol{D}^2}{2\upsilon_{pre}^2}\right)$$

where α_{pre} is the magnitude of the Gaussian process spatial random effect for the pre-burn time. $\boldsymbol{D}$ is the $L \times L$ matrix of pairwise distances (in meters) between samples within a plot. υ_{pre} is the length scale parameter for the Gaussian process spatial random effect for the pre-burn time, controlling the rate at which the autocorrelation between samples decays as the distance between them increases. Likewise,

$\boldsymbol{GPPOST}_{1:L,p[i]} \sim \mathrm{MVN}(\mathbf{0}, \boldsymbol{\Sigma}_{post})$. $\boldsymbol{\Sigma}_{post}$ is constructed in the same way as $\boldsymbol{\Sigma}_{pre}$ but with parameters α_{post} and υ_{post}.

Each fine woody debris component (tally of 1-hour, 10-hour, and 100-hour fuels) is modeled separately: Though the models share the same structure, the data and parameters are separate for each component. The structure of the fine woody debris models is identical to that used for litter and duff, with two exceptions. First, $L = 32$ for the fine woody debris data. Second, the covariance matrix for the fine woody debris models is composed as:

Equation 21

$$\boldsymbol{\Sigma}_{pre} = \alpha_{pre}^2 \times \exp(\frac{-\boldsymbol{D}^2}{2\upsilon_{pre}^2}) + (\boldsymbol{I} \times \tau_{pre})$$

where α_{pre}, $\boldsymbol{D}$, and υ_{pre} are as above (Equation 20). $\boldsymbol{I}$ is an $L \times L$ identity matrix with 1s on the diagonal and 0s otherwise. τ_{pre} is Gaussian process nugget, controlling the covariance between samples which share a common location (beyond that which would be expected by their pairwise distance being 0 m). There is likewise a parameter τ_{post} for the post-burn observations. I include the parameters τ_{pre} and τ_{post} for the fine woody debris models because there were replicate observations (two orthogonal 1-meter subtransects) for each spatial location (the center point of each subtransect).

Data preparation, statistical analysis, and processing of results were performed in R version 4.1.1 (R Core Team, 2021) using the packages bayesplot (Gabry and Mahr, 2021), bayestestR (Makowski *et al.*, 2019), cmdstanr (Gabry *et al.*, 2022), cowplot (Wilke, 2020), elevatr (Hollister, 2021), here (Müller, 2020), posterior (Bürkner *et al.*, 2021), raster (Hijmans, 2021), sf (Pebesma, 2018), tidyverse (Wickham *et al.*, 2019), and tmap (Tennekes, 2018). Models for litter and duff depths and tallies of 1-hour, 10-hour, and 100-hour fine woody debris were fit separately using Bayesian parameter estimation (specifically, Hamiltonian Monte Carlo) as implemented in Stan version 2.29.1 (Stan Development Team, 2022b). Parameters were estimated using four chains of 2,000 samples each, with the first 1,000 samples of each chain discarded as warmup. For all models, Normal(0,5) priors were used for β, σ, α_{pre} and α_{post}, InvGamma(5,40) priors were used for υ_{pre} and υ_{post}, and a Half-Cauchy(0,5) prior was used for κ. These priors were selected to be as broad as possible while still allowing for model convergence.

7.2.5 Model validation

The basic diagnostics provided by cmdstanr (assessment of divergences, R-hat values, and effective sample sizes) were inspected for evidence of convergence and between-chain consistency or signs of difficulty estimating parameters. Posterior distributions for all parameters were visually compared with prior distributions to assess the degree to which the data informed posterior parameter estimates. 10% of observations (i.e., individual scalar observations) were randomly held out of the training dataset used to estimate parameters and were only used to assess the out-of-sample predictive performance of the models. For both the training and validation datasets, posterior prediction data were generated using the posterior parameter values. In order to assess model performance, numerous data visualizations and summary statistics were used to explore the relationship between the observed data and the posterior predictions. To evaluate the error in model predictions, I calculated mean absolute errors (MAEs) and weighted mean absolute percentage errors (wMAPEs; MAE divided by the observed mean) for the mean posterior predicted observations against the observed value for each observation in both the training and validation datasets. I also plotted the mean predicted values against the observed values to check for bias (a linear relationship between observed and predicted whose slope is far from one). To check that the observed distributions were consistent with model-predicted distributions, I also compared the distributions of observed data (e.g. the histogram of observed duff and litter depths) against the ensemble of simulated distributions from the posterior predictions (Gabry *et al.*, 2019). For the ease of readers familiar with frequentist statistics, I adopt a hypothesis testing framework to evaluate whether the prescribed burns affected the fine-scale spatial patterns of fuel loads. Specifically, I consider fixed effects whose 89% credible interval (CI; specifically, a shortest probability interval, Liu *et al.*, 2015) excludes 0 to be significantly different from 0. For the Gaussian process parameters which are of primary interest in this study, I consider the prescribed fire to have altered some feature of the spatial pattern if the 89% CIs for the pre-burn and post-burn parameters do not overlap. 89% was selected as the threshold per the recommendation of McElreath (2016), with the acknowledgement that the selection of any significance threshold is somewhat arbitrary.

7.3 RESULTS

Prescribed burns caused large (≥ 30%) proportional reductions in the fuel loads of most fuel components, while also causing a mild (16%) proportional reduction in the stem density of trees and only weakly (5%) reducing stem densities (Table 11).

Basic model diagnostics performed by the cmdstan_diagnose function (Gabry *et al.*, 2022) indicate that the Hamiltonian Monte Carlo algorithm performed satisfactorily for all models. Posterior distributions are clearly different from prior distributions for most parameters (Supplementary Figure 52, Supplementary Figure 53, Supplementary Figure 54, Supplementary Figure 55), indicating that posterior estimates are almost always strongly informed by the data rather than the prior assumptions. The sole exception is the posterior estimate for ν_{post} for the 100-hour fine woody debris model, which substantially overlaps with the prior distribution for that parameter. This indicates that the posterior estimates for ν_{post} for the 100-hour fine woody debris model are only weakly informed by the data and should not be considered meaningful.

The model for litter and duff depths performs well in making pointwise predictions of the training observations and the validation observations. wMAPE (MAE, mean) of the litter and duff depths is 0.30 (1.3 cm, 4.4 cm) on the training data and 0.29 (1.4 cm, 4.6 cm) on the validation data, and there is little or no bias in predicting depths (Supplementary Figure 56 and Supplementary Figure 58). However, the litter and duff observations exhibit an unmodeled tendency towards even-numbered values (Supplementary Figure 57 and Supplementary Figure 59), likely the result of observer bias.

For the 1-hour fine woody debris tallies the wMAPE (MAE, mean) values are 0.24 (2.4 particles, 9.9 particles) for the training data and 0.28 (2.5 particles, 8.9 particles) for the validation data. There is a mild bias towards underpredicting tallies above approximately 25 particles for both the training and validation datasets (Supplementary Figure 60 and Supplementary Figure 62) and the model underpredicts the frequency of 1- or 2-tally observations in both the training and validation datasets (Supplementary Figure 61 and Supplementary Figure 63).

The wMAPE values for the 10-hour fine woody debris tallies are slightly worse at 0.36 (1.0 particles, 2.9 particles) for the training data and 0.38 (1.0 particles, 2.5 particles) for the validation data. The 10-hour fine woody debris tallies model also tends to underpredict tallies above approximately 15 particles (Supplementary Figure 64 and Supplementary Figure 66). However, the frequency distribution of tallies predicted by the model is consistent with both the training and validation data (Supplementary Figure 65 and Supplementary Figure 67).

The wMAPE values for the 100-hour fine woody debris tallies are much worse at 0.78 (0.4 particles, 0.5 particles) for the training data and 0.70 (0.4 particles, 0.6 particles) for the validation data. The 100-hour fine woody debris tallies model tends to underpredict the observed tallies in the training, but not the validation data (Supplementary Figure 68 and Supplementary Figure 70). For both the training and validation datasets, the observed frequency distribution of tallies is consistent with model predictions (Supplementary Figure 69 and Supplementary Figure 71). Given the poor wMAPE values and the influence of the prior on the posterior estimates for ν_{post}, I refrain from further interpretation of the model for 100-hour fine woody debris. The results for the 100-hour fine woody debris tallies are included in tables and figures for completeness.

Fixed effects for the remaining components show that the prescribed fires reduced the overall amount of fuel consistently across all experimental units for litter and duff depths, 1-hour tallies, and 10-hour tallies (Table 12). 89% credible intervals for the main effects of experimental unit include 0, meaning that the units had similar fuel loads pre-burn. Credible intervals for the main effects of post-burn time are negative and exclude 0, indicating that post-burn loads were lower than pre-burn loads in Unit A. Finally, credible intervals for an interaction between experimental unit and time include 0, meaning that the fire's effect on fuel loads was equivalent on units A, B, and C.

For depth of litter and duff and tally of 1-hour and 10-hour fuels, the magnitude of the Gaussian process effect is higher post-burn than pre-burn (Figure 13 and Table 12). The length scale parameter for the Gaussian process spatial random effect is smaller in the post-burn time than the pre-burn time for the litter and duff model. By contrast, the 1-hour fine woody debris model the length scale parameter is higher for post-burn observations (Figure 14). The length scale parameter did not change for the 10-hour fine woody debris. The Gaussian process nugget is higher for the post-burn time in the 1-hour fine woody debris model (Figure 15). The noise parameter is equivalent in the pre-burn and post-burn times for the 10-hour fine woody debris.

7.4 DISCUSSION

To my knowledge, this is the first study to examine the effects of prescribed fire on the fine-scale spatial distribution of surface fuel loads using a replicated experiment study design. This is also the first study to describe the patterns of spatial autocorrelation for surface and ground fuels in a typical unburned second-growth Sierra Nevada mixed conifer forest and in a Sierra Nevada mixed conifer forest after the reintroduction of fire. The fitted parameter values for the hierarchical spatial models for fuel loads of duff, litter, and fine woody debris are given in Table 12. This table addresses my first question by providing a quantitative description of the fine-scale spatial pattern of fuel loads for these fuel components in two contexts: Unburned second-growth MCF and recently burned second-growth MCF. These parameter values can be used to compare to other contexts (assuming they are modeled using the approach described in this dissertation) and/or used to generate continuous simulated fuel beds to feed into a spatially explicit fire model (Linn *et al.*, 2002, 2020).

The second question for this study is what effects prescribed fire, a crucial practice in the management of MCF (North, 2012; Hessburg *et al.*, 2016), has on the fine-scale spatial pattern of litter, duff, and fine woody debris fuel loads. The effects of prescribed fire on the magnitude of the Gaussian process effect (describing the influence of the spatial pattern on fuel loads), the length scale of the Gaussian process effect (describing the distance at which the spatial pattern occurs), and the nugget of the Gaussian process effect (describing additional covariance between co-located observations not accounted for by the spatial pattern) are all affected by the prescribed fire, at least for some fuel components.

This study finds that prescribed fire increased the magnitude of the Gaussian process spatial random effect for litter and duff, 1-hour fine woody debris, and 10-hour fine woody debris samples. Thus, the processes of fuel consumption and post-fire deposition had the effect of magnifying the difference between jackpots (spatial regions with relatively high fuel loads) and gaps (regions with low fuel loads) within each fuel component. This is not the first study to find that disturbances alter the strength of fine-scale spatial patterns: Vakili *et al.* (2016a) examined the effect of thinning and thin-and-burn treatments on the spatial pattern of surface fuels and found that disturbances affected semi-variogram sills, which are analogous to the Gaussian process magnitude. Spatial variation in the effects of consumption and deposition could have contributed to this magnification in the strength of spatial pattern (Hiers *et al.*, 2009; Loudermilk *et al.*, 2014), though more research is needed to better understand the mechanisms by which prescribed fire alters spatial pattern. However, the results presented here differ from those of Vakili *et al.* (2016a) in that here, the spatial pattern in fuel loads was stronger on disturbed (post-burn) plots than on undisturbed (pre-burn) plots for all fuel components. By contrast, Vakili *et al.* (2016a) found that the spatial pattern was generally stronger on undisturbed plots than on plots affected by thinning or thin-and-burn treatments.

Vakili *et al.* (2016a) also studied the effects of disturbances on the length scale of spatial autocorrelation, with results broadly similar to those of this study: The effect of disturbances on the length scale of autocorrelation varied across fuel components. This study found that prescribed fire alone decreased the length scale of autocorrelation (the spatial size of jackpots and gaps) for litter and duff, increased it for 1-hour fuels, and did not affect it for 10-hour fuels (Table 12, Figure 14). Vakili *et al.* (2016a) found that thin-and-burn treatments reduced the range of autocorrelation (analogous to the Gaussian process length scale) for 1-hour fine woody debris, increased it for 100-hour fine woody debris, and did not affect it for duff, litter, or 10-hour fuels.

Unlike Vakili *et al.* (2016a), this study also includes an analysis of changes in the Gaussian process nugget (the amount of covariance between co-located observations beyond that which would be expected on the basis of there being 0 meters separating them) for 1-hour, 10-hour, and 100-hour fuels. Prescribed fire increased the value of the nugget for 1-hour fuels and did not affect it for 10-hour fuels (Table 12, Figure 15). One interpretation of the nugget effect is that it results from very fine-scale spatial variation within each observation (i.e., within the 1 m2 area sampled by the two orthogonal one meter subtransects; Diggle and Ribiero, 2007). It is possible that the effects of the prescribed fire on consumption and deposition of the 1-hour fine woody debris particles made the fuel loads of 1-hour fine woody debris clumpier at these very fine-scales while coarser 10-hour particles were not affected as strongly by consumption and/or deposition.

The specific results related to the strength of the spatial patterns and the characteristic length scales of the patterns differed between this study and the most comparable work in the literature, Vakili *et al.* (2016a). This contrast in results could be due to the fact that the different disturbances altered the fuel bed in different ways: Prescribed fire consumes fuel in a spatially heterogeneous pattern (Robichaud and Miller, 2000) and leads to a spatially heterogeneous flush of post-burn deposition from scorched crowns (York *et al.*, 2022). By contrast, the cut-to-length thinning treatments studied by Vakili *et al.* (2016a) result in the movement of foliage and branch biomass from the canopy onto the surface where the trees are processed and in skid trails which break up continuity of surface fuels. This study also examined fuels shortly after (within a few months of) the prescribed burns, while Vakili *et al.* (2016a) sampled fuels 3 to 7 years post-disturbance, giving more time for the processes of deposition and decomposition to influence the post-disturbance fuel bed (Keane, 2008; Fry *et al.*, 2018). Whether these differences are due to the different disturbances, the different ecosystems studied, or some other factor will need to be explored by gathering more data describing the spatial pattern of surface fuels in different contexts.

Both Vakili *et al.* (2016a) and this study found that the effect of disturbances on the parameters of spatial autocorrelation varied by fuel component. One explanation for this finding is that, like thinning and thin-and-burn treatments, prescribed fire affects different fuel components differently. Fine fuels such as litter and 1-hour fine woody debris tend to be more completely consumed and thus more strongly affected by prescribed fire than 10-hour or 100-hour fuels (Levine *et al.*, 2020). This expectation is consistent with the results of this study (Table 11), which found that prescribed fire changed the magnitude and the length scale of the Gaussian process spatial random effect for litter and duff and changed the magnitude, length scale, and nugget parameters for 1-hour fine woody debris but changed only the magnitude of the Gaussian process spatial random effect for 10-hour fine woody debris. Unlike Vakili *et al.* (2016a) and Keane *et al.* (2012a), this study did not find that the range of spatial autocorrelation consistently increased with increased particle size. While litter and duff had the shortest length scale in this study, the length scales for 1-hour fine woody debris, and 10-hour fine woody debris were similar pre-burn. Furthermore, the length scale for 1-hour fuels was longer than that for 10-hour fuels post-burn (Figure 14). However, this study concurs with existing research showing that surface and ground fuel loads vary at fine spatial scales (Keane *et al.*, 2012a; Vakili *et al.*, 2016a).

The prescribed fires studied here had clear effects on both the overall fuel loads (Table 11) and the fine-scale spatial pattern of litter and duff and fine woody debris. The reduction in fuel loads is a well-understood effect of prescribed fires and is likely to reduce the severity of any subsequent fires (Agee and Skinner, 2005; Hille and Stephens, 2005; Stephens *et al.*, 2009, 2012; van Mantgem *et al.*, 2011; Ritter *et al.*, 2022). The pre-fire pattern of surface fuels in this long unburned forest was likely the result of spatially heterogeneous deposition and decomposition (Hille and Stephens, 2005; Keane, 2008, 2016) as well as the site's history of timber harvests. The altered spatial pattern of surface fuels implies that the pattern of fuel consumption in the prescribed burns was itself spatially heterogeneous (Robichaud and Miller, 2000; Hiers *et al.*, 2009; Loudermilk *et al.*, 2014; Ritter *et al.*, 2020). Fine-scale spatial variation in fire behavior and effects was likely driven by fine-scale variation in microclimate (Miyanishi and Johnson, 2002; Hille and Stephens, 2005; Kreye *et al.*, 2020), airflow (Banerjee, 2020; Ritter *et al.*, 2020; Atchley *et al.*, 2021), and pre-fire fuel characteristics (Mitchell *et al.*, 2009; O'Brien *et al.*, 2016a).

Changes to the fine-scale spatial patterns of fuels have important ecological implications (Loudermilk *et al.*, 2022). The altered spatial pattern of the fine fuels which drive fire behavior is likely to change fire behavior and effects at multiple scales (Thaxton and Platt, 2006; O'Brien *et al.*, 2016a; Ziegler *et al.*, 2017; Atchley *et al.*, 2021). For example, tree mortality is elevated by high litter and duff depths because these contribute to long-duration smoldering combustion which damages fine roots and cambium. Therefore, changes to the spatial pattern of litter and duff are likely to affect the spatial pattern of tree survival in the event of a wildfire or prescribed fire (Stephens and Finney, 2002; Hille and Stephens, 2005). Likewise, jackpots of fine woody debris release greater amounts of heat and are likely to result in local areas of increased crown damage and canopy mortality (Reinhardt and Ryan, 1988). Tree species have evolved to take advantage of such fine-scale variation in fuel properties and fire behavior to exclude competitor species (Williamson and Black, 1981). Likewise, the altered spatial distribution of bare mineral soils (regions where litter and duff depth is zero) will likely affect the spatial distribution of tree regeneration and understory vegetation (Rice, 1993; Hiers *et al.*, 2007; York *et al.*, 2012), shaping the future spatial pattern of the forest. This study demonstrates the use of hierarchical spatial models to quantify fine-scale spatial patterns in fuel loads, a crucial first step in understanding how management decisions are likely to affect fine-scale spatial patterns and thus forest processes.

However, more study is needed to conclusively demonstrate a causal connection whereby different fine-scale spatial patterns of surface fuel produce different patterns of coarse-scale fire behavior and effects. For example, Atchley *et al.* (2021) created simulated fuel beds and used the FIRETEC computational fluid dynamics fire model to show that different fine-scale arrangements of canopy fuels have major implications for coarse-scale fire behavior by affecting airflow and fire-atmosphere feedbacks. However, that study used simulated surface fuels that were set to mirror the canopy, with litter under tree crowns and grass elsewhere. A follow-up study could use grids of litter fuel loads simulated from the models described here to test whether changes to fine-scale spatial pattern of fuel loads affect coarse-scale fire behavior. Crucially, using simulated data would allow researchers to disentangle the effects of fuel reduction from those of an altered spatial pattern.

This study describes the fine-scale spatial pattern of litter and duff and 1-hour, 10-hour, and 100-hour fine woody fuels both before and after prescribed fires in a second-growth Sierra Nevada mixed conifer forest. It finds that prescribed fire not only reduces the amount of fuel but also alters the fine-scale spatial distribution. These results suggest that pattern-process feedbacks shaping the interplay between fine-scale forest structure and fire (Mitchell *et al.*, 2009; Ritter *et al.*, 2020; Loudermilk *et al.*, 2022) are not limited to the realm of canopy fuels. Fire also has clear effects on the spatial distribution of surface and ground fuels, likely with important implications for the behavior and effects of future fires. This study also provides important insight into the structure of fine-scale spatial variation in surface fuels in a second-growth mixed conifer forest both before and after prescribed fire, which will be crucial for studying how fine-scale spatial pattern influences coarse-scale fire behavior and effects. Ultimately, more research is needed to provide managers with a better understanding of how disturbance processes shape, and are shaped by, fine-scale spatial patterns of fuel loads.

7.5 TABLES

Metric	Pre-burn mean (SD)	Post-burn mean (SD)
Stem density (trees/ha)	382.1 (104.1)	321.1 (102.5)
Basal area (m^2/ha)	44.5 (17.7)	42.1 (16.9)
Duff depth (cm)	2.4 (1.1)	1.4 (1)
Duff load (Mg/ha)	37.5 (16.8)	22.3 (15.6)
Litter depth (cm)	3.8 (0.9)	1.3 (0.7)
Litter load (Mg/ha)	33.9 (7.8)	11.8 (7.2)
1-hour count (particles/m)	16.3 (5.5)	3.4 (2.1)
1-hour load (Mg/ha)	1.2 (0.4)	0.3 (0.1)
10-hour count (particles/m)	4.4 (1.1)	1.3 (0.6)
10-hour load (Mg/ha)	4.1 (1)	1.3 (0.5)
100-hour count (particles/m)	0.7 (0.3)	0.3 (0.2)
100-hour load (Mg/ha)	8.3 (3.8)	3.6 (1.7)
1000-hour load (Mg/ha)	17.3 (8.4)	9.9 (4.9)
Shrub biomass (Mg/ha)	1.3 (1.2)	0.9 (0.8)

Table 11: Summary statistics for forest structure metrics both pre- and post-burn. Values are the mean and standard deviation across all 19 inventory plots, where within-plot subsamples (e.g., duff depths) were averaged to create plot-level means.

	Litter and duff	**1-hour FWD**	**10-hour FWD**	**100-hour FWD**
Intercept	1.51 (1.34, 1.69)	2.63 (2.47, 2.81)	1.3 (1.15, 1.44)	-0.6 (-0.88, -0.31)
compB	-0.11 (-0.38, 0.21)	-0.27 (-0.54, 0.02)	-0.17 (-0.43, 0.07)	-0.38 (-0.87, 0.08)
compC	0.29 (-0.01, 0.55)	-0.24 (-0.55, 0.04)	-0.23 (-0.48, 0)	-0.56 (-1.03, -0.09)
timePost	-1.45 (-1.67, -1.23)	-2.3 (-2.62, -1.96)	-1.44 (-1.64, -1.22)	-1.17 (-1.54, -0.84)
compBtimePost	-0.03 (-0.39, 0.34)	0.01 (-0.55, 0.57)	0.09 (-0.28, 0.41)	0.29 (-0.26, 0.83)
compCtimePost	0.27 (-0.1, 0.6)	-0.36 (-0.89, 0.24)	0.17 (-0.16, 0.52)	0.55 (0.02, 1.14)
Plot SD	0.23 (0.12, 0.35)	0.24 (0.12, 0.37)	0.16 (0.05, 0.28)	0.35 (0.2, 0.55)
GP magnitude (pre)	0.77 (0.71, 0.83)	0.63 (0.57, 0.69)	0.61 (0.53, 0.69)	0.92 (0.78, 1.08)
GP magnitude (post)	1.4 (1.28, 1.52)	1.37 (1.18, 1.54)	0.89 (0.78, 1.02)	0.85 (0.53, 1.16)
GP length scale (pre)	1.58 (1.3, 1.84)	3.52 (2.96, 4.1)	2.86 (2.26, 3.44)	3.25 (2.51, 4.01)
GP length scale (post)	1.03 (0.92, 1.13)	6.84 (5.79, 8.09)	2.96 (2.47, 3.48)	4.71 (2.5, 7.83)
GP nugget (pre)	NA	0.08 (0.06, 0.11)	0.13 (0.08, 0.18)	0.11 (0, 0.23)
GP nugget (post)	NA	0.44 (0.33, 0.55)	0.15 (0.05, 0.26)	0.67 (0.24, 1.08)
NB Dispersion	29.58 (15.77, 49.95)	36.37 (26.23, 48.92)	149.62 (19.94, 836.8)	87.27 (6.94, 462.57)

Table 12: Parameter estimates for litter and duff and 1-hour, 10-hour, and 100-hour fine woody debris models, all of which include a negative binomial response and a log link. Parameter values are the posterior median and an 89% shortest probability interval credible interval in parenthesis. The fixed effects are compartment crossed with time: Intercept is the (log) mean value in compartment A pre-burn, "compB" is the main effect of compartment B, "compC" is the main effect of compartment C, "timePost" is the main effect of the post-burn time, "compBtimePost" is the interaction between compartment B and the post-burn time, and "compCtimePost" is the interaction between compartment C and the post-burn time. "Plot SD" is the standard deviation of the plot random effect. "GP magnitude (pre)" AND "GP magnitude (post)" are the effect magnitudes of the Gaussian process spatial random effects for pre-burn and post-burn observations, respectively. "GP length scale (pre)" and "GP length scale (post)" are the length scale parameters controlling the decay rate of the spatial autocorrelation in the Gaussian process spatial random effects for the pre-burn and post-burn observations, respectively. "GP nugget (pre)" and "GP nugget (post)" are the Gaussian process noise parameters describing the covariance between observations from the same spatial location in the pre-burn and post-burn times, respectively. "NB Dispersion" is the parameter controlling the overdispersion in the negative binomial response distribution (with higher values reducing the overdispersion).

7.6 FIGURES

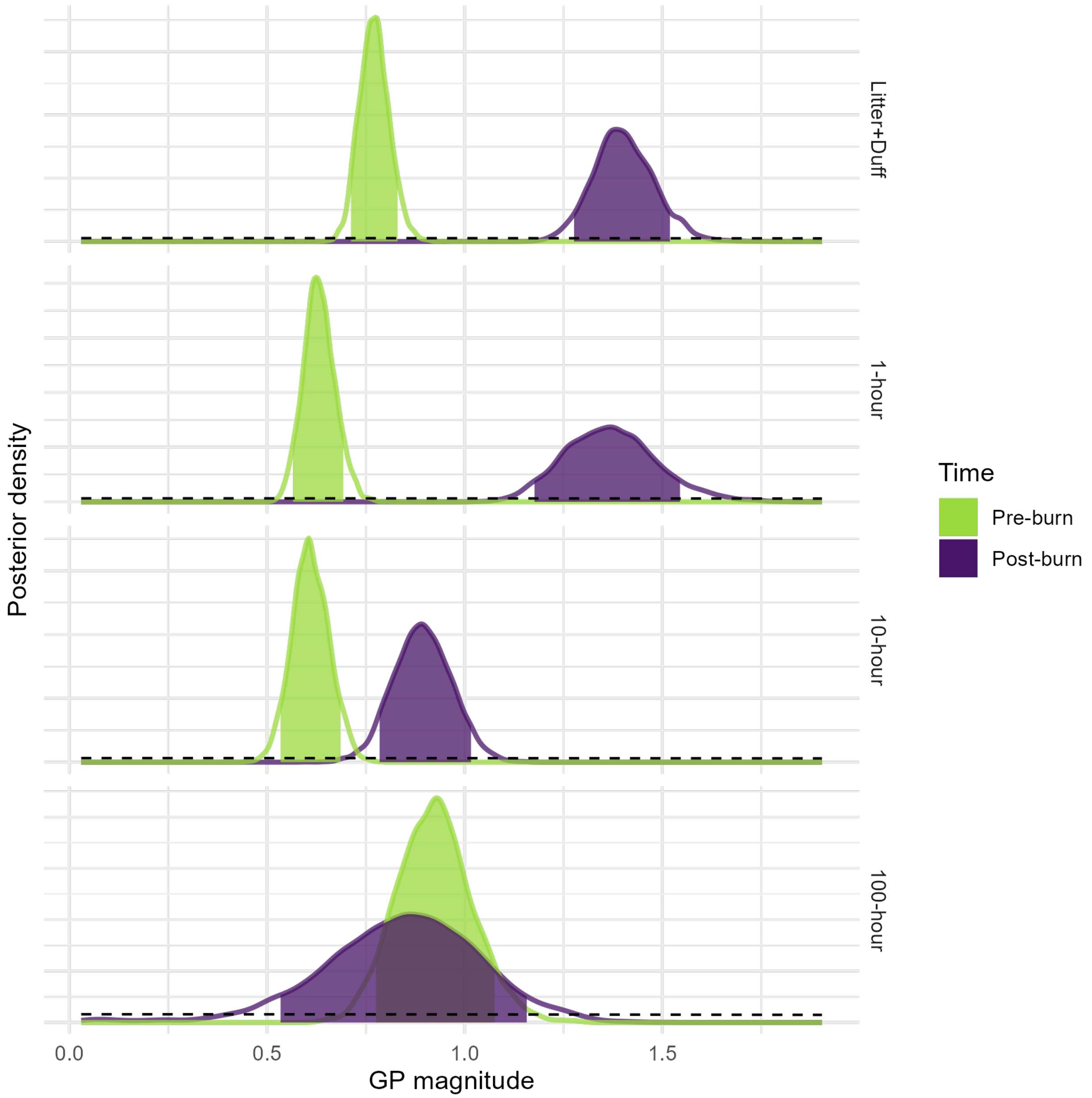

Figure 13: Posterior distributions for Gaussian process magnitudes in pre-burn and post-burn times for litter and duff and 1-hour, 10-hour, and 100-hour fine woody debris fuels. Parameter values are on the x-axis, probability density on the y-axis. The shaded region under each curve is an 89% credible interval (specifically, a shortest probability interval). The prior probability density is shown as the dashed black line.

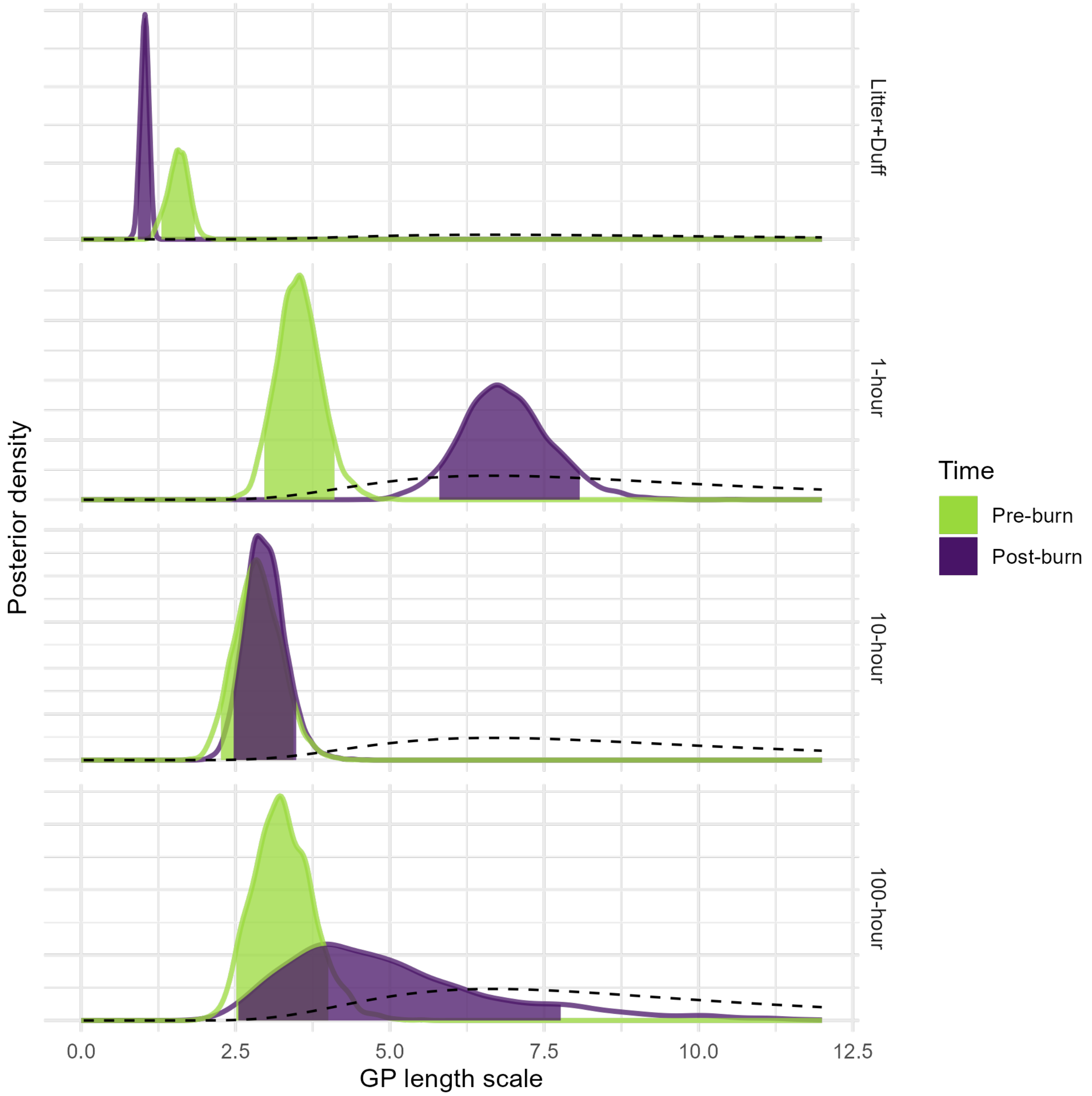

Figure 14: Posterior distributions for Gaussian process length scale parameters in pre-burn and post-burn times for litter and duff, 1-hour, 10-hour, and 100-hour fine woody debris fuels. Parameter values are on the x-axis, probability density on the y-axis. The shaded region under each curve is an 89% credible interval (specifically, a shortest probability interval). The prior probability density is shown as the dashed black line.

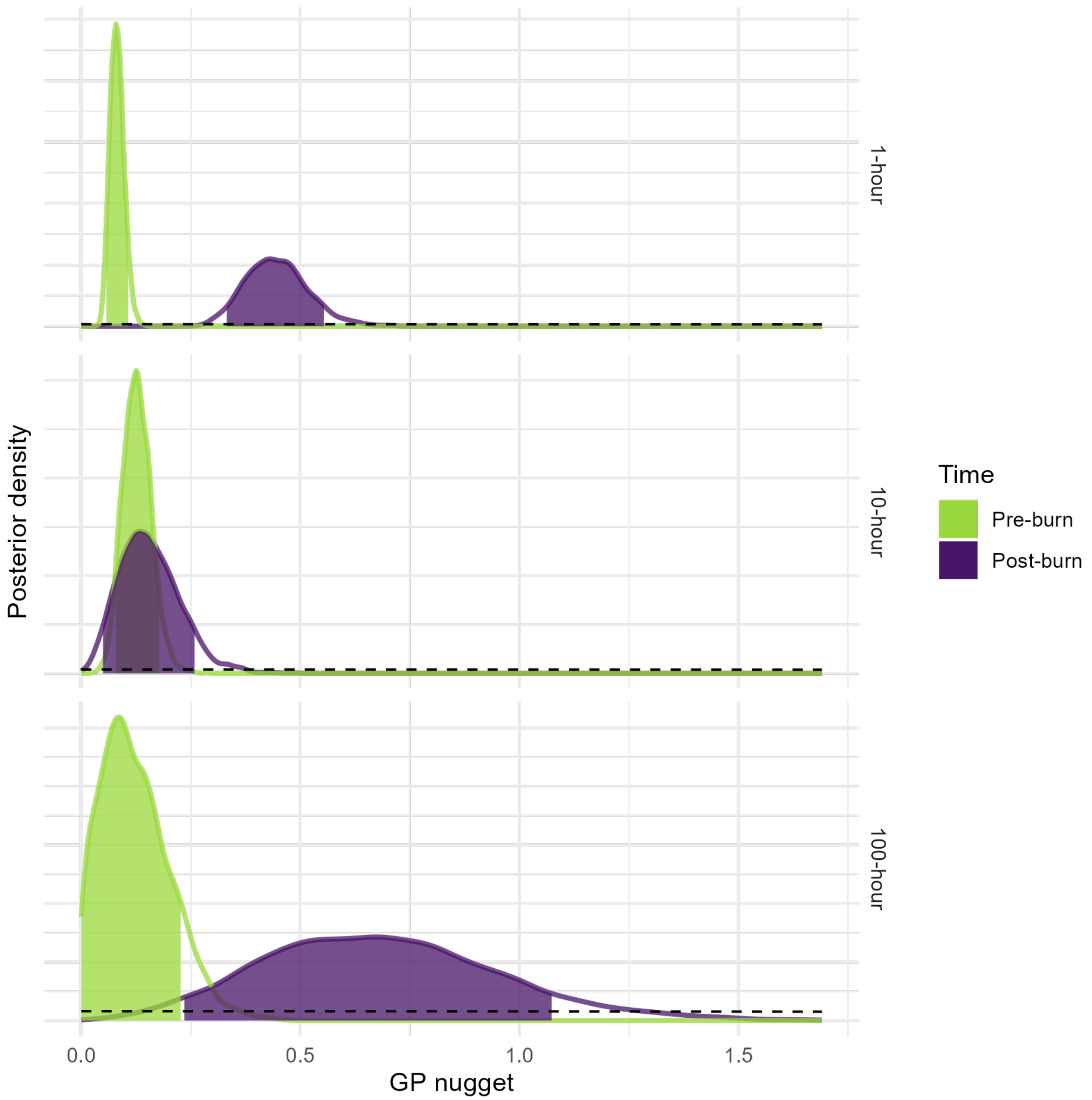

Figure 15: Posterior distribution for Gaussian process noise parameters in pre-burn and post-burn times for 1-hour, 10-hour, and 100-hour fine woody debris fuels. No noise parameter was included in the litter and duff models because there was only a single observation at each spatial location in the litter and duff data. Parameter values are on the x-axis, probability density on the y-axis. The shaded region under each curve is an 89% credible interval (specifically, a shortest probability interval). The prior probability density is shown as the dashed black line.

8 TRANSITION

In the second chapter, I applied hierarchical spatial models to better understand the ecological effects of prescribed fire, an important management practice in Sierra Nevada mixed conifer forests. That second study examined the effects of a disturbance process on the spatial pattern of forest biomass at fine scales. In the final chapter, I consider pattern-process relationships on a much larger scale, examining the effect of disturbance processes on the population-wide demographic structure and trajectory of an important tree species. This chapter focuses less on pioneering methods and basic science, instead emphasizing the applied management question of how best to prioritize among a variety of threats impacting a target species.

9 DEMOGRAPHIC STATUS, TRAJECTORY, AND STRESSORS OF *SUGAR PINE* ACROSS THE WESTERN USA

9.1 INTRODUCTION

Novel anthropogenic stressors threaten species but may be amenable to management (Millar and Stephenson, 2015; Hessburg *et al.*, 2021). However, given the scarcity of resources, it is often necessary to prioritize some stressors over others (North *et al.*, 2009, 2019; National Park Service, 2013). Demographic models built from large, longitudinal datasets (such as the Forest Inventory and Analysis, or FIA, dataset) can provide detailed insight into how stressors impact species of concern across wide geographic ranges (Davis *et al.*, 2019; Shriver *et al.*, 2021). In this study, I use data from the national forest inventory to fit vital rate models that explicitly include effects of major stressors. By comparing their effects on vital rates and demographic summary statistics (such as the asymptotic population growth rate), I can assess the relative importance of the stressors and highlight the mechanisms by which they influence the population trajectory. Findings from such demographic analyses can provide crucial information about how best to prioritize varied stressors in making management decisions (Shriver *et al.*, 2019; Bradford *et al.*, 2022; McCauley *et al.*, 2022).

Like many plant species, sugar pine (*Pinus lambertiana*) faces numerous challenges in the Anthropocene (Kress and Krupnick, 2022). Managers and policymakers are concerned about the future status of the species (Kinloch, Jr. *et al.*, 1996). Sugar pine is the largest pine species in both height and volume; it is an important timber species; and it is a component of several dry western conifer forest types (Kinloch, Jr. and Scheuner, 1990). In the extensive Sierra Nevada mixed conifer forest, sugar pine typically comprises 5-25% of basal area (Safford and Stevens, 2017; Bohlman *et al.*, 2021). Its range extends through much of the North American Mediterranean zone throughout mountain ranges in California and central Oregon. There is a small population in northwestern Mexico but California encompasses the heart of its range (Kinloch, Jr. and Scheuner, 1990). Sugar pine seeds are an important food source for animal species (Fowells and Schubert, 1956; Thayer *et al.*, 2005; Murray and Tomback, 2010), and mature sugar pines are large-diameter trees which play a key role in the structure and function of ecosystems in which they occur (Lutz *et al.*, 2013, 2018, 2020). However, sugar pines face numerous challenges in the Anthropocene.

First, disruptions to the fire regime impact the fitness of this moderately shade-tolerant, fire-surviving species (Schwilk and Ackerly, 2001; Niinemets and Valladares, 2006). In California, sugar pine reaches its greatest dominance in frequent fire forest types with mean fire return intervals of at most 11-16 years (Yeaton, 1983, 1984; Safford and Stevens, 2017; Bohlman *et al.*, 2021). Large adults typically survive low-to-moderate severity wildfires and produce recruits that can take advantage of the reduced competition for light and water in the post-fire environment. However, changes in forest structure wrought by historical timber harvests and fire suppression, coupled with a warming climate, have increased sugar pine's exposure to high severity wildfire (Safford and Stevens, 2017; Stevens *et al.*, 2017; Parks and Abatzoglou, 2020; Bohlman *et al.*, 2021). This altered fire regime threatens not only the persistence of sugar pine but also the mixed conifer forest type as a whole (Steel *et al.*, 2015; Shive *et al.*, 2018; Coop *et al.*, 2020).

Second, an invasive fungal pathogen, *Cronartium ribicola* (white pine blister rust; WPBR) has spread across much of sugar pine's range since its introduction to North America in the early 20th century, causing substantial mortality (Van Mantgem *et al.*, 2004; Maloney *et al.*, 2011; Dudney *et al.*, 2020).

WPBR affects white pines (subgenus *Strobus*, excluding the pinyon pines in subsection *Cembroides*) by parasitizing foliage, shoots, inner bark, and outer xylem, causing the formation of cankers which can reduce vigor and kill outright by girdling the stem (Geils *et al.*, 2010). The epidemic in the western United States has been severe enough to cause the related species, *Pinus albicaulis*, to be listed as endangered (Mahalovich and Stritch, 2013). There has likewise been considerable concern about the outlook for sugar pine (Kinloch, Jr. *et al.*, 1996).

Third, there is evidence that the contemporary forest structure impacts the population dynamics of sugar pine, beyond its contribution to an altered fire regime, by increasing competitive stress. Effective fire suppression, which was instituted across much of sugar pine's range in the 20th century, has resulted in an overall densification of these forests (Stephens *et al.*, 2015; Safford and Stevens, 2017; Bohlman *et al.*, 2021; North *et al.*, 2022). In these dense forests, sugar pine saplings do not thrive like the more shade-tolerant constituents of the mixed conifer forest such as *Abies concolor* and *Calodecrus decurrens* (Ansley and Battles, 1998; Levine *et al.*, 2016). There is also evidence that increased competition in a densified forest structure has reduced the vigor of adult sugar pines, thus reducing their ability to resist other stresses (Young *et al.*, 2017; Restaino *et al.*, 2019; Furniss *et al.*, 2021; North *et al.*, 2022).

Finally, the changing climate may increase the duration and severity of droughts and thus water stress. Heighted water stress at the landscape scale can drive bark beetle epidemics, which are already causing mass mortality events in sugar pine's range (Fettig *et al.*, 2019; Stephenson *et al.*, 2019; Steel *et al.*, 2021a). Once these epidemics are underway, bark beetles tend to preferentially target large and reproductively-valuable sugar pines, independent of individuals' stress (Stephenson *et al.*, 2019), exacerbating the impact of this stressor on the demographic outlook for sugar pine. Water stress can also kill trees, especially small individuals, more directly via hydraulic failure and/or carbon starvation (Moran *et al.*, 2019).

Given these threats, there are widespread concerns about the future of sugar pine (Kinloch, Jr. *et al.*, 1996). Proposed management options range from reducing tree density via restoration thinning and beneficial fire (Stephens *et al.*, 2009; Restaino *et al.*, 2019; Steel *et al.*, 2021a) to out planting seedlings with genetic resistance to WPBR (Aitken and Whitlock, 2013; North *et al.*, 2019). However, many of these options are expensive and/or difficult to implement (Heywood, 2017). In a context where natural resource management funding is constrained, it is important to understand the status and demographic outlook for sugar pine as a species. This study seeks to inform decisions about when and where to prioritize management actions to conserve sugar pine. To that end, I address two questions:

1) What is the current trajectory of abundance across the range-wide ensemble of sugar pine populations?
2) What is the relative importance of the various stressors (fire, WPBR, competition, and water stress) acting on sugar pine?

The first question is evaluated directly using data from the FIA program. To answer the second question, I quantify the effects of the stressors by first using the FIA data to estimate the parameters for vital rate functions as a function of individual size and the presence or severity of the stressors (Eitzel *et al.*, 2013, 2015; Kohyama *et al.*, 2018; Shriver *et al.*, 2021). Once the impacts of stressors on individual vital rates are quantified, I predict population trajectory in response to each stressor by synthesizing the vital rates in an integral projection model (IPM; Merow *et al.,* 2014; Needham *et al.*, 2018; Doak *et al.*, 2021). This approach illuminates the ways in which the stressors' impacts on individual trees scale up to affect range-wide trends.

9.2 METHODS

9.2.1 Study area

The area of interest for this study is that part of the range of sugar pine which is within the contiguous United States (Figure 16). This is the vast majority of sugar pine's range, excluding only an isolated population in Baja California. The range of sugar pine in the United States extends from 33.7°N to 45.3°N throughout much of the Sierra Nevada and Klamath mountains, and parts of the Transverse, Peninsular, and Southern Cascades ranges in the US states of California and Oregon. Sugar pine is widely distributed throughout this range as an important element of the mixed conifer forest belt at elevations ranging from 1000 m to 2700 m (Safford and Stevens, 2017; Bohlman *et al.*, 2021). The climate throughout this range is Mediterranean, with a cool-wet season and a warm-dry season (Safford and Stevens, 2017).

9.2.2 Inventory data

The Forest Inventory and Analysis program (FIA) conducts the national forest inventory program for the United States (Bechtold and Patterson, 2005). Since 2001, the empirical foundation to the national inventory consists of a network of repeat-measure, tagged-tree, fixed-area plots measured at decal frequency in the western United States (Phase 2 plots, Bechtold and Patterson, 2005). Here, I use 1,221 Phase 2 plots from California and Oregon (FIA Phase 2 Database version 1.8.0.03) where live sugar pine was present in the plot at either the initial measurement (2001-2009) or first remeasurement (2010-2019).

In the public database, the geographic coordinates listed for the FIA plots are not exact. To protect privacy and preserve plot integrity, the coordinates are "fuzzed." This fuzzing includes randomly perturbing the location of all plots so that most fuzzed locations are within 0.8 km of the true location and no fuzzed location is more than 1.6 km from the true location. In addition, between 0% and 10% of plot locations are swapped with a compositionally and structurally similar plot in the same county (Bechtold and Patterson, 2005). FIA plots are placed on a hexagonal grid with a density of approximately 1 plot per 2,429 ha. Each plot is revisited approximately once every 10 years, which I treat as the census interval for the purpose of modeling population dynamics. Of the plots used for this study, 90% had an inventory interval from 9.6 to 10.3 years, with a mean interval of 10.0 years, a minimum interval of 7.9 years, and a maximum interval of 12.3 years. Each included plot was remeasured one time in this study. Thus, there is one census interval per plot, with the initial censuses taking place from 2001-2009 and the remeasurements from 2011-2019.

The design of the FIA Phase 2 tree inventory relies on both spatial adjacency and nesting to conduct a statistically robust sample of trees at each location. Thus, each Phase 2 plot is a constellation of fixed-area samples. Trees ≥ 12.7 cm diameter at breast height (1.37 m, DBH) are inventoried on four 168 m^2 permanent subplots. Small trees from 2.54-12.7 cm DBH are inventoried on four 13.5 m^2 microplots nested within the subplots, and large trees (≥ 70.0 cm or ≥ 91.4 cm DBH, depending on the plot) on four 1012 m^2 macroplots that include the subplot. Data inventoried for each individual stem include the species, live/dead status, DBH, and a "damage agent" code indicating whether some agent (e.g., white pine blister rust) is visibly affecting the individual's health. Trees (all stems ≥ 2.54 cm DBH) are physically tagged to facilitate relocation of specific individuals at remeasurement.

These repeated inventories of individual trees were used to estimate parameters for vital rate functions (described in detail below) of growth, survival, and recruitment across the range of sugar pine. The survival or death of 3,530 sugar pine individuals was tracked to estimate the parameters of the survival function, and growth of the 2,821 surviving individuals was used to estimate the parameters of the growth function. The number of new recruits (stems with DBH between 2.54 cm and 12.7 cm which were not present on the microplot at initial census but appeared in the second census) was calculated on 967 plots with sugar pine present at initial census to estimate the fecundity (the number of new recruits per existing individual).

I included harvested trees as mortalities in the survival data for two reasons. First, the goal is to understand the actual population dynamics of sugar pine across its range, inclusive of mortality caused by harvests. Second, the prevalence of post-fire salvage harvests on some land ownerships across the range of sugar pine make it likely that some mortalities caused by fire, disease, competition, or water stress were later harvested, and it is important to include these mortalities in vital rates estimation. In addition to the tree-level data collected, the FIA program also records information about forest conditions, including the presence of significant disturbances (e.g., fire), the ecological subsection the plot is located within (Bailey, 2016), and the fuzzed GPS coordinates of the plot center.

To assess the current trajectory of sugar pine abundance across its range, I calculated the per-plot basal area and stem densities for individuals greater than 2.54 cm DBH on every plot where sugar pine was present at initial measurement or remeasurement (1,221 plots). Across-plot means and standard errors were calculated and plotted for both basal area and stem density.

9.2.3 Climate

To assess the level of water stress that sugar pine individuals were exposed to, I extracted monthly climatic water deficit (CWD) estimates for each nominal plot location from the TerraClimate dataset (Abatzoglou *et al.*, 2018). CWD is a measure of evaporative demand not met by available water (Stephenson, 1998). The TerraClimate dataset provides modeled estimates of CWD at approximately 4 km resolution for the years 1958-2020. The 4 km resolution approximately matches the degree of fuzzing associated with the FIA plot locations, so that fuzzing is unlikely to add substantial error in the estimation of CWD experienced at the true plot location. Mean growing season (May-October) CWD estimates for each year between a plot's initial measurement and its revisit provide a proxy for the water stress experienced by individuals between the two censuses. The annual mean growing season CWD estimates were summarized in two ways. First, the 20-year mean of the annual CWD estimates provides a measure of the usual climatic dryness characteristic of each site, enabling the comparison of typically wetter vs. typically drier locations across space. Second, the 90th percentile of the annual departures from the site-specific mean CWD provide a measure of the most severe drought (departure from usual climatic conditions) experienced by each plot location between the initial observation and the remeasurement.

9.2.4 Vital rates models

I initially modeled survival, growth, and fecundity jointly, closely following the approach described in Shriver *et al.* (2021) in order to leverage the FIA data's microplot seedling (< 2.54 cm DBH) tallies when estimating recruitment. However, that approach performed poorly. A minor overestimation of the growth rate for the smallest stems resulted in a major overestimation of the recruitment rate, due to the way the three vital rate models are interlinked in the Shriver *et al.* (2021) approach. For this study survival, growth, and fecundity functions were independently estimated based on the observed data, and only stems appearing on subplots (≥ 2.54 cm DBH) counted as new recruits. The model for survival is:

Equation 22

$$s_i \sim \text{Bernoulli}(p_i)$$

Equation 23

$$\text{logit}(p_i) = \mathbf{X}_{i,*}\beta_{(s)} + \gamma_{(s)j} + \delta_{(s)k}$$

where s_i is an integer indicating the live/dead status (1 if live, 0 if dead) of individual i at the revisit measurement (approximately 10 years after initial measurement), p_i is the probability of survival from initial measurement to remeasurement, $\mathbf{X}_{i,*}$ is a row vector of covariates (described below) for individual i, $\beta_{(s)}$ is a column vector of fixed effect coefficients for the survival sub model, $\gamma_{(s)}$ is a vector of plot-level random effects indexed by the plot j for individual i with $\gamma_{(s)j} \sim \mathrm{N}(0, \sigma^2_{\gamma(s)})$, and $\delta_{(s)}$ is a vector of ecoregion subsection-level random effects indexed by the ecoregion subsection k for individual i with $\delta_{(s)k} \sim \mathrm{N}(0, \sigma^2_{\delta(s)})$. Plot and ecoregion random effects were included to ensure independence of residuals in a context where there are potentially unmeasured covariates affecting vital rates at fine spatial scales (plot level random effects) or coarse spatial scales (ecoregion level random effects).

The fixed effects covariates for each individual i in the row vector $\mathbf{X}_{i,*}$ were selected to represent individual size and the four stressors (fire, WPBR, competition, and water stress). A quadratic effect of size was included to allow the vital rate functions to capture potentially nonlinear relationships between size and vital rates, and interactions between size (and quadratic size) and the stressors were included because existing research suggests that the effects of these stressors are size-contingent (Hood *et al.*, 2007; Stephenson *et al.*, 2019; Dudney *et al.*, 2020). The fixed effects are: The intercept ($INTERCEPT$), the DBH in meters at initial measurement (DBH), the squared DBH (DBH^2), a binary flag indicating whether the individual's plot experienced a fire at least 0.404 ha in size that killed or damaged at least 25% of trees between initial measurement and remeasurement ($FIRE$), a binary flag indicating whether any trees in the individual's plot displayed signs of white pine blister rust infection at initial measurement ($WPBR$), the plot-level basal area (BA) at initial measurement (BA; a proxy for competition), the plot-level 90th percentile of growing season departure from mean climatic water deficit ($DROUGHT$) between initial measurement and remeasurement, the plot-level growing season mean climatic water deficit over the period 2000-2020 ($DRYNESS$), and interactions between DBH and DBH^2 and all other variables ($DBH \times FIRE$, $DBH^2 \times FIRE$, $DBH \times WPBR$, $DBH^2 \times WPBR$, $DBH \times BA$, $DBH^2 \times BA$, $DBH \times DROUGHT$, $DBH^2 \times DROUGHT$, $DBH \times DRYNESS$, and $DBH^2 \times DRYNESS$). BA, $DROUGHT$, and $DRYNESS$ were centered and scaled to have 0 mean and unit variance across all plots. I used size on the meter scale so that size was on a similar scale as the other explanatory variables, which improved the model's performance during parameter estimation (details below).

The model for growth is:

Equation 24

$$z_i \sim \mathrm{Normal}(\mu_i, \sigma^2_\varepsilon)\mathrm{T}[0.0254,]$$

Equation 25

$$\mu_i = \mathbf{X}_{i,*}\beta_{(z)} + \gamma_{(z)j} + \delta_{(z)k}$$

where z_i is the DBH in meters of individual i at remeasurement drawn from a truncated normal distribution (to prevent excluded-by-sampling-design size below 2.54 cm DBH), μ_i is the mean predicted DBH of individual i at remeasurement, σ^2_ε is the residual variance, $\mathbf{X}_{i,*}$ is a row vector of the fixed effects covariates, and the other parameters are as defined for the survival sub model, though here indexed z to indicate that they are the parameters specifically for the growth sub model. The fixed effect covariates for the growth model are the same as those for the survival model. Note that the coefficient for the main effect of initial size should be very close to 1, because the size at remeasurement is primarily determined by the initial size.

The response distribution for the fecundity model is:

Equation 26

$$\mathrm{c}'_j \sim \text{Neg.Binomial}(\mathbf{n}'_j \times a, \kappa)$$

where c'_j is the observed count of new recruits (individuals between 2.54 cm and 12.7 cm DBH which were newly present at the follow up census) on plot j. $\mathbf{n}'_j$ is the area-standardized occurrence rate of new recruits on plot j at remeasurement, a gives the total plot area surveyed for individuals between 2.54 cm and 12.7 cm DBH, and κ is the dispersion parameter for the negative binomial distribution.

The area-standardized occurrence rate of new recruits ($\mathbf{n}'_j$) is the sum of the fecundity of each of 99 size classes (2.54 to 250.4 cm DBH in 2.54 cm wide bins):

Equation 27

$$\mathbf{n}'_j = \sum_{k=1}^{99} f \times \mathbf{n}_{j,k}$$

where f is the fecundity (the number of new recruits produced per existing individual) and $\mathbf{n}_{j,k}$ is the area-standardized occurrence rate of individuals in the kth size class at the initial census. The low frequencies of new recruits in the data (942 of the 967 observed plots had no new recruits) precluded estimation of a more complex fecundity function which would have allowed fecundity rates to vary by individual sizes and/or the presence of stressors, as with the survival and growth functions. Instead, I estimate a simple overall fecundity rate using an intercept-only linear model with a log link:

Equation 28

$$\log f = \beta_{0(f)}$$

where $\beta_{0(f)}$ is the intercept for the log-scale linear predictor of fecundity.

Model data were prepared using the tidyverse package (Wickham *et al.*, 2019) in R Version 4.1.1 (R Core Team, 2021), and Bayesian parameter estimation was performed using Hamiltonion Monte Carlo as implemented in Stan version 2.28.2 (Stan Development Team, 2022b). The sampler was run in four chains for 2000 iterations per chain (discarding the first 1000 iterations as warmup). The prior distribution specified for all parameters was Normal(0,5) (with variance terms restricted to positive values) except for the negative binomial dispersion parameter κ, which received a Cauchy(0,5) prior following Shriver et al. 2021. Other R packages used for data preparation, statistical analysis, and processing of results were bayesplot (Gabry and Mahr, 2021), cmdstanr (Gabry *et al.*, 2022), cowplot (Wilke, 2020), DBI (R-SIG-DB *et al.*, 2021), ggspatial (Dunnington, 2021), here (Müller, 2020), posterior (Bürkner *et al.*, 2021), raster (Hijmans, 2021), RSQLite (Müller *et al.*, 2021), sf (Pebesma, 2018), spData (Bivand *et al.*, 2021), tmap (Tennekes, 2018), units (Pebesma *et al.*, 2016), and USAboundaries (Mullen and Bratt, 2018).

9.2.5 Model validation

The basic diagnostics provided by cmdstanr (R-hat values, trace plots, per-chain posterior density plots, posterior pair plots, and assessment of divergences) were inspected for evidence of convergence and between-chain consistency or signs of difficulty estimating parameters. To assess the out-of-sample predictive performance of the models, 10% of plots were randomly held out of the training dataset used to estimate parameters. For both the training and validation data sets, the central tendency and spread of data simulated using posterior parameter values (posterior predictions) were compared to the true observed values of individual growth and individual survival to assess whether model results were consistent with empirical results. Likewise, I compared histograms of observed vs. simulated counts using the estimated fecundity rate to assess whether model results were consistent with real data.

9.2.6 Evaluation of vital rate functions and integral projection models

Once parameters were estimated and model validity checked, the fitted model for vital rate functions was used to assess the impact of the various stressors (fire, WPBR, competition, and water stress) on the vital rates of growth and survival. Effect strength was assessed in relative terms based on the magnitude of the median parameter estimate and the coverage of the 90% quantile-based credible interval (CI). For the survival model, fixed effects coefficients whose median absolute value exceeded 2.0 (on the logit scale) were interpreted as strong, while effects whose median absolute value was less than 2.0 but whose CI excluded 0 were interpreted as moderate. For the growth model, fixed effects coefficients whose CI excluded 0 were interpreted as significant. For both models, the effect of a stressor on a vital rate was interpreted as weak or uncertain if the CI for the associated fixed effect included 0. The choice of 90% quantile-based credible intervals is following the conventions of the posterior package in R (Bürkner *et al.*, 2021), though any specific threshold for significance is somewhat arbitrary (McElreath, 2016). To provide more nuanced insight into the effects of the various stressors than simple hypothesis tests, I constructed posterior predictions using hypothetical data. Idealized explanatory data were constructed representing a suite of environmental scenarios corresponding to situations where a single stressor is present (in the case of the discrete explanatory variables $FIRE$ and $WPBR$) or elevated/depressed by one standard deviation (in the case of the continuous variables BA, $DROUGHT$, and $DRYNESS$), while other stressors are absent or held at their mean value (0 for scaled variables). Given these environmental contexts, vital rates for individuals ranging in size from 0.0254-1.25 m DBH (up to approximately the 95th percentile individual size observed) were predicted using the parameters from each posterior sample, and the predicted response plotted against DBH and stressor.

To understand the demographic implications of the stressors' impacts on vital rates, I constructed a suite of integral projection models (Merow *et al.*, 2014; Needham *et al.*, 2018; Doak *et al.*, 2021). For each environmental scenario j (as described above) and posterior draw d I generated an integral projection model transition kernel**.** Each transition model kernel $\mathbf{A}_{d,j,*,*}$ is a 99×99 discretized integral projection model kernel describing the rates of transition from each $v = 1,2,\ldots,99$ size classes (each 2.54 cm DBH wide) into $u = 1,2,\ldots,99$ size classes over the course of a single 10-year census interval, which includes fecundity as well as growth and survival. The largest individual appearing in the vital rates datasets was 2.45 m DBH, though even larger sugar pines have been recorded. The elements of this matrix are a function of the parameters for the survival, growth, and fecundity functions and the data describing scenario-specific covariates, as described below. A separate $\mathbf{A}_{d,j,*,*}$ exists for each plot j and posterior draw d. The elements of $\mathbf{A}_{d,j,*,*}$ for each plot j and draw d are given by:

Equation 29

$$\mathbf{A}_{d,j,u,v} = p_{d,j,v} \cdot g_{d,j,u,v} + r_u \cdot f_d$$

where $p_{d,j,v}$ is the proportion of individuals in size class v which will survive the 10-year census interval on plot j using the dth draw of the survival parameters, $g_{d,j,u,v}$ is the proportion of surviving individuals in class v which grow into class u during the census interval on plot j using the dth draw of growth parameters, r_u is the probability that a new recruit will transition into size class u by the end of the

10-year interval, and f_d is the number of new recruits generated per existing individual using draw d of the fecundity parameters.

Following the recommendations of Doak *et al.* (2021), the continuous growth kernel described in Equation 24 is discretized into size class transition probabilities using the cumulative density function difference method. That is, $g_{d,j,u,v}$ is the probability that an individual on plot j with DBH equal to the midpoint of size class v will have a DBH at remeasurement somewhere between the upper and lower bounds of size class u, and is given by:

Equation 30

$$g_{d,j,u,v} = \frac{\Phi\left(\text{Upper}_u | \mu_{d,j,v}, \sigma^2_{\varepsilon,d}\right) - \Phi\left(\text{Lower}_u | \mu_{d,j,v}, \sigma^2_{\varepsilon,d}\right)}{1 - \Phi\left(0.0254 | \mu_{d,j,v}, \sigma^2_{\varepsilon,d}\right)}$$

where Φ is the cumulative probability density function of a normal distribution with mean $\mu_{d,j,v}$ and variance $\sigma^2_{\varepsilon,d}$ evaluated at three locations: 1) The upper bound of size class u (Upper_u), 2) the lower bound of size class u (Lower_u), or 3) at 0.0254 cm (the minimum modeled size). This is an exact method for calculating the area under the probability density function for the growth kernel and normalizing it by that portion of the kernel which is in the modeled size range. $\mu_{d,j,v}$ is calculated for each draw d, plot j, and size class v from Equation 25 using the midpoint DBH of size class v and the environmental covariates associated with plot j. Because the objective was to better understand the influence of the stressors on vital rates (i.e., the fixed effects), the calculation assumes that both the plot random effect and the ecoregion random effect are equal to 0.

Likewise, $p_{d,j,v}$ is calculated using Equation 23 to predict the proportion of those individuals whose DBH is equal to the midpoint of size class v on plot j which survive to the second census (using parameter values from draw d). I used the observed size distribution of new recruits to calculate the proportion of new recruits falling into each 2.54 cm bin, giving $r_u \cong [0.72, 0.10, 0.10, 0.08, 0, \ldots, 0]$. Eviction from the largest size class is avoided by setting an extremely high upper size bound for the largest class, such that portion of individuals growing beyond the maximum bound is numerically indistinguishable from 0.

The largest real eigenvalue of each full transition matrix corresponds to the asymptotic population growth rate $\lambda_{d,j}$ for posterior draw d and environmental context j. The distribution of $\lambda_{j,*}$ for each environmental context j was plotted to understand how the presence or absence of different stressors is expected to shape the asymptotic population growth rate of sugar pine.

I also used the constructed transition kernels to project the average population trends over the course of a single census interval:

Equation 31

$$\mathbf{n'}_{d,j,*} = \mathbf{A}_{d,j,*,*} \times \mathbf{n}_*$$

where $\mathbf{n'}_{d,j,*}$ is the 99×1 vector giving the projected stem density of individuals in each of the 99 size classes for draw d and scenario j, $\mathbf{A}_{d,j,*,*}$ is the transition kernel for draw d and scenario j, and $\mathbf{n}_*$ is the 99×1 vector giving the mean (across all real plots) stem densities of individuals in each of the 99 size classes. These projected size distributions were summed to get a total stem density projection for each draw d and scenario j to better understand how the various stressors contributed to the observed trends in abundance on the FIA plots. For these single-step projections, the posterior estimates of the random effect realizations for both the plot random effect and the ecoregion random effect were included.

9.3 RESULTS

9.3.1 Trends in abundance

The abundance of sugar pine on plots where it was present at either census declined between initial censuses (2001-2009) and remeasurements (2011-2019). Basal area declined from a mean of 4.25 m^2/ha (standard error 0.14 m^2/ha) to a mean of 4.06 (0.14) m^2/ha (Figure 17a). Stem density declined from 54.5 (4.6) stems/ha to 48.4 (4.2) stems/ha (Figure 17b). Because these figures include only plots where sugar pine was present, they should be interpreted as upper bounds on the actual density of sugar pine across its range. Rather than estimate true abundance, they provide insight into the relative change in abundance across the decade between initial measurement and remeasurement.

9.3.2 Vital rate models validation

Diagnostics for mixing, convergence, R-hat, and transitions all indicated that the model fitting algorithm performed well. Comparisons of posterior distributions with prior distributions showed that the posterior was strongly informed by the data, rather than the prior, for most parameters (Supplementary Figures 72-77). The exception, where the posterior was only weakly informed by the data, were the estimates for the interactions of WPBR with size and quadratic size affecting survival. This uncertainty regarding interactions involving WPBR was likely due to the relatively low frequency of WPBR presence in the data. Posterior predictions generated using the posterior parameter samples and the training data as explanatory variables were consistent with the true values observed in the training data, with the true values nearly always falling within the range of variation predicted by the model (Supplementary Figure 78, Supplementary Figure 79, and Supplementary Figure 80). The survival model appeared slightly underconfident, in that true survival rates were slightly lower than predicted survival rates for $p_s < 0.8$, and true survival rates were slightly higher than predicted survival rates for $p_s > 0.8$. The growth model performed well, with a strong linear relationship between mean predicted and observed individual size at remeasurement. The frequency distribution of simulated new recruit counts closely matched the observed frequency distribution of recruit counts. Simulations generated using the posterior parameter samples and the held-out validation data as explanatory variables were broadly consistent with the true values observed in the validation data (Supplementary Figure 81, Supplementary Figure 82, and Supplementary Figure 83).

9.3.3 Survival

There was a strong positive effect of size on survival, with a negative quadratic effect (Table 13). Median posterior predicted 10-year survival rates increased from approximately 84% for stems with 0.0254 m DBH up to a maximum of 96.5% for stems with 0.88 m DBH, before falling off for the largest stems (Figure 18a). Of the 171 individuals with DBH > 1.25 m at the initial census, only 135 (78.9%) survived to the remeasurement. However, there was large uncertainty about survival rates for the largest stems because there were few extremely large individuals. There was a strong negative main effect of fire, a positive interaction between fire and size, and a negative interaction between fire and squared size. These results indicate that fire substantially reduced survival, particularly for the smallest and largest trees (Figure 18b). There were moderate negative effects of WPBR and basal area on survival (Figure 18c and Figure 18d). Other effects were weak or uncertain (their 90% quantile-based credible intervals overlapped 0; Figure 18e and Figure 18f).

9.3.4 Individual size (growth)

The posterior median for the intercept of the model for size at the second census was 0.018, with a 90% credible interval from 0.014 to 0.022 (Table 14). The effect of initial size was, as expected, very close to 1, and the quadratic effect of initial size was negative. Together, these results indicate that the smallest and largest trees grew approximately 2.5 cm DBH in the 10 years between initial and follow-up census, with midsize trees (initial DBH approx. 0.70 m) growing faster, at around 4.4 cm in 10 years (Figure 19a). Though all three fire effects were weak or uncertain individually (Table 14), their aggregate effect was to significantly reduce the growth rate of stems greater than approximately 0.30 m DBH (Figure 19b). White pine blister rust presence actually increased the growth of the smallest stems, perhaps due to cankers increasing stem diameter (Figure 19c). By contrast, increased neighborhood basal area reduced the growth of small stems but not large ones (Figure 19d). Site dryness also had a negative main effect and a positive interaction with initial size, plus a negative interaction with quadratic size: For the smallest and largest stems growth was lower on dry sites, whereas for stems between approximately 40 cm and 110 cm DBH growth was higher on dry sites (Figure 19f). Other effects were weak or uncertain (Table 14).

9.3.5 Fecundity

The posterior median value for the intercept of the fecundity model was -2.92, with a 90% CI from -3.29 to -2.56 (Table 15). These figures indicate that the average number of new recruits produced per existing tree per 10 years was 0.05 (0.04-0.08).

9.3.6 10-year projections

Total stem densities were projected to decline over the duration of a single census under nearly all hypothetical scenarios, the only exception being the low basal area scenario (Figure 20). The decline was particularly severe in the burned scenario, followed by the WPBR scenario. Declines were predicted even for undisturbed plots, with similar declines in the high BA, high drought, and high site dryness scenarios.

9.3.7 Asymptotic population growth rates

Figure 21 shows the posterior distribution of the asymptotic population growth rate (λ) predicted from IPMs built on a variety of hypothetical scenarios. In each scenario, each posterior sample of the parameters is used to calculate a transition matrix for a population of sugar pines on an idealized plot where the fixed effect covariates (other than size) for the vital rate models are held to specific values representing each scenario. For each of the nine scenarios, one transition matrix is constructed using the parameter values from each of the 4,000 posterior draws. The dominant eigenvalue of each matrix gives the estimate of λ for that scenario and draw.

In the undisturbed scenario, categorical stressors (fire and WPBR) were absent, while continuous stressors (basal area, drought, and site dryness) were held at zero (their scaled means). Under these circumstances, the asymptotic growth rate is near or slightly below one, with a median posterior value of λ of 0.980 and a 90% quantile-based CI from 0.953 to 1.005 (Figure 21, Supplementary Table 1). Where fire is present, λ is strongly reduced (median 0.643, CI 0.521 to 0.788). Where WPBR is present, the posterior distribution for λ is below 1 (median 0.948, CI 0.857 to 0.994). When basal area is lower than average, the posterior distribution of λ is near or slightly above one (median 1.002, CI 0.974 to 1.029). By contrast, when basal area is higher than average the posterior distribution of λ is below one (median 0.946, CI 0.912 to 0.977) and is clearly lower than the undisturbed scenario. For sites experiencing low amounts of drought, the median is 0.991 and the 90% CI of λ straddles one, while for sites experiencing high drought the posterior distribution of λ is below one (median 0.967, 90% CI from 0.933 to 0.998). Likewise, on particularly dry sites the posterior distribution of λ is below one (median 0.953, 90% CI from 0.918 to 0.986). Fire has the clearest effect on λ, followed by WPBR and high basal area, and then drought and site dryness. However, the posterior median value of λ is below one even in the undisturbed scenario, suggesting that even under "unstressed" conditions the population of sugar pine may be declining.

9.4 DISCUSSION

This study is the first range-wide assessment of stressors impacting the vital rates and population dynamics of sugar pine. It finds that the abundance of sugar pine is declining slightly in terms of both basal area and stem density. This observed decline is consistent with the asymptotic population growth rates and the 10-year stem density projections, both of which project the abundance of sugar pine to decline even in the undisturbed scenario (Figure 20 and Figure 21). The analysis described here allows direct comparison of the influence of fire, WPBR, stand density, short-term drought, and long-term site dryness, providing valuable guidance for managers seeking to prioritize efforts to prevent further decline.

The results of this study highlight fire as a key stressor negatively impacting demographic rates of sugar pine. Fire strongly reduces survival of individual trees, particularly small ones. This finding is broadly consistent with the existing literature, which has documented many cases of negative (and size-dependent) impacts of fire on survival of sugar pine (van Mantgem *et al.*, 2004; Hood *et al.*, 2010; Nesmith *et al.*, 2015; Furniss *et al.*, 2018; Dudney *et al.*, 2020). Fire can also injure surviving trees, reducing their growth rate as seen in this study and others (Foster *et al.*, 2020). Reduced growth rates may have particularly strong effects on the asymptotic population growth rate in species where large and old individuals disproportionately contribute to reproduction (Shriver *et al.*, 2019); Sugar pine is one such species, though this study was unable to estimate a relationship between size and fecundity. The literature suggests that a core way in which fire influences the population dynamics of sugar pine is by killing large high-fecundity individuals (van Mantgem *et al.*, 2004). The most extreme form of this dynamic results in type conversion, where high severity fire locally extirpates sugar pine and other mixed conifer species, resulting in the loss of mixed conifer forest generally (Shive *et al.*, 2018; North *et al.*, 2019; Coop *et al.*, 2020).

In this study, the effects of fire on survival and growth combine with low observed fecundity to result in posterior λ values well below one for burned plots (Figure 21), and sharp declines in stem density projected for a single census interval (Figure 20). However, I caution that the asymptotic population growth rates presented in this study should not be interpreted as predictions, because in reality fire is unlikely to repeatedly occur on the same site during every census interval. Instead, the asymptotic population growth rates give some insight into the overall influence of each stressor on population dynamics, which is supplemented by the single-step projections. Existing literature has shown that most trees killed by fire die within 1 year of the fire (Furniss *et al.*, 2018) and mortality rates in stands affected by prescribed fire returned to background levels approximately six years postfire (van Mantgem *et al.*, 2011). These details suggest that the negative effects of fire on survival are transient. However, there is abundant evidence that the ecological footprint of fire, in particular high severity wildfire, is increasing throughout the range of sugar pine because of climate changes and biomass accumulation resulting from fire suppression (Parks and Abatzoglou, 2020; Alizadeh *et al.*, 2021). Given this context and the results of this study, it is clear that the disrupted fire regime is a core threat facing sugar pine.

Though their effects are less severe than those of fire, both WPBR and densification negatively impact sugar pine's population dynamics in this study. The data here show that WPBR negatively impacts survival (Figure 18). Numerous other studies have shown that blister rust tends to kill smaller trees (van Mantgem *et al.*, 2004) and negatively affects survival rates of sugar pine and other vulnerable species

(Maloney *et al.*, 2011; Dudney *et al.*, 2020). The presence of WPBR on individual trees (and thus on their plots) may be difficult to detect (Dudney *et al.*, 2020), and is likely that WPBR was only detected in this study where it caused a particularly severe infection in a sampled tree. There are two likely effects of this sampling bias towards under detection: The data may underreport the true prevalence of WPBR, and the analysis presented here may overestimate the true impact of its presence on a plot.

This study also finds that relatively high competition (neighborhood basal area) results in lower rates of survival for all size classes (Figure 18). It also results in lower growth for small individuals (Figure 19). There is extensive evidence in the literature that high neighborhood density and other proxies for competition negatively impact sugar pine survival (van Mantgem *et al.*, 2004; Maloney *et al.*, 2011; Levine *et al.*, 2016) and growth (Latham and Tappeiner, 2002; Das, 2012; Eitzel *et al.*, 2013; Steel *et al.*, 2021a). Though this study is unable to estimate how stressors affected fecundity, the literature suggests that competition may result in decreased reproduction due to stress of parent trees or decreased survival and/or growth of new recruits (Schubert, 1956; York *et al.*, 2004, 2012; van Mantgem *et al.*, 2006; Angell *et al.*, 2014; Levine *et al.*, 2016; Moran *et al.*, 2019). In this study, high neighborhood basal area and presence of WPBR both reduce the expected asymptotic growth rate relative to an unstressed site, though negative impacts are weaker than that of fire (Figure 21, Supplementary Table 1). By contrast, reducing neighborhood basal area to one standard deviation below the mean has positive effects on λ (Figure 21).

This study finds that long-term site dryness has clearer effects on population dynamics than does drought (departure from average climate), with site dryness having a negative impact on the growth of the largest and smallest trees. However, the asymptotic population growth rate is below one for both populations on dry sites and those experiencing drought (Supplementary Table 1). Other literature has emphasized the role of moisture stress in increased mortality rates and reduced growth among sugar pine both directly and indirectly via decreased ability of trees to resist mountain pine beetle (Das *et al.*, 2007, 2013; van Mantgem and Stephenson, 2007; Paz-Kagan *et al.*, 2017; Restaino *et al.*, 2019; Bohner and Diez, 2021). However, Furniss *et al.* (2021) found that stand density played a more important role than climate variables in shaping mortality dynamics after fire and/or drought. Stephenson *et al.* (2019) examined the role of mountain pine beetle as the primary mortality agent taking advantage of widespread stress among sugar pine populations affected by drought. Intermittent droughts and/or long-term mean climatic conditions may particularly challenge small trees, causing recruitment failures even on sites where adult trees are able to persist (Bell *et al.*, 2014; Maloney, 2014; Davis *et al.*, 2019; Moran *et al.*, 2019; Stewart *et al.*, 2021). However, this study does not find strong effects of drought on survival. Though the extreme drought from 2012-2016 resulted in beetle epidemics that caused massive mortality among sugar pine (Stephenson *et al.*, 2019), drought may be a necessary but not sufficient condition for causing such epidemics, with some droughts not resulting in widespread mortality.

One unexplained but troubling finding of this study is the relatively low survival rates observed for the largest sugar pines. One possible explanation is bark beetles, which are a driver of mortality for these trees: Once an outbreak is underway, beetles often preferentially kill large individuals (Stephenson *et al.*, 2019), and localized beetle outbreaks could explain the low survival of the largest trees in these data. However, this study's finding is based on relatively few data points and should be interpreted with caution. This uncertainty regarding the outlook for the largest individuals, which are an important ecological resource (Lutz *et al.*, 2018), highlights a need for further research.

An important limitation of this study is that it does not test for interaction between stressors in shaping vital rates of sugar pine. I do not test for interactions because including numerous three-way interactions between size and two stressors would have resulted in difficult-to-interpret vital rate models. The literature suggests that a variety of such interactions may be important. For example, water stress increases the likelihood of regeneration failure, which may be a particularly acute problem in postfire landscapes where seed sources and shade trees may be limited (Davis *et al.*, 2019; Stewart *et al.*, 2021). A warmer and dryer climate may provide some relief from WPBR for sugar pine, as the disease's climatic envelope shifts upslope away from existing populations of sugar pine (Maloney, 2011; Dudney *et al.*, 2021). A relationship between fire exclusion, competition, and WPBR infection has been suggested (Dudney *et al.*, 2020), but evidence is mixed. Some studies have found that conspecific basal area was an important driver of sugar pine mortality (Das *et al.*, 2008), but others have failed to find evidence linking fire exclusion to elevated rates of WPBR infection (van Mantgem *et al.*, 2004; Dudney *et al.*, 2020). Water stress and/or competition may decrease trees' ability to resist wildfire (Nesmith *et al.*, 2015; Furniss *et al.*, 2018, 2021; van Mantgem *et al.*, 2018, 2020), and beetle epidemics may kill off the largest and most fire-resistant individuals (Stephenson *et al.*, 2019; Steel *et al.*, 2021a). Water stress and densification both alter the fuel bed in ways that may increase the intensity of wildfires (Hicke *et al.*, 2012; Stephens *et al.*, 2018; Wayman and Safford, 2021). Likewise, wildfires may decrease trees' ability to resist bark beetles, facilitating epidemic outbreaks in the event of a post-fire drought (Davis *et al.*, 2012; Furniss *et al.*, 2021). Competition tends to reduce trees' ability to resist water stress and beetle epidemics (Young *et al.*, 2017; Furniss *et al.*, 2021; Bradford *et al.*, 2022). Finally, there is potential for stressors to mitigate one another, primarily by a mechanism where mortality caused by one stressor results in less competitive stress and increased resilience to other stressors (van Mantgem *et al.*, 2016; Voelker *et al.*, 2019; North *et al.*, 2022). For example, wildfire could reduce basal area, leaving the surviving trees better able to resist water stress over the long term. Exploring how stressors are likely to interact and shape population dynamics is another goal for future research.

The results of this study provide clear guidance for managers interested in conserving sugar pine. This study's findings, which point at fire, WPBR, and competition as major stressors of sugar pine, suggest that fuel treatments with a density reduction component could substantially benefit sugar pine populations. Fuel treatments to reduce or rearrange the dead biomass which fuels wildfires have been proven to reduce the hazard of severe wildfire (Stephens and Moghaddas, 2005a; Foster *et al.*, 2020), and in many cases have the co-benefit of reducing basal area (Hessburg *et al.*, 2016; North *et al.*, 2021). This study's findings, and other studies examining the effects of prescribed fire on sugar pine mortality (van Mantgem *et al.*, 2004; Steel *et al.*, 2021a), suggest that managers should be careful in their application of prescribed fire to reduce wildfire hazard and consider measures such as raking or local density reduction to protect individual trees where pre-fire fuels are abundant (Nesmith *et al.*, 2010; Furniss *et al.*, 2021). Mechanical fuel treatments will provide some protection from wildfire and can be applied in combination with timber harvests, for a dual benefit of reducing wildfire hazard and competition (Collins *et al.*, 2014; Restaino *et al.*, 2019). Managers can take advantage of established programs producing WPBR-resistant seedlings in reforestation efforts aimed at restoring sugar pine on landscapes impacted by high severity fire (Kinloch, Jr. *et al.*, 2018). Investments in artificial regeneration should likewise be made deliberately and secured with follow up treatments for wildfire hazard (North *et al.*, 2019) and pruning to limit the effects of WPBR (Bronson *et al.*, 2018). The findings of this study indicate that managers can substantially benefit sugar pine populations by investing resources in addressing the tractable challenges posed by fire, competition, and white pine blister rust.

9.5 TABLES

Parameter	Mean	Median	StDev	q5	q95	rhat	ess_bulk	ess_tail
Intercept	1.59	1.58	0.26	1.17	2.01	1.00	1456.24	2098.04
DBH (m)	4.00	3.99	0.79	2.68	5.34	1.00	1336.35	2155.84
DBH^2 (m)	-2.29	-2.28	0.56	-3.22	-1.36	1.00	1397.96	2151.10
Fire	-4.07	-4.06	0.59	-5.05	-3.11	1.00	1629.72	2176.19
WPBR	-1.05	-1.04	0.56	-1.99	-0.13	1.00	1582.57	2456.43
Basal Area	-0.65	-0.65	0.23	-1.03	-0.27	1.00	1641.95	2121.95
Drought	-0.18	-0.18	0.21	-0.52	0.16	1.00	1333.50	2379.36
Site Dryness	-0.34	-0.34	0.23	-0.73	0.04	1.00	1502.16	2478.08
DBH x Fire	3.67	3.62	1.51	1.22	6.16	1.00	1432.73	2296.75
DBH^2 x Fire	-1.64	-1.63	0.96	-3.24	-0.10	1.00	1401.16	2199.19
DBH x WPBR	-0.04	0.00	1.84	-3.06	2.98	1.00	2131.47	2735.02
DBH^2 x WPBR	0.56	0.54	1.40	-1.66	2.94	1.00	2393.36	2598.78
DBH x BA	0.71	0.70	0.57	-0.23	1.65	1.00	1458.07	1935.68
DBH^2 x BA	-0.08	-0.08	0.33	-0.62	0.45	1.00	1490.06	2207.10
DBH x Drought	-0.02	-0.02	0.60	-1.01	0.95	1.00	1497.81	2284.53
DBH^2 x Drought	0.08	0.08	0.41	-0.58	0.79	1.00	1565.87	2268.01
DBH x Dryness	0.66	0.64	0.69	-0.44	1.80	1.00	1414.52	2218.03
DBH^2 x Dryness	-0.64	-0.62	0.49	-1.46	0.15	1.00	1426.39	2469.34
SD Plots	2.00	2.00	0.16	1.76	2.26	1.00	1193.61	2227.74
SD Ecoregions	0.28	0.26	0.19	0.03	0.61	1.01	403.37	997.11

Table 13: Summary of results for survival sub model, giving the mean, median, standard deviation, 5th percentile, and 95th percentile of posterior samples for each parameter, plus diagnostics R-hat, effective sample size (bulk), and effective sample size (tail).

Parameter	Mean	Median	StDev	q5	q95	rhat	ess_bulk	ess_tail
Intercept	0.018	0.018	0.003	0.014	0.022	1.00	1932.23	2370.47
DBH (m)	1.076	1.076	0.006	1.067	1.086	1.00	3524.26	3051.14
DBH^2 (m)	-0.056	-0.056	0.004	-0.063	-0.049	1.00	3626.18	3225.29
Fire	-0.007	-0.007	0.007	-0.019	0.005	1.00	2513.11	2712.72
WPBR	0.011	0.011	0.005	0.003	0.020	1.00	2895.99	2856.91
Basal Area	-0.013	-0.013	0.002	-0.017	-0.010	1.00	4376.90	3496.19
Drought	-0.002	-0.002	0.002	-0.005	0.000	1.00	3798.53	3164.24
Site Dryness	-0.007	-0.007	0.002	-0.010	-0.003	1.00	3209.21	3237.66
DBH x Fire	-0.012	-0.012	0.018	-0.042	0.018	1.00	2332.80	2469.12
DBH^2 x Fire	0.007	0.007	0.011	-0.011	0.024	1.00	2432.29	2427.42
DBH x WPBR	-0.012	-0.012	0.016	-0.038	0.015	1.00	3008.42	2767.14
DBH^2 x WPBR	0.000	0.000	0.011	-0.018	0.018	1.00	3138.79	2684.75
DBH x BA	0.018	0.018	0.005	0.010	0.025	1.00	4579.41	3151.88
DBH^2 x BA	-0.003	-0.003	0.003	-0.008	0.001	1.00	4548.37	2823.81
DBH x Drought	0.003	0.002	0.005	-0.006	0.011	1.00	4215.27	3110.52
DBH^2 x Drought	0.002	0.002	0.004	-0.004	0.007	1.00	4124.82	3026.97
DBH x Dryness	0.024	0.024	0.006	0.015	0.034	1.00	3594.70	2575.45
DBH^2 x Dryness	-0.016	-0.016	0.004	-0.023	-0.010	1.00	3577.96	2781.10
SD Plots	0.017	0.017	0.001	0.016	0.018	1.00	1346.76	2286.28

Table 14: Summary of results for growth sub model, giving the mean, median, standard deviation, 5th percentile, and 95th percentile of posterior samples for each parameter, plus diagnostics R-hat, effective sample size (bulk), and effective sample size (tail).

Parameter	Mean	Median	StDev	q5	q95	rhat	ess_bulk	ess_tail
Intercept	-2.93	-2.92	0.22	-3.29	-2.56	1.00	2564.66	2375.05
NB Dispersion	0.06	0.06	0.03	0.03	0.12	1.00	2990.07	2402.26

Table 15: Summary of results for recruitment sub model, giving the mean, median, standard deviation, 5th percentile, and 95th percentile of posterior samples for each parameter, plus diagnostics R-hat, effective sample size (bulk), and effective sample size (tail).

9.6 FIGURES

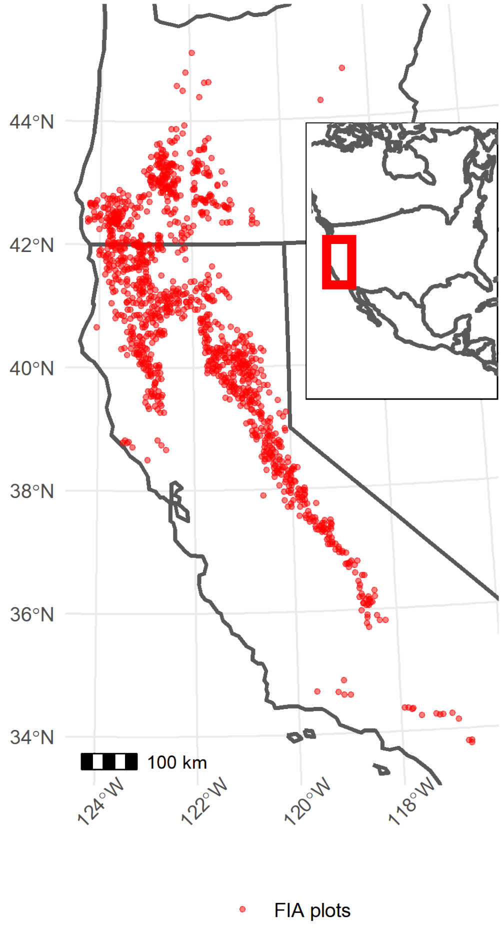

Figure 16: 1,221 Forest Inventory and Analysis (FIA) plots where live sugar pine was present at initial measurement (2001-2009) or remeasurement (2010-2019) with US state borders. Plot locations based on the nominal, rather than true, coordinates. Inset shows position relative to North America and national borders.

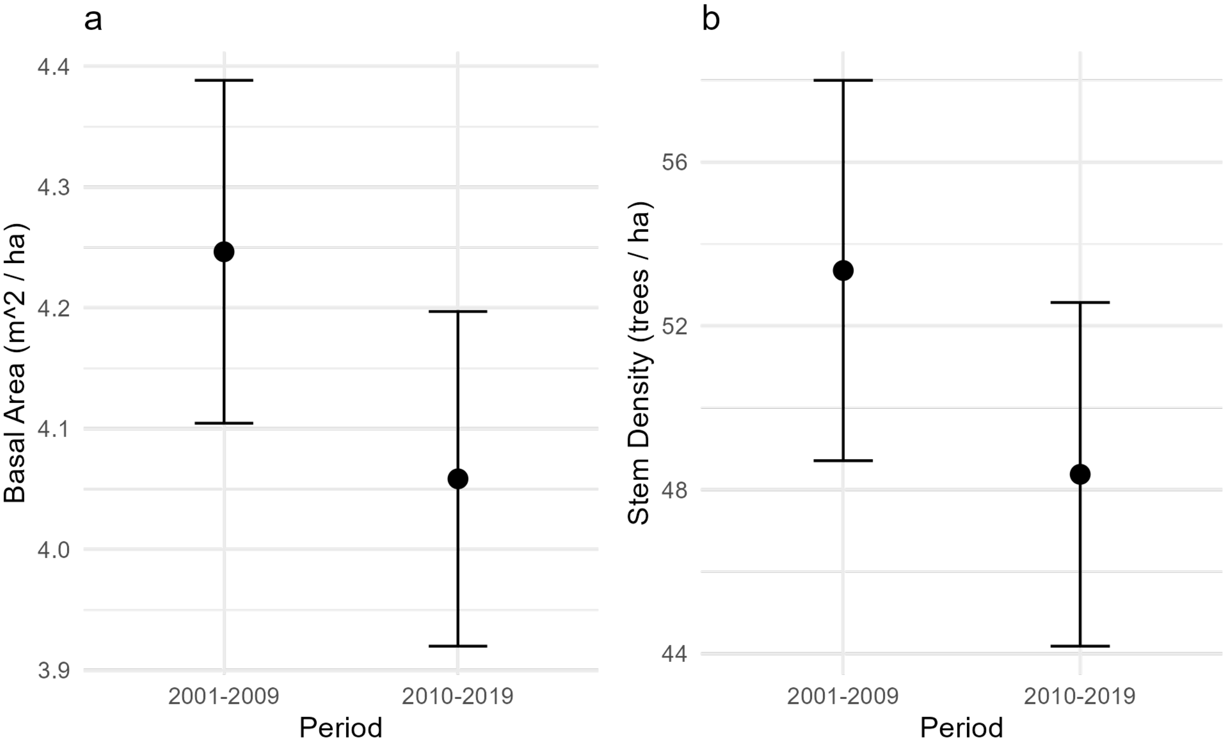

Figure 17: Changes in plot-level basal area (a) and stems per hectare (b) for 1,221 plots where sugar pine was present at initial measurement (2001-2009) or remeasurement (2010-2019). Points are means and error bars are +/- one standard error across plots. Totals include only stems greater than or equal to 2.54 cm DBH.

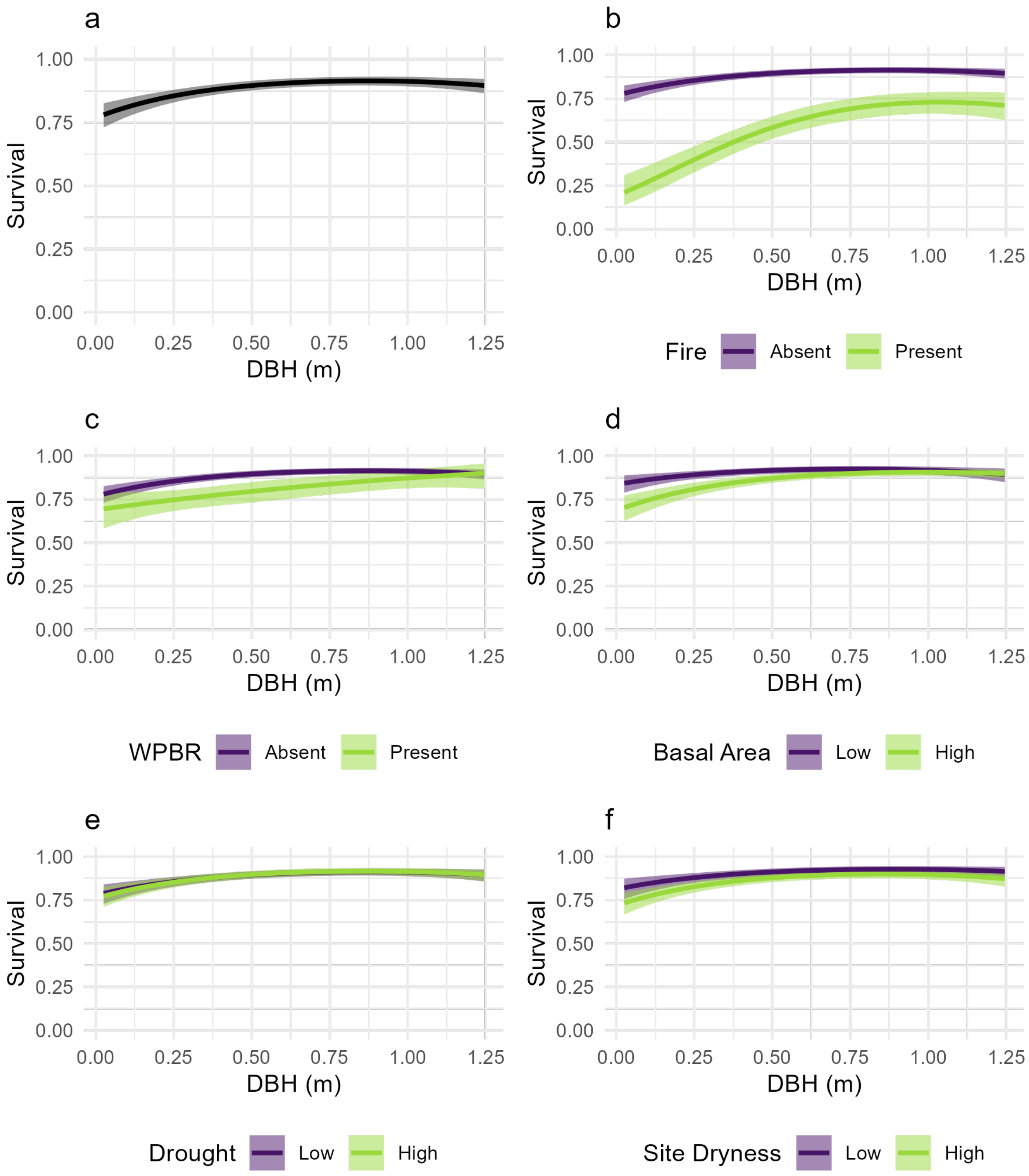

Figure 18: Fixed effects of initial DBH, fire, WPBR, neighborhood basal area, drought, and site dryness on 10-year survival probability. In panel (a), probability of survival (Y-axis) is predicted for stems of various initial size (X-axis), holding other variables at "Absent" (for fire and WPBR) or 0 (scaled mean, for basal area, drought, and site dryness). In the other panels (b-f), probability of survival is predicted for stems of various sizes and across two levels of each other explanatory variable: with or without disturbance, or at high (1.0) or low (-1.0) values for scaled continuous variables. Predictions were generated using the posterior samples for model parameters, resulting in a range of predicted survival for each set of explanatory variable values. Lines show the median predicted survival and lighter ribbons show a 90% quantile-based credible interval. Random effects were held at 0. 1.25 m is approximately the 95th percentile DBH of trees used to train the model.

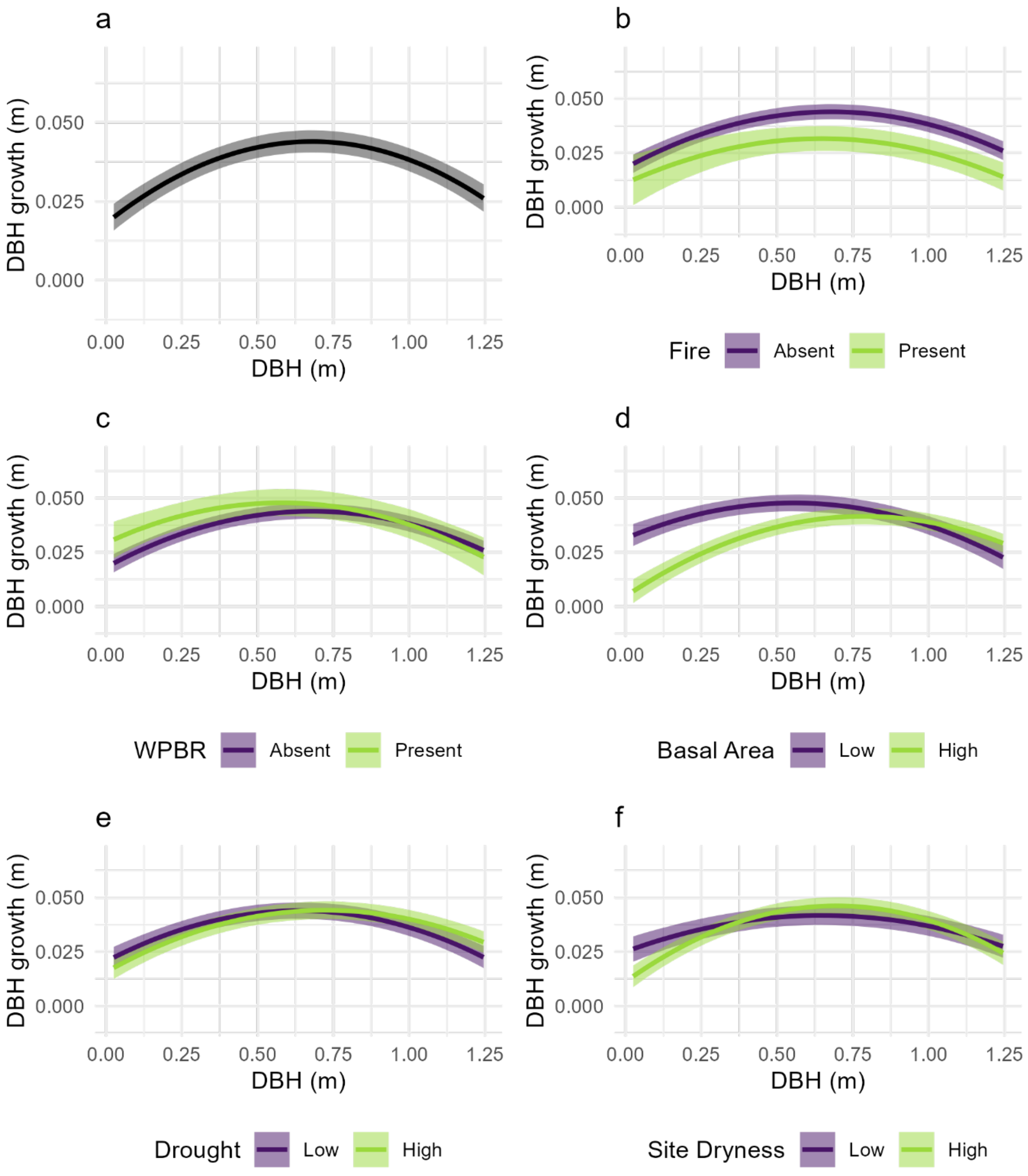

Figure 19: Fixed effects of initial DBH, fire, WPBR, neighborhood basal area, drought, and site dryness on 10-year diameter growth. In panel (a), DBH growth over the 10 years between censuses (Y-axis) is predicted for stems of various initial size (X-axis), holding other variables at "Absent" (for fire and WPBR) or 0 (scaled mean, for basal area, drought, and site dryness). In the other panels (b-f), growth is predicted for stems of various sizes and across two levels of each other explanatory variable: with or without disturbance, or at high (1.0) or low (-1.0) values for scaled continuous variables. Predictions were generated using the posterior samples for model parameters, resulting in a range of predicted survival for each set of explanatory variable values. Lines show the median predicted survival and lighter ribbons show a 90% quantile-based credible interval. Random effects were held at 0.

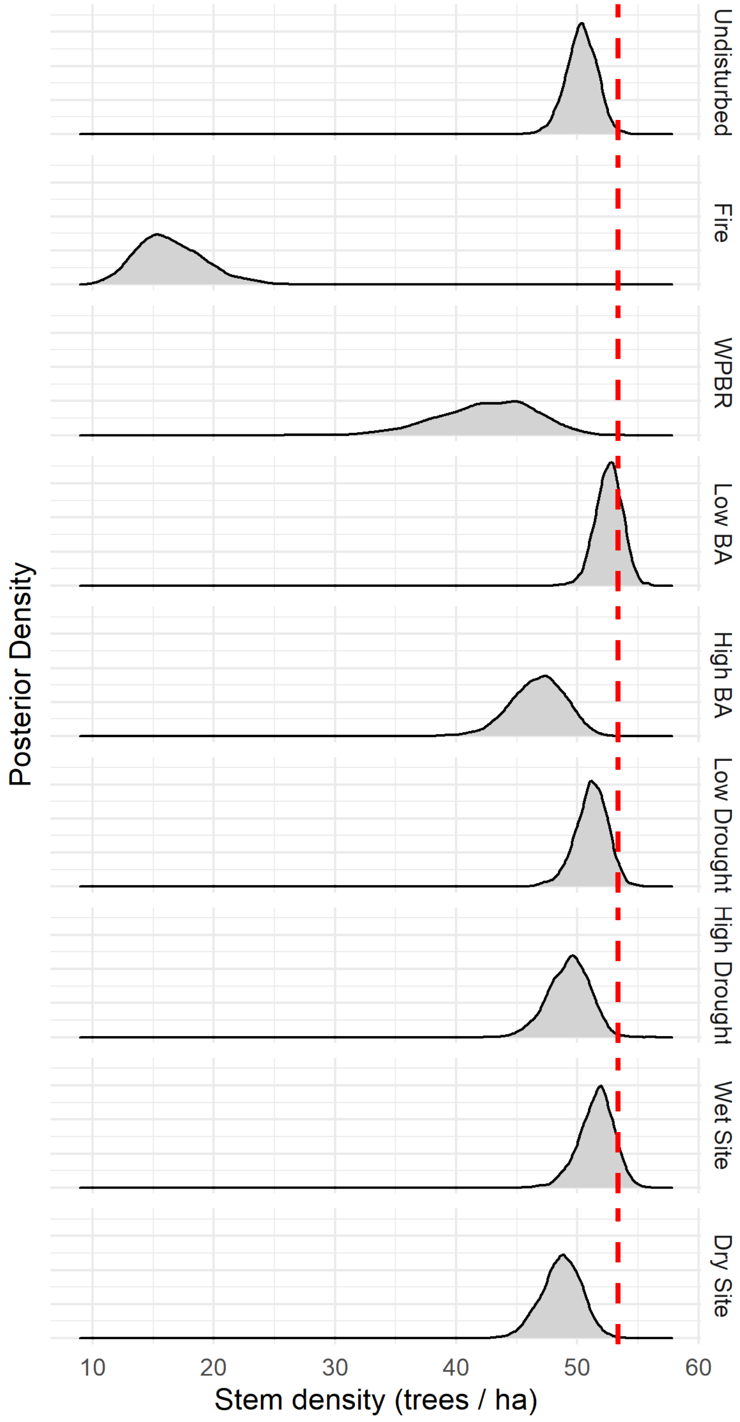

Figure 20: Posterior distribution of projected stem density (starting with observed mean density) under a variety of hypothetical scenarios, each corresponding to the presence or absence of a specific stressor. In the "Undisturbed" scenario, all fixed effect covariates other than the intercept are held at 0 (representing the absence of fire and WPBR, and basal area, drought, and site dryness at average levels). In each other scenario, a single stressor is set to TRUE (for fire and WPBR), -1 (low levels of basal area, drought, or site dryness), or +1 (high levels of basal area, drought, or site dryness). Random effect values are held at 0, representing an average plot in an average ecoregion.

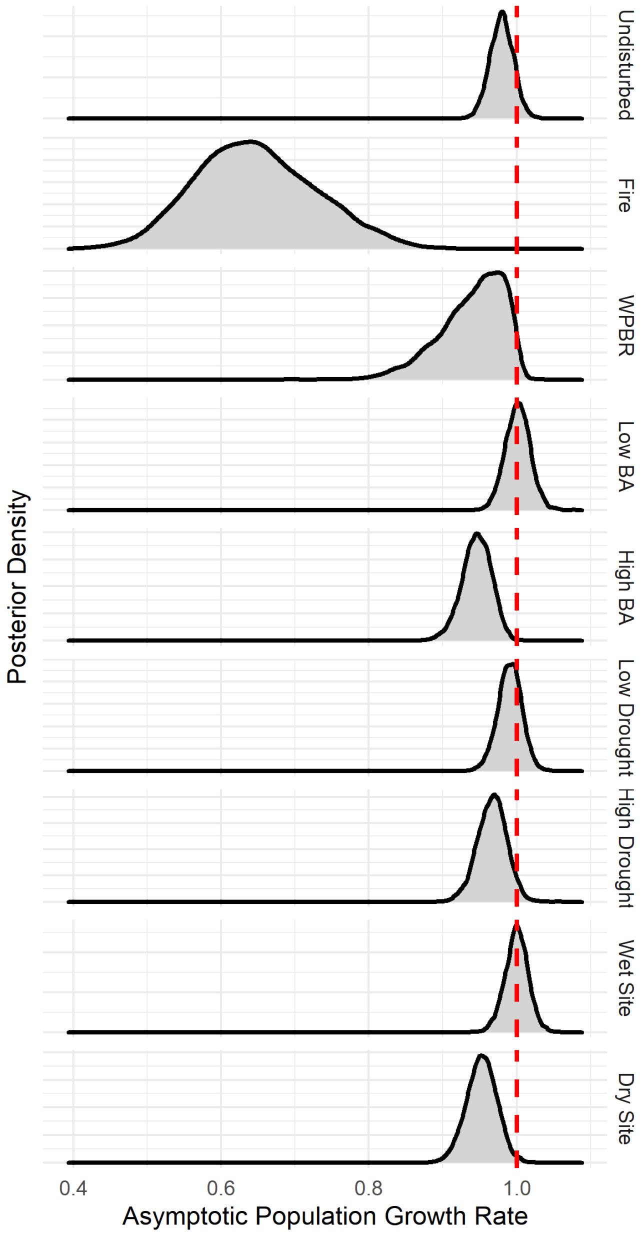

Figure 21: Posterior distribution of asymptotic population growth rate. In the "Undisturbed" scenario, all fixed effect covariates other than the intercept are held at 0 (representing the absence of fire and WPBR, and basal area, drought, and site dryness at average levels). In each other scenario, a single stressor is set to TRUE (for fire and WPBR), -1 (low levels of basal area, drought, or site dryness), or +1 (high levels of basal area, drought, or site dryness). Random effect values are held at 0, representing an average plot in an average ecoregion.

10 CONCLUSION

This dissertation builds upon existing work describing the disturbance ecology of Sierra Nevada mixed conifer forests. In the first chapter, I describe and evaluate a suite of hierarchical spatial statistical models characterizing the fine-scale spatial distribution of wildland fuels. These hierarchical spatial statistical models can be used to provide spatially explicit fuel load information to wildfire models able to take advantage of such data, an important step forward in the use of coupled atmosphere-fire fire behavior models. The hierarchical spatial statistical models also provide a clear way to test hypotheses about the disturbance ecology of fine-scale spatial patterns by quantifying those patterns as the parameters controlling a Gaussian process spatial random effect, as seen in the second chapter of this dissertation. That chapter finds that prescribed fires in a mixed conifer forest not only reduced the mean amount of litter, duff, and fine woody debris, they also altered the fine-scale spatial pattern of the fuel loads of these components. The implications of this alteration for the behavior and effects of future fires are an important topic for further research. Finally, the third chapter of this dissertation provides valuable information for efforts to conserve the Queen of the Sierras, *Pinus lambertiana*, by quantifying the impact of various stressors on the demography of this iconic tree species.

There are some important differences between these three chapters. First, the patterns and processes explored in each study vary drastically in their spatial and temporal scale. The first chapter examines the effects of a disturbance process taking place over several years on spatial patterns occurring at a range of several meters, while the second chapter considers those same spatial scales in relation to a disturbance occurring over a few hours. The third chapter, by contrast, considers the effects of disturbances on demographic processes occurring on the scale of decades across the entire range of sugar pine. Another notable difference among my chapters is that multiple study types are represented: The first and third chapters are observational studies synthesizing field data with remote sensing datasets, while the second chapter is an experimental manipulation. Finally, the application of these findings varies from piloting sampling and analytical methods in the first chapter, to providing a more complete understanding of management effectiveness in the second chapter, to prioritizing conservation efforts in the third chapter.

However, these studies share essential traits. In all three chapters, I rely heavily on field data collected at the sub-hectare scale. Such data provide crucial information for disturbance ecology, such as the fine-scale pattern of fuel loads and the growth of individual trees, which are not available using coarser remote sensing methods. Likewise, all three chapters make extensive use of hierarchical statistical regression models. These models are a powerful and flexible tool enabling both understanding and prediction of complex systems, though they are not without limitations, as seen in all three chapters. Finally, all three chapters share a common topic in that they describe the relationships between disturbance processes (such as fire, drought, and disease) and forest patterns (such as the fine-scale spatial distribution of biomass or the demographic structure of sugar pine populations) in Sierra Nevada mixed conifer forests. These studies present novel methods, applications, and findings of disturbance ecology in an effort to benefit future study and management of these forests.

11 REFERENCES

Abatzoglou, J.T., Dobrowski, S.Z., Parks, S.A. and Hegewisch, K.C. (2018) 'TerraClimate, a high-resolution global dataset of monthly climate and climatic water balance from 1958-2015', *Scientific Data*, 5, pp. 1–12. Available at: https://doi.org/10.1038/sdata.2017.191.

Agee, J.K. and Skinner, C.N. (2005) 'Basic principles of forest fuel reduction treatments', *Forest Ecology and Management*, 211(1–2), pp. 83–96. Available at: https://doi.org/10.1016/j.foreco.2005.01.034.

Airey Lauvaux, C., Skinner, C.N. and Taylor, A.H. (2016) 'High severity fire and mixed conifer forest-chaparral dynamics in the southern Cascade Range, USA', *Forest Ecology and Management*, 363, pp. 74–85. Available at: https://doi.org/10.1016/j.foreco.2015.12.016.

Aitken, S.N. and Whitlock, M.C. (2013) 'Assisted Gene Flow to Facilitate Local Adaptation to Climate Change', *Annual Review of Ecology, evolution, and Systematics*, 44, pp. 367–88. Available at: https://doi.org/10.1146/annurev-ecolsys-110512-135747.

Alizadeh, M.R., Abatzoglou, J.T., Luce, C.H., Adamowski, J.F., Farid, A. and Sadegh, M. (2021) 'Warming enabled upslope advance in western US forest fires', *Proceedings of the National Academy of Sciences*, 118(22), p. e2009717118. Available at: https://doi.org/10.1073/pnas.2009717118.

Allen, C.D., Breshears, D.D. and McDowell, N.G. (2015) 'On underestimation of global vulnerability to tree mortality and forest die-off from hotter drought in the Anthropocene', *Ecosphere*, 6(8), pp. 1–55. Available at: https://doi.org/10.1890/ES15-00203.1.

Anderegg, W.R.L., Hicke, J.A., Fisher, R.A., Allen, C.D., Aukema, J., Bentz, B., Hood, S., Lichstein, J.W., Macalady, A.K., Mcdowell, N., Pan, Y., Raffa, K., Sala, A., Shaw, J.D., Stephenson, N.L., Tague, C. and Zeppel, M. (2015) 'Tree mortality from drought, insects, and their interactions in a changing climate', *New Phytologist*, 208(3), pp. 674–683. Available at: https://doi.org/10.1111/nph.13477.

Anderson, H.E. (1982) 'Aids to determining fuel models for estimating fire behavior', *Gen. Tech. Rep. INT-122*. Ogden, UT: USDA Forest Service, Intermountain Forest and Range Experiment Station. 22p. Available at: https://doi.org/10.2737/INT-GTR-122.

Angell, N., Waring, K.M. and Graves, T.A. (2014) 'Predicting height growth of sugar pine regeneration using stand and individual tree characteristics', *Forestry*, 87(1), pp. 85–97. Available at: https://doi.org/10.1093/forestry/cpt028.

Ansley, J.-A.S. and Battles, J.J. (1998) 'Forest Composition, Structure, and Change in an Old-Growth Mixed Conifer Forest in the Northern Sierra Nevada', *The Journal of the Torrey Botanical Society*, 125(4), pp. 297–308. Available at: http://www.jstor.org/stable/29972.

Asner, G.P., Brodrick, P.G., Anderson, C.B., Vaughn, N., Knapp, D.E. and Martin, R.E. (2015) ‘Progressive forest canopy water loss during the 2012–2015 California drought’, *Proceedings of the National Academy of Sciences*, 113(2), pp. 249-255; Available at: https://doi.org/10.1073/pnas.1523397113.

Atchley, A.L., Linn, R.R., Jonko, A., Hoffman, C.M., Hyman, J.D., Pimont, F., Sieg, C. and Middleton, R. (2021) ‘Effects of fuel spatial distribution on wildland fire behavior’, *International Journal of Wildland Fire*, 30(3), pp. 179-189; Available at: https://doi.org/10.1071/WF20096.

Baguskas, S.A., Peterson, S.H., Bookhagen, B. and Still, C.J. (2014) ‘Evaluating spatial patterns of drought-induced tree mortality in a coastal California pine forest’, *Forest Ecology and Management*, 315, pp. 43–53. Available at: https://doi.org/10.1016/j.foreco.2013.12.020.

Bailey, R.G. (2016) ‘Bailey’s ecoregions and subregions of the United States, Puerto Rico, and the U.S. Virgin Islands’. Fort Collins, CO: Forest Service Research Data Archive. Available at: https://doi.org/10.2737/RDS-2016-0003.

Banerjee, T. (2020) ‘Impacts of forest thinning on wildland fire behavior’, *Forests*, 11(9). Available at: https://doi.org/10.3390/F11090918.

Bechtold, W.A. and Patterson, P.L. (2005) ‘The Enhanced Forest Inventory and Analysis Program — National Sampling Design and Estimation Procedures’, *GTR-SRS-80*. Asheville, NC: USDA Forest Service, Southern Research Station. 85 p. Available at: https://doi.org/10.2737/SRS-GTR-80

Bell, D.M., Bradford, J.B. and Lauenroth, W.K. (2014) ‘Early indicators of change: Divergent climate envelopes between tree life stages imply range shifts in the western United States’, *Global Ecology and Biogeography*, 23(2), pp. 168–180. Available at: https://doi.org/10.1111/geb.12109.

Betancourt, M. (2020a) *Robust Gaussian Process Modeleing*. Available at: https://github.com/betanalpha/knitr_case_studies/tree/master/gaussian_processes.

Betancourt, M. (2020b) *Towards a Principled Bayesian Workflow*. Available at: https://betanalpha.github.io/assets/case_studies/principled_bayesian_workflow.html.

Bivand, R.S., Pebesma, E., Gómez-Rubio, V. (2013) *Applied Spatial Data Analysis with R*. Springer Science+Business Media, New York, NY. eBook ISBN: 978-1-4614-7618-4. Available at: https://doi.org/10.1007/978-1-4614-7618-4

Bivand, R.S., Nowosad, J. and Lovelace, R. (2021) ‘spData: Datasets for Spatial Analysis’. Available at: https://cran.r-project.org/package=spData.

Blomdahl, E.M., Kolden, C.A., Meddens, A.J.H. and Lutz, J.A. (2019) ‘The importance of small fire refugia in the central Sierra Nevada, California, USA’, *Forest Ecology and Management*, 432(October 2018), pp. 1041–1052. Available at: https://doi.org/10.1016/j.foreco.2018.10.038.

Bohlman, G.N., Safford, H.D. and Skinner, C.N. (2021) ‘Natural range of variation for yellow pine and mixed-conifer forests in northwestern California and southwestern Oregon’, *Gen. Tech. Rep. PSW-GTR-273.* Albany, CA: US Department of Agriculture, Forest Service, Pacific Southwest Research Station. 146 p.

Bohner, T. and Diez, J. (2021) ‘Tree resistance and recovery from drought mediated by multiple abiotic and biotic processes across a large geographic gradient’, *Science of The Total Environment*, 789(1) October, 147744. Available at: https://doi.org/10.1016/j.scitotenv.2021.147744.

Bourguignon, M. and Gallardo, D.I. (2020) ‘Reparameterized inverse gamma regression models with varying precision’, *Statistica Neerlandica*, 74(4), pp. 611–627. Available at: https://doi.org/10.1111/stan.12221.

Bradford, J.B., Shriver, R.K., Robles, M.D., McCauley, L.A., Woolley, T.J., Andrews, C.A., Crimmins, M. and Bell, D.M. (2022) ‘Tree mortality response to drought-density interactions suggests opportunities to enhance drought resistance’, *Journal of Applied Ecology*, 59(2), pp. 549–559. Available at: https://doi.org/10.1111/1365-2664.14073.

Bronson, J., Petrick, J. and Danchok, R. (2018) ‘Efficacy of Early Pruning to Reduce the Incidence of White Pine Blister Rust on Sugar Pine (Pinus lambertiana)’. In: Schoettle, A.W., Sniezko, R. A., Kliejunas, J. T., eds. *Proceedings of the IUFRO joint conference: Genetics of five-needle pines, rusts of forest trees, and Strobusphere; 2014 June 15-20*. Fort Collins, CO. Proc. RMRS-P-76. Fort Collins, CO: U.S. Department of Agriculture, Forest Service, Rocky Mountain Research Station. p. 205-208. Available at: https://www.fs.usda.gov/research/treesearch/56737

Brown, J.K. (1974) 'Handbook for Inventorying Downed Woody Material,' *General Technical Report INT-16.* Ogden, UT: USDA Forest Service, Intermountain Forest and Range Experiment Station. 24 p. Available at: https://www.fs.usda.gov/research/treesearch/28647

Burgan, R.E. and Rothermel, R.C. (1984) *BEHAVE: Fire Behavior Prediction and Fuel Modeling.* GTR INT-194. Ogden, Utah. Available at: https://doi.org/10.2737/INT-GTR-167

Bürkner, P., Gabry, J., Kay, M. and Vehtari, A. (2021) ‘posterior: Tools for Working with Posterior Distributions’. Available at: https://mc-stan.org/posterior/.

Collins, B.M., Das, A.J., Battles, J.J., Fry, D.L., Krasnow, K.D. and Stephens, S.L. (2014) ‘Beyond Reducing Fire Hazard’, *Ecological Applications*, 24(8), pp. 1879–1886. Available at: https://doi.org/10.1890/14-0971.1.

Collins, B.M. and Roller, G.B. (2013) ‘Early forest dynamics in stand-replacing fire patches in the northern Sierra Nevada, California, USA’, *Landscape Ecology*, 28(9), pp. 1801–1813. Available at: https://doi.org/10.1007/s10980-013-9923-8.

Coop, J.D. *et al.* (2020) ‘Wildfire-Driven Forest Conversion in Western North American Landscapes’, *BioScience*, 70(8), pp. 659–673. Available at: https://doi.org/10.1093/biosci/biaa061.

Coppoletta, M., Merriam, K.E. and Collins, B.M. (2016) 'Post-fire vegetation and fuel development influences fire severity patterns in reburns', *Ecological Applications*, 26(3), pp. 686–699. Available at: https://doi.org/10.1890/15-0225.

Das, A., Battles, J., van Mantgem, P.J. and Stephenson, N.L. (2008) 'Spatial elements of mortality risk in old-growth forests', *Ecology*, 89(6), pp. 1744–1756. Available at: https://doi.org/10.1890/07-0524.1.

Das, A. (2012) 'The effect of size and competition on tree growth rate in old-growth coniferous forests', *Canadian Journal of Forest Research*, 42(11), pp. 1983–1995. Available at: https://doi.org/10.1139/x2012-142.

Das, A.J., Battles, J.J., Stephenson, N.L. and van Mantgem, P.J. (2007) 'The relationship between tree growth patterns and likelihood of mortality: A study of two tree species in the Sierra Nevada', *Canadian Journal of Forest Research*, 37(3), pp. 580–597. Available at: https://doi.org/10.1139/X06-262.

Das, A.J., Stephenson, N.L., Flint, A., Das, T. and van Mantgem, P.J. (2013) 'Climatic Correlates of Tree Mortality in Water- and Energy-Limited Forests', *PLoS ONE*, 8(7). Available at: https://doi.org/10.1371/journal.pone.0069917.

Datta, A., Banerjee, S., Finley, A.O. and Gelfand, A.E. (2016) 'Hierarchical Nearest-Neighbor Gaussian Process Models for Large Geostatistical Datasets', *Journal of the American Statistical Association*, 111(514), pp. 800–812. Available at: https://doi.org/10.1080/01621459.2015.1044091.

Davis, K.T., Dobrowski, S.Z., Higuera, P.E., Holden, Z.A., Veblen, T.T., Rother, M.T., Parks, S.A., Sala, A. and Maneta, M.P. (2019) 'Wildfires and climate change push low-elevation forests across a critical climate threshold for tree regeneration', *Proceedings of the National Academy of Sciences of the United States of America*, 116(13), pp. 6193–6198. Available at: https://doi.org/10.1073/pnas.1815107116.

Davis, R.S., Hood, S. and Bentz, B.J. (2012) 'Fire-injured ponderosa pine provide a pulsed resource for bark beetles', *Canadian Journal of Forest Research*, 42(12), pp. 2022–2036. Available at: https://doi.org/10.1139/x2012-147.

Diggle, P.J. and Ribiero, P.J. (2007) *Model-based geostatistics*. New York, NY: Springer Science+Business Media, LLC. Available at: https://doi.org/10.1007/978-0-387-48536-2

DiMario, A.A., Kane, J.M. and Jules, E.S. (2018) 'Characterizing Forest Floor Fuels Surrounding Large Sugar Pine (Pinus lambertiana) in the Klamath Mountains, California', *Northwest Science*, 92(3), pp. 181–190. Available at: https://doi.org/10.3955/046.092.0305.

Doak, D.F., Waddle, E., Langendorf, R.E., Louthan, A.M., Isabelle Chardon, N., Dibner, R.R., Keinath, D.A., Lombardi, E., Steenbock, C., Shriver, R.K., Linares, C., Begoña Garcia, M., Funk, W.C., Fitzpatrick, S.W., Morris, W.F. and Peterson, M.L. (2021) 'A critical comparison of integral projection and matrix projection models for demographic analysis', *Ecological Monographs*, 91(2). Available at: https://doi.org/10.1002/ecm.1447.

Dolanc, C.R., Safford, H.D., Thorne, J.H. and Dobrowski, S.Z. (2014) ‘Changing forest structure across the landscape of the Sierra Nevada, CA, USA, since the 1930s’, *Ecosphere*, 5(8). Available at: https://doi.org/10.1890/ES14-00103.1.

Donato, D.C., Harvey, B.J., Romme, W.H., Simard, M. and Turner, M.G. (2013) ‘Bark beetle effects on fuel profiles across a range of stand structures in Douglas-fir forests of Greater Yellowstone’, *Ecological Applications*, 23(1), pp. 3–20. Available at: https://doi.org/10.1890/12-0772.1.

Dudney, J., Willing, C.E., Das, A.J., Latimer, A.M., Nesmith, J.C.B. and Battles, J.J. (2021) ‘Nonlinear shifts in infectious rust disease due to climate change’, *Nature Communications*, 12(1). Available at: https://doi.org/10.1038/s41467-021-25182-6.

Dudney, J.C., Nesmith, J.C.B., Cahill, M.C., Cribbs, J.E., Duriscoe, D.M., Das, A.J., Stephenson, N.L. and Battles, J.J. (2020) ‘Compounding effects of white pine blister rust, mountain pine beetle, and fire threaten four white pine species’, *Ecosphere*, 11(October). Available at: https://doi.org/10.1002/ecs2.3263.

Dunn, P.K. and Smyth, G.K. (2005) ‘Series evaluation of Tweedie exponential dispersion model densities’, *Statistics and Computing*, 15(4), pp. 267–280. Available at: https://doi.org/10.1007/s11222-005-4070-y.

Dunn, P.K. and Smyth, G.K. (2008) ‘Evaluation of Tweedie exponential dispersion model densities by Fourier inversion’, *Statistics and Computing*, 18(1), pp. 73–86. Available at: https://doi.org/10.1007/s11222-007-9039-6.

Dunnington, D. (2021) ‘ggspatial: Spatial Data Framework for ggplot2’. Available at: https://cran.r-project.org/package=ggspatial.

Eitzel, M., Battles, J., York, R., Knape, J. and de Valpine, P. (2013) ‘Estimating tree growth from complex forest monitoring data’, *Ecological Applications*, 23(6), pp. 1288–1296. Available at: https://doi.org/10.1890/12-0504.1.

Eitzel, M. V., Battles, J., York, R. and de Valpine, P. (2015) ‘Can’t see the trees for the forest: Complex factors influence tree survival in a temperate second growth forest’, *Ecosphere*, 6(11), pp. 1–17. Available at: https://doi.org/10.1890/ES15-00105.1.

Ellis, T.M., Bowman, D.M.J.S., Jain, P., Flannigan, M.D. and Williamson, G.J. (2021) ‘Global increase in wildfire risk due to climate-driven declines in fuel moisture’, *Global Change Biology*, (November 2021), pp. 1544–1559. Available at: https://doi.org/10.1111/gcb.16006.

Eskelson, B.N.I. and Monleon, V.J. (2018) ‘Post-fire surface fuel dynamics in California forests across three burn severity classes’, *International Journal of Wildland Fire*, 27(2), pp. 114–124. Available at: https://doi.org/10.1071/WF17148.

Eskelson, B.N.I., Monleon, V.J. and Fried, J.S. (2016) ‘A 6 year longitudinal study of post-fire woody carbon dynamics in California’s forests’, *Canadian Journal of Forest Research*, 46(5), pp. 610–620. Available at: https://doi.org/10.1139/cjfr-2015-0375.

Ferrari, J.B. (1999) ‘Fine-scale patterns of leaf litterfall and nitrogen cycling in an old-growth forest’, *Canadian Journal of Forest Research*, 29(3), pp. 291–302. Available at: https://doi.org/10.1139/cjfr-29-3-291.

Fettig, C.J., Mortenson, L.A., Bulaon, B.M. and Foulk, P.B. (2019) ‘Tree mortality following drought in the central and southern Sierra Nevada, California, U.S.’, *Forest Ecology and Management*, 432(August 2018), pp. 164–178. Available at: https://doi.org/10.1016/j.foreco.2018.09.006.

Finley, A.O., Datta, A. and Banerjee, S. (2020) ‘spNNGP R package for Nearest Neighbor Gaussian Process models’, (2017). Available at: http://arxiv.org/abs/2001.09111.

Finney, M.A. (1998) 'FARSITE: Fire Area Simulator - Model Development and Evaluation', *Res. Pap. RMRS-RP-4, Revised 2004.* Ogden, UT: USDA Forest Service, Rocky Mountain Research Station. 47p. Available at: https://doi.org/10.2737/RMRS-RP-4

Finney, M.A. (2006) ‘A Computational Method for Optimizing Fuel Treatment Locations’. In: Andrews, P.L., Butler, B.W., comps. 2006. *Fuels Management—How to Measure Success: Conference Proceedings 28-30 March 2006, Portland, OR.* Proceedings RMRS-P-41. Fort Collins, CO: USDA Forest Service, Rocky Mountain Research Station. pp. 107–123. Available at: https://www.fs.usda.gov/research/treesearch/25940.

Finney, M.A., Cohen, J.D., Grenfell, I.C. and Yedinak, K.M. (2010) ‘An examination of fire spread thresholds in discontinuous fuel beds’, *International Journal of Wildland Fire*, 19(2), pp. 163–170. Available at: https://doi.org/10.1071/WF07177.

Foster, D.E., Battles, J.J., Collins, B.M., York, R.A. and Stephens, S.L. (2020) ‘Potential wildfire and carbon stability in frequent-fire forests in the Sierra Nevada: trade-offs from a long-term study’, *Ecosphere*, 11(8). Available at: https://doi.org/10.1002/ecs2.3198.

Fowells, H.A. and Schubert, G.H. (1956) ‘Seed crops of forest trees in the pine region of California’. Technical Bulletin 1150. Washington, DC: USDA. 48 p. Available at: https://www.fs.usda.gov/research/treesearch/41063

Fry, D.L., Stevens, J.T., Potter, A.T., Collins, B.M. and Stephens, S.L. (2018) ‘Surface fuel accumulation and decomposition in old-growth pine-mixed conifer forests, northwestern Mexico’, *Fire Ecology*, 14(2). Available at: https://doi.org/10.1186/s42408-018-0017-5.

Furniss, T.J., Larson, A.J., Kane, V.R. and Lutz, J.A. (2018) ‘Multi-scale assessment of post-fire tree mortality models’, *International Journal of Wildland Fire*, 28(1), pp. 46-61. Available at: https://doi.org/10.1071/WF18031.

Furniss, T.J., Das, A.J., Mantgem, P.J., Stephenson, N.L. and Lutz, J.A. (2021) ‘Crowding, climate, and the case for social distancing among trees’, *Ecological Applications*, (June 2021), pp. 1–14. Available at: https://doi.org/10.1002/eap.2507.

Gabry, J., Simpson, D., Vehtari, A., Betancourt, M. and Gelman, A. (2019) ‘Visualization in Bayesian workflow’, *Journal of the Royal Statistical Society. Series A: Statistics in Society*, 182(2), pp. 389–402. Available at: https://doi.org/10.1111/rssa.12378.

Gabry, J., Češnovar, R., Bales, B., Morris, M., Popov, M., Lawrence, M., Michael Landau, W. and Socolar, J. (2022) ‘cmdstanr’. Available at: https://github.com/stan-dev/cmdstanr/.

Gabry, J. and Mahr, T. (2021) ‘bayesplot: Plotting for Bayesian Models’. Available at: https://mc-stan.org/bayesplot/.

Geils, B.W., Hummer, K.E. and Hunt, R.S. (2010) ‘White pines, Ribes, and blister rust: A review and synthesis’, *Forest Pathology*, 40(3–4), pp. 147–185. Available at: https://doi.org/10.1111/j.1439-0329.2010.00654.x.

Gelman, A., Carlin, J.B., Stern, H.S., Dunson, D.B., Vehtari, A. and Rubin, D.B. (2021) *Bayesian Data Analysis*. 3rd edn. Available at: http://www.stat.columbia.edu/~gelman/book/.

Gray, C.A., Toone, C., Jenkins, M.J., Null, S.E. and Yocom, L.L. (2021) ‘Spatial and temporal fuels changes in whitebark pine (Pinus albicaulis) from mountain pine beetle (Dendroctonus ponderosae)’, *Forest Ecology and Management*, 482(November 2020), p. 118789. Available at: https://doi.org/10.1016/j.foreco.2020.118789.

Hart, S.C., Firestone, M.K. and Paul, E.A. (1992) ‘Decomposition and nutrient dynamics of ponderosa pine needles in a Mediterranean-type climate’, *Canadian Journal of Forest Research*, 22(3), pp. 306–314. Available at: https://doi.org/10.1139/x92-040.

Hartsough, B.R., Abrams, S., Barbour, R.J., Drews, E.S., McIver, J.D., Moghaddas, J.J., Schwilk, D.W. and Stephens, S.L. (2008) ‘The economics of alternative fuel reduction treatments in western United States dry forests: Financial and policy implications from the National Fire and Fire Surrogate Study’, *Forest Policy and Economics*, 10(6), pp. 344–354. Available at: https://doi.org/10.1016/j.forpol.2008.02.001.

Hawley, C.M., Loudermilk, E.L., Rowell, E.M. and Pokswinski, S. (2018) ‘A novel approach to fuel biomass sampling for 3D fuel characterization’, *MethodsX*, 5(September), pp. 1597–1604. Available at: https://doi.org/10.1016/j.mex.2018.11.006.

Heaton, M.J., Datta, A., Finley, A.O., Furrer, R., Guinness, J., Guhaniyogi, R., Gerber, F., Gramacy, R.B., Hammerling, D., Katzfuss, M., Lindgren, F., Nychka, D.W., Sun, F. and Zammit-Mangion, A. (2019) ‘A Case Study Competition Among Methods for Analyzing Large Spatial Data’, *Journal of Agricultural, Biological, and Environmental Statistics*, 24(3), pp. 398–425. Available at: https://doi.org/10.1007/s13253-018-00348-w.

Hessburg, P.F., Spies, T.A., Perry, D.A., Skinner, C.N., Taylor, A.H., Brown, P.M., Stephens, S.L., Larson, A.J., Churchill, D.J., Povak, N.A., Singleton, P.H., McComb, B., Zielinski, W.J., Collins, B.M., Salter, R.B., Keane, J.J., Franklin, J.F. and Riegel, G. (2016) ‘Tamm Review: Management of mixed-severity fire regime forests in Oregon, Washington, and Northern California’, *Forest Ecology and Management*, 366, pp. 221–250. Available at: https://doi.org/10.1016/j.foreco.2016.01.034.

Hessburg, P.F., Prichard, S.J., Hagmann, R.K., Povak, N.A. and Lake, F.K. (2021) ‘Wildfire and climate change adaptation of western North American forests: a case for intentional management’, *Ecological Applications*, 31(8), e02432. Available at: https://doi.org/10.1002/eap.2432.

Heywood, V.H. (2017) ‘Plant conservation in the Anthropocene – Challenges and future prospects’, *Plant Diversity*, 39(6), pp. 314–330. Available at: https://doi.org/10.1016/j.pld.2017.10.004.

Hicke, J.A., Johnson, M.C., Hayes, J.L. and Preisler, H.K. (2012) ‘Effects of bark beetle-caused tree mortality on wildfire’, *Forest Ecology and Management*, 271, pp. 81–90. Available at: https://doi.org/10.1016/j.foreco.2012.02.005.

Hiers, J.K., O’Brien, J.J., Will, R.E. and Mitchell, R.J. (2007) ‘Forest floor depth mediates understory vigor in xeric Pinus palustris ecosystems’, *Ecological Applications*, 17(3), pp. 806–814. Available at: https://doi.org/10.1890/06-1015.

Hiers, J.K., O’Brien, J.J., Mitchell, R.J., Grego, J.M. and Loudermilk, E.L. (2009) ‘The wildland fuel cell concept: An approach to characterize fine-scale variation in fuels and fire in frequently burned longleaf pine forests’, *International Journal of Wildland Fire*, 18(3), pp. 315–325. Available at: https://doi.org/10.1071/WF08084.

Hiers, J.K. *et al.* (2020) ‘Prescribed fire science: the case for a refined research agenda’, *Fire Ecology*, 16(1). Available at: https://doi.org/10.1186/s42408-020-0070-8.

Hiers, Q.A., Loudermilk, E.L., Hawley, C.M., Hiers, J.K., Pokswinski, S., Hoffman, C.M. and O’Brien, J.J. (2021) ‘Non-Destructive Fuel Volume Measurements Can Estimate Fine-Scale Biomass across Surface Fuel Types in a Frequently Burned Ecosystem’, *Fire*, 4(3), 36. Available at: https://doi.org/10.3390/fire4030036.

Hijmans, R.J. (2021) ‘raster: Geographic Data Analysis and Modeling’. Available at: https://cran.r-project.org/package=raster.

Hille, M.G. and Stephens, S.L. (2005) ‘Mixed conifer forest duff consumption during prescribed fires: Tree crown impacts’, *Forest Science*, 51(5), pp. 417–424. Available at: https://doi.org/10.1093/forestscience/51.5.417

Hoffman, C., Morgan, P., Mell, W., Parsons, R., Strand, E.K. and Cook, S. (2012a) ‘Numerical simulation of crown fire hazard immediately after bark beetle-caused mortality in lodgepole pine forests’, *Forest Science*, 58(2), pp. 178–188. Available at: https://doi.org/10.5849/forsci.10-137.

Hoffman, C.M., Sieg, C.H., McMillin, J.D. and Fuĺ, P.Z. (2012b) ‘Fuel loadings 5 years after a bark beetle outbreak in south-western USA ponderosa pine forests’, *International Journal of Wildland Fire*, 21(3), pp. 306–312. Available at: https://doi.org/10.1071/WF11019.

Hollister, J.W. (2021) ‘elevatr: Access Elevation Data from Various APIs’. Available at: https://cran.r-project.org/package=elevatr/.

Hood, S.M., McHugh, C.W., Ryan, K.C., Reinhardt, E. and Smith, S.L. (2007) ‘Evaluation of a post-fire tree mortality model for western USA conifers’, *International Journal of Wildland Fire*, 16(6), pp. 679–689. Available at: https://doi.org/10.1071/WF06122.

Hood, S.M., Smith, S.L. and Cluck, D.R. (2010) ‘Predicting mortality for five California conifers following wildfire’, *Forest Ecology and Management*, 260(5), pp. 750–762. Available at: https://doi.org/10.1016/j.foreco.2010.05.033.

Hurteau, M.D., Koch, G.W. and Hungate, B.A. (2008) ‘Carbon protection and fire risk reduction: Toward a full accounting of forest carbon offsets’, *Frontiers in Ecology and the Environment*, 6(9), pp. 493–498. Available at: https://doi.org/10.1890/070187.

Ives, A.R. (2022) ‘Random errors are neither: On the interpretation of correlated data’, *Methods in Ecology and Evolution*, 13(10), pp. 2092-2105. Available at: https://doi.org/10.1111/2041-210X.13971.

Jakubowksi, M.K., Guo, Q., Collins, B.M., Stephens, S.L. and Kelly, M. (2013) ‘Predicting Surface Fuel Models and Fuel Metrics Using Lidar and CIR Imagery in a Dense, Mountainous Forest’, *Photogrammetric Engineering and Remote Sensing*, 79(1), pp. 37–49. Available at: https://doi.org/10.14358/PERS.79.1.37.

Jenkins, J.C., Chojnacky, D.C., Heath, L.S., and Birdsey, R.A. (2003) 'National-scale biomass estimators for United States tree species', *Forest Science*, 49(1), pp. 12-35. Available at: https://www.fs.usda.gov/research/treesearch/6996

Jeronimo, S.M.A., Kane, V.R., Churchill, D.J., McGaughey, R.J. and Franklin, J.F. (2018) ‘Applying LiDAR individual tree detection to management of structurally diverse forest landscapes’, *Journal of Forestry*, 116(4), pp. 336–346. Available at: https://doi.org/10.1093/jofore/fvy023.

Jeronimo, S.M.A., Kane, V.R., Churchill, D.J., Lutz, J.A., North, M.P., Asner, G.P. and Franklin, J.F. (2019) ‘Forest structure and pattern vary by climate and landform across active-fire landscapes in the montane Sierra Nevada’, *Forest Ecology and Management*, 437(January), pp. 70–86. Available at: https://doi.org/10.1016/j.foreco.2019.01.033.

Keane, R. and Lutes, D. (2016) ‘First Order Fire Effects Model (FOFEM)’. Available at: https://www.firelab.org/project/fofem.

Keane, R.E. (2008) ‘Biophysical controls on surface fuel litterfall and decomposition in the northern Rocky Mountains, USA’, *Canadian Journal of Forest Research*, 38(6), pp. 1431–1445. Available at: https://doi.org/10.1139/X08-003.

Keane, R.E., Gray, K., Bacciu, V. and Leirfallom, S. (2012a) ‘Spatial scaling of wildland fuels for six forest and rangeland ecosystems of the northern Rocky Mountains, USA’, *Landscape Ecology*, 27(8), pp. 1213–1234. Available at: https://doi.org/10.1007/s10980-012-9773-9.

Keane, R.E., Gray, K. and Bacciu, V. (2012b) 'Spatial Variability of Wildland Fuel Characteristics in Northern Rocky Mountain Ecosystems', *Res. Pap. RMRS-RP-98*. Fort Collins, CO: U.S. Department of Agriculture, Forest Service, Rocky Mountain Research Station. 56 p.

Keane, R.E. (2013) 'Describing wildland surface fuel loading for fire management: A review of approaches, methods and systems', *International Journal of Wildland Fire*, 22(1), pp. 51–62. Available at: https://doi.org/10.1071/WF11139.

Keane, R.E., Herynk, J.M., Toney, C., Urbanski, S.P., Lutes, D.C. and Ottmar, R.D. (2013) 'Evaluating the performance and mapping of three fuel classification systems using Forest Inventory and Analysis surface fuel measurements', *Forest Ecology and Management*, 305, pp. 248–263. Available at: https://doi.org/10.1016/j.foreco.2013.06.001.

Keane, R.E. (2015) *Wildland Fuel Fundamentals and Application*. Springer Cham. ISBN 978-3-310-09015-3. Available at: https://doi.org/10.1007/978-3-319-09015-3.

Keane, R.E. (2016) 'Spatiotemporal Variability of Wildland Fuels in US Northern Rocky Mountain Forests', *Forests*, 7(7), p. 129. Available at: https://doi.org/10.3390/f7070129.

Kinloch, Jr., B.B., Sniezko, R.A., Savin, D.P., Danchok, R. and Kegley, A. (2018) 'Patterns of Variation in Blister Rust Resistance in Sugar Pine (Pinus lambertiana)', in Schoettle, A.W., Sniezko, R.A., Kliejunas, J.T., eds. *Proceedings of the IUFRO joint conference: Genetics of five-needle pines, rusts of forest trees, and Strobusphere; 2014 June 15–20; Fort Collins, CO.* Proc. RMRS-P-76. Fort Collins, CO, pp. 124–128. Available at: https://www.fs.usda.gov/research/treesearch/56712

Kinloch, Jr., B.B., Marosy, M. and Huddleston, M.E., eds. (1996) *Sugar pine: status, values, and roles in ecosystems: Proceedings of a symposium presented by the California Sugar Pine Management Committee, March 30 - April 1, 1992*. University of California, Division of Agriculture and Natural Resources, Davis, CA. Publication 3362. Available at: https://books.google.com/books?id=VwRj7T5-kNEC&printsec=frontcover&source=gbs_ge_summary_r&cad=0#v=onepage&q&f=false

Kinloch, Jr., B.B. and Scheuner, W.H. (1990) 'Pinus lambertiana Dougl.', in Burns, R.M. and Honkala, B.H., eds. *Silvics of North America Vol. 1: Conifers*. Washington, D.C.: Agriculture Handbook 654. U.S. Department of Agriculture, Forest Service, pp. 370–380. Available at: https://www.fs.usda.gov/research/treesearch/1547

Kohyama, T.S., Kohyama, T.I. and Sheil, D. (2018) 'Definition and estimation of vital rates from repeated censuses: Choices, comparisons and bias corrections focusing on trees', *Methods in Ecology and Evolution*, 9(4), pp. 809–821. Available at: https://doi.org/10.1111/2041-210X.12929.

Koltunov, A., Ramirez, C.M., Ustin, S.L., Slaton, M. and Haunreiter, E. (2020) 'eDaRT: The Ecosystem Disturbance and Recovery Tracker system for monitoring landscape disturbances and their cumulative effects', *Remote Sensing of Environment*, 238(September 2019), p. 111482. Available at: https://doi.org/10.1016/j.rse.2019.111482.

Krebs, M.A., Reeves, M.C. and Baggett, L.S. (2019) ‘Predicting understory vegetation structure in selected western forests of the United States using FIA inventory data’, *Forest Ecology and Management*, 448(June), pp. 509–527. Available at: https://doi.org/10.1016/j.foreco.2019.06.024.

Kress, W.J. and Krupnick, G.A. (2022) ‘Lords of the biosphere: Plant winners and losers in the Anthropocene’, *Plants People Planet*, 4(4), pp. 350–366. Available at: https://doi.org/10.1002/ppp3.10252.

Kreye, J.K., Kane, J.M., Varner, J.M. and Hiers, J.K. (2020) ‘Radiant heating rapidly increases litter flammability through impacts on fuel moisture’, *Fire Ecology*, 16(1). Available at: https://doi.org/10.1186/s42408-020-0067-3.

Kreye, J.K., Varner, J.M. and Dugaw, C.J. (2014) ‘Spatial and temporal variability of forest floor duff characteristics in long-unburned Pinus palustris forests’, *Canadian Journal of Forest Research*, 44(12), pp. 1477–1486. Available at: https://doi.org/10.1139/cjfr-2014-0223.

Lanini, W.T. and Radosevich, S.R. (1986) ‘Response of three conifer species to site preparation and shrub control.’, *Forest Science*, 32(1), pp. 61–77. Available at: https://doi.org/10.1093/forestscience/32.1.61.

Latham, P. and Tappeiner, J. (2002) ‘Response of old-growth conifers to reduction in stand density in western Oregon forests’, *Tree Physiology*, 22(2–3), pp. 137–146. Available at: https://doi.org/10.1093/treephys/22.2-3.137.

Leite, R. *et al.* (2022) ‘Large scale multi-layer fuel load characterization in tropical savanna using GEDI spaceborne lidar data’, *Remote Sensing of Environment*, 268(October 2021). Available at: https://doi.org/10.1016/j.rse.2021.112764.

Levine, C.R., Krivak-Tetley, F., van Doorn, N.S., Ansley, J.-A.S. and Battles, J.J. (2016) ‘Long-term demographic trends in a fire-suppressed mixed-conifer forest’, *Canadian Journal of Forest Research*, 46(5), pp. 745–752. Available at: https://doi.org/10.1139/cjfr-2015-0406.

Levine, J.I., Collins, B.M., York, R.A., Foster, D.E., Fry, D.L. and Stephens, S.L. (2020) ‘Forest stand and site characteristics influence fuel consumption in repeat prescribed burns’, *International Journal of Wildland Fire*, 29(2), pp. 148–159. Available at: https://doi.org/10.1071/WF19043.

Li, W., Guo, Q., Jakubowski, M.K. and Kelly, M. (2013) ‘A New Method for Segmenting Individual Trees from the Lidar Point Cloud’, *Photogrammetric Engineering & Remote Sensing*, 78(1), pp. 75–84. Available at: https://doi.org/10.14358/pers.78.1.75.

Liang, S., Hurteau, M.D. and Westerling, A.L.R. (2017) ‘Response of Sierra Nevada forests to projected climate–wildfire interactions’, *Global Change Biology*, 23(5), pp. 2016–2030. Available at: https://doi.org/10.1111/gcb.13544.

Linn, R., Reisner, J., Colman, J.J. and Winterkamp, J. (2002) ‘Studying wildfire behavior using FIRETEC’, *International Journal of Wildland Fire*, 11(3–4), pp. 233–246. Available at: https://doi.org/10.1071/wf02007.

Linn, R., Winterkamp, J., Colman, J.J., Edminster, C. and Bailey, J.D. (2005) ‘Modeling interactions between fire and atmosphere in discrete element fuel beds’, *International Journal of Wildland Fire*, 14(1), pp. 37–48. Available at: https://doi.org/10.1071/WF04043.

Linn, R.R., Goodrick, S.L., Brambilla, S., Brown, M.J., Middleton, R.S., O’Brien, J.J. and Hiers, J.K. (2020) ‘QUIC-fire: A fast-running simulation tool for prescribed fire planning’, *Environmental Modelling and Software*, 125(August 2019). Available at: https://doi.org/10.1016/j.envsoft.2019.104616.

Liu, Y., Gelman, A. and Zheng, T. (2015) ‘Simulation-efficient shortest probability intervals’, *Statistics and Computing*, 25(4), pp. 809–819. Available at: https://doi.org/10.1007/s11222-015-9563-8.

Loudermilk, E.L., Hiers, J.K., O’Brien, J.J., Mitchell, R.J., Singhania, A., Fernandez, J.C., Cropper, W.P. and Slatton, K.C. (2009) ‘Ground-based LIDAR: A novel approach to quantify fine-scale fuelbed characteristics’, *International Journal of Wildland Fire*, 18(6), pp. 676–685. Available at: https://doi.org/10.1071/WF07138.

Loudermilk, E.L., O’Brien, J.J., Mitchell, R.J., Cropper, W.P., Hiers, J.K., Grunwald, S., Grego, J. and Fernandez-diaz, J.C. (2012) ‘Linking complex forest fuel structure and fire behaviour at fine scales’, *International Journal of Wildland Fire*, 21(7), pp. 882–893. Available at: https://ezp.lib.unimelb.edu.au/login?url=https://search.ebscohost.com/login.aspx?direct=true&db=edswsc&AN=000310004400008&scope=site%5Cnhttp://www.publish.csiro.au.ezp.lib.unimelb.edu.au/?paper=WF10116.

Loudermilk, E.L., Achtemeier, G.L., O’Brien, J.J., Hiers, J.K. and Hornsby, B.S. (2014) ‘High-resolution observations of combustion in heterogeneous surface fuels’, *International Journal of Wildland Fire*, 23(7), pp. 1016–1026. Available at: https://doi.org/10.1071/WF13160.

Loudermilk, E.L., O’Brien, J.J., Goodrick, S.L., Linn, R.R., Skowronski, N.S. and Hiers, J.K. (2022) ‘Vegetation’s influence on fire behavior goes beyond just being fuel’, *Fire Ecology*, 18(1). Available at: https://doi.org/10.1186/s42408-022-00132-9.

Lutes, D.C., Keane, R.E., Caratti, J.F., Key, C.H., Benson, N.C., Sutherland, S. and Gangi, L.J. (2006) ‘FIREMON: Fire effects monitoring and inventory system', *RMRS-GTR-164-CD.* Fort Collins, CO: USDA Forest Service, Rocky Mountain Research Station. Available at: https://doi.org/10.2737/RMRS-GTR-164.

Lutz, J.A., Larson, A.J., Freund, J.A., Swanson, M.E. and Bible, K.J. (2013) ‘The importance of large-diameter trees to forest structural heterogeneity’, *PLoS ONE*, 8(12). Available at: https://doi.org/10.1371/journal.pone.0082784.

Lutz, J.A., Furniss, T.J., Germain, S.J., Becker, K.M.L., Blomdahl, E.M., Jeronimo, S.M.A., Cansler, C.A., Freund, J.A., Swanson, M.E. and Larson, A.J. (2017) ‘Shrub communities, spatial patterns, and shrub-mediated tree mortality following reintroduced fire in Yosemite National Park, California, USA’, *Fire Ecology*, 13(1), pp. 104–126. Available at: https://doi.org/10.4996/fireecology.1301104.

Lutz, J.A. *et al.* (2018) 'Global importance of large-diameter trees', *Global Ecology and Biogeography*, 27(7), pp. 849–864. Available at: https://doi.org/10.1111/geb.12747.

Lutz, J.A., Struckman, S., Furniss, T.J., Cansler, C.A., Germain, S.J., Yocom, L.L., McAvoy, D.J., Kolden, C.A., Smith, A.M.S., Swanson, M.E. and Larson, A.J. (2020) 'Large-diameter trees dominate snag and surface biomass following reintroduced fire', *Ecological Processes*, 9(1). Available at: https://doi.org/10.1186/s13717-020-00243-8.

Lydersen, J.M., North, M.P., Knapp, E.E. and Collins, B.M. (2013) 'Quantifying spatial patterns of tree groups and gaps in mixed-conifer forests: Reference conditions and long-term changes following fire suppression and logging', *Forest Ecology and Management*, 304, pp. 370–382. Available at: https://doi.org/10.1016/j.foreco.2013.05.023.

Lydersen, J.M., Collins, B.M., Knapp, E.E., Roller, G.B. and Stephens, S.L. (2015) 'Relating fuel loads to overstorey structure and composition in a fire-excluded Sierra Nevada mixed conifer forest', *International Journal of Wildland Fire*, 24(4), pp. 484–494. Available at: https://doi.org/10.1071/WF13066.

Lydersen, J.M., Collins, B.M., Coppoletta, M., Jaffe, M.R., Northrop, H. and Stephens, S.L. (2019) 'Fuel dynamics and reburn severity following high-severity fire in a Sierra Nevada, USA, mixed-conifer forest', *Fire Ecology*, 15(1). Available at: https://doi.org/10.1186/s42408-019-0060-x.

Mahalovich, M. and Stritch, L. (2013) 'Pinus albicaulis. The IUCN Red List of Threatened Species 2013'. Available at: https://dx.doi.org/10.2305/IUCN.UK.2013-1.RLTS.T39049A2885918.en.

Makowski, D., Ben-Shachar, M. and Lüdecke, D. (2019) 'bayestestR: Describing Effects and their Uncertainty, Existence and Significance within the Bayesian Framework', *Journal of Open Source Software*, 4(40), p. 1541. Available at: https://doi.org/10.21105/joss.01541.

Maloney, P.E. (2011) 'Incidence and distribution of white pine blister rust in the high-elevation forests of California', *Forest Pathology*, 41(4), pp. 308–316. Available at: https://doi.org/10.1111/j.1439-0329.2011.00732.x.

Maloney, P.E., Vogler, D.R., Eckert, A.J., Jensen, C.E. and Neale, D.B. (2011) 'Population biology of sugar pine (Pinus lambertiana Dougl.) with reference to historical disturbances in the Lake Tahoe Basin: Implications for restoration', *Forest Ecology and Management*, 262(5), pp. 770–779. Available at: https://doi.org/10.1016/j.foreco.2011.05.011.

Maloney, P.E. (2014) 'The multivariate underpinnings of recruitment for three Pinus species in montane forests of the Sierra Nevada, USA', *Plant Ecology*, 215(2), pp. 261–274. Available at: https://doi.org/10.1007/s11258-013-0295-6.

McCaskill, G.L. (2018) 'The Hungry Bob Fire&Fire Surrogate Study: A 20-Year Evaluation of the Treatment Effects', *Forests*, 10(1), p. 15. Available at: https://doi.org/10.3390/f10010015.

McCauley, L.A., Bradford, J.B., Robles, M.D., Shriver, R.K., Woolley, T.J. and Andrews, C.A. (2022) 'Landscape-scale forest restoration decreases vulnerability to drought mortality under climate change in southwest USA ponderosa forest', *Forest Ecology and Management*, 509(February), p. 120088. Available at: https://doi.org/10.1016/j.foreco.2022.120088.

McElreath, R. (2016) *Statistical Rethinking: A Bayesian Course with Examples in R and STAN*, 1st ed. 2016 Chapman and Hall / CRC. New York, NY. ISBN 9781315372495. Available at: https://xcelab.net/rm/statistical-rethinking/

McGinnis, T.W., Shook, C.D. and Keeley, J.E. (2010) ‘Estimating aboveground biomass for broadleaf woody plants and young conifers in Sierra Nevada, California, forests’, *Western Journal of Applied Forestry*, 25(mm), pp. 203–209.

Merow, C., Dahlgren, J.P., Metcalf, C.J.E., Childs, D.Z., Evans, M.E.K., Jongejans, E., Record, S., Rees, M., Salguero-Gómez, R. and Mcmahon, S.M. (2014) ‘Advancing population ecology with integral projection models: A practical guide’, *Methods in Ecology and Evolution*, 5(2), pp. 99–110. Available at: https://doi.org/10.1111/2041-210X.12146.

Millar, C.I. and Stephenson, N.L. (2015) ‘Temperate forest health in an era of emerging megadisturbance’, *Science*, 349(6250), pp. 823–826. Available at: https://doi.org/10.1126/science.aaa9933.

Mitchell, R.J., Hiers, J.K., O’Brien, J.J. and Starr, G. (2009) ‘Ecological forestry in the southeast: Understanding the ecology of fuels’, *Journal of Forestry*, 107(8), pp. 391–397. Available at: https://doi.org/10.1093/jof/107.8.391.

Miyanishi, K. and Johnson, E.A. (2002) ‘Process and patterns of duff consumption in the mixedwood boreal forest’, *Canadian Journal of Forest Research*, 32(7), pp. 1285–1295. Available at: https://doi.org/10.1139/x02-051.

Moghaddas, E.E.Y. and Stephens, S.L. (2007) ‘Thinning, burning, and thin-burn fuel treatment effects on soil properties in a Sierra Nevada mixed-conifer forest’, *Forest Ecology and Management*, 250(3), pp. 156–166. Available at: https://doi.org/10.1016/j.foreco.2007.05.011.

Moran, E. V., Das, A.J., Keeley, J.E. and Stephenson, N.L. (2019) ‘Negative impacts of summer heat on Sierra Nevada tree seedlings’, *Ecosphere*, 10(6). Available at: https://doi.org/10.1002/ecs2.2776.

Mueller, E. V., Skowronski, N.S., Clark, K.L., Gallagher, M.R., Mell, W.E., Simeoni, A. and Hadden, R.M. (2021) ‘Detailed physical modeling of wildland fire dynamics at field scale - An experimentally informed evaluation’, *Fire Safety Journal*, 120, p. 103051. Available at: https://doi.org/10.1016/j.firesaf.2020.103051.

Mullen, L.A. and Bratt, J. (2018) ‘USAboundaries: Historical and Contemporary Boundaries of the United States of America’, *Journal of Open Source Software*, 3(23), p. 314. Available at: https://doi.org/10.21105/joss.00314.

Müller, K. (2020) ‘here: A Simpler Way to Find Your Files’. Available at: https://cran.r-project.org/package=here.

Müller, K., Wickham, H., James, D.A. and Falcon, S. (2021) ‘RSQLite: “SQLite” Interface for R’. Available at: https://cran.r-project.org/package=RSQLite.

Murray, M.P. and Tomback, D.F. (2010) ‘Clark’s nutcrackers harvest sugar pine seeds from cones’, *Western North American Naturalist*, 70(3), pp. 413–414. Available at: https://doi.org/10.3398/064.070.0314.

Nagel, L.M., Palik, B.J., Battaglia, M.A., D’Amato, A.W., Guldin, J.M., Swanston, C.W., Janowiak, M.K., Powers, M.P., Joyce, L.A., Millar, C.I., Peterson, D.L., Ganio, L.M., Kirschbaum, C. and Roske, M.R. (2017) ‘Adaptive silviculture for climate change: A national experiment in manager-scientist partnerships to apply an adaptation framework’, *Journal of Forestry*, 115(3), pp. 167–178. Available at: https://doi.org/10.5849/jof.16-039.

National Park Service (2013) 'A natural resource conditoin assessment for Sequoia and Kings Canyon National Parks'. *Natural Resource Report NPS/SEKI/NRR-2013/665.* National Park Service, Fort Collins, CO. Available at: https://www.nps.gov/subjects/science/nrca_seki.htm

Needham, J., Merow, C., Chang-Yang, C.H., Caswell, H. and McMahon, S.M. (2018) ‘Inferring forest fate from demographic data: From vital rates to population dynamic models’, *Proceedings of the Royal Society B: Biological Sciences*, 285(1874). Available at: https://doi.org/10.1098/rspb.2017.2050.

Nesmith, J.C.B., O’Hara, K.L., van Mantgem, P.J. and de Valpine, P. (2010) ‘The effects of raking on sugar pine mortality following prescribed fire in sequoia and kings canyon national parks, California, USA’, *Fire Ecology*, 6(3), pp. 97–116. Available at: https://doi.org/10.4996/fireecology.0603097.

Nesmith, J.C.B., Das, A.J., O’Hara, K.L. and van Mantgem, P.J. (2015) ‘The influence of prefire tree growth and crown condition on postfire mortality of sugar pine following prescribed fire in Sequoia National Park’, *Canadian Journal of Forest Research*, 45(7), pp. 910–919. Available at: https://doi.org/10.1139/cjfr-2014-0449.

Newman, E.A. (2019) ‘Disturbance Ecology in the Anthropocene’, *Frontiers in Ecology and Evolution*, 7(May). Available at: https://doi.org/10.3389/fevo.2019.00147.

Niinemets, Ü. and Valladares, F. (2006) ‘Tolerance to shade, drought, and waterlogging of temperate northern hemisphere trees and shrubs’, *Ecological Monographs*, 76(4), pp. 521–547. Available at: https://doi.org/10.1890/0012-9615(2006)076[0521:TTSDAW]2.0.CO;2.

North, M., Stine, P., O’Hara, K., Zielinski, W., Stephens, S.L., Service, F. and Hara, K.O. (2009) ‘An ecosystem management strategy for Sierran mixed- conifer forests’, *USDA Forest Service, Pacific Southwest Research Station, General Technical Report*, (March), p. PSW-GTR-220.

North, M., ed. (2012) ‘Managing Sierra Nevada forests’, *PSW-GTR-237*. Albany, CA: USDA Forest Service, Pacific Southwest Research Station. 184 p. Available at: https://doi.org/10.2737/PSW-GTR-237.

North, M.P. *et al.* (2019) ‘Tamm Review: Reforestation for resilience in dry western U.S. forests’, *Forest Ecology and Management*, 432(July 2018), pp. 209–224. Available at: https://doi.org/10.1016/j.foreco.2018.09.007.

North, M.P., York, R.A., Collins, B.M., Hurteau, M.D., Jones, G.M., Knapp, E.E., Kobziar, L., Mccann, H., Meyer, M.D., Stephens, S.L., Tompkins, R.E. and Tubbesing, C.L. (2021) ‘Pyrosilviculture needed for landscape resilience of dry western United States forests’, *Journal of Forestry*, pp. 1–25. Available at: https://doi.org/10.1093/jofore/fvab026.

North, M.P., Tompkins, R.E., Bernal, A.A., Collins, B.M., Stephens, S.L. and York, R.A. (2022) ‘Operational resilience in western US frequent-fire forests’, *Forest Ecology and Management*, 507(November 2021), p. 120004. Available at: https://doi.org/10.1016/j.foreco.2021.120004.

O’Brien, J.J., Loudermilk, E.L., Hiers, J.K., Pokswinski, S.M., Hornsby, B., Hudak, A.T., Strother, D., Rowell, E. and Bright, B.C. (2016a) ‘Canopy-Derived Fuels Drive Patterns of In-Fire Energy Release and Understory Plant Mortality in a Longleaf Pine (Pinus palustris) Sandhill in Northwest Florida, USA’, *Canadian Journal of Remote Sensing*, 42(5), pp. 489–500. Available at: https://doi.org/10.1080/07038992.2016.1199271.

O’Brien, J.J., Loudermilk, E.L., Hornsby, B., Hudak, A.T., Bright, B.C., Dickinson, M.B., Hiers, J.K., Teske, C. and Ottmar, R.D. (2016b) ‘High-resolution infrared thermography for capturing wildland fire behaviour: RxCADRE 2012’, *International Journal of Wildland Fire*, 25(1), pp. 62–75. Available at: https://doi.org/10.1071/WF14165.

Ottmar, R.D., Sandberg, D. V., Riccardi, C.L. and Prichard, S.J. (2007) ‘An overview of the Fuel Characteristic Classification System — Quantifying, classifying, and creating fuelbeds for resource planningThis article is one of a selection of papers published in the Special Forum on the Fuel Characteristic Classification Syste’, *Canadian Journal of Forest Research*, 37(12), pp. 2383–2393. Available at: https://doi.org/10.1139/X07-077.

Parks, S.A. and Abatzoglou, J.T. (2020) ‘Warmer and Drier Fire Seasons Contribute to Increases in Area Burned at High Severity in Western US Forests From 1985 to 2017’, *Geophysical Research Letters*, 47(22), pp. 1–10. Available at: https://doi.org/10.1029/2020GL089858.

Pawlikowski, N.C., Coppoletta, M., Knapp, E. and Taylor, A.H. (2019) ‘Spatial dynamics of tree group and gap structure in an old-growth ponderosa pine-California black oak forest burned by repeated wildfires’, *Forest Ecology and Management*, 434(October 2018), pp. 289–302. Available at: https://doi.org/10.1016/j.foreco.2018.12.016.

Paz-Kagan, T., Brodrick, P.G., Vaughn, N.R., Das, A.J., Stephenson, N.L., Nydick, K.R. and Asner, G.P. (2017) ‘What mediates tree mortality during drought in the southern Sierra Nevada’, *Ecological Applications*, 27(8), pp. 2443–2457. Available at: https://doi.org/10.1002/eap.1620.

Pebesma, E. (2018) ‘Simple features for R: Standardized support for spatial vector data’, *R Journal*, 10(1), pp. 439–446. Available at: https://doi.org/10.32614/rj-2018-009.

Pebesma, E., Mailund, T. and Hiebert, J. (2016) ‘Measurement Units in R’, *R Journal*, 8(2), pp. 490–498. Available at: https://doi.org/10.32614/rj-2016-061.

Pebesma, E.J. (2004) ‘Multivariable geostatistics in S: The gstat package’, *Computers and Geosciences*, 30(7), pp. 683–691. Available at: https://doi.org/10.1016/j.cageo.2004.03.012.

Perry, D.A., Hessburg, P.F., Skinner, C.N., Spies, T.A., Stephens, S.L., Taylor, A.H., Franklin, J.F., McComb, B. and Riegel, G. (2011) 'The ecology of mixed severity fire regimes in Washington, Oregon, and Northern California', *Forest Ecology and Management*, 262(5), pp. 703–717. Available at: https://doi.org/10.1016/j.foreco.2011.05.004.

R-SIG-DB, Wickham, H. and Müller, K. (2021) 'DBI: R Database Interface'. Available at: https://cran.r-project.org/package=DBI.

R Core Team (2021) 'R: A language and environment for statistical computing.' Vienna, Austria: R Foundation for Statistical Computing. Available at: https://www.r-project.org.

Raaflaub, L.D., Valeo, C. and Johnson, E.A. (2012) 'Slope effects on the spatial variations in duff moisture', *Ecohydrology*, 5(6), pp. 819–825. Available at: https://doi.org/10.1002/eco.272.

Rakhmatulina, E., Stephens, S.L. and Thompson, S. (2021) 'Soil moisture influences on Sierra Nevada dead fuel moisture content and fire risks', *Forest Ecology and Management*, 496(June), p. 119379. Available at: https://doi.org/10.1016/j.foreco.2021.119379.

Reinhardt, E.D. and Ryan, K.C. (1988) 'Predicting postfire mortality of seven western conifers', *Canadian Journal of Forest Research*, 18, pp. 1291–11297.

Restaino, C., Young, D.J.N., Estes, B., Gross, S., Wuenschel, A., Meyer, M. and Safford, H. (2019) 'Forest structure and climate mediate drought-induced tree mortality in forests of the Sierra Nevada , USA', *Ecological Applications*, 29(December 2017), pp. 1–14. Available at: https://doi.org/10.1002/eap.1902.

Rice, S.K. (1993) ' Vegetation establishment in post-fire Adenostoma chaparral in relation to fine-scale pattern in fire intensity and soil nutrients ', *Journal of Vegetation Science*, 4(1), pp. 115–124. Available at: https://doi.org/10.2307/3235739.

Ritter, S.M., Hoffman, C.M., Battaglia, M.A., Stevens-Rumann, C.S. and Mell, W.E. (2020) 'Fine-scale fire patterns mediate forest structure in frequent-fire ecosystems', *Ecosphere*, 11(7). Available at: https://doi.org/10.1002/ecs2.3177.

Ritter, S.M., Hoffman, C.M., Battaglia, M.A. and Jain, T.B. (2022) 'Restoration and fuel hazard reduction result in equivalent reductions in crown fire behavior in dry conifer forests', *Ecological Applications*, 32(7), p. e2682. Available at: https://doi.org/10.1002/eap.2682.

Robichaud, P.R. and Miller, S.M. (2000) 'Spatial Interpolation and Simulation of Post-burn Duff Thickness after Prescribed Fire', *International Journal of Wildland Fire*, 9(2), pp. 137–143. Available at: https://doi.org/10.1071/wf00018.

Rocca, M.E. (2009) 'Fine-scale Patchiness in Fuel Load Can Influence Initial Post-fire Understory Composition in a Mixed Conifer Forest, Sequoia National Park, California', *Natural Areas Journal*, 29(2), pp. 126–132. Available at: https://doi.org/10.3375/043.029.0204.

Rothermel, R.C. (1972) 'A Mathematical Model for Predicting Fire Spread in Wildland Fuels', *Research Paper INT-115*. Ogden, UT: USDA Forest Service, Intermountain Forest and Range Experiment Station. Available at: https://www.fs.usda.gov/research/treesearch/32533.

Safford, H.D. and Stevens, J.T. (2017) ‘Natural Range of Variation (NRV) for yellow pine and mixed conifer forests in the bioregional assessment area, including the Sierra Nevada, southern Cascades, and Modoc and Inyo National Forests’, *Gen. Tech. Rep. PSW-GTR-2562*. Alvany, CA: USDA Forest Service, Pacific Southwest Research Station. 229 p. Available at: https://doi.org/10.2737/PSW-GTR-256

Sandberg, D. V., Ottmar, R.D. and Cushon, G.H. (2001) ‘Characterizing fuels in the 21st century’, *International Journal Of Wildland Fire*, 10(4), pp. 381–387. Available at: https://doi.org/10.1071/WF01036.

Sandberg, D. V., Riccardi, C.L. and Schaaf, M.D. (2007) ‘Reformulation of Rothermel’s wildland fire behaviour model for heterogeneous fuelbeds’, *Canadian Journal of Forest Research*, 37(12), pp. 2438–2455. Available at: https://doi.org/10.1139/X07-094.

Schaedel, M.S., Larson, A.J., Weisbrod, C.J. and Keane, R.E. (2017) ‘Density-dependent woody detritus accumulation in an even-aged, single-species forest’, *Canadian Journal of Forest Research*, 47(9), pp. 1215–1221. Available at: https://doi.org/10.1139/cjfr-2017-0129.

Schubert, G.H. (1956) 'Effect of fertilizer on cone production of sugar pine', *Res. Note 116*. Berkeley, CA: USDA Forest Service, California Forest and Range Experiment Station. 4 p. Available at: https://www.fs.usda.gov/psw/pubs/60127

Schwilk, D.W., Keeley, J.E., Knapp, E.E., McIver, J., Bailey, J.D., Fettig, C.J., Fiedler, C.E., Harrod, R.J., Moghaddas, J.J., Outcalt, K.W., Skinner, C.N., Stephens, S.L., Waldrop, T.A., Yaussy, D.A. and Youngblood, A. (2009) ‘The national Fire and Fire Surrogate study: effects of fuel reduction methods on forest vegetation structure and fuels’, *Ecological Applications*, 19(March), pp. 285–304. Available at: https://doi.org/10.1890/07-1747.1.

Schwilk, D.W. and Ackerly, D.D. (2001) ‘Flammability and Serotiny as Strategies: Correlated Evolution in Pines’, *Oikos*, 94(2), pp. 326–336. Available at: https://www.jstor.org/stable/3547577

Scott, J.H. and Burgan, R.E. (2005) ‘Standard fire behavior fuel models: A comprehensive set for use with Rothermel’s surface fire spread model’, *RMRS-GTR-153*. Fort Collins, CO: USDA Forest Service, Rocky Mountain Research Station. 72 p. Available at: https://doi.org/10.2737/RMRS-GTR-153.

Shive, K.L., Preisler, H.K., Welch, K.R., Safford, H.D., Butz, R.J., O’Hara, K.L. and Stephens, S.L. (2018) ‘From the stand scale to the landscape scale: predicting the spatial patterns of forest regeneration after disturbance’, *Ecological Applications*, 28(6), pp. 1626–1639. Available at: https://doi.org/10.1002/eap.1756.

Shriver, R.K., Andrews, C.M., Arkle, R.S., Barnard, D.M., Duniway, M.C., Germino, M.J., Pilliod, D.S., Pyke, D.A., Welty, J.L. and Bradford, J.B. (2019) ‘Transient population dynamics impede restoration and may promote ecosystem transformation after disturbance’, *Ecology Letters*, 22(9), pp. 1357–1366. Available at: https://doi.org/10.1111/ele.13291.

Shriver, R.K., Yackulic, C.B., Bell, D.M. and Bradford, J.B. (2021) ‘Quantifying the demographic vulnerabilities of dry woodlands to climate and competition using range-wide monitoring data’, *Ecology*, 0(0), pp. 1–12. Available at: https://doi.org/10.1002/ecy.3425.

Stan Development Team (2022a) 'Divergent transitions', in *Stan Reference Manual v2.31*. Available at: https://mc-stan.org/docs/reference-manual/divergent-transitions.html.

Stan Development Team (2022b) ‘Stan Modeling Language Users Guide and Reference Manual’. Available at: https://mc-stan.org.

Steel, Z.L., Goodwin, M., Meyer, M., Fricker, G.A., Zald, H. and Hurteau, M.D. (2021a) ‘Do Forest Fuel Reduction Treatments Confer Resistance to Beetle Infestation and Drought Mortality?’, *Ecosphere*, 12(January). Available at: https://doi.org/10.1002/ecs2.3344.

Steel, Z.L., Foster, D.E., Coppoletta, M., Lydersen, J.M., Stephens, S.L., Paudel, A., Markwith, S.H., Merriam, K. and Collins, B.M. (2021b) ‘Ecological resilience and vegetation transition in the face of two successive large wildfires’, *Journal of Ecology*, 109(9), pp. 3340–3355. Available at: https://doi.org/10.1111/1365-2745.13764.

Steel, Z.L., Safford, H.D. and Viers, J.H. (2015) ‘The fire frequency-severity relationship and the legacy of fire suppression in California forests’, *Ecosphere*, 6(1), pp. 1-23. Available at: https://doi.org/10.1890/ES14-00224.1.

Stephens, S.L., Moghaddas, J.J., Edminster, C., Fiedler, C.E., Haase, S., Harrington, M., Keeley, J.E., Knapp, E.E., McIver, J.D., Metlen, K., Skinner, C.N. and Youngblood, A. (2009) ‘Fire Treatment Effects on Vegetation Structure, Fuels, and Potential Fire Severity in Western U.S. Forests’, *Ecological Applications*, 19(2), pp. 305–320. Available at: https://doi.org/10.1890/07-1755.1.

Stephens, S.L., McIver, J.D., Boerner, R.E.J., Fettig, C.J., Fontaine, J.B., Hartsough, B.R., Kennedy, P.L. and Schwilk, D.W. (2012) ‘The Effects of Forest Fuel-Reduction Treatments in the United States’, *Bioscience*, 62(6), pp. 549–560. Available at: https://doi.org/10.1525/bio.2012.62.6.6.

Stephens, S.L., Lydersen, J., Collins, B.M. and Fry, D. (2015) ‘Historical and current landscape-scale ponderosa pine and mixed conifer forest structure in the Southern Sierra Nevada’, *Ecosphere*, 6(May), pp. 1–63. Available at: https://doi.org/10.1890/ES14-00379.1.

Stephens, S.L., Collins, B.M., Fettig, C.J., Finney, M.A., Hoffman, C.M., Knapp, E.E., North, M.P., Safford, H. and Wayman, R.B. (2018) ‘Drought, Tree Mortality, and Wildfire in Forests Adapted to Frequent Fire’, *BioScience*, 68(2), pp. 77–88. Available at: https://doi.org/10.1093/biosci/bix146.

Stephens, S.L. and Collins, B.M. (2004) ‘Fire regimes of mixed conifer forests in the north-central Sierra Nevada at multiple spatial scales’, *Northwest Science*, 78(1), pp. 12–23.

Stephens, S.L. and Finney, M.A. (2002) ‘Prescribed fire mortality of Sierra Nevada mixed conifer tree species: Effects of crown damage and forest floor combustion’, *Forest Ecology and Management*, 162(2–3), pp. 261–271. Available at: https://doi.org/10.1016/S0378-1127(01)00521-7.

Stephens, S.L. and Moghaddas, J.J. (2005a) ‘Experimental fuel treatment impacts on forest structure, potential fire behavior, and predicted tree mortality in a California mixed conifer forest’, *Forest Ecology and Management*, 215(1–3), pp. 21–36. Available at: https://doi.org/10.1016/j.foreco.2005.03.070.

Stephens, S.L. and Moghaddas, J.J. (2005b) ‘Silvicultural and reserve impacts on potential fire behavior and forest conservation: Twenty-five years of experience from Sierra Nevada mixed conifer forests’, *Biological Conservation*, 125(3), pp. 369–379. Available at: https://doi.org/10.1016/j.biocon.2005.04.007.

Stephenson, N.L. (1998) ‘Actual evapotranspiration and deficit: Biologically meaningful correlates of vegetation distribution across spatial scales’, *Journal of Biogeography*, 25(5), pp. 855–870. Available at: https://doi.org/10.1046/j.1365-2699.1998.00233.x.

Stephenson, N.L., Das, A.J., Ampersee, N.J., Cahill, K.G., Caprio, A.C., Sanders, J.E. and Williams, A.P. (2018) ‘Patterns and correlates of giant sequoia foliage dieback during California’s 2012–2016 hotter drought’, *Forest Ecology and Management*, 419–420(November 2017), pp. 268–278. Available at: https://doi.org/10.1016/j.foreco.2017.10.053.

Stephenson, N.L., Das, A.J., Ampersee, N.J., Bulaon, B.M. and Yee, J.L. (2019) ‘Which trees die during drought? The key role of insect host-tree selection’, *Journal of Ecology*, 107(5), pp. 2383–2401. Available at: https://doi.org/10.1111/1365-2745.13176.

Stevens, J.T., Collins, B.M., Miller, J.D., North, M.P. and Stephens, S.L. (2017) ‘Changing spatial patterns of stand-replacing fire in California conifer forests’, *Forest Ecology and Management*, 406(August), pp. 28–36. Available at: https://doi.org/10.1016/j.foreco.2017.08.051.

Stewart, J.A.E., van Mantgem, P.J., Young, D.J.N., Shive, K.L., Preisler, H.K., Das, A.J., Stephenson, N.L., Keeley, J.E., Safford, H.D., Wright, M.C., Welch, K.R. and Thorne, J.H. (2021) ‘Effects of postfire climate and seed availability on postfire conifer regeneration’, *Ecological Applications*, 31(3), pp. 1–14. Available at: https://doi.org/10.1002/eap.2280.

Taylor, A.H., Vandervlugt, A.M., Maxwell, R.S., Beaty, R.M., Airey Lauvaux, C. and Skinner, C.N. (2014) ‘Changes in forest structure, fuels and potential fire behaviour since 1873 in the Lake Tahoe Basin, USA’, *Applied Vegetation Science*, 17(1), pp. 17–31. Available at: https://doi.org/10.1111/avsc.12049.

Tennekes, M. (2018) ‘Tmap: Thematic maps in R’, *Journal of Statistical Software*, 84(6). Available at: https://doi.org/10.18637/jss.v084.i06.

Thaxton, J.M. and Platt, W.J. (2006) ‘Small-scale fuel variation alters fire intensity and shrub abundance in a pine savanna’, *Ecology*, 87(5), pp. 1331–1337. Available at: https://doi.org/10.1890/0012-9658(2006)87[1331:SFVAFI]2.0.CO;2.

Thayer, T.C., Wall, S.B. Vander, Journal, S. and Mar, N. (2005) ‘Interactions between Steller’s Jays and Yellow Pine Chipmunks over Scatter-Hoarded Sugar Pine Seeds’, *Journal of Animal Ecology*, 74(2), pp. 365–374. Available at: https://www.jstor.org/stable/3505625.

Tomback, D.F. and Achuff, P. (2010) ‘Blister rust and western forest biodiversity: Ecology, values and outlook for white pines’, *Forest Pathology*, 40(3–4), pp. 186–225. Available at: https://doi.org/10.1111/j.1439-0329.2010.00655.x.

Tsujino, R., Yumoto, T., Kitamura, S., Djamaluddin, I. and Darnaedi, D. (2016) ‘History of forest loss and degradation in Indonesia’, *Land Use Policy*, 57, pp. 335–347. Available at: https://doi.org/10.1016/j.landusepol.2016.05.034.

Ucitel, D., Christian, D.P. and Graham, J.M. (2003) ‘Vole Use of Coarse Woody Debris and Implications for Habitat and Fuel Management’, *The Journal of Wildlife Management*, 67(1), pp. 65–72. Available at: http://www.jstor.org/stable/3803.

USDA Forest Service (2009) ‘Vegetation Descriptions: South Sierran Ecological Province’, pp. 1–24. Available at: https://www.fs.usda.gov/Internet/FSE_DOCUMENTS/fsbdev3_046270.pdf.

Vakili, E., Hoffman, C.M., Keane, R.E., Tinkham, W.T. and Dickinson, Y. (2016a) ‘Spatial variability of surface fuels in treated and untreated ponderosa pine forests of the southern Rocky Mountains’, *International Journal of Wildland Fire*, 25(11), pp. 1156–1168. Available at: https://doi.org/10.1071/WF16072.

Vakili, E., Hoffman, C.M. and Keane, R.E. (2016b) ‘Fine woody fuel particle diameters for improved planar intersect fuel loading estimates in Southern Rocky Mountain ponderosa pine forests’, *International Journal of Wildland Fire*, 25(7), pp. 780–784. Available at: https://doi.org/10.1071/WF15029.

Vanderwel, M.C., Zeng, H., Caspersen, J.P., Kunstler, G. and Lichstein, J.W. (2016) ‘Demographic controls of aboveground forest biomass across North America’, *Ecology Letters*, 19(4), pp. 414–423. Available at: https://doi.org/10.1111/ele.12574.

van Mantgem, P.J., Stephenson, N.L., Knapp, E., Battles, J. and Keeley, J.E. (2011) ‘Long-term effects of prescribed fire on mixed conifer forest structure in the Sierra Nevada, California’, *Forest Ecology and Management*, 261(6), pp. 989–994. Available at: https://doi.org/10.1016/j.foreco.2010.12.013.

van Mantgem, P.J., Caprio, A.C., Stephenson, N.L. and Das, A.J. (2016) ‘Does Prescribed Fire Promote Resistance To Drought in Low Elevation Forests of the Sierra Nevada, California, USA?’, *Fire Ecology*, 12(1), pp. 5–15. Available at: https://doi.org/10.4996/fireecology.1201013.

van Mantgem, P.J., Falk, D.A., Williams, E.C., Das, A.J. and Stephenson, N.L. (2018) ‘Pre-fire drought and competition mediate post-fire conifer mortality in western U.S. National Parks’, *Ecological Applications*, 28(7), pp. 1730–1739. Available at: https://doi.org/10.1002/eap.1778.

van Mantgem, P.J., Stephenson, N.L., Keifer, M.B. and Keeley, J. (2004) ‘Effects of an introduced pathogen and fire exclusion on the demography of sugar pine’, *Ecological Applications*, 14(5), pp. 1590–1602. Available at: https://doi.org/10.1890/03-5109.

van Mantgem, P.J., Falk, D.A., Williams, E.C., Das, A.J. and Stephenson, N.L. (2020) 'The influence of pre-fire growth patterns on post-fire tree mortality for common conifers in western US parks', *International Journal of Wildland Fire*, 29(6), pp. 513–518. Available at: https://doi.org/10.1071/WF19020.

van Mantgem, P.J. and Stephenson, N.L. (2007) 'Apparent climatically induced increase of tree mortality rates in a temperate forest', *Ecology Letters*, 10(10), pp. 909–916. Available at: https://doi.org/10.1111/j.1461-0248.2007.01080.x.

van Mantgem, P.J., Stephenson, N.L. and Keeley, J.E. (2006) 'Forest reproduction along a climatic gradient in the Sierra Nevada, California', *Forest Ecology and Management*, 225(1–3), pp. 391–399. Available at: https://doi.org/10.1016/j.foreco.2006.01.015.

van Wagner, C.E. (1982) 'Practical aspects of the line intersect method', *Information Report PI-X-12E*. Fredericton, New Brunswick: Canadian Forestry Service, Maritimes Forest Research Centre. 11 p. Available at: https://cfs.nrcan.gc.ca/publications?id=6862.

van Wagtendonk, J.W., Benedict, J.M. and Sydoriak, W.M. (1996) 'Physical properties of woody fuel particles of Sierra Nevada conifers', *International Journal of Wildland Fire*, 6(3), pp. 117–123. Available at: https://doi.org/10.1071/WF9960117.

van Wagtendonk, J.W., Benedict, J.M. and Sydoriak, W.M. (1998) 'Fuel bed characteristics of Sierra Nevada conifers', *Western Journal of Applied Forestry*, 13(3), pp. 73–84. Available at: https://doi.org/10.1093/wjaf/13.3.73

Vegetation Classification and Mapping (2022) *USDA Forest Service Region 5*. Available at: https://www.fs.usda.gov/detail/r5/landmanagement/resourcemanagement/?cid=stelprdb5347192 (Accessed: 11 February 2022).

Vehtari, A., Gelman, A., Simpson, D., Carpenter, B. and Burkner, P.C. (2021) 'Rank-Normalization, Folding, and Localization: An Improved (Formula presented) for Assessing Convergence of MCMC (with Discussion)', *Bayesian Analysis*, 16(2), pp. 667–718. Available at: https://doi.org/10.1214/20-BA1221.

Vilanova, E., Mortonson, L.A., Cox, L.E., Bulaon, B.M., Lydersen, J.M., Fettig, C.J., Battles, J.J. and Axelson, J.N. (in review) 'Characterizing ground and surface fuels across Sierra Nevada forests shortly after the 2012-2016 drought', *Forest Ecology and Management*, In review.

Voelker, S.L., Merschel, A.G., Meinzer, F.C., Ulrich, D.E.M., Spies, T.A. and Still, C.J. (2019) 'Fire deficits have increased drought sensitivity in dry conifer forests: Fire frequency and tree-ring carbon isotope evidence from Central Oregon', *Global Change Biology*, 25(4), pp. 1247–1262. Available at: https://doi.org/10.1111/gcb.14543.

Wayman, R.B. and Safford, H.D. (2021) 'Recent bark beetle outbreaks influence wildfire severity in mixed-conifer forests of the Sierra Nevada, California, USA', *Ecological Applications*, 31(3), pp. 1–19. Available at: https://doi.org/10.1002/eap.2287.

Weise, D.R. and Wright, C.S. (2014) ‘Wildland fire emissions, carbon and climate: Characterizing wildland fuels’, *Forest Ecology and Management*, 317, pp. 26–40. Available at: https://doi.org/10.1016/j.foreco.2013.02.037.

Werner, C.M., Harrison, S.P., Safford, H.D., Bohlman, G.N. and Serata, R. (2021) *Extreme pre-fire drought decreases shrub regeneration on fertile soils*, *Ecological Applications*. Available at: https://doi.org/10.1002/eap.2464.

Westerling, A.L., Hidalgo, H.G., Cayan, D.R. and Swetnam, T.W. (2006) ‘Warming and earlier spring increase Western U.S. forest wildfire activity’, *Science*, 313(5789), pp. 940–943. Available at: https://doi.org/10.1126/science.1128834.

Westerling, A.L., Bryant, B.P., Preisler, H.K., Holmes, T.P., Hidalgo, H.G., Das, T. and Shrestha, S.R. (2011) ‘Climate change and growth scenarios for California wildfire’, *Climatic Change*, 109, pp. 445–463. Available at: https://doi.org/10.1007/s10584-011-0329-9.

White, P.S. (1979) ‘Pattern, process, and natural disturbance in vegetation’, *The Botanical Review*, 45(3), pp. 229–299. Available at: https://doi.org/10.1007/BF02860857.

White, P.S. and Pickett, S.T.A. (1985) ‘Natural Disturbance and Patch Dynamics: An Introduction’, in *The Ecology of Natural Disturbance and Patch Dynamics*. Acadameic Press, Inc., pp. 3–13. Available at: https://doi.org/10.1016/b978-0-12-554520-4.50006-x.

Wickham, H., Averick, M., Bryan, J., Chang, W., McGowan, L.D., Francois, R., Grolemund, G., Hayes, A., Henry, L., Hester, J., Kuhn, M., Pedersen, T.L., Miller, E., Bache, S.M., Müller, K., Ooms, J., Robinson, D., Seidel, D.P., Spinu, V., Takahashi, K., Vaughan, D., Wilke, C., Woo, K., and Yutani, H. (2019) ‘Welcome to the Tidyverse’, *Journal of Open Source Software*, 4(43), p. 1686. Available at: https://doi.org/10.21105/joss.01686.

Wiggers, M.S., Kirkman, L.K., Boyd, R.S. and Hiers, J.K. (2013) ‘Fine-scale variation in surface fire environment and legume germination in the longleaf pine ecosystem’, *Forest Ecology and Management*, 310, pp. 54–63. Available at: https://doi.org/10.1016/j.foreco.2013.07.030.

Wilke, C.O. (2020) ‘cowplot: Streamline Plot Theme and Plot Annotations for “ggplot2”’. Available at: https://cran.r-project.org/package=cowplot.

Williamson, G.B. and Black, E.M. (1981) ‘High temperature of forest fires under pines as a selective advantage over oaks’, *Nature*, 293(5834), pp. 643–644. Available at: https://doi.org/10.1038/293643a0.

Woodall, C.W. and Graham, J.M. (2004) ‘A technique for conducting point pattern analysis of cluster plot stem-maps’, *Forest Ecology and Management*, 198(1–3), pp. 31–37. Available at: https://doi.org/10.1016/j.foreco.2004.03.037.

Woodall, C.W. and Monleon, V.J. (2008) ‘Sampling protocol, estimation, and analysis procedures for the down woody materials indicator of the FIA Program’, *GTR-NRS-22*. Newton Square, PA: USDA Forest Service, Northern Research Station. 68 p. Available at: https://doi.org/10.2737/NRS-GTR-22

Yeaton, R.I. (1983) ‘The Successional Replacement of Ponderosa Pine by Sugar Pine in the Sierra Nevada’, *Bulletin of the Torrey Botanical Club*, 110(3), pp. 292–297. Available at: https://doi.org/10.2307/2996181

Yeaton, R.I. (1984) ‘Aspects of the Population Biology of Sugar Pine (Pinus lambertiana Dougl.) on an Elevational Gradient in the Sierra Nevada of Central California’, *The American Midland Naturalist*, 111(1), pp. 126–137. Available at: https://www.jstor.org/stable/2425550.

York, R.A., Heald, R.C., Battles, J.J. and York, J.D. (2004) ‘Group selection management in conifer forests: Relationships between opening size and tree growth’, *Canadian Journal of Forest Research*, 34(3), pp. 630–641. Available at: https://doi.org/10.1139/x03-222.

York, R.A., Battles, J.J., Wenk, R.C. and Saah, D. (2012) ‘A gap-based approach for regenerating pine species and reducing surface fuels in multi-aged mixed conifer stands in the Sierra Nevada, California’, *Forestry*, 85(2), pp. 203–213. Available at: https://doi.org/10.1093/forestry/cpr058.

York, R.A., Noble, H., Quinn-Davidson, L.N. and Battles, J.J. (2021) ‘Pyrosilviculture: Combining prescribed fire with gap-based silviculture in mixed-conifer forests of the sierra nevada’, *Canadian Journal of Forest Research*, 51(6), pp. 781–791. Available at: https://doi.org/10.1139/cjfr-2020-0337.

York, R.A., Russell, K.W. and Noble, H. (2022) ‘Merging prescribed fires and timber harvests in the Sierra Nevada: Burn season and pruning influences in young mixed conifer stands’, *Trees, Forests and People*, 9(April), p. 100309. Available at: https://doi.org/10.1016/j.tfp.2022.100309.

Young, D.J.N., Stevens, J.T., Earles, J.M., Moore, J., Ellis, A., Jirka, A.L. and Latimer, A.M. (2017) ‘Long-term climate and competition explain forest mortality patterns under extreme drought’, *Ecology Letters*, 20(1), pp. 78–86. Available at: https://doi.org/10.1111/ele.12711.

Zhang, Y. (2013) 'Likelihood-based and Bayesian methods for Tweedie compound Poisson linear mixed models', *Statistical Computing,* 23, pp. 743-757. Available at: https://doi.org/10.1007/s11222-012-9343-7.

Ziegler, J.P., Hoffman, C., Battaglia, M. and Mell, W. (2017) ‘Spatially explicit measurements of forest structure and fire behavior following restoration treatments in dry forests’, *Forest Ecology and Management*, 386, pp. 1–12. Available at: https://doi.org/10.1016/j.foreco.2016.12.002.

12 SUPPLEMENTARY MATERIALS FOR “QUANTIFYING FINE-SCALE HETEROGENEITY IN WILDLAND FUELS”

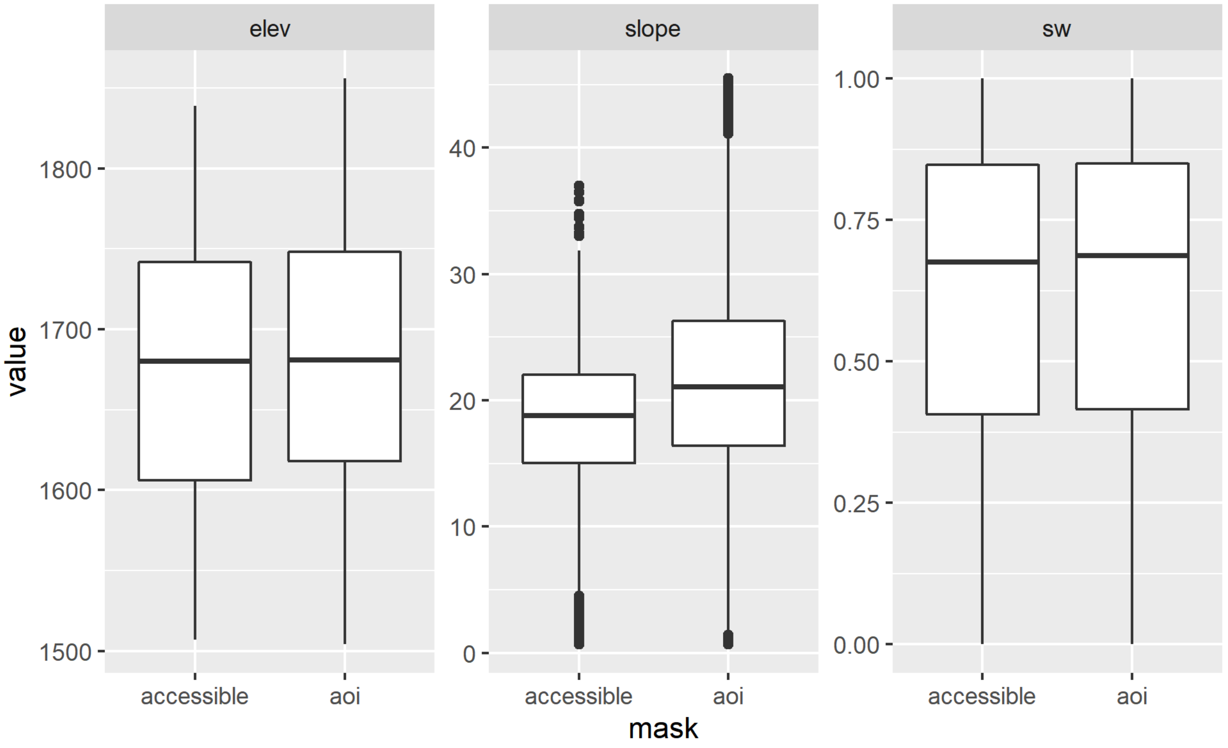

Supplementary Figure 1: Comparison of elevation, slope, and southwestness index between the entire area of interest (CALVEG-mapped mixed conifer forest (pine) vegetation type between 1,500 and 1,850 m elevation in the vicinity of Crystal Cave Road in Sequoia National Park) and the subset of the area of interest which was accessible for sampling purposes (< 25° slopes and located 50-600 m from a road or trail). Histograms are of pixel values for topographic rasters derived from a 30.7 x 30.6 m resolution DEM. The distribution of topographic characteristics within the accessible area is very similar to the distribution of topographic characteristics within the entire area of interest, except that the accessible area has lower slopes on average. The pixels from the accessible area with a slope greater than 25 degrees were included because of edge artifacts when converting between raster and vector data types.

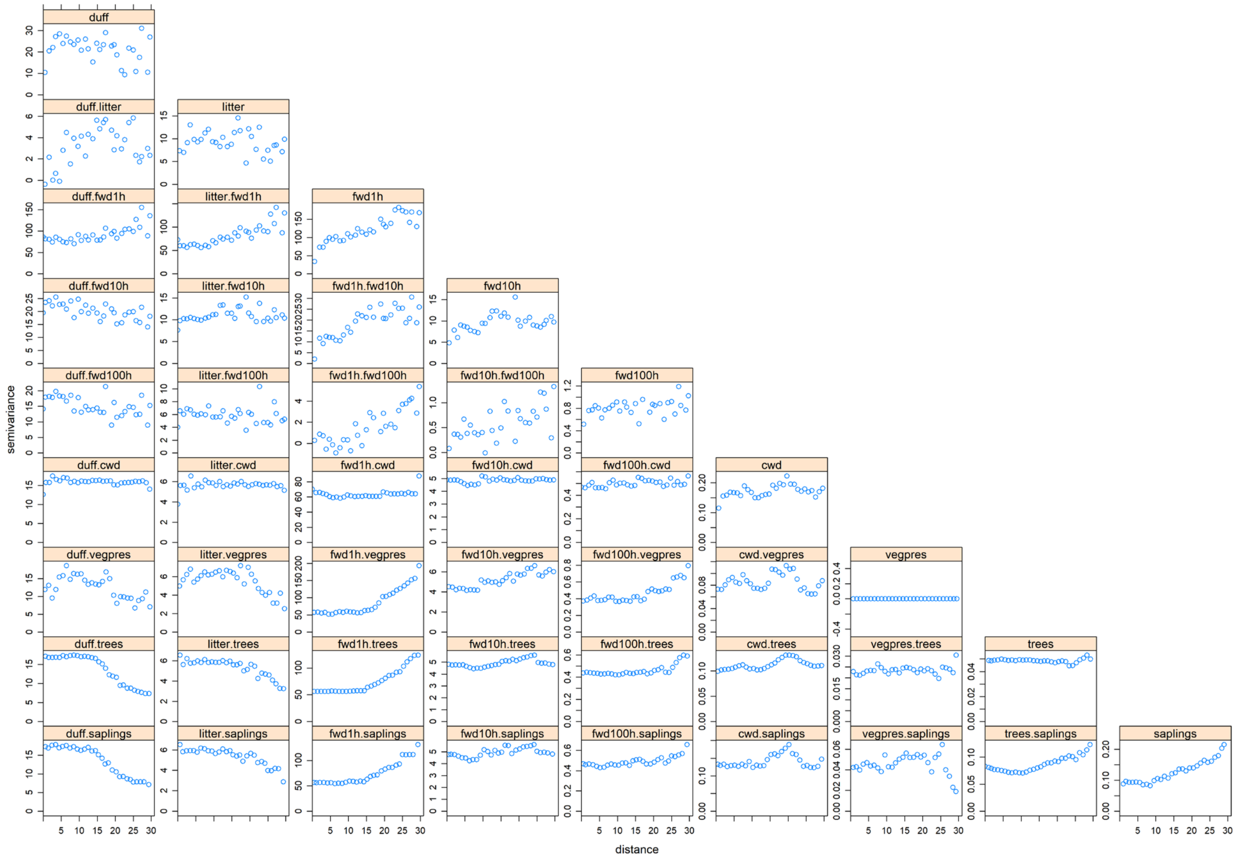

Supplementary Figure 2: Sample variograms for data from plots with low drought mortality. In each panel, the pairwise distance between observations (in meters) is on the x-axis and the semi-variance between observations at that distance (in 1-meter distance bins) is plotted on the y-axis. Increases in the semi-variance between observations as the distance between them increases are evidence of spatial autocorrelation. The variograms become noisier for distances above ~10m for which there are fewer pairs of observations. The diagonal panels show the variograms within each fuel component (spatial autocorrelation), and the off-diagonal panels show the cross-variograms between different fuel components (spatial cross-correlation). There is clear evidence of spatial autocorrelation for all fuel components except litter, vegetation presence, and trees, for which the variograms are ambiguous. There is noisy evidence of spatial cross correlation between duff and litter, between 1-hour and 100-hour fine woody debris, and between 10-hour and 100-hour fine woody debris. There is clear evidence of spatial cross correlation between 1-hour and 10-hour fine woody debris.

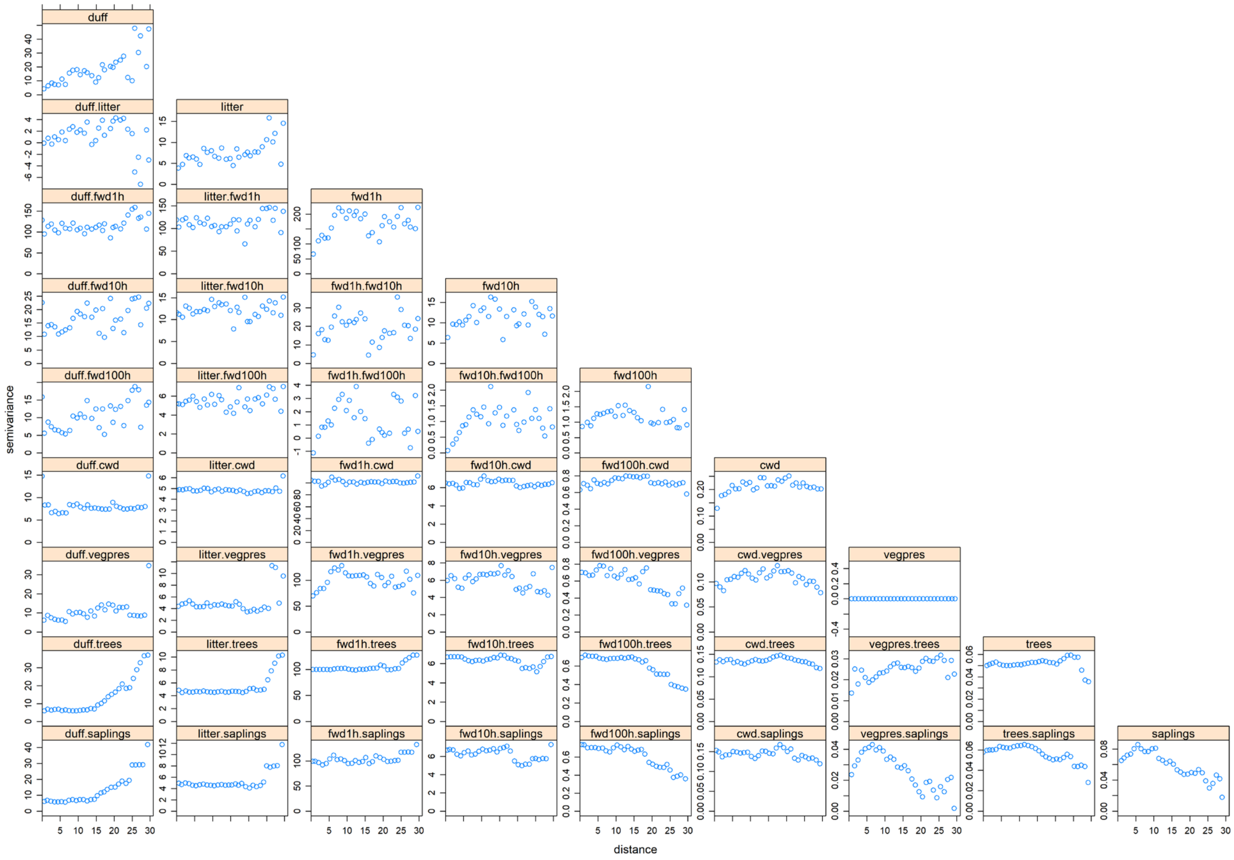

Supplementary Figure 3: Sample variograms for data from plots with medium drought mortality. In each panel, the pairwise distance between observations (in meters) is on the x-axis and the semi-variance between observations at that distance (in 1-meter distance bins) is plotted on the y-axis. Increases in the semi-variance between observations as the distance between them increases are evidence of spatial autocorrelation. The variograms become noisier for distances above ~10m for which there are fewer pairs of observations. The diagonal panels show the variograms within each fuel component (spatial autocorrelation), and the off-diagonal panels show the cross-variograms between different fuel components (spatial cross-correlation). There is clear evidence of spatial autocorrelation for all fuel components except vegetation presence, trees, and saplings. There is noisy evidence of spatial cross correlation between 1-hour and 10-hour fine woody debris and between 1-hour and 100-hour fine woody debris. There is clear evidence of spatial cross correlation between 10-hour and 100-hour fine woody debris, between 1-hour fine woody debris and vegetation presence, and between vegetation presence and saplings.

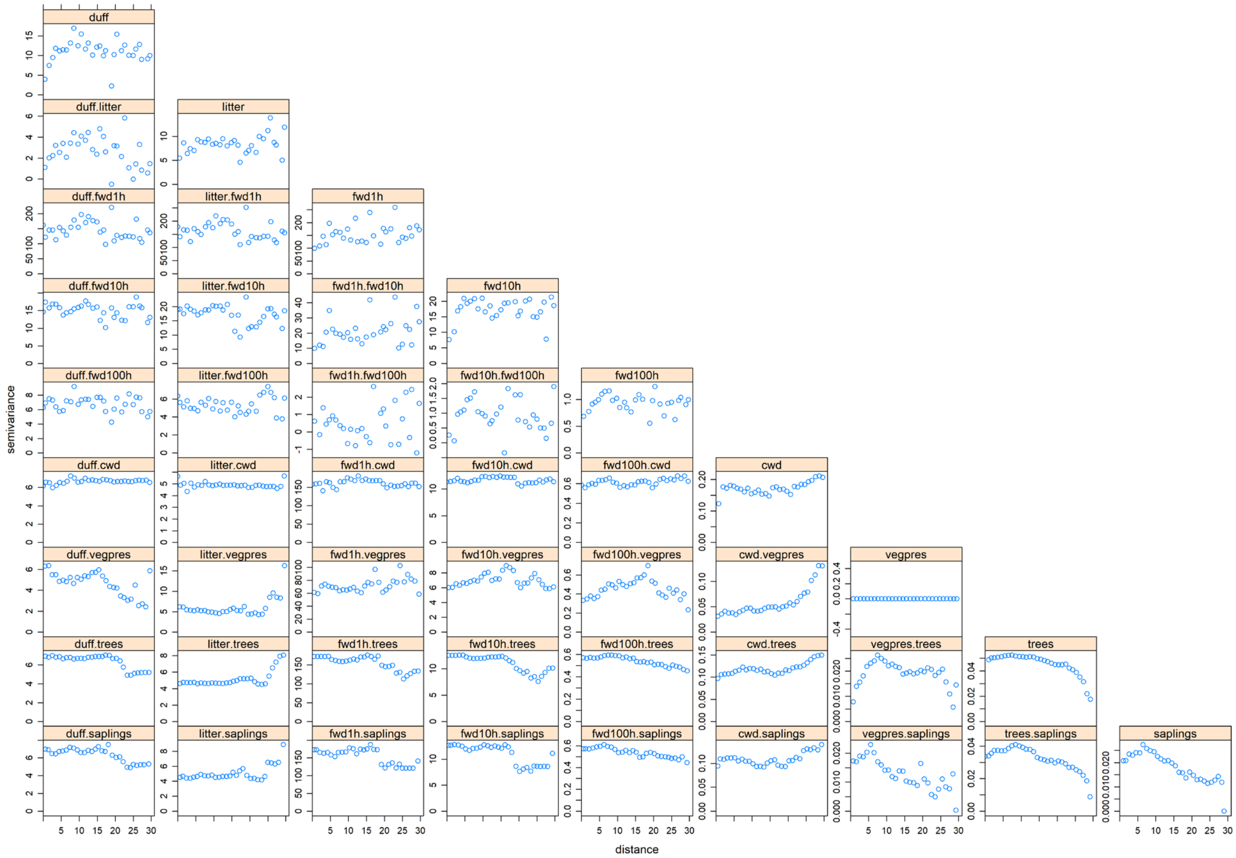

Supplementary Figure 4: Sample variograms for data from plots with high drought mortality. In each panel, the pairwise distance between observations (in meters) is on the x-axis and the semi-variance between observations at that distance (in 1-meter distance bins) is plotted on the y-axis. Increases in the semi-variance between observations as the distance between them increases are evidence of spatial autocorrelation. The variograms become noisier for distances above ~10m for which there are fewer pairs of observations. The diagonal panels show the variograms within each fuel component (spatial autocorrelation), and the off-diagonal panels show the cross-variograms between different fuel components (spatial cross-correlation). There is clear evidence of spatial autocorrelation for all fuel components except litter, for which the variogram is ambiguous, vegetation presences, and tree counts. There is noisy evidence of spatial cross correlation between 1-hour and 10-hour fine woody debris, between 10-hour and 100-hour fine woody debris, between 100-hour fine woody debris and vegetation presences, and between vegetation presences and tree counts. There is clear evidence of spatial cross correlation between duff and litter and between 10-hour fine woody debris and vegetation heights.

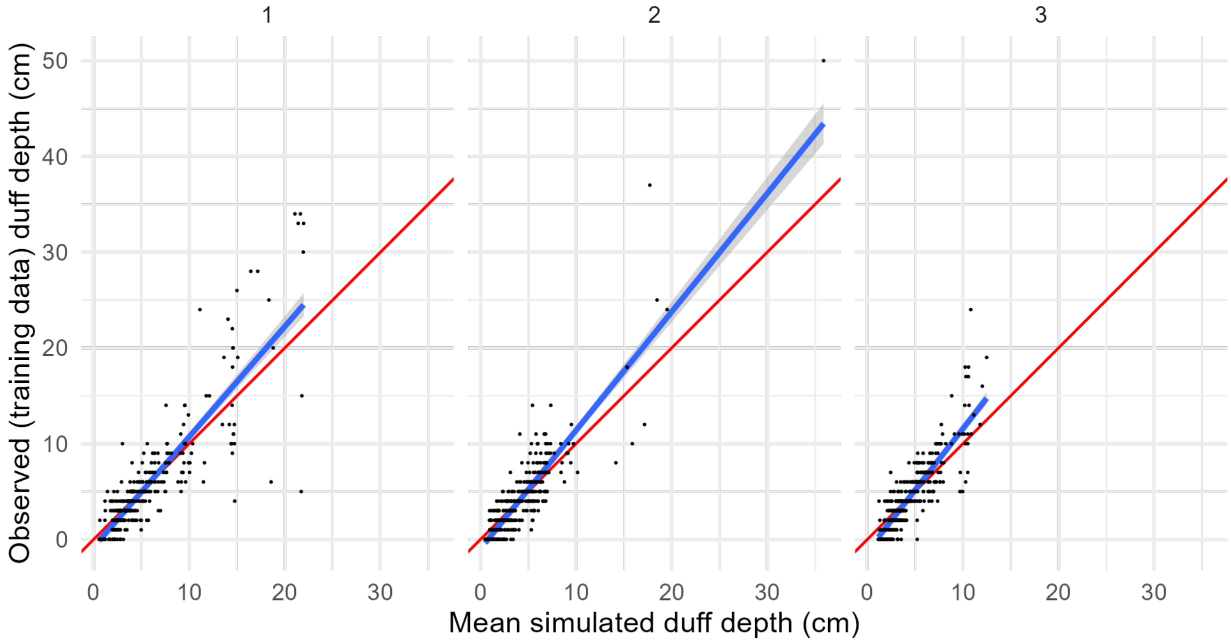

Supplementary Figure 5: Per-observation comparisons of mean predicted and observed values for the training data and the duff depths model. Panels show posterior predictions generated using the posterior parameter values and the training data for each of the three submodels representing low, medium, and high drought mortality (1, 2, and 3, respectively). In each panel, the posterior mean value of simulated duff depth for each observation is on the x-axis, and the observed depth for that observation on the y-axis, with points for each observation in the training dataset. Simulated data are conditional on the posterior samples of random effect realizations. A 1:1 line (representing perfect prediction) is shown in red, and a linear fit between the simulated and observed values shown in blue. There is a generally good but noisy fit between the simulated and observed data, though the model tends to underpredict slightly for higher observed depths and overpredict slightly for lower observed depths.

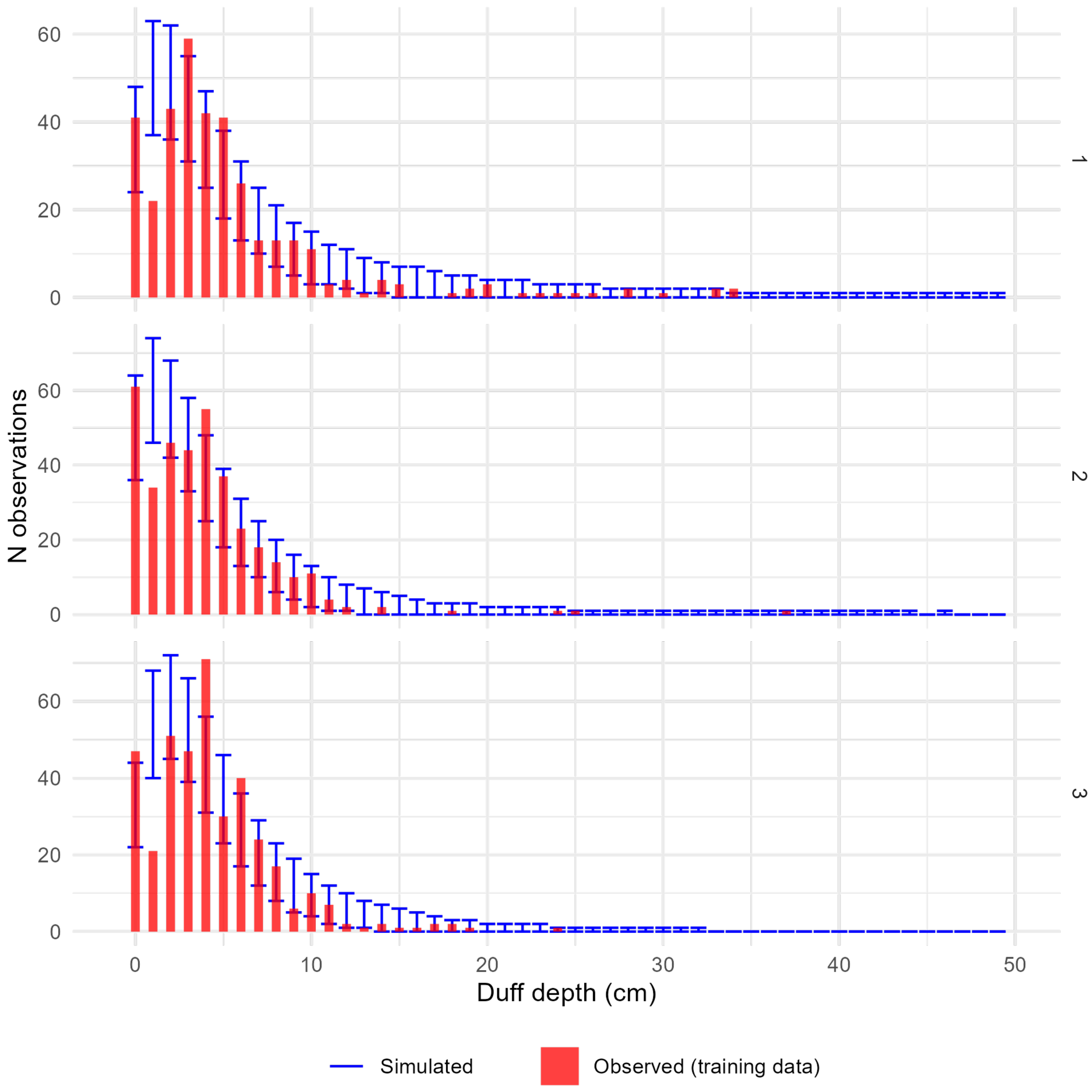

Supplementary Figure 6: Comparison of observed and simulated frequency distributions for the training data and the duff depths model. Panels show posterior predictions generated using the posterior parameter values and the training data for each of the three submodels representing low, medium, and high drought mortality (1, 2, and 3, respectively). In each panel, the x-axis shows an (observed or simulated) depth of duff and the y-axis shows the frequency of samples from a dataset of 1,107 duff depth measurements having that depth (i.e., a histogram). The observed distribution of duff depths is plotted as the red histogram. The error bars within each depth value show the 2.5th and 97.5th percentile of the frequency of simulated samples having that depth value, across each of the 4,000 posterior draws showing the variation in model-predicted frequency distributions. The observed data are generally within the range of behaviors predicted by the model, except that the model appears to underpredict the proportion of 0 cm samples, overpredict the proportion of 1 cm samples, and underpredict the proportion of 3 cm samples. The x-axis has been restricted to improve readability.

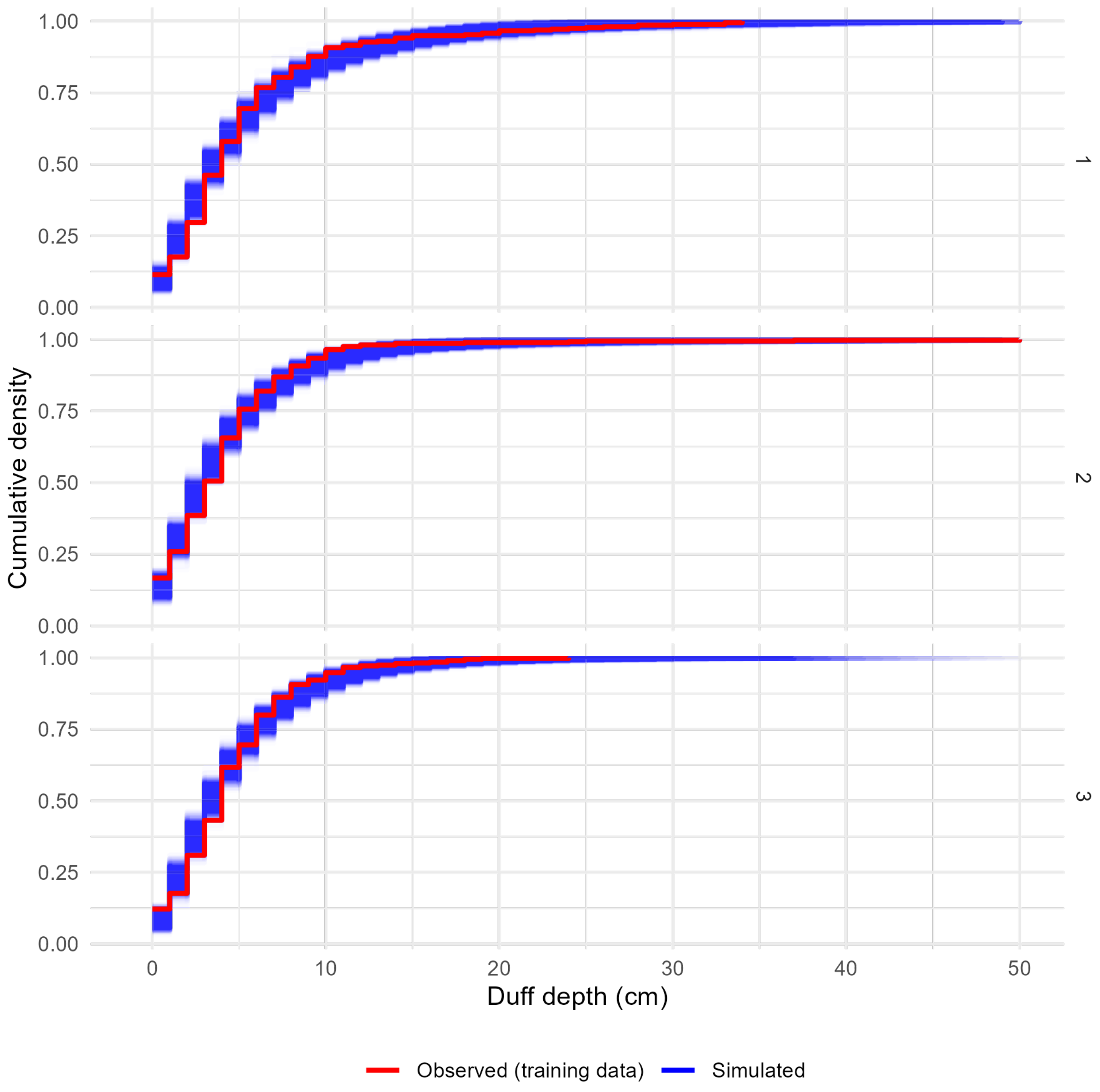

Supplementary Figure 7: Comparison of the observed and simulated cumulative density functions for the training data and the duff depths model. Panels show the cumulative density functions of the observed training data (red) and each of 4,000 simulated datasets generated using posterior parameter values and random effect realizations (blue) for each of the three sub-models corresponding to low, medium, or high levels of drought mortality. The observed cumulative density functions fall within the range of behaviors predicted by the model, indicating good agreement between the model and reality. The x-axis has been restricted for readability.

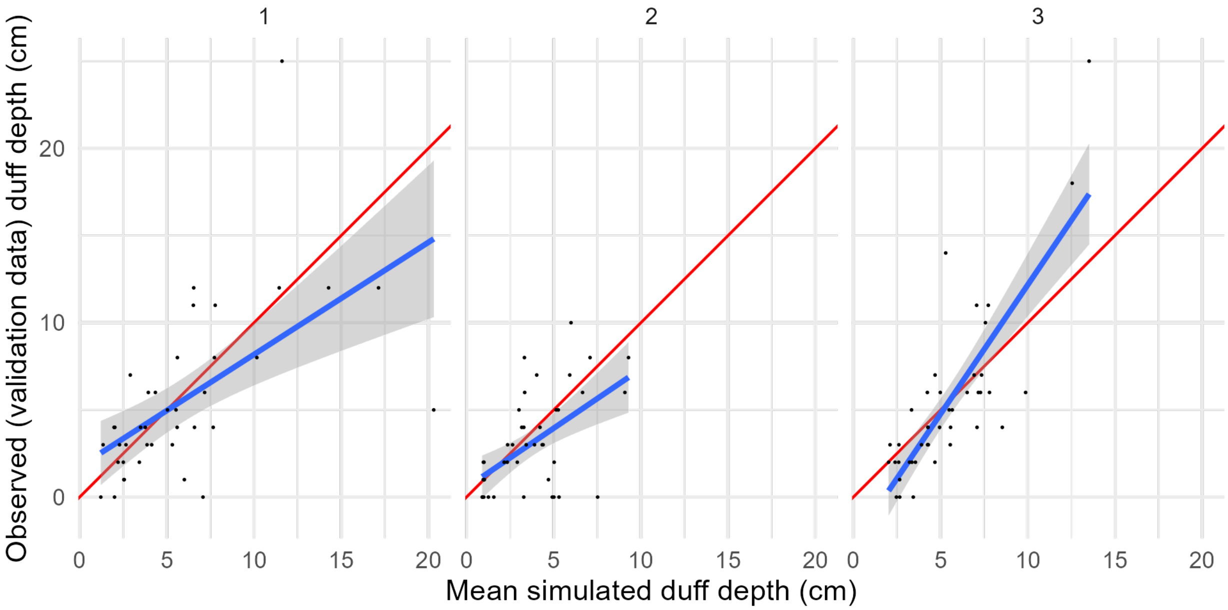

Supplementary Figure 8: Per-observation comparisons of mean predicted and observed values for the validation data and the duff depths model. Panels show posterior predictions generated using the posterior parameter values and the validation data for each of the three submodels representing low, medium, and high drought mortality (1, 2, and 3, respectively). In each panel, the posterior mean value of simulated duff depth for each observation is on the x-axis, and the observed depth for that observation on the y-axis, with points for each observation in the training dataset. Simulated data are conditional on the posterior samples of random effect realizations. A 1:1 line (representing perfect prediction) is shown in red, and a linear fit between the simulated and observed values shown in blue. The relationship between the observed and simulated data has a slope near 1, though the relationship is noisy.

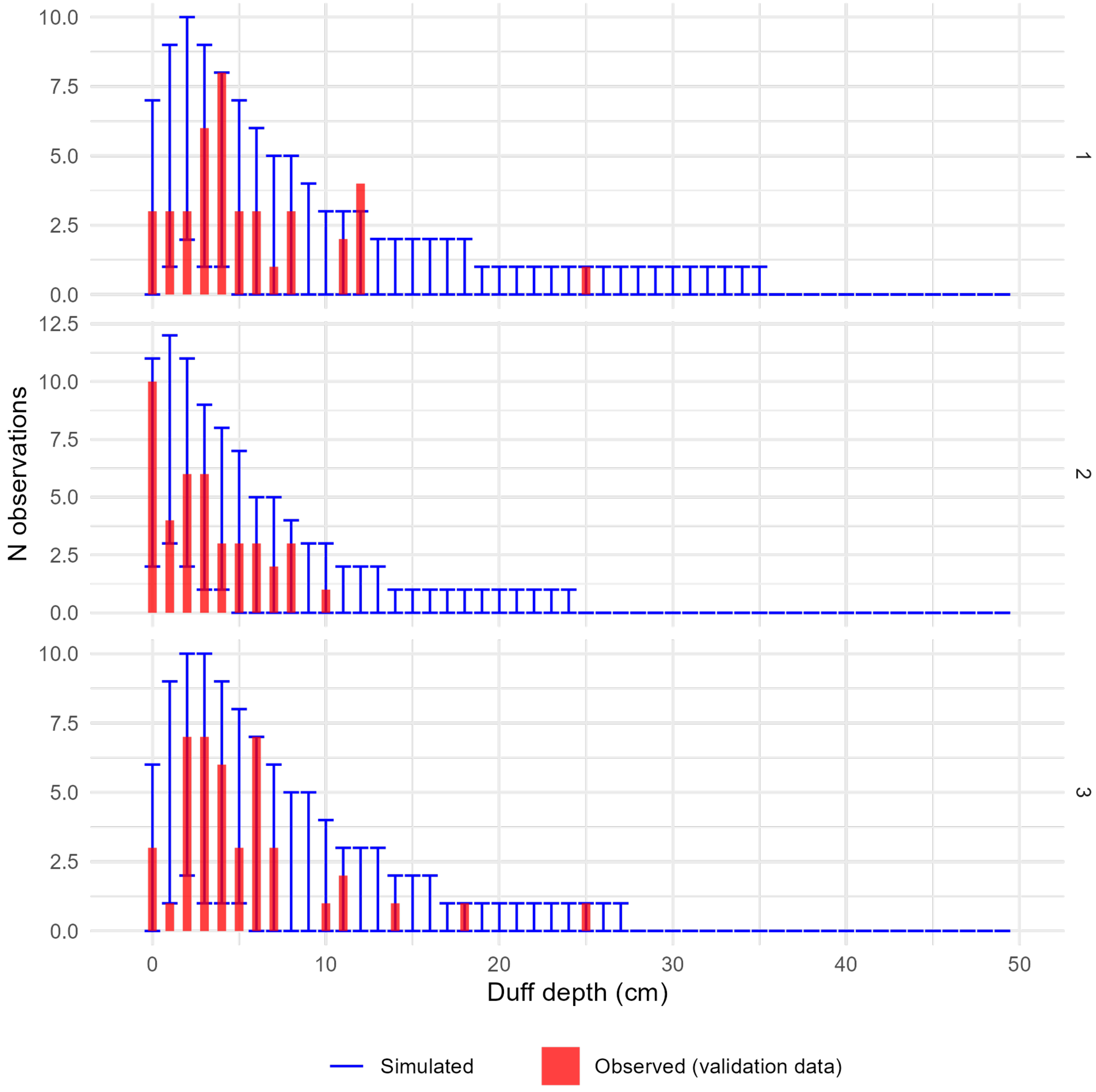

Supplementary Figure 9: Comparison of observed and simulated density distributions for the validation data and the duff depths model. Panels show posterior predictions generated using the posterior parameter values and the validation data for each of the three submodels representing low, medium, and high drought mortality (1, 2, and 3, respectively). In each panel, the x-axis shows an (observed or simulated) depth of duff and the y-axis shows the frequency of samples from a dataset of 124 duff depth measurements having that depth (i.e., a histogram). The observed distribution of duff depths is plotted as the red histogram. The error bars within each depth value show the 2.5th and 97.5th percentile of the frequency of simulated samples having that depth value, across each of the 4,000 posterior draws showing the variation in model-predicted frequency distributions. The x-axis bounds have been limited to improve readability. The observed data are generally within the range of behaviors predicted by the model, though with so few data points the simulated depth distributions are noisy resulting in wide ranges for the proportion of samples falling in each bin.

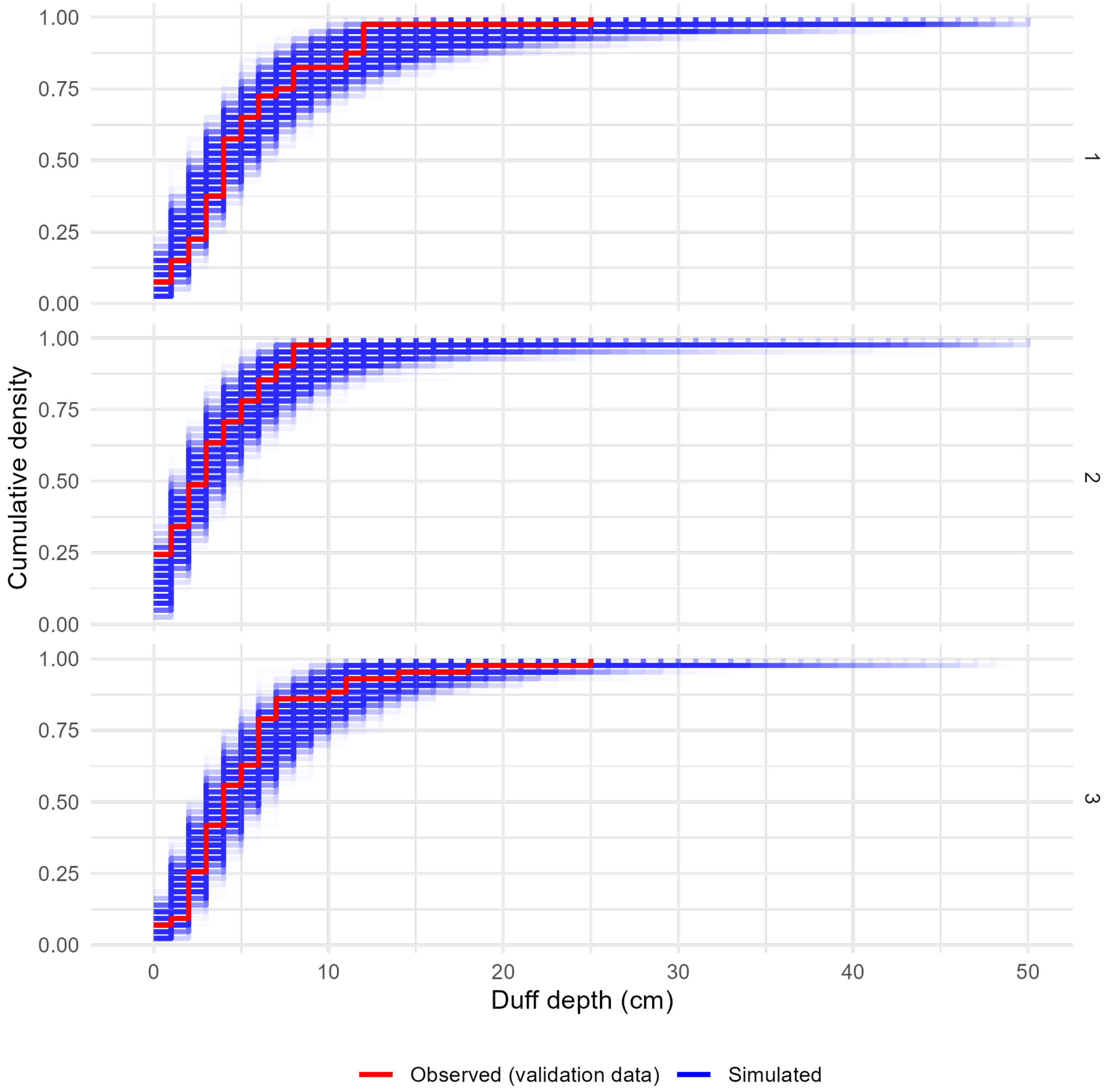

Supplementary Figure 10: Comparison of the observed and simulated cumulative density functions for the validation data and the duff depths model. Panels show the cumulative density functions of the observed validation data (red) and each of 4,000 simulated datasets generated using posterior parameter values and random effect realizations (blue) for each of the three sub-models corresponding to low, medium, or high levels of drought mortality. The x-axis bounds have been limited to improve readability. The observed cumulative density functions fall within the range of behaviors predicted by the model, indicating good agreement between the model and reality.

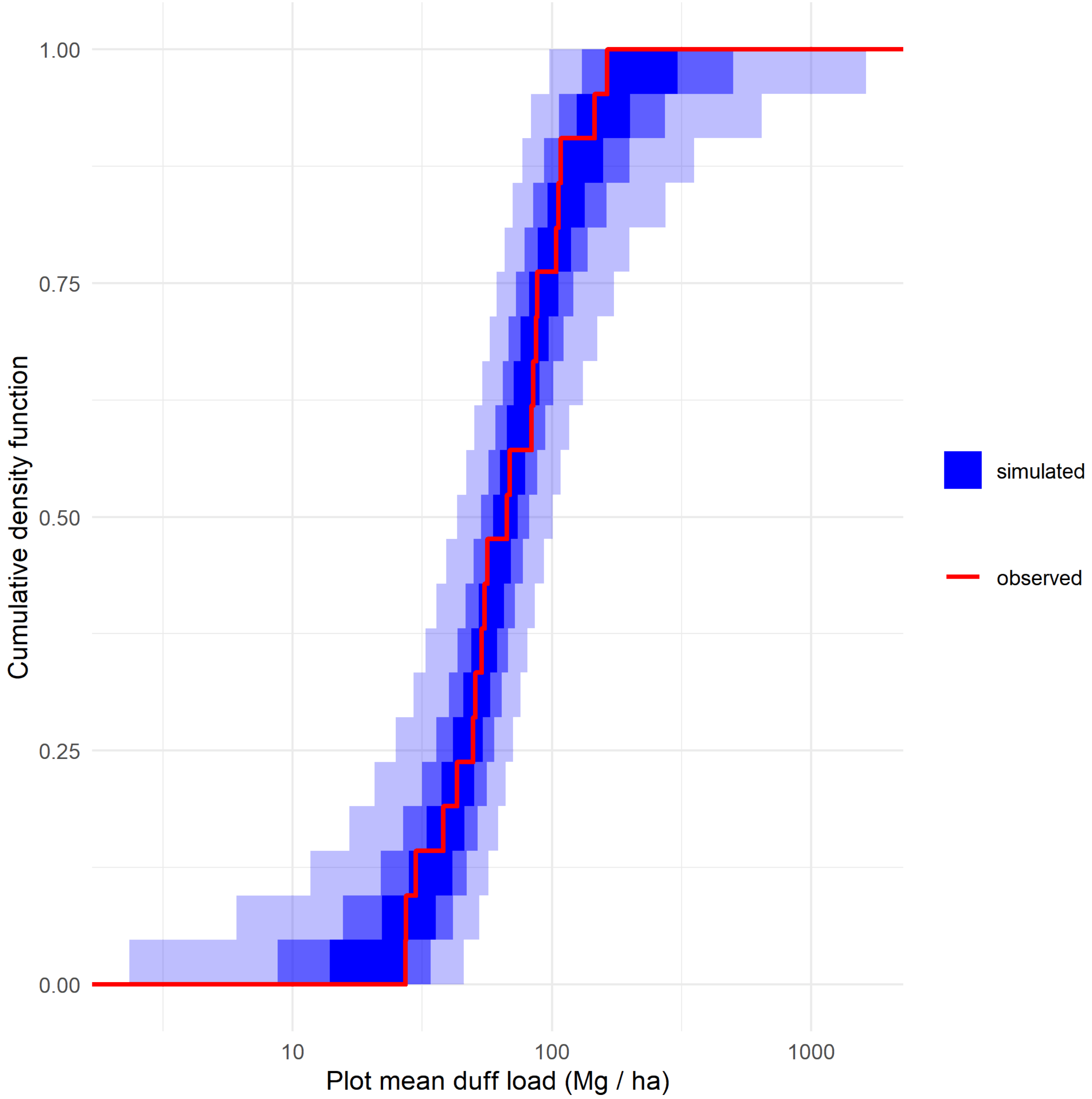

Supplementary Figure 11: Plot-level duff simulations. For each of 4,000 posterior draws, 1,107 depth samples were simulated using posterior parameter values and drawing new random effect realizations for both fine-scale (Gaussian process) and coarse-scale (normally distributed plot intercepts) random effects. The depth samples were converted to biomass estimates and averaged at the plot level, giving 21 simulated plot-level fuel loads per posterior draw. The red cumulative density function is the cumulative density function of plot-level fuel loads calculated from the observed data. The blue bands show an envelope containing 50% (darkest), 90%, and 99% (lightest) of the cumulative density functions from the simulated draws. The observed data are within the range of behaviors predicted by the model, but the model predictions do include rare outcomes (plot-level fuel loads greater than 1000 Mg/ha or less than 1 Mg/ha) which are more extreme than is ecologically plausible.

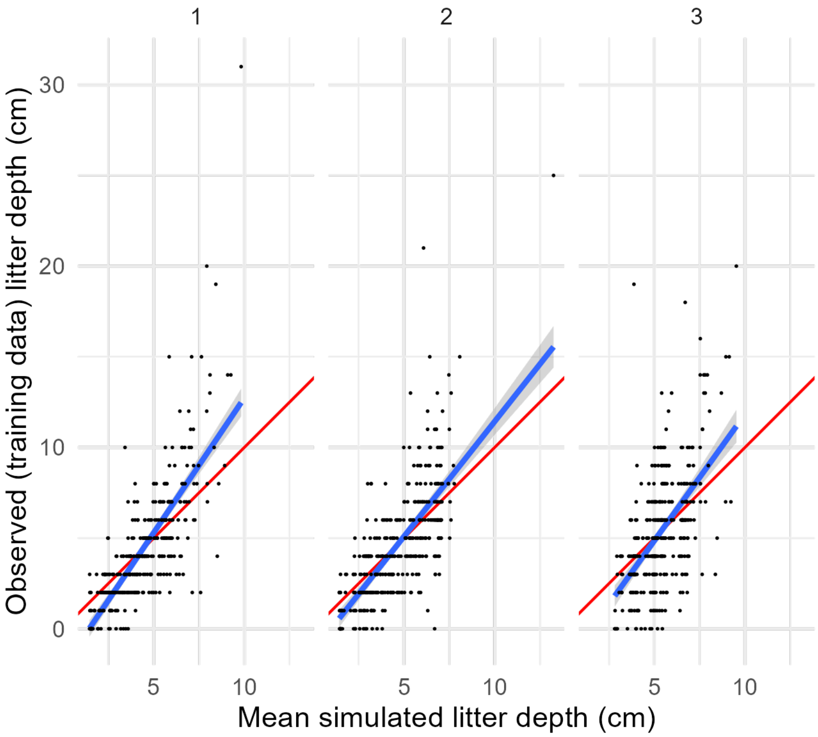

Supplementary Figure 12: Per-observation comparisons of mean predicted and observed values for the training data and the litter depths model. Panels show posterior predictions generated using the posterior parameter values and the training data for each of the three submodels representing low, medium, and high drought mortality (1, 2, and 3, respectively). In each panel, the posterior mean value of simulated litter depth for each observation is on the x-axis, and the observed depth for that observation on the y-axis, with points for each observation in the training dataset. Simulated data are conditional on the posterior samples of random effect realizations. A 1:1 line (representing perfect prediction) is shown in red, and a linear fit between the simulated and observed values shown in blue. There is a generally good but noisy fit between the simulated and observed data, though the model tends to underpredict for observed depths above ~5 cm and overpredict for observed depths below ~5 cm.

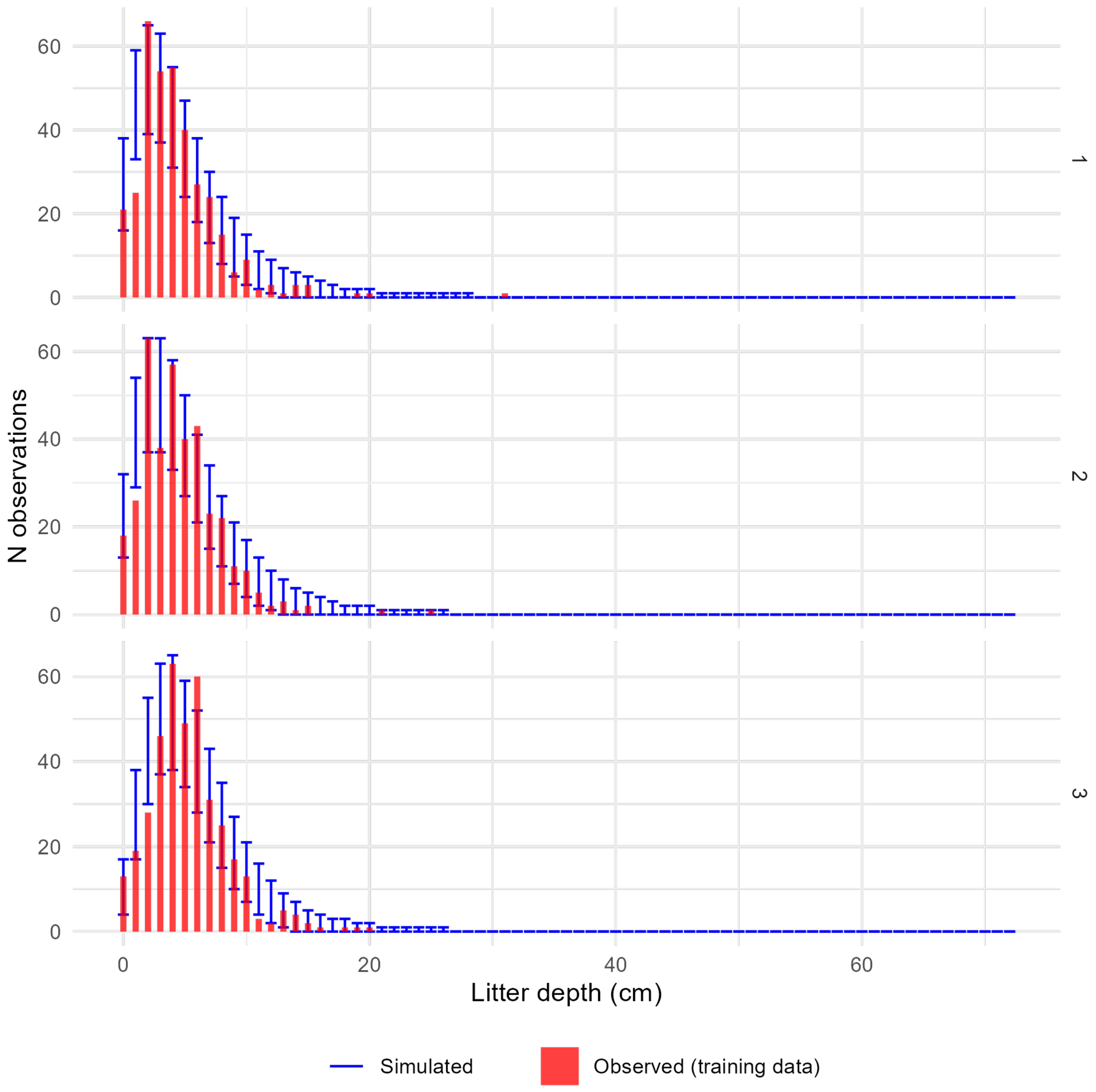

Supplementary Figure 13: Comparison of observed and simulated frequency distributions for the training data and the litter depths model. Panels show posterior predictions generated using the posterior parameter values and the training data for each of the three submodels representing low, medium, and high drought mortality (1, 2, and 3, respectively). In each panel, the x-axis shows an (observed or simulated) depth of litter and the y-axis shows the frequency of samples from a dataset of 1,107 litter depth measurements having that depth (i.e., a histogram). The observed distribution of litter depths is plotted as the red histogram. The error bars within each depth value show the 2.5th and 97.5th percentile of the frequency of simulated samples having that depth value, across each of the 4,000 posterior draws showing the variation in model-predicted frequency distributions. The observed data are generally within the range of behaviors predicted by the model, except that the model appears to overpredict the proportion of 1 cm samples, and underpredict the proportion of 2 cm samples.

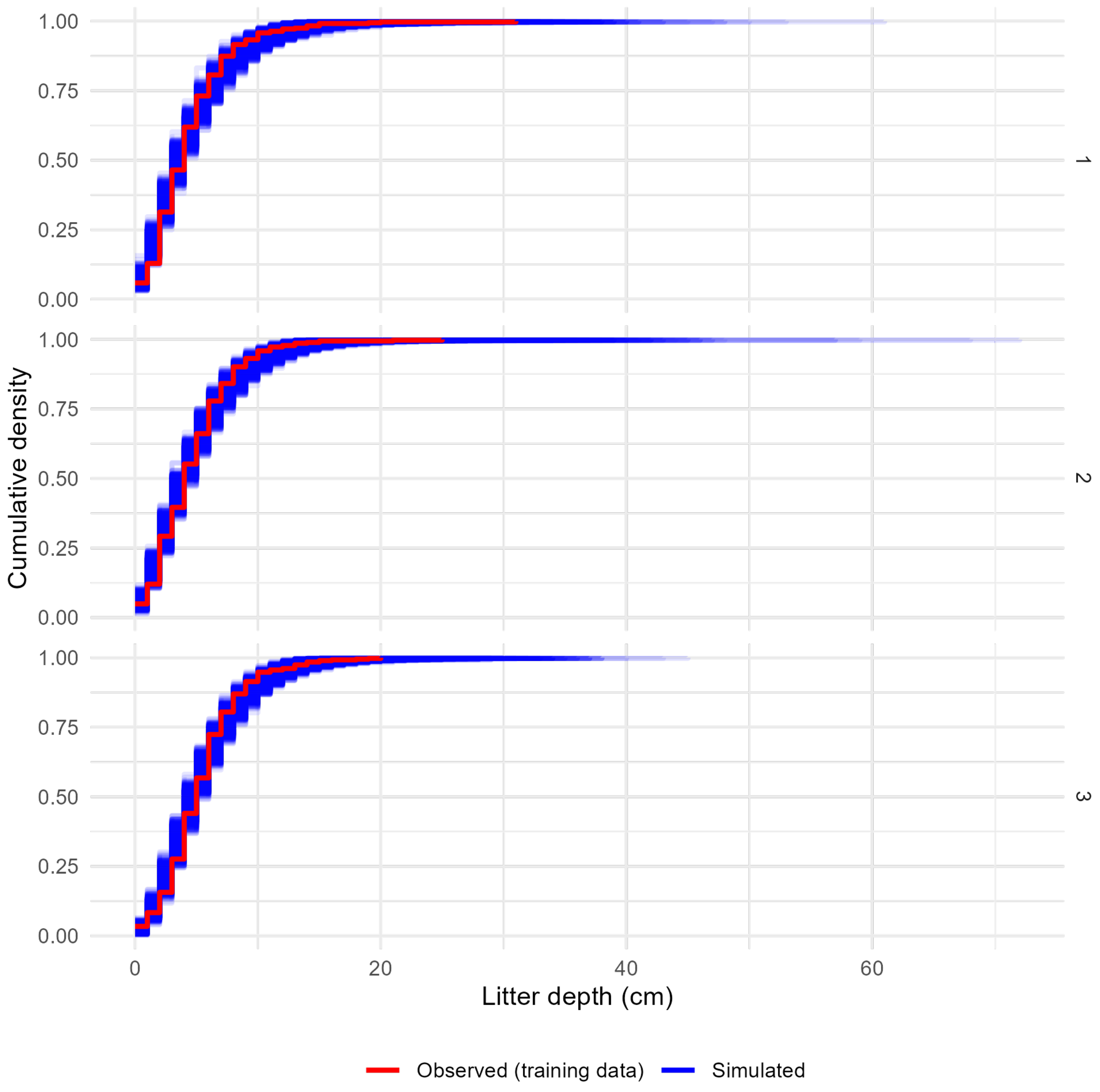

Supplementary Figure 14: Comparison of the observed and simulated cumulative density functions for the training data and the litter depths model. Panels show the cumulative density functions of the observed training data (red) and each of 4,000 simulated datasets generated using posterior parameter values and random effect realizations (blue) for each of the three sub-models corresponding to low, medium, or high levels of drought mortality. The observed cumulative density functions fall within the range of behaviors predicted by the model, indicating good agreement between the model and reality.

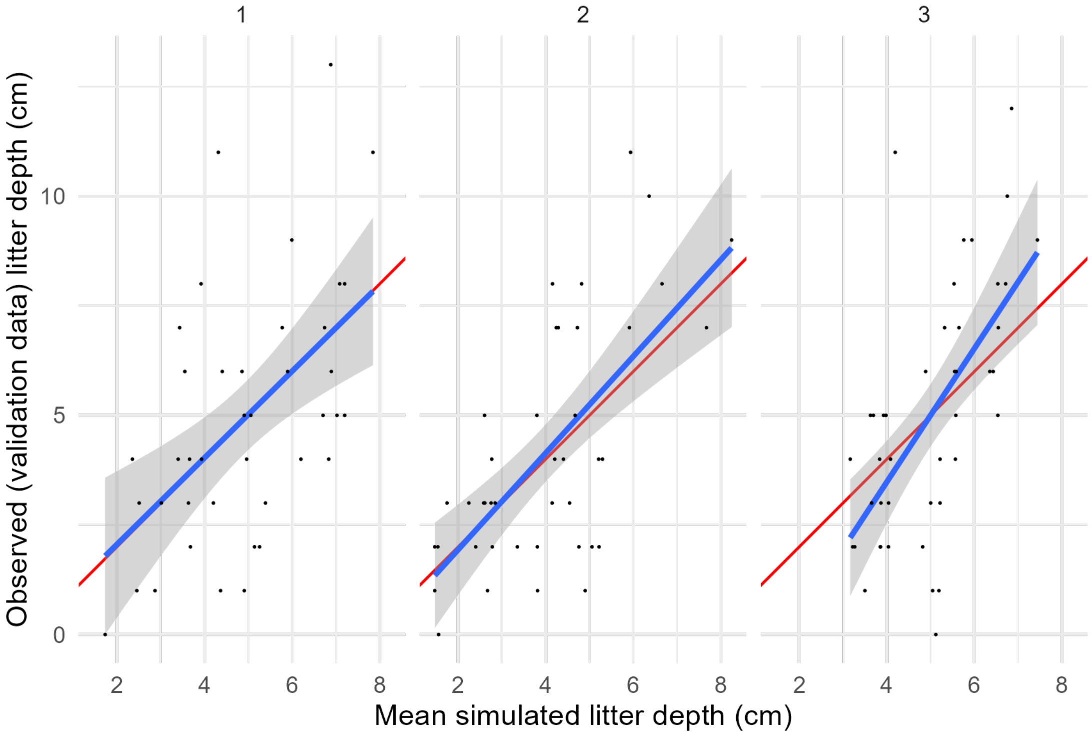

Supplementary Figure 15: Per-observation comparisons of mean predicted and observed values for the validation data and the litter depths model. Panels show posterior predictions generated using the posterior parameter values and the validation data for each of the three submodels representing low, medium, and high drought mortality (1, 2, and 3, respectively). In each panel, the posterior mean value of simulated litter depth for each observation is on the x-axis, and the observed depth for that observation on the y-axis, with points for each observation in the training dataset. Simulated data are conditional on the posterior samples of random effect realizations. A 1:1 line (representing perfect prediction) is shown in red, and a linear fit between the simulated and observed values shown in blue. There is a generally good but noisy fit between the simulated and observed data, with some tendency to underpredict for high observed depths and overpredict for low observed depths.

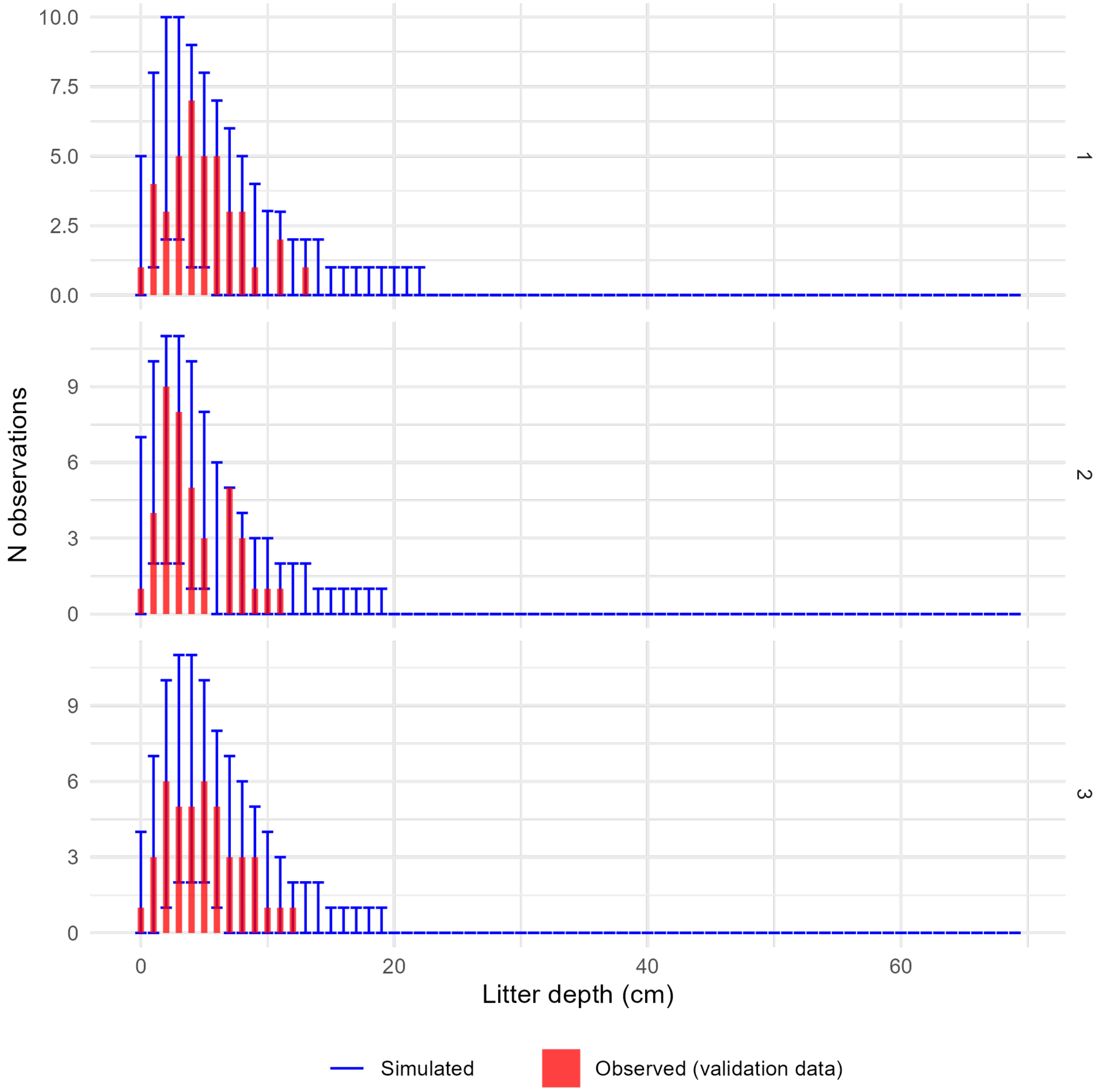

Supplementary Figure 16: Comparison of observed and simulated density distributions for the validation data and the litter depths model. Panels show posterior predictions generated using the posterior parameter values and the validation data for each of the three submodels representing low, medium, and high drought mortality (1, 2, and 3, respectively). In each panel, the x-axis shows an (observed or simulated) depth of litter and the y-axis shows the frequency of samples from a dataset of 124 litter depth measurements having that depth (i.e., a histogram). The observed distribution of litter depths is plotted as the red histogram. The error bars within each depth value show the 2.5th and 97.5th percentile of the frequency of simulated samples having that depth value, across each of the 4,000 posterior draws showing the variation in model-predicted frequency distributions. The observed data are generally within the range of behaviors predicted by the model, though with so few data points the simulated depth distributions are noisy resulting in wide ranges for the proportion of samples falling in each bin.

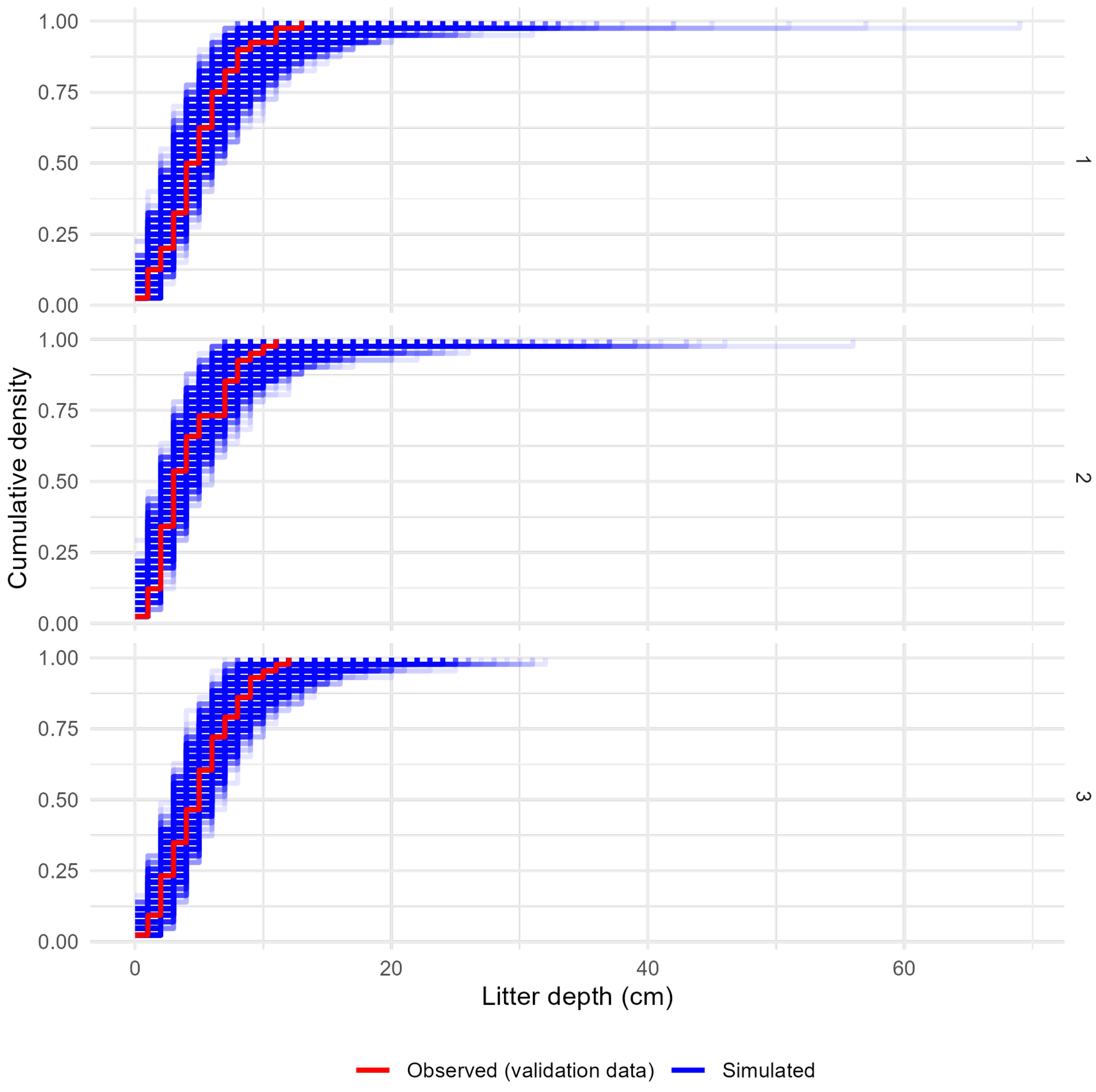

Supplementary Figure 17: Comparison of the observed and simulated cumulative density functions for the validation data and the litter depths model. Panels show the cumulative density functions of the observed validation data (red) and each of 4,000 simulated datasets generated using posterior parameter values and random effect realizations (blue) for each of the three sub-models corresponding to low, medium, or high levels of drought mortality. The observed cumulative density functions fall within the range of behaviors predicted by the model, indicating good agreement between the model and reality.

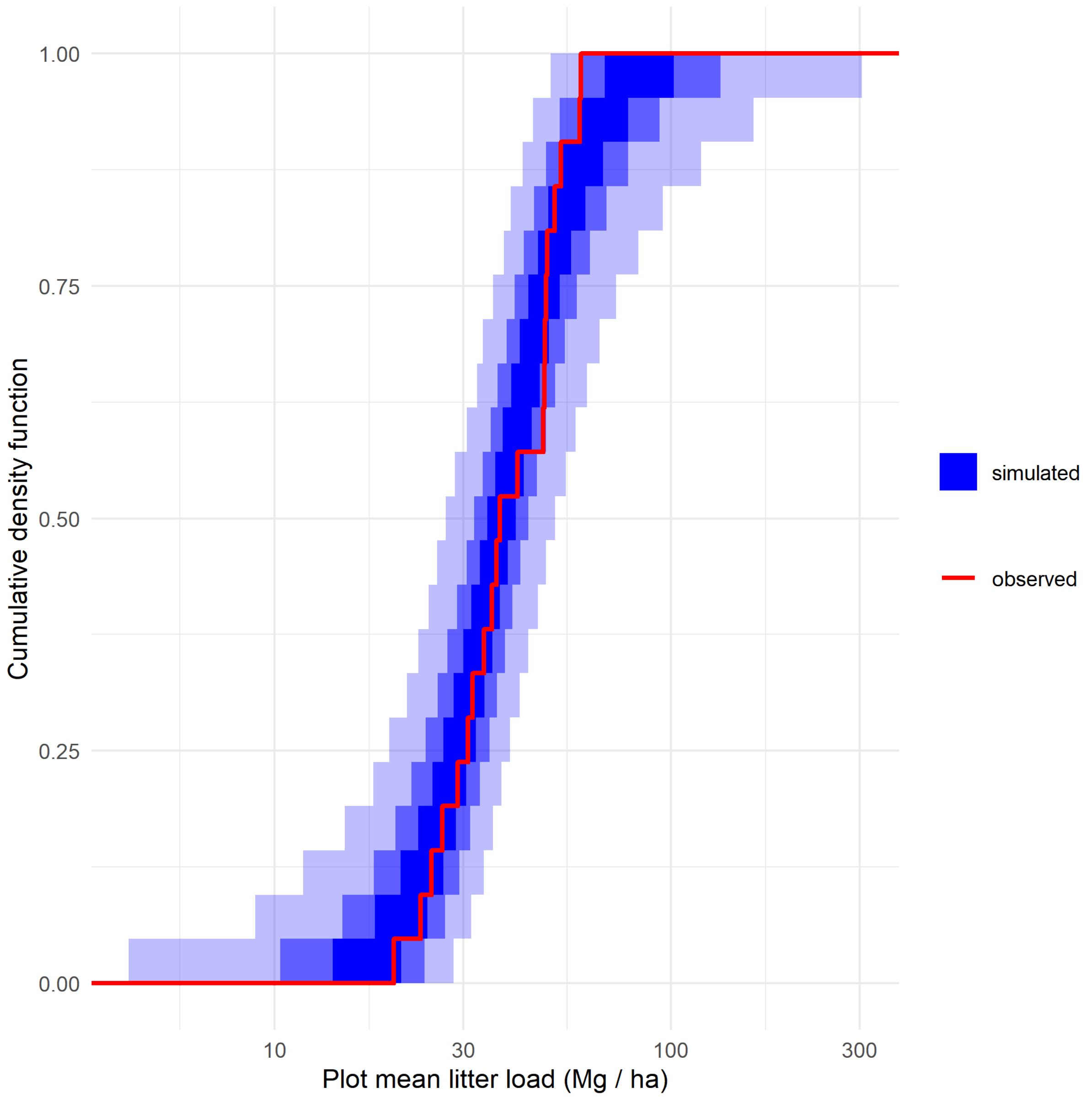

Supplementary Figure 18: Plot-level litter simulations. For each of 4,000 posterior draws, 1,107 depth samples were simulated using posterior parameter values and drawing new random effect realizations for both fine-scale (Gaussian process) and coarse-scale (normally distributed plot intercepts) random effects. The depth samples were converted to biomass estimates and averaged at the plot level, giving 21 simulated plot-level fuel loads per posterior draw. The red cumulative density function is the cumulative density function of plot-level fuel loads calculated from the observed data. The blue bands show an envelope containing 50% (darkest), 90%, and 99% (lightest) of the cumulative density functions from the simulated draws. The observed data are within the range of behaviors predicted by the model, but the highest observed plot-level fuel loads are lower than the upper quantiles of most simulated fuel loads (top of figure).

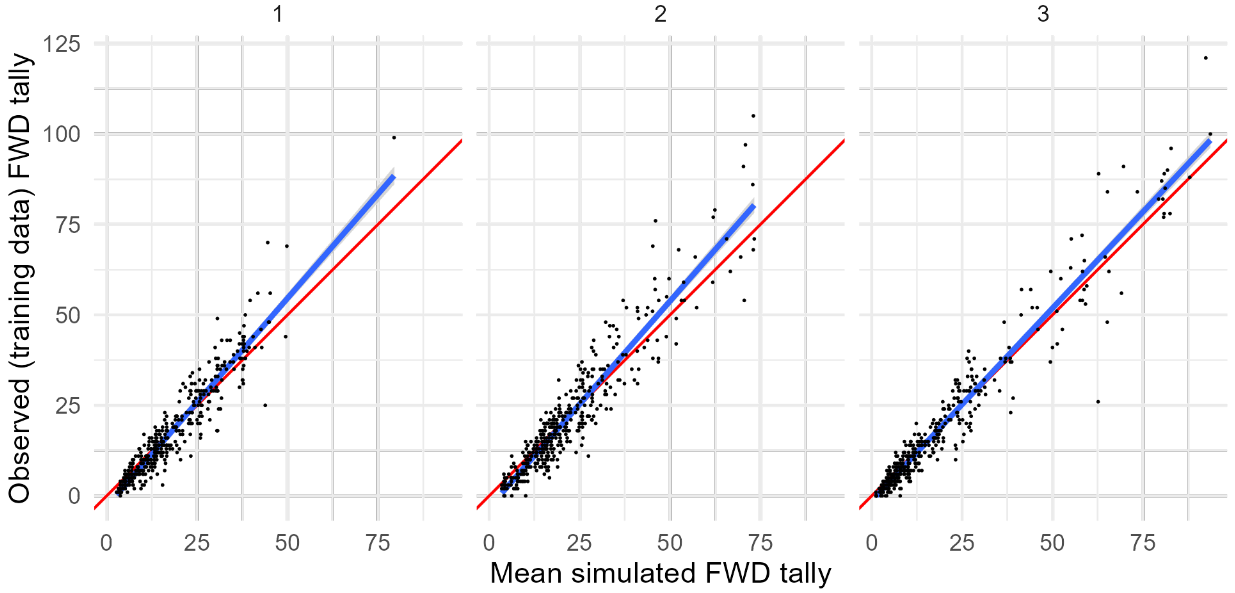

Supplementary Figure 19: Per-observation comparisons of mean predicted and observed values for the training data and the fine woody debris tallies model. Panels show posterior predictions generated using the posterior parameter values and the training data for each of the three submodels representing low, medium, and high drought mortality (1, 2, and 3, respectively). In each panel, the posterior mean value of simulated fine woody debris tally for each observation is on the x-axis, and the observed tally for that observation on the y-axis, with points for each observation in the training dataset. Simulated data are conditional on the posterior samples of random effect realizations. A 1:1 line (representing perfect prediction) is shown in red, and a linear fit between the simulated and observed values shown in blue. There is a good fit between predicted and observed values.

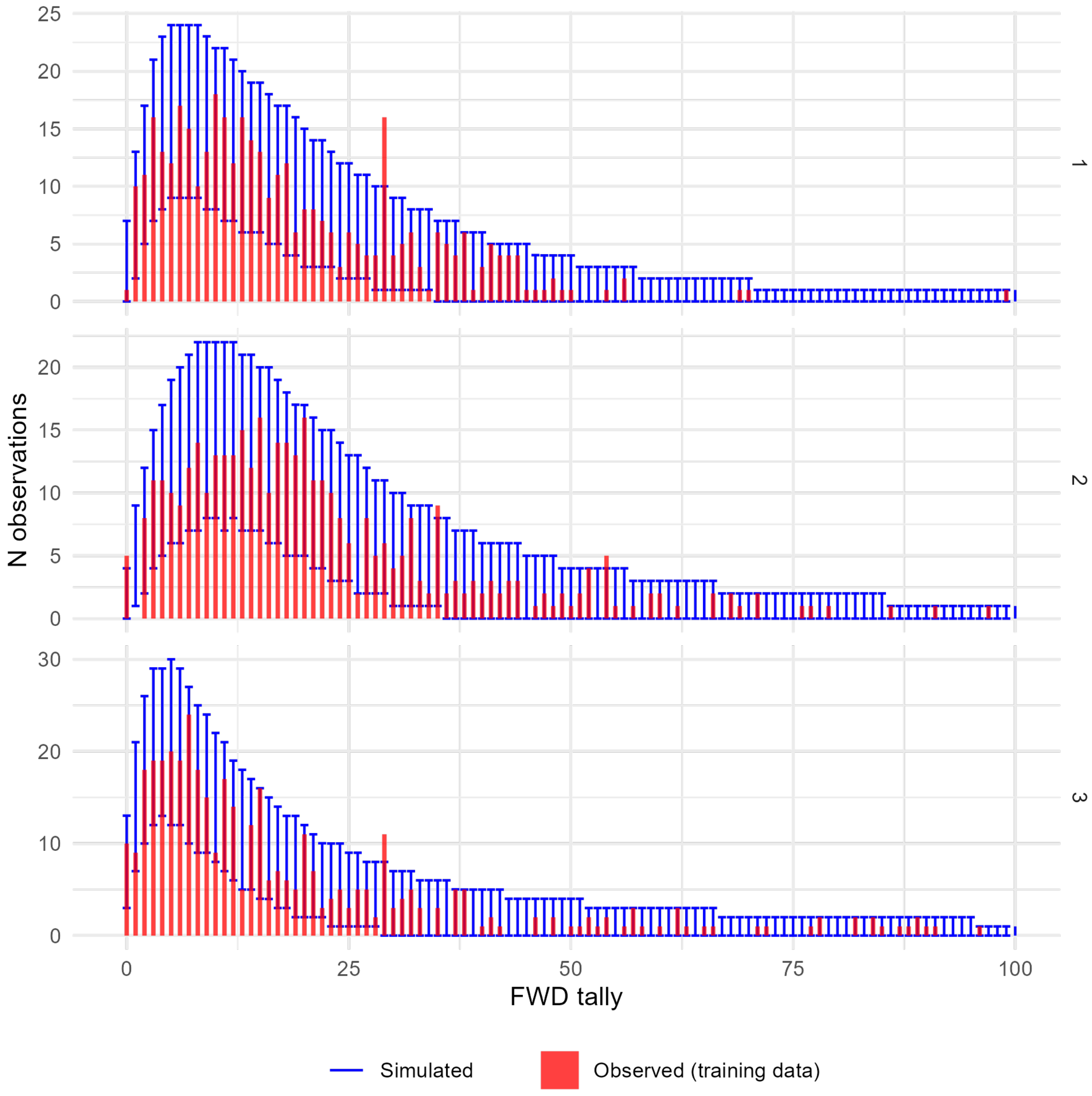

Supplementary Figure 20: Comparison of observed and simulated frequency distributions for the training data and the fine woody debris tallies model. Panels show posterior predictions generated using the posterior parameter values and the training data for each of the three submodels representing low, medium, and high drought mortality (1, 2, and 3, respectively). In each panel, the x-axis shows an (observed or simulated) tally of fine woody debris and the y-axis shows the frequency of samples from a dataset of 1,183 one meter subtransects having that tally (i.e., a histogram). The observed distribution of FWD tallies is plotted as the red histogram. The error bars within each tally value show the 2.5th and 97.5th percentile of the frequency of simulated samples having that tally value, across each of the 4,000 posterior draws showing the variation in model-predicted frequency distributions. The x-axis bounds have been limited to improve readability. The observed data are generally within the range of behaviors predicted by the model. The x-axis has been restricted for readability.

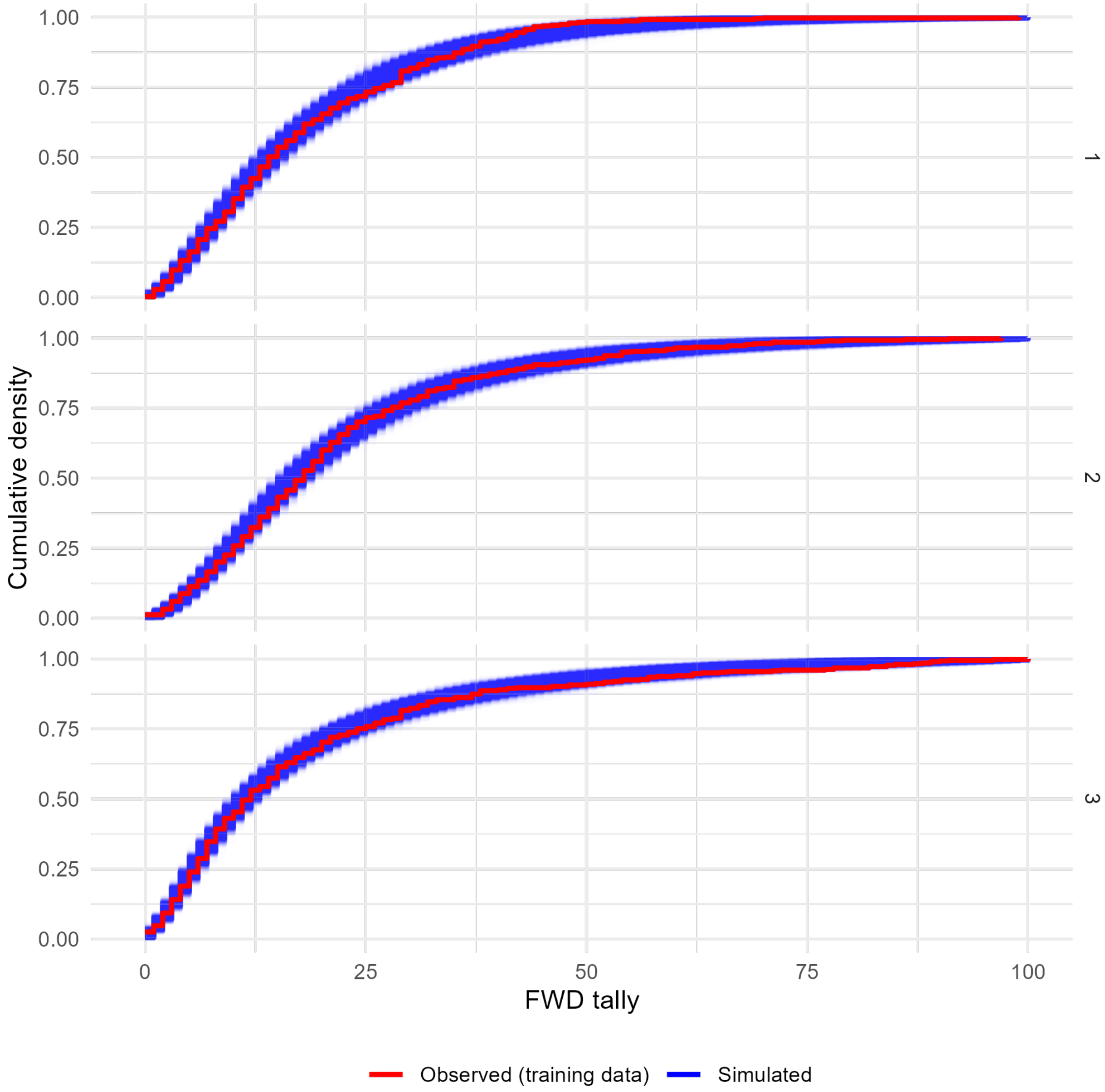

Supplementary Figure 21: Comparison of the observed and simulated cumulative density functions for the training data and the fine woody debris tallies model. Panels show the cumulative density functions of the observed training data (red) and each of 4,000 simulated datasets generated using posterior parameter values and random effect realizations (blue) for each of the three sub-models corresponding to low, medium, or high levels of drought mortality. The x-axis bounds have been limited to improve readability. The observed cumulative density functions fall within the range of behaviors predicted by the model, indicating good agreement between the model and reality.

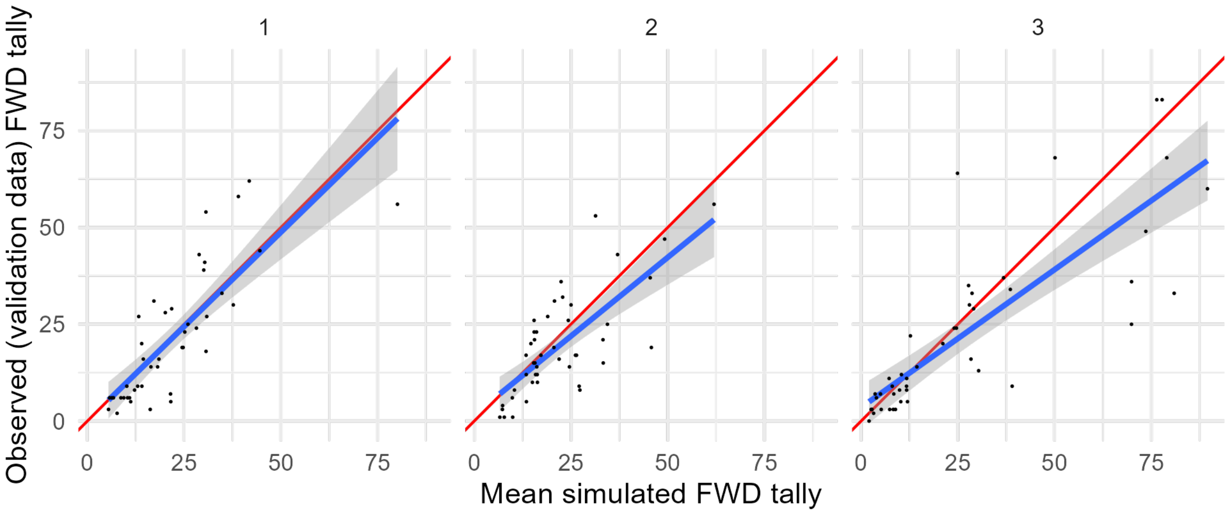

Supplementary Figure 22: Per-observation comparisons of mean predicted and observed values for the validation data and the fine woody debris tallies model. Panels show posterior predictions generated using the posterior parameter values and the validation data for each of the three submodels representing low, medium, and high drought mortality (1, 2, and 3, respectively). In each panel, the posterior mean value of simulated fine woody debris tally for each observation is on the x-axis, and the observed tally for that observation on the y-axis, with points for each observation in the validation dataset. Simulated data are conditional on the posterior samples of random effect realizations. A 1:1 line (representing perfect prediction) is shown in red, and a linear fit between the simulated and observed values shown in blue. The fit between observed and predicted values is noisy, and for sub-models 2 and 3 (medium and high drought mortality) the model tends to under-predict tallies above ~25.

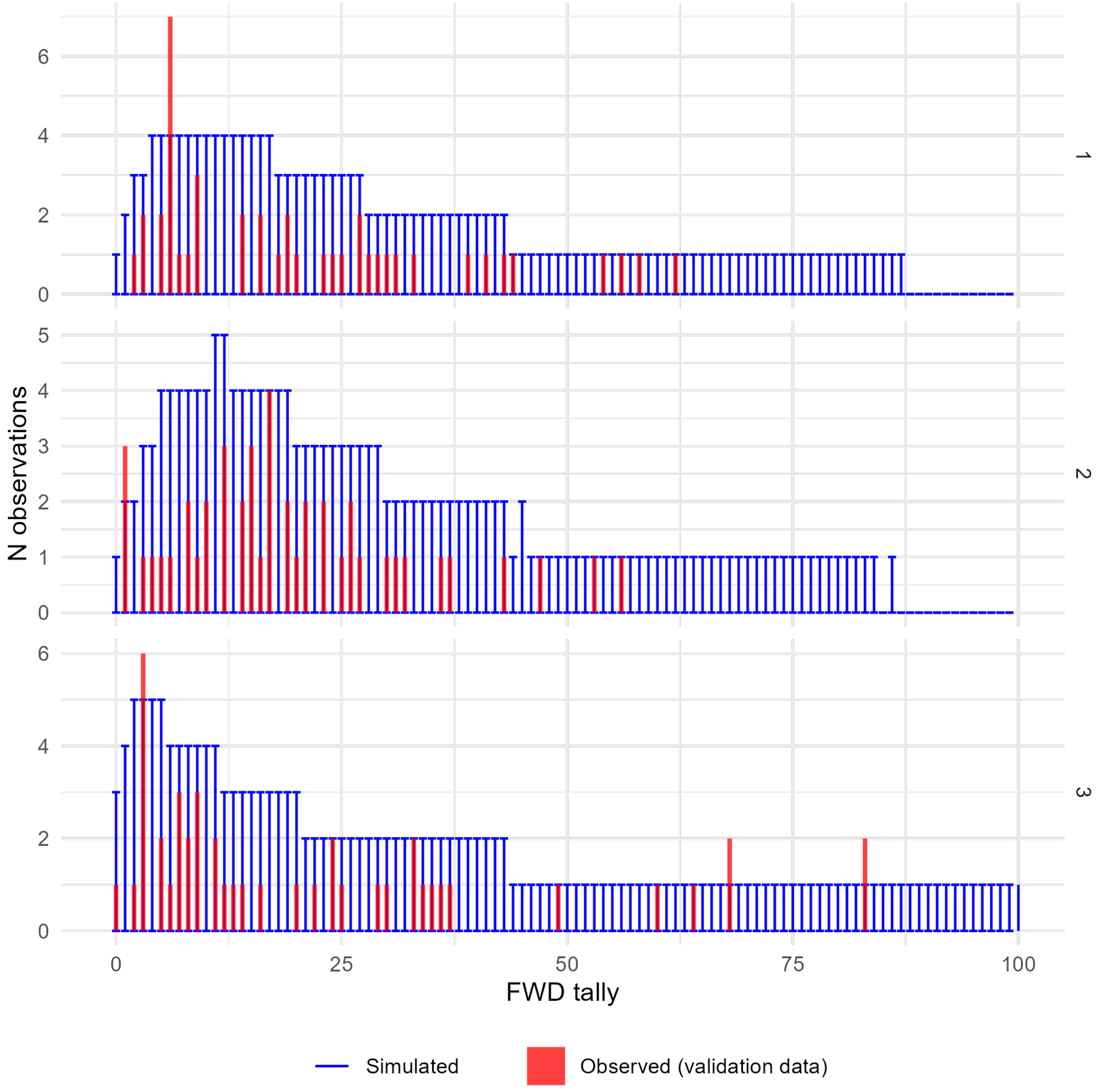

Supplementary Figure 23: Comparison of observed and simulated density distributions for the validation data and the fine woody debris tallies model. Panels show posterior predictions generated using the posterior parameter values and the validation data for each of the three submodels representing low, medium, and high drought mortality (1, 2, and 3, respectively). In each panel, the x-axis shows an (observed or simulated) tally of fine woody debris and the y-axis shows the frequency of samples from a dataset of 133 one meter subtransects having that tally (i.e., a histogram). The observed distribution of FWD tallies is plotted as the red histogram. The error bars within each tally value show the 2.5th and 97.5th percentile of the frequency of simulated samples having that tally value, across each of the 4,000 posterior draws showing the variation in model-predicted frequency distributions. The x-axis bounds have been limited to improve readability. The observed data are generally within the range of behaviors predicted by the model, though with so few data points the simulated depth distributions are noisy resulting in wide ranges for the proportion of samples falling in each bin.

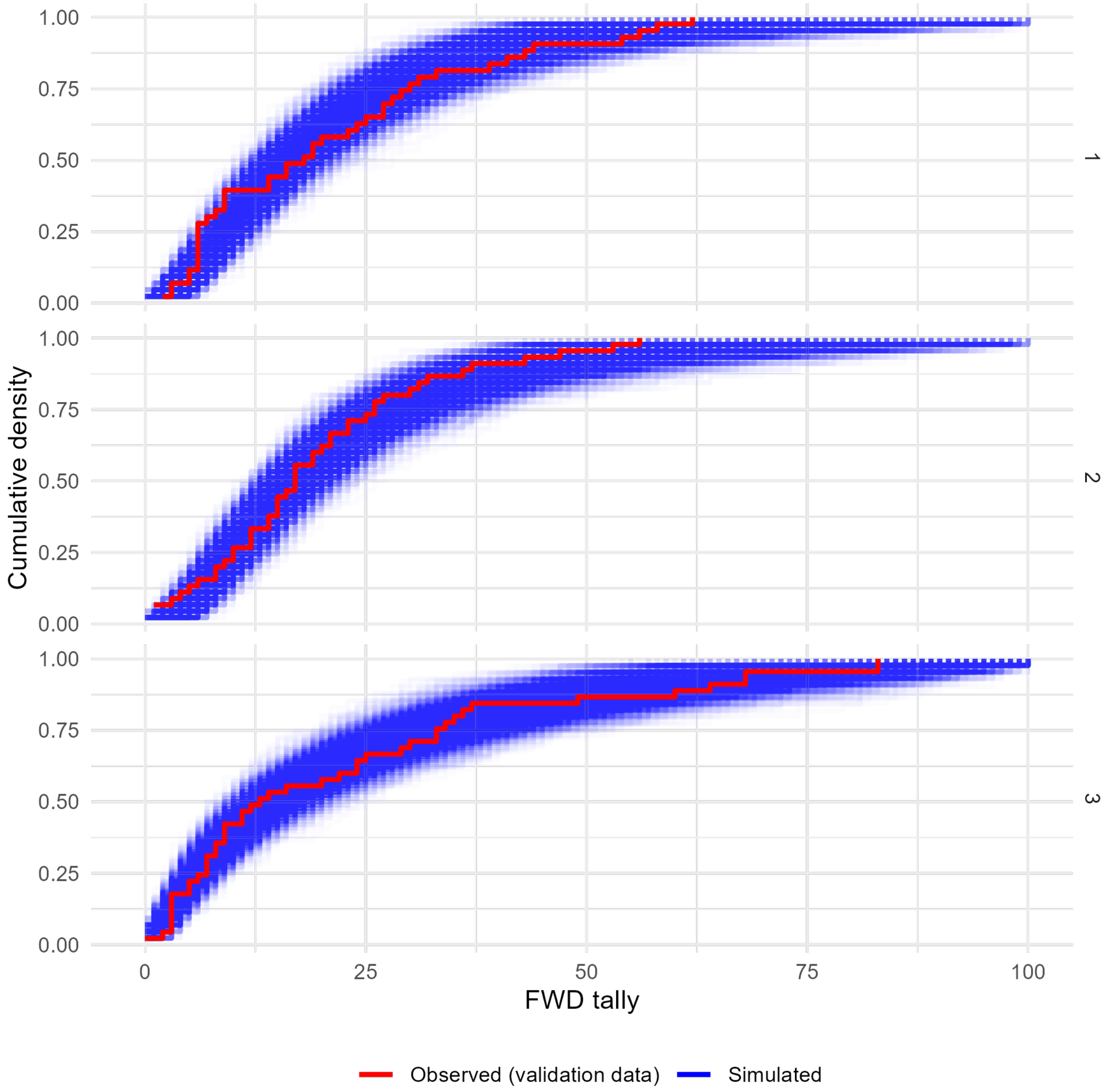

Supplementary Figure 24: Comparison of the observed and simulated cumulative density functions for the validation data and the fine woody debris tallies model. Panels show the cumulative density functions of the observed validation data (red) and each of 4,000 simulated datasets generated using posterior parameter values and random effect realizations (blue) for each of the three sub-models corresponding to low, medium, or high levels of drought mortality. The x-axis bounds have been limited to improve readability. The observed cumulative density functions fall within the range of behaviors predicted by the model, indicating good agreement between the model and reality.

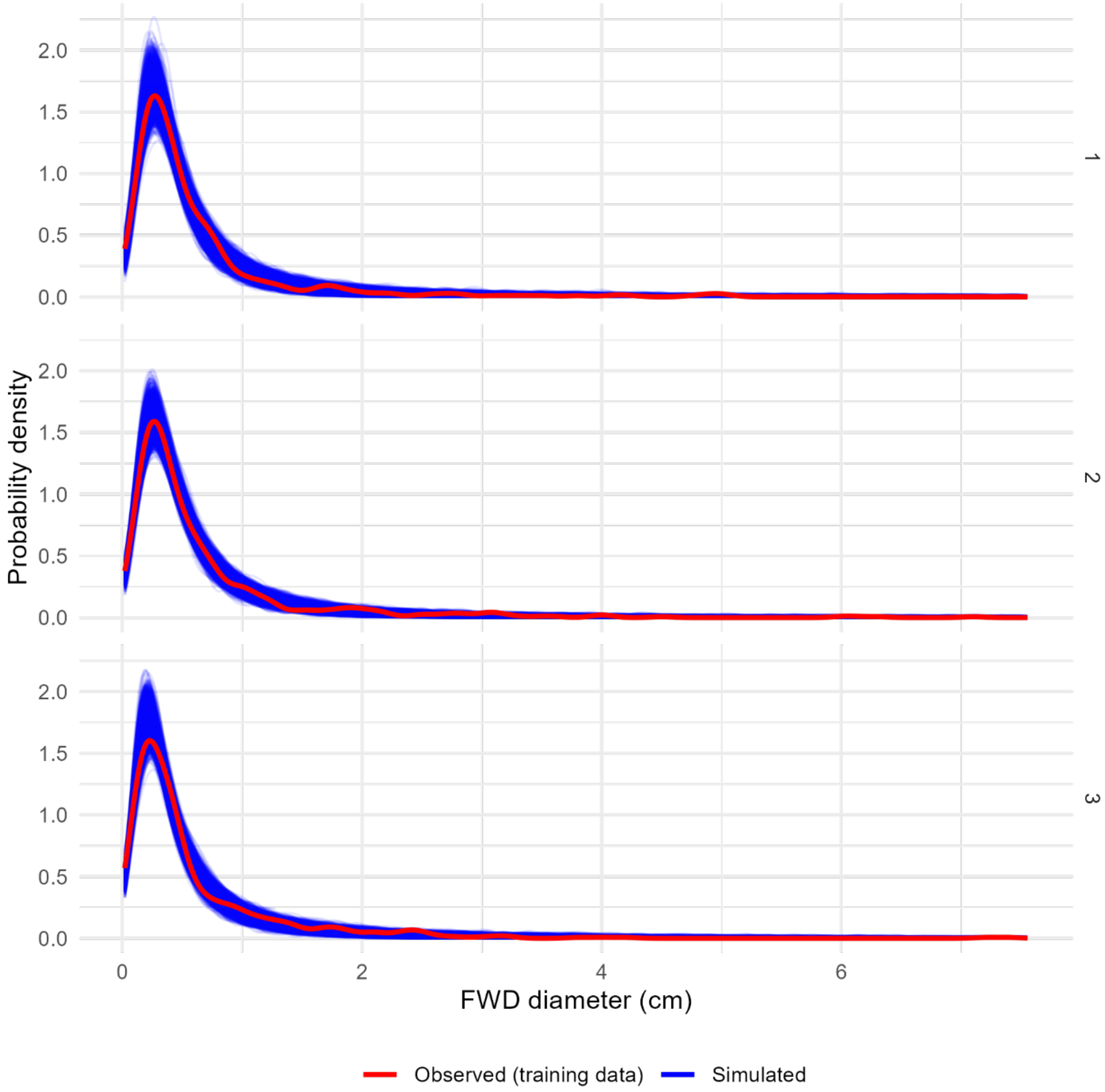

Supplementary Figure 25: Comparison of observed and simulated density distributions for the training data and the fine woody debris diameters model. Panels show the probability density functions of the observed training data (red) and each of 4,000 simulated datasets generated using posterior parameter values and random effect realizations (blue) for each of the three sub-models corresponding to low, medium, or high levels of drought mortality. For the most part, observed cumulative density functions fall within the range of behaviors predicted by the model, indicating good agreement between the model and reality.

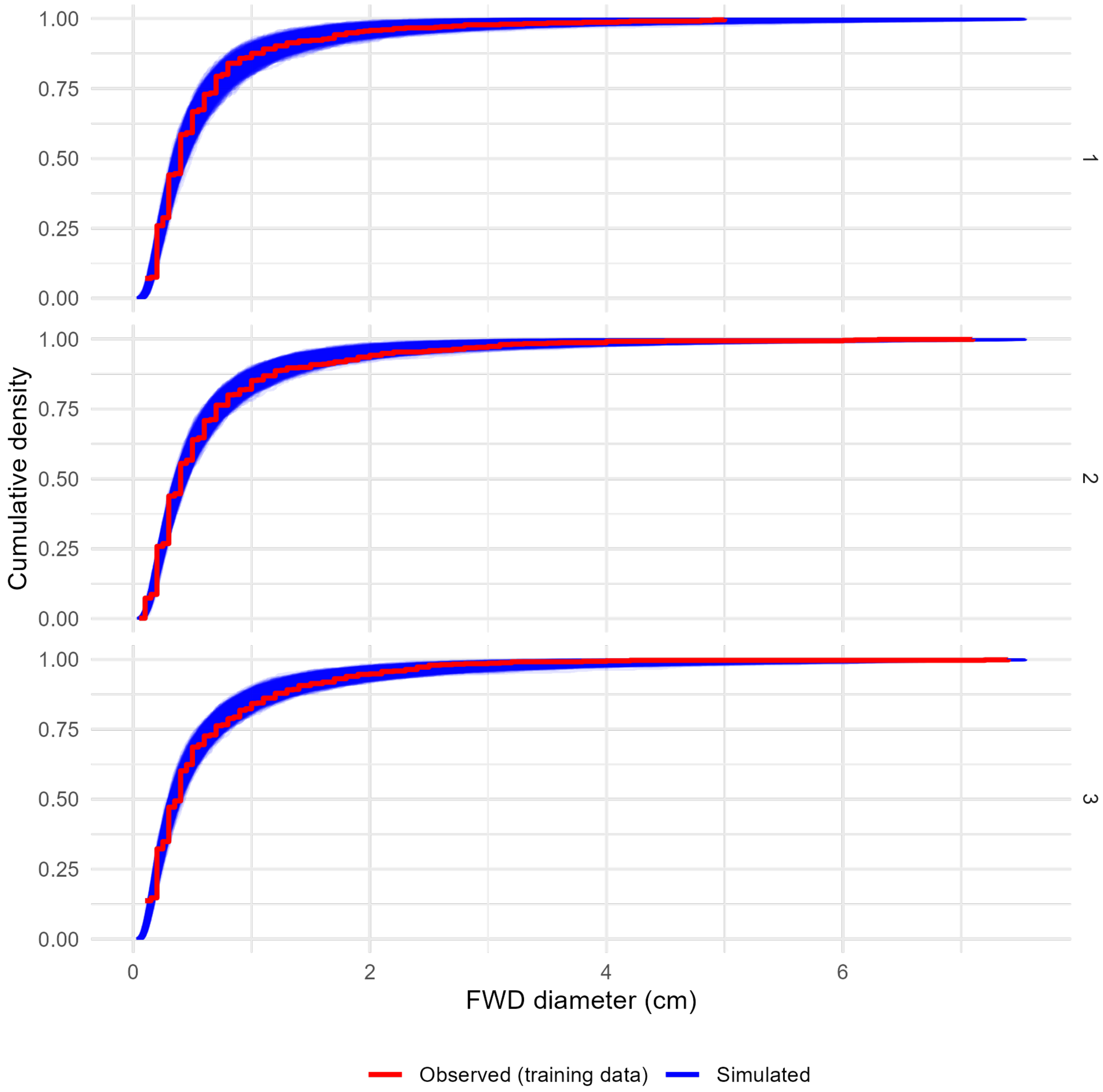

Supplementary Figure 26: Comparison of the observed and simulated cumulative density functions for the training data and the fine woody debris diameters model. Panels show the cumulative density functions of the observed training data (red) and each of 4,000 simulated datasets generated using posterior parameter values and random effect realizations (blue) for each of the three sub-models corresponding to low, medium, or high levels of drought mortality. For the most part, observed cumulative density functions fall within the range of behaviors predicted by the model, indicating good agreement between the model and reality. However, for all three levels of drought mortality the rounding of the observed diameters to the nearest 0.1 cm is evident in the pronounced stepwise character of the (red) observed cumulative density function, which at the steps falls outside or on the edge of the (blue) cumulative density functions generated from truly continuous model-simulated diameters.

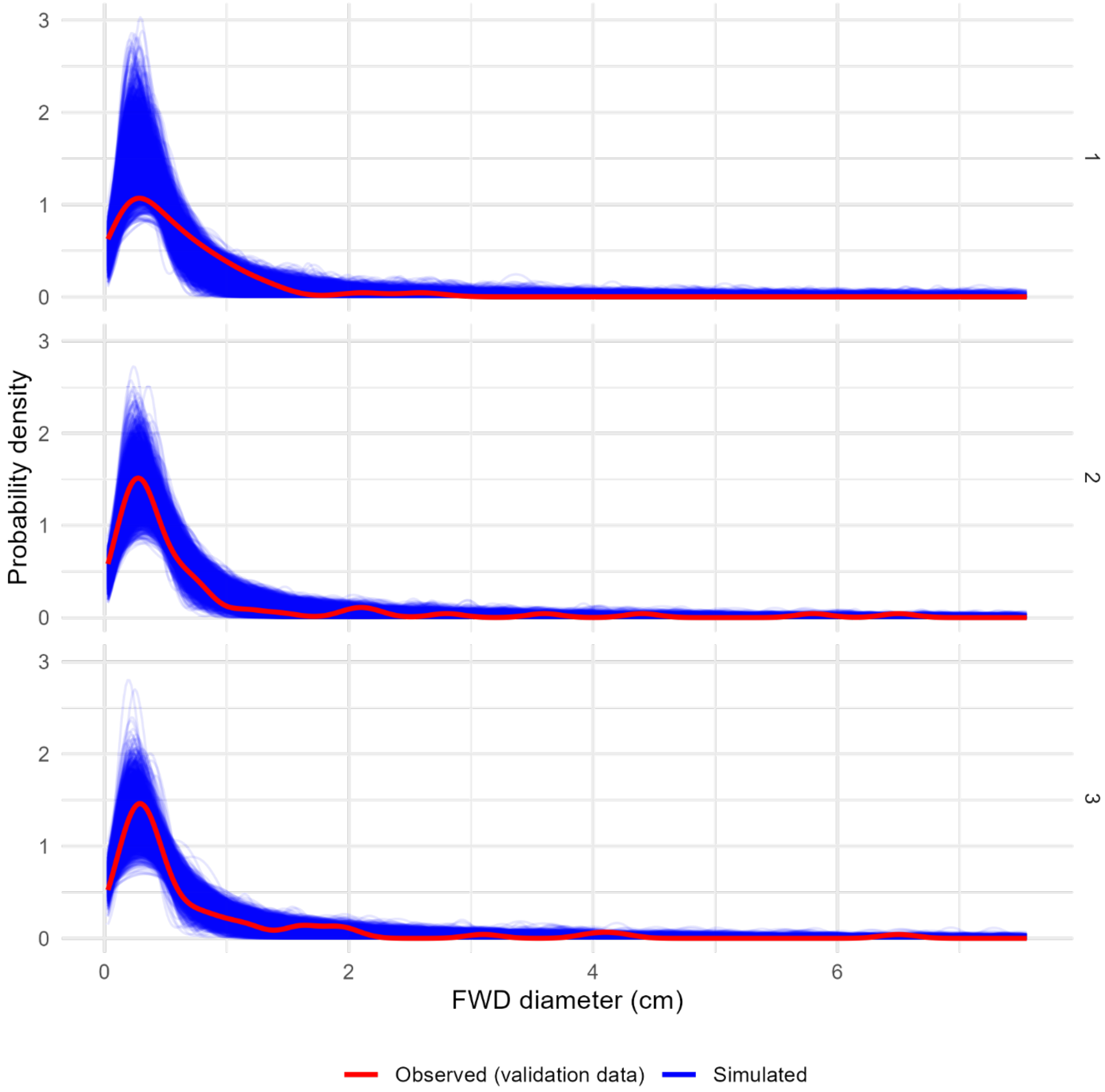

Supplementary Figure 27: Comparison of observed and simulated density distributions for the validation data and the fine woody debris diameters model. Panels show the probability density functions of the observed validation data (red) and each of 4,000 simulated datasets generated using posterior parameter values and random effect realizations (blue) for each of the three sub-models corresponding to low, medium, or high levels of drought mortality. Observed cumulative density functions fall within the range of behaviors predicted by the model, indicating good agreement between the model and reality.

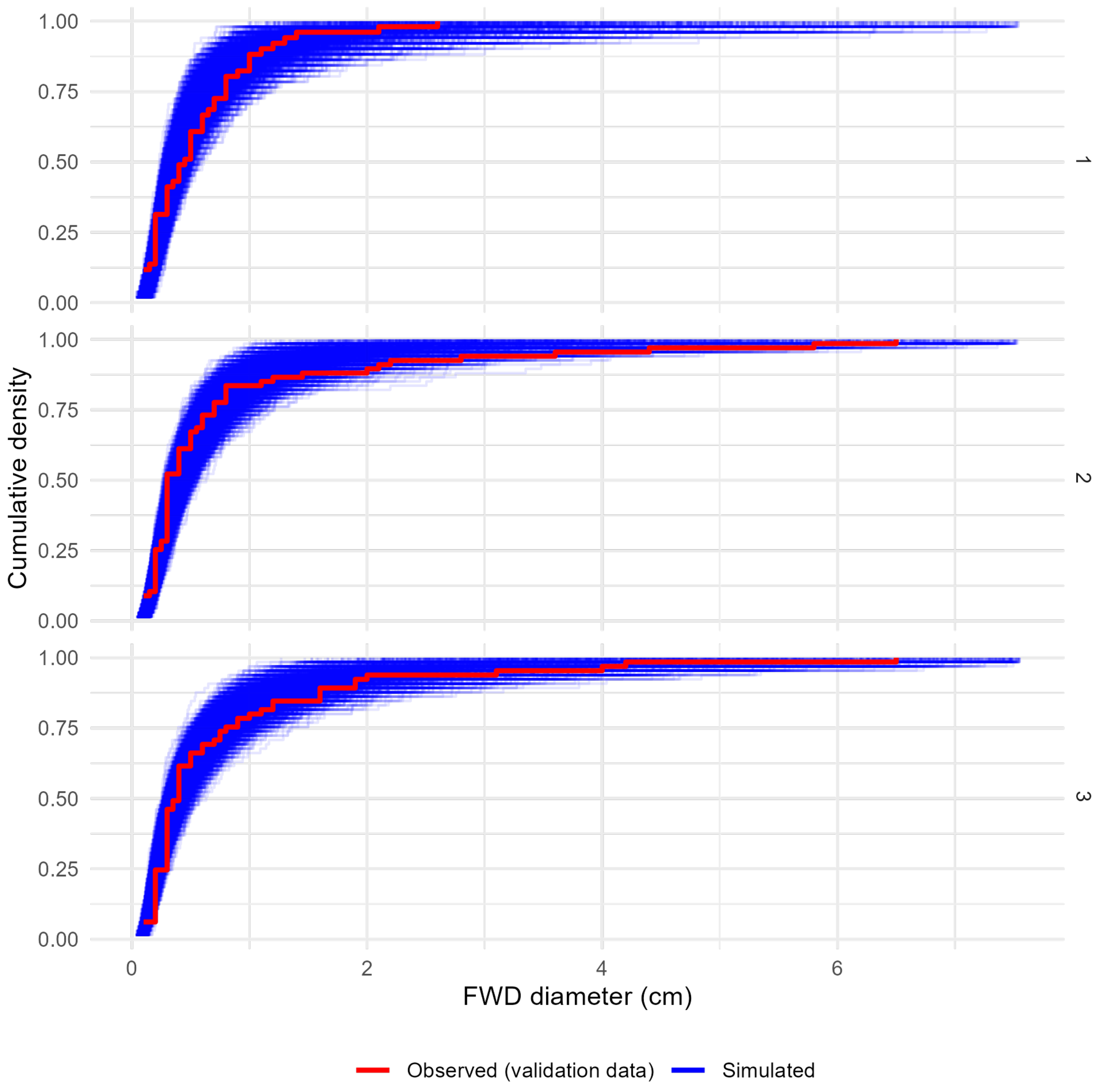

Supplementary Figure 28: Comparison of the observed and simulated cumulative density functions for the validation data and the fine woody debris diameters model. Panels show the cumulative density functions of the observed validation data (red) and each of 4,000 simulated datasets generated using posterior parameter values and random effect realizations (blue) for each of the three sub-models corresponding to low, medium, or high levels of drought mortality. For the most part, observed cumulative density functions fall within the range of behaviors predicted by the model, indicating good agreement between the model and reality. The exception, where observed behavior lies outside (or on the edge of) model predictions is that there were the observed proportion of particles with diameters equal to 0.1 cm was lower in the observed data than in most simulated datasets, for the third group (high drought mortality).

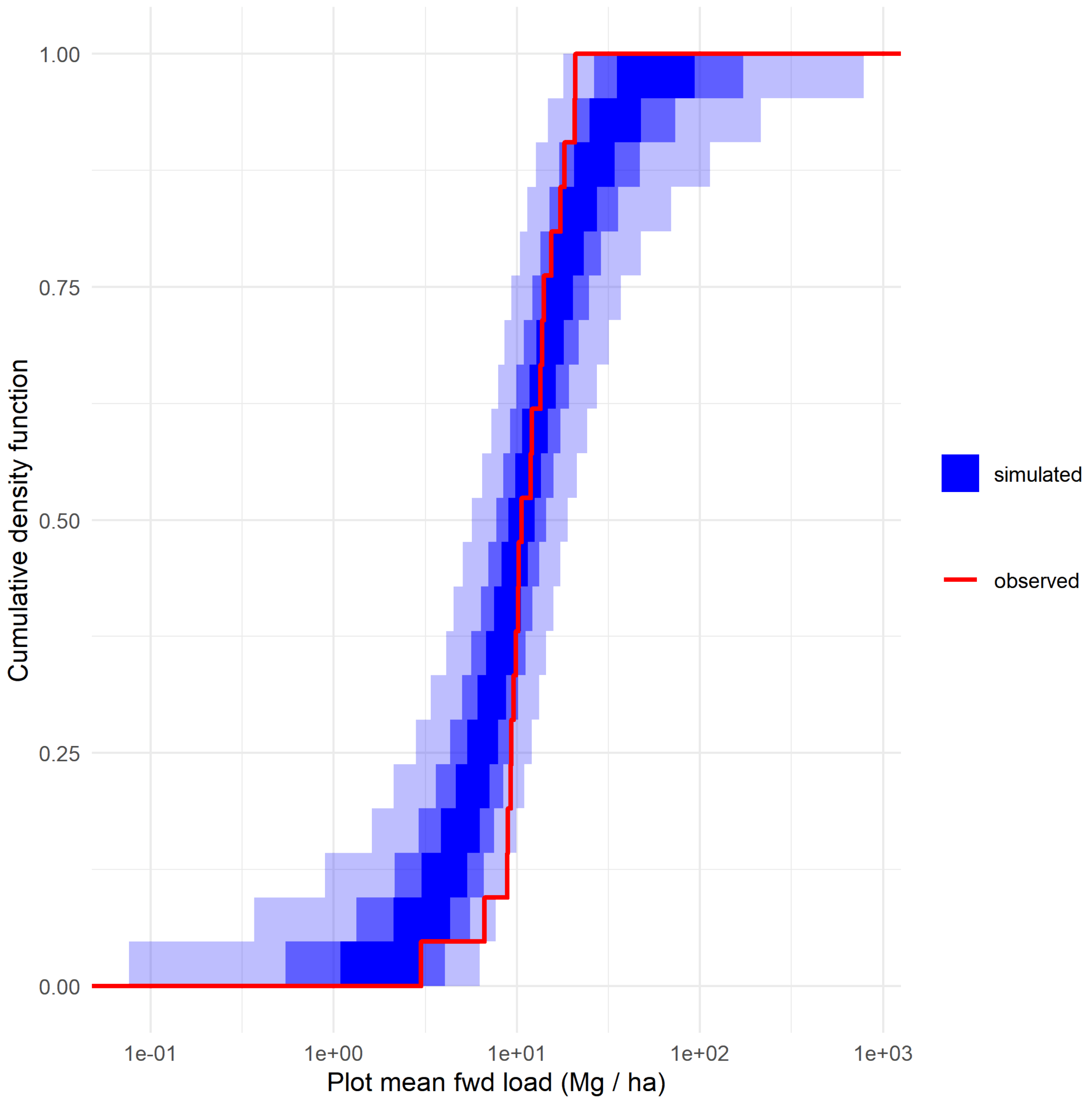

Supplementary Figure 29: Plot-level fine woody debris simulations. For each of 4,000 posterior draws, 1,183 tallies of fine woody debris on 1-meter subtransects were simulated using posterior parameter values from the fine woody debris tallies model and drawing new random effect realizations for both fine-scale (Gaussian process) and coarse-scale (normally distributed plot intercepts) random effects. Then, for each simulated particle, a diameter was simulated using the fine woody debris diameters model. The simulated particles on each subtransect were aggregated by size class, converted to biomass estimates and averaged at the plot level, giving 21 simulated plot-level fuel loads per posterior draw. The red cumulative density function is the cumulative density function of plot-level fuel loads calculated from the observed data. The blue bands show an envelope containing 50% (darkest), 90%, and 99% (lightest) of the cumulative density functions from the simulated draws. The observed data are within the range of behaviors predicted by the model, but the observed distribution of plot-level means is very tight relative to model predictions. This can be seen in the way the lowest fuel load observed plots have higher fuel loads than most of the lowest-load simulated plots (red line is on the right edge of the envelope at the bottom of the figure), while the highest-load simulated plots are generally more heavily loaded than the highest-loaded observed plots (red line is on the left edge of the envelope at the top of the figure).

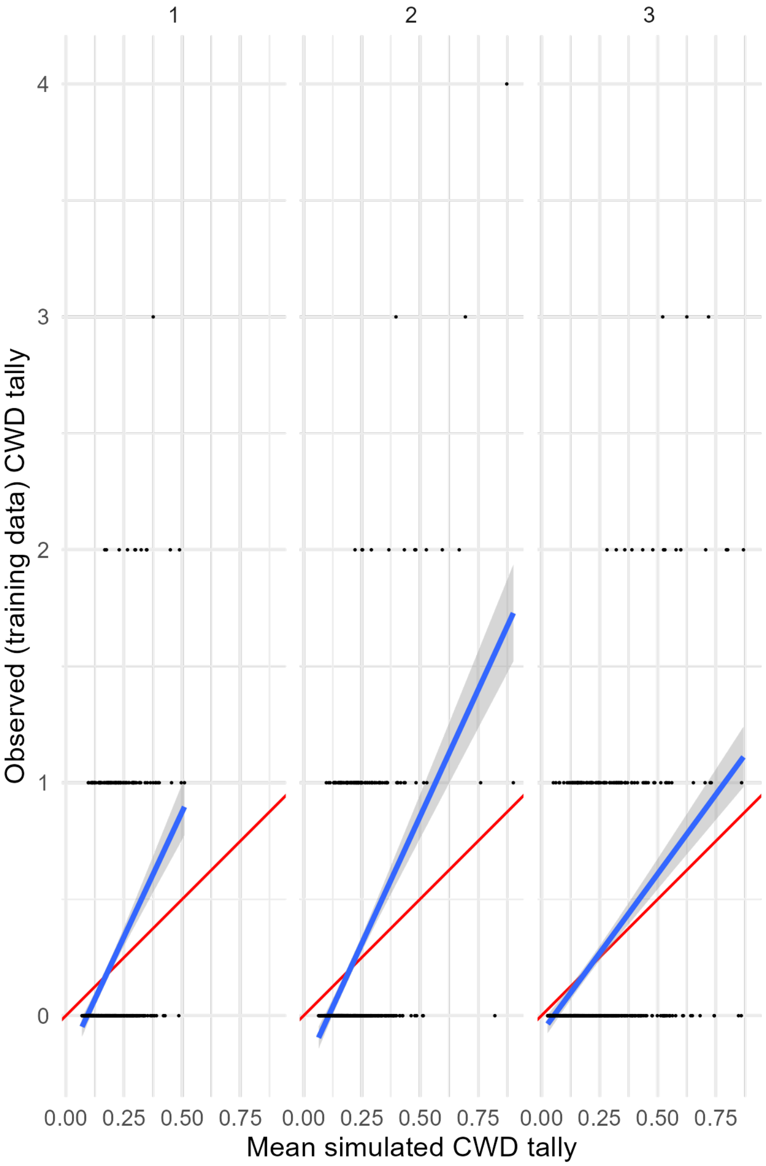

Supplementary Figure 30: Per-observation comparisons of mean predicted and observed values for the training data and the coarse woody debris tallies model. Panels show posterior predictions generated using the posterior parameter values and the training data for each of the three submodels representing low, medium, and high drought mortality (1, 2, and 3, respectively). In each panel, the posterior mean value of simulated CWD tally for each observation is on the x-axis, and the observed tally for that observation on the y-axis, with points for each observation in the training dataset. Simulated data are conditional on the posterior samples of random effect realizations. A 1:1 line (representing perfect prediction) is shown in red, and a linear fit between the simulated and observed values shown in blue. As expected, the average simulated tally for samples where the observed tally was 0 is greater than 0. However, the average simulated tally for samples where the observed tally was 1, 2, 3, or 4 consistently underpredicts the true tally.

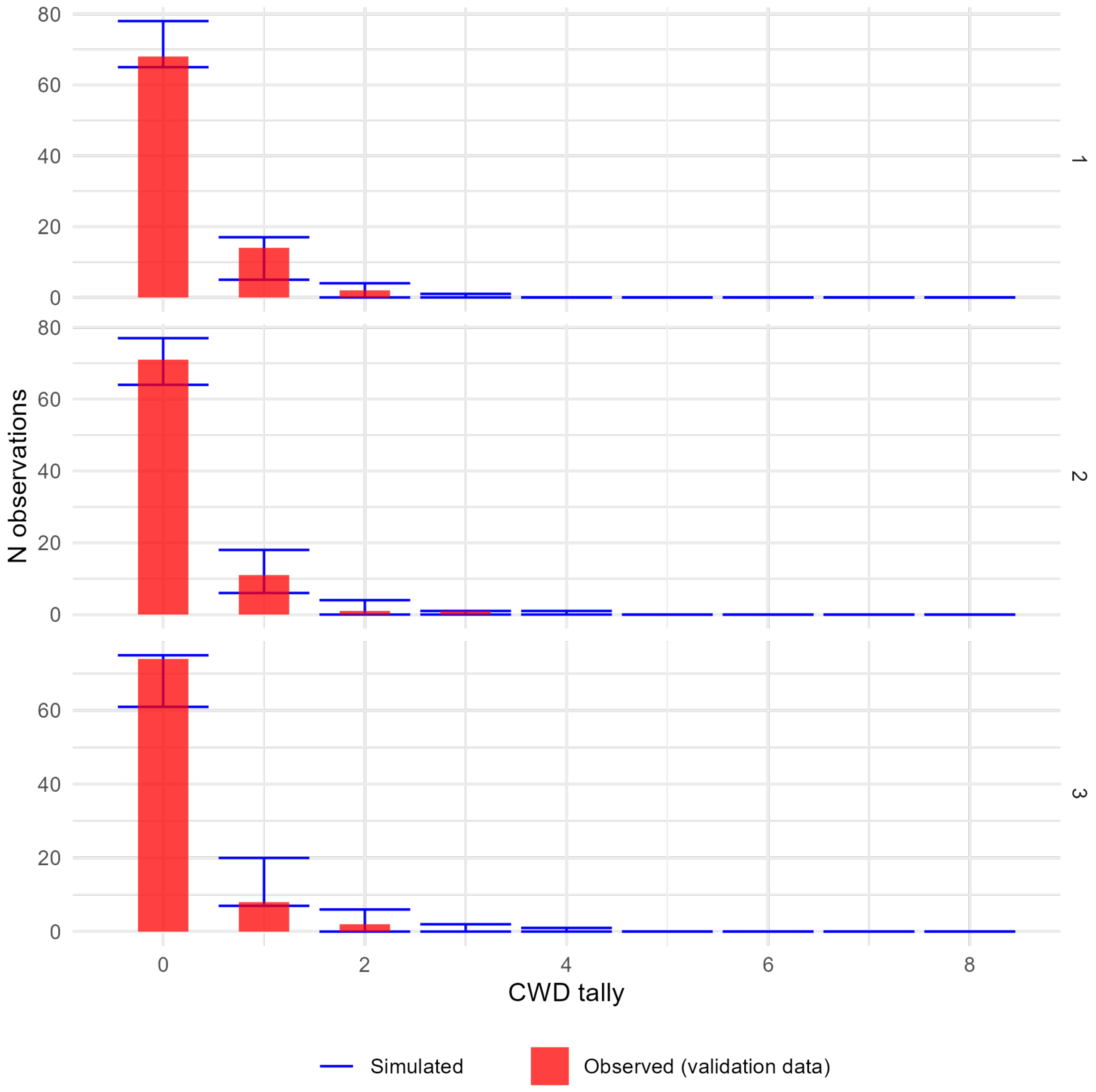

Supplementary Figure 31: Comparison of observed and simulated density distributions for the training data and the coarse woody debris tallies model. Panels show posterior predictions generated using the posterior parameter values and the training data for each of the three submodels representing low, medium, and high drought mortality (1, 2, and 3, respectively). In each panel, the x-axis shows an (observed or simulated) tally of coarse woody debris and the y-axis shows the frequency of samples from a dataset of 2,268 one meter subtransects having that tally (i.e., a histogram). The observed distribution of CWD tallies is plotted as the red histogram. The error bars within each tally value show the 2.5th and 97.5th percentile of the frequency of simulated samples having that tally value, across each of the 4,000 posterior draws showing the variation in model-predicted frequency distributions. The observed data are consistently within the range of behaviors predicted by the model.

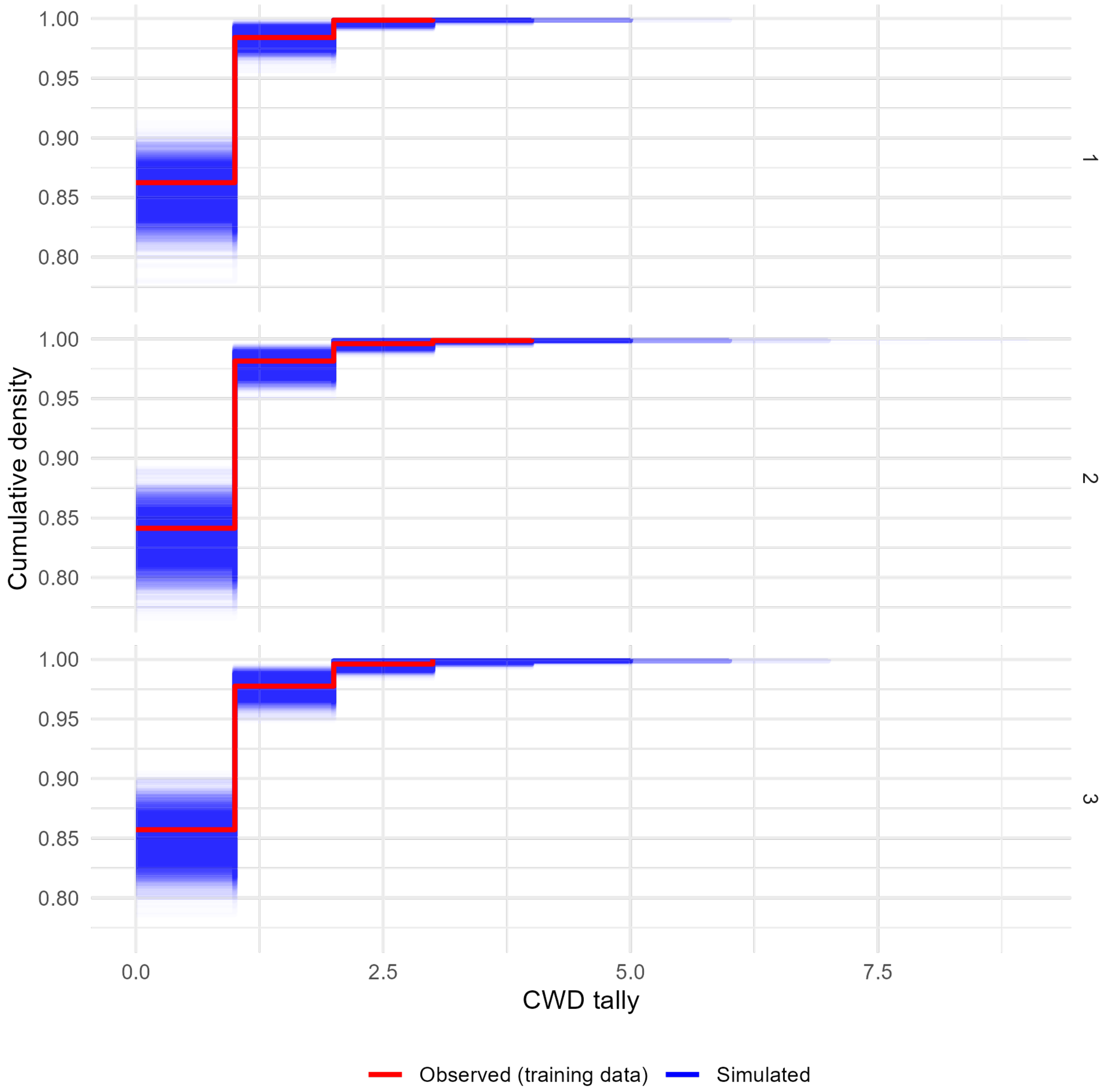

Supplementary Figure 32: Comparison of the observed and simulated cumulative density functions for the training data and the coarse woody debris tallies model. Panels show the cumulative density functions of the observed training data (red) and each of 4,000 simulated datasets generated using posterior parameter values and random effect realizations (blue) for each of the three sub-models corresponding to low, medium, or high levels of drought mortality. The observed cumulative density functions fall within the range of behaviors predicted by the model, indicating good agreement between the model and reality.

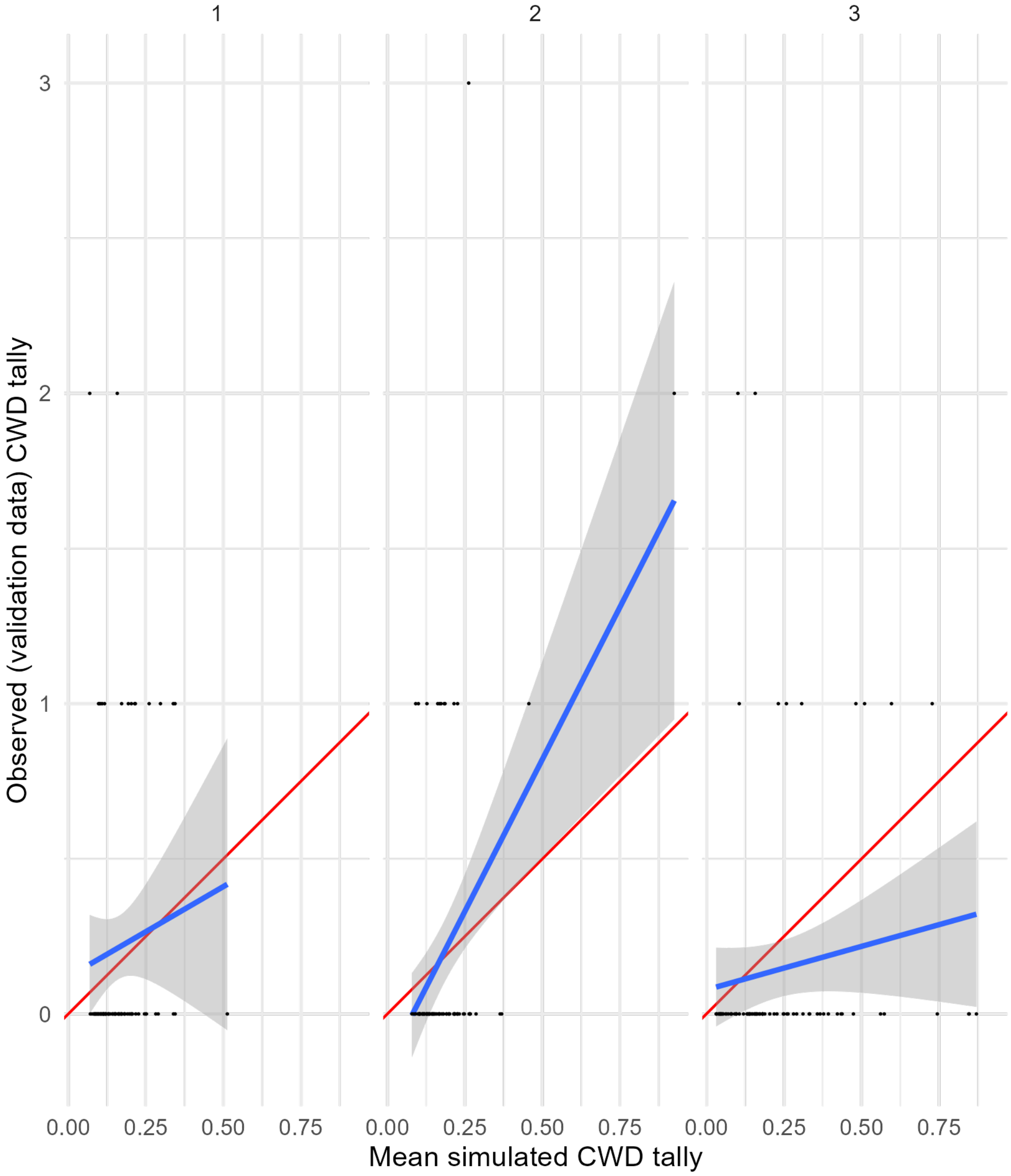

Supplementary Figure 33: Per-observation comparisons of mean predicted and observed values for the validation data and the coarse woody debris tallies model. Panels show posterior predictions generated using the posterior parameter values and the validation data for each of the three submodels representing low, medium, and high drought mortality (1, 2, and 3, respectively). In each panel, the posterior mean value of simulated CWD tally for each observation is on the x-axis, and the observed tally for that observation on the y-axis, with points for each observation in the training dataset. Simulated data are conditional on the posterior samples of random effect realizations. A 1:1 line (representing perfect prediction) is shown in red, and a linear fit between the simulated and observed values shown in blue. For two of the three submodels, there is a weak or nonexistent relationship between the simulated counts and the observed counts, though with such low observed counts it is difficult to interpret the figure.

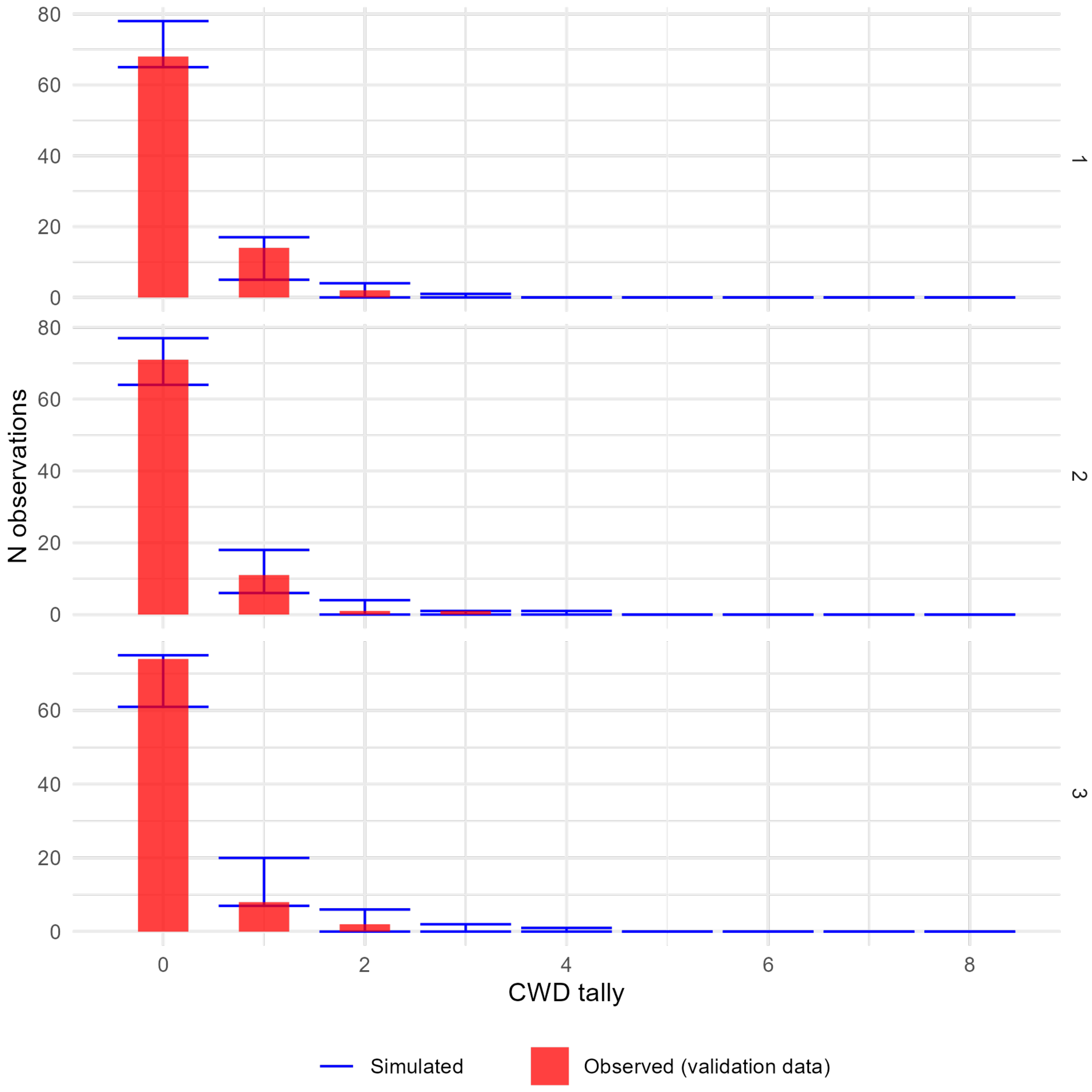

Supplementary Figure 34: Comparison of observed and simulated density distributions for the validation data and the coarse woody debris tallies model. Panels show posterior predictions generated using the posterior parameter values and the validation data for each of the three submodels representing low, medium, and high drought mortality (1, 2, and 3, respectively). In each panel, the x-axis shows an (observed or simulated) tally of coarse woody debris and the y-axis shows the frequency of samples from a dataset of 252 one meter subtransects having that tally (i.e., a histogram). The observed distribution of CWD tallies is plotted as the red histogram. The error bars within each tally value show the 2.5th and 97.5th percentile of the frequency of simulated samples having that tally value, across each of the 4,000 posterior draws showing the variation in model-predicted frequency distributions. The observed data are consistently within the range of behaviors predicted by the model.

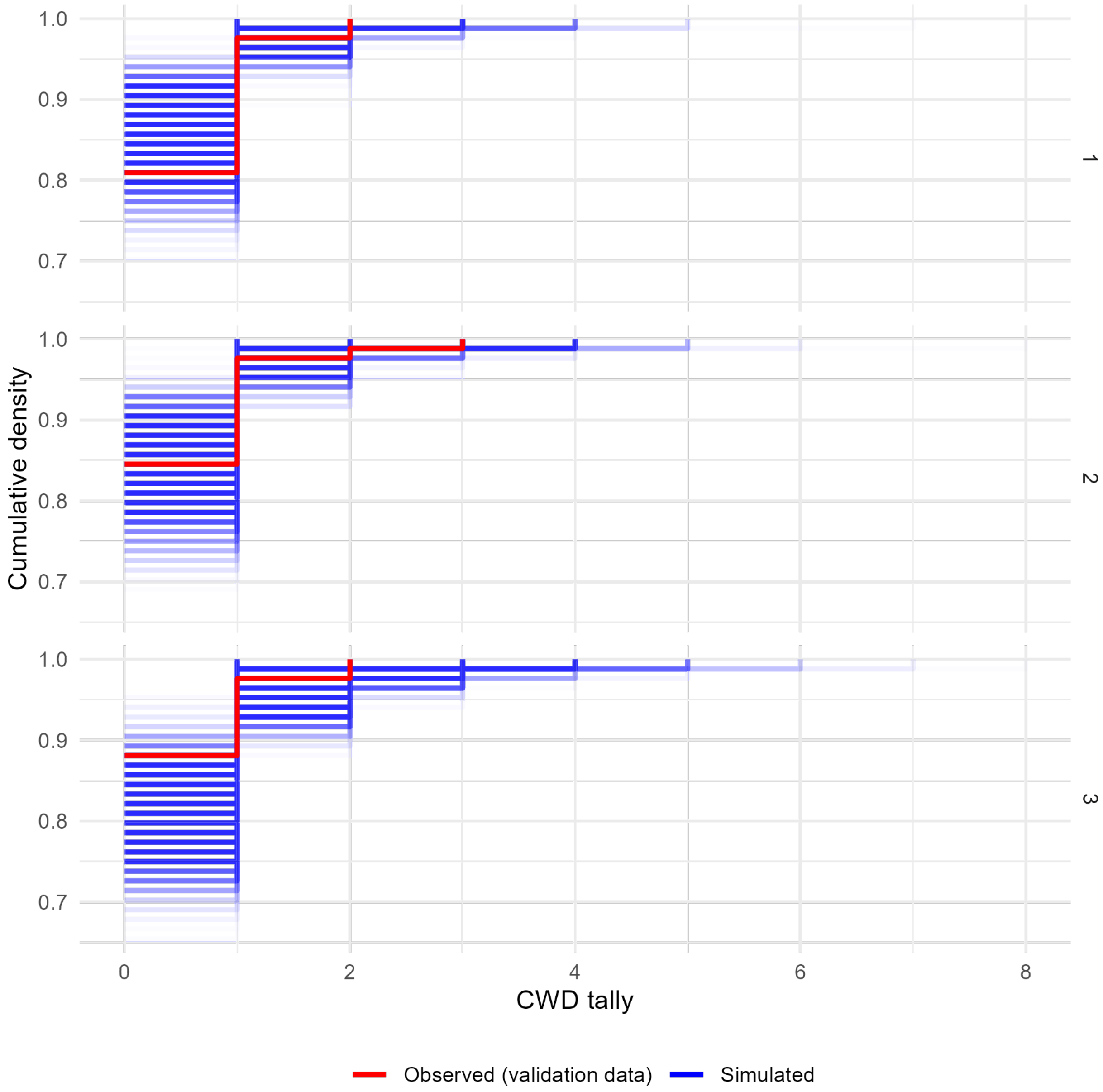

Supplementary Figure 35: Comparison of the observed and simulated cumulative density functions for the validation data and the coarse woody debris tallies model. Panels show the cumulative density functions of the observed validation data (red) and each of 4,000 simulated datasets generated using posterior parameter values and random effect realizations (blue) for each of the three sub-models corresponding to low, medium, or high levels of drought mortality. The observed cumulative density functions fall within the range of behaviors predicted by the model, indicating good agreement between the model and reality.

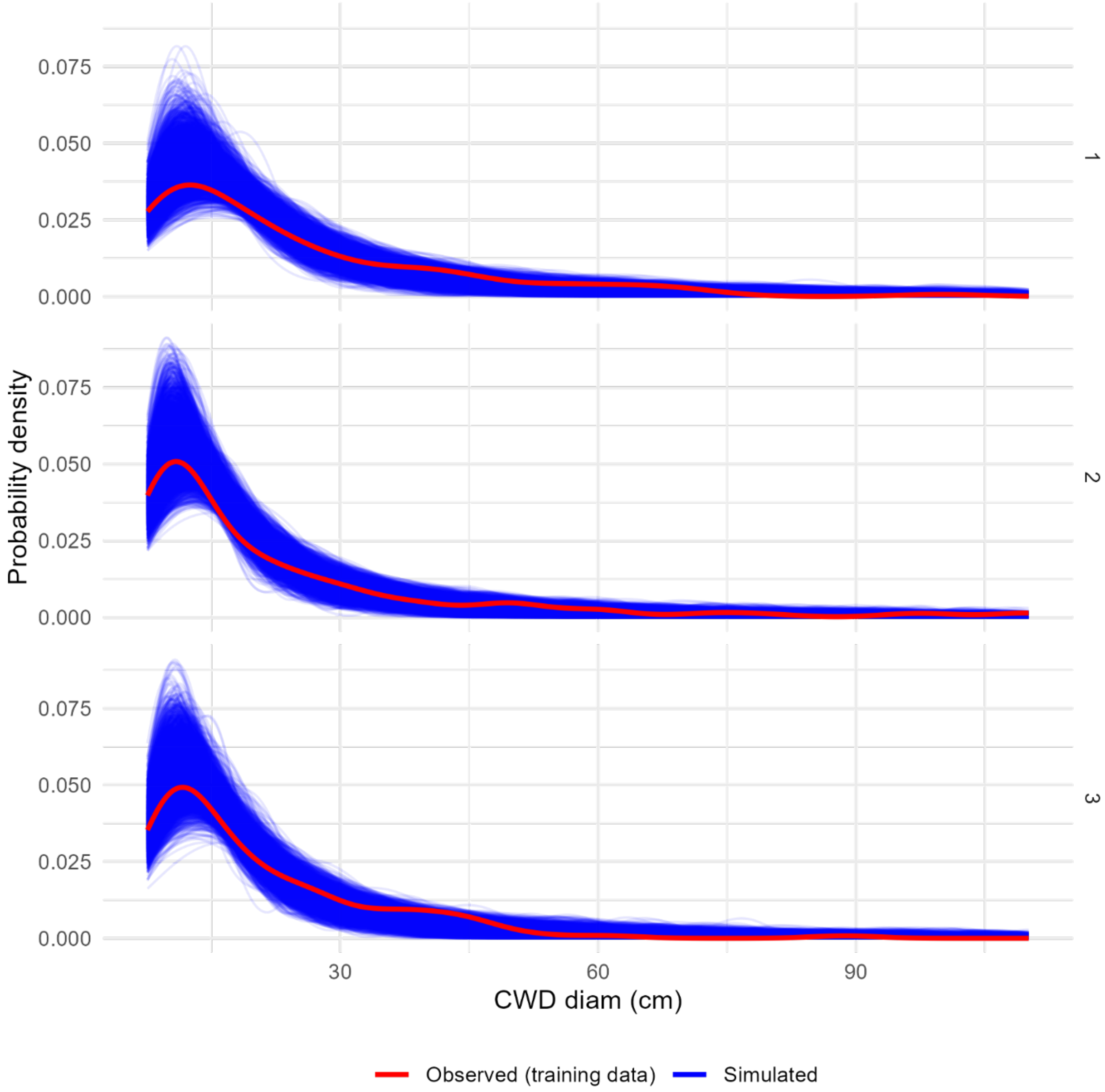

Supplementary Figure 36: Comparison of observed and simulated density distributions for training data and the coarse woody debris diameters model. Panels show the probability density functions of the observed training data (red) and each of 4,000 simulated datasets generated using posterior parameter values and random effect realizations (blue) for each of the three sub-models corresponding to low, medium, or high levels of drought mortality. Observed cumulative density functions fall within the range of behaviors predicted by the model, indicating good agreement between the model and reality.

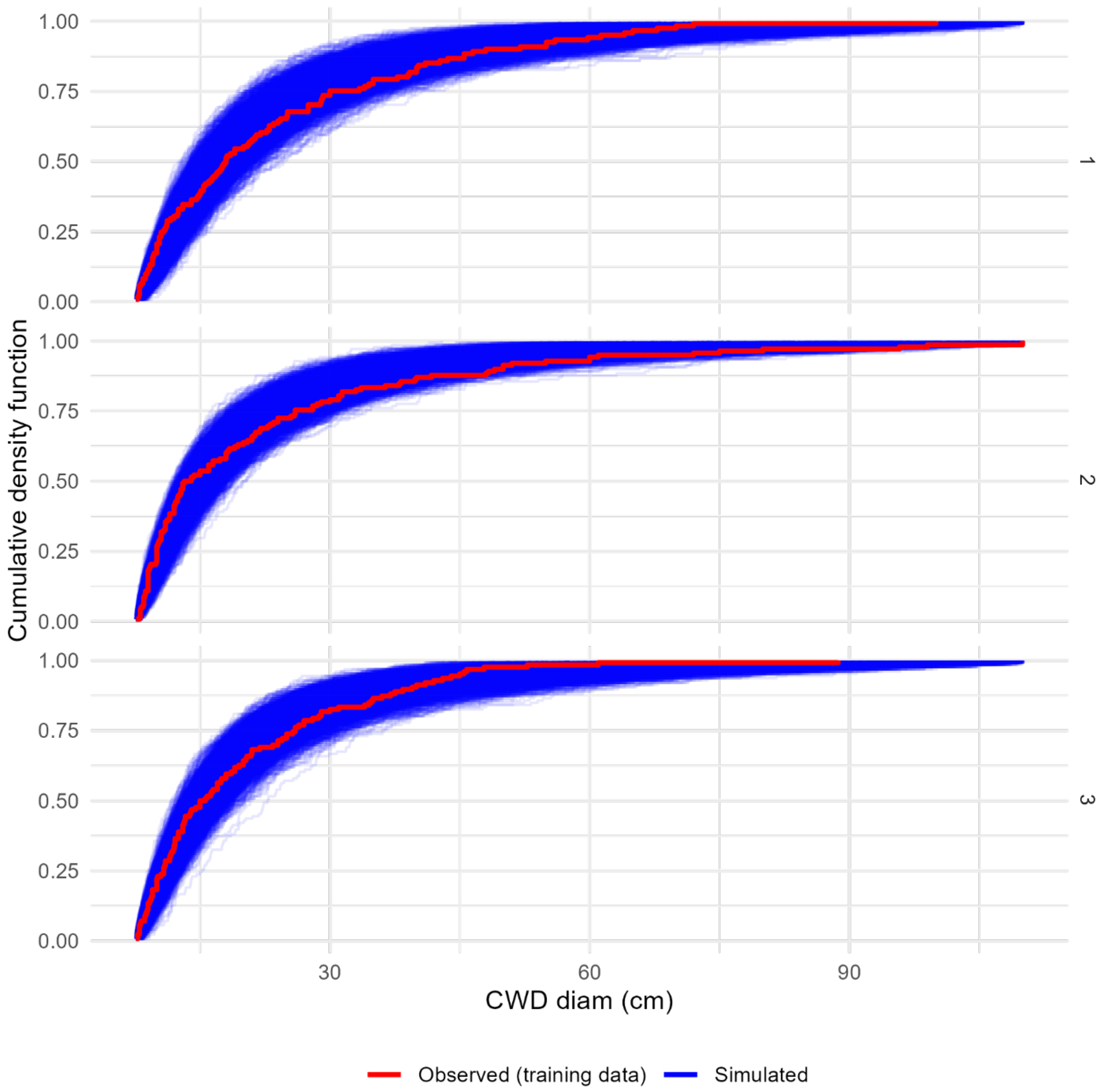

Supplementary Figure 37: Comparison of the observed and simulated cumulative density functions for the training data and the coarse woody debris diameters model. Panels show the cumulative density functions of the observed training data (red) and each of 4,000 simulated datasets generated using posterior parameter values and random effect realizations (blue) for each of the three sub-models corresponding to low, medium, or high levels of drought mortality. Observed cumulative density functions fall within the range of behaviors predicted by the model, indicating good agreement between the model and reality.

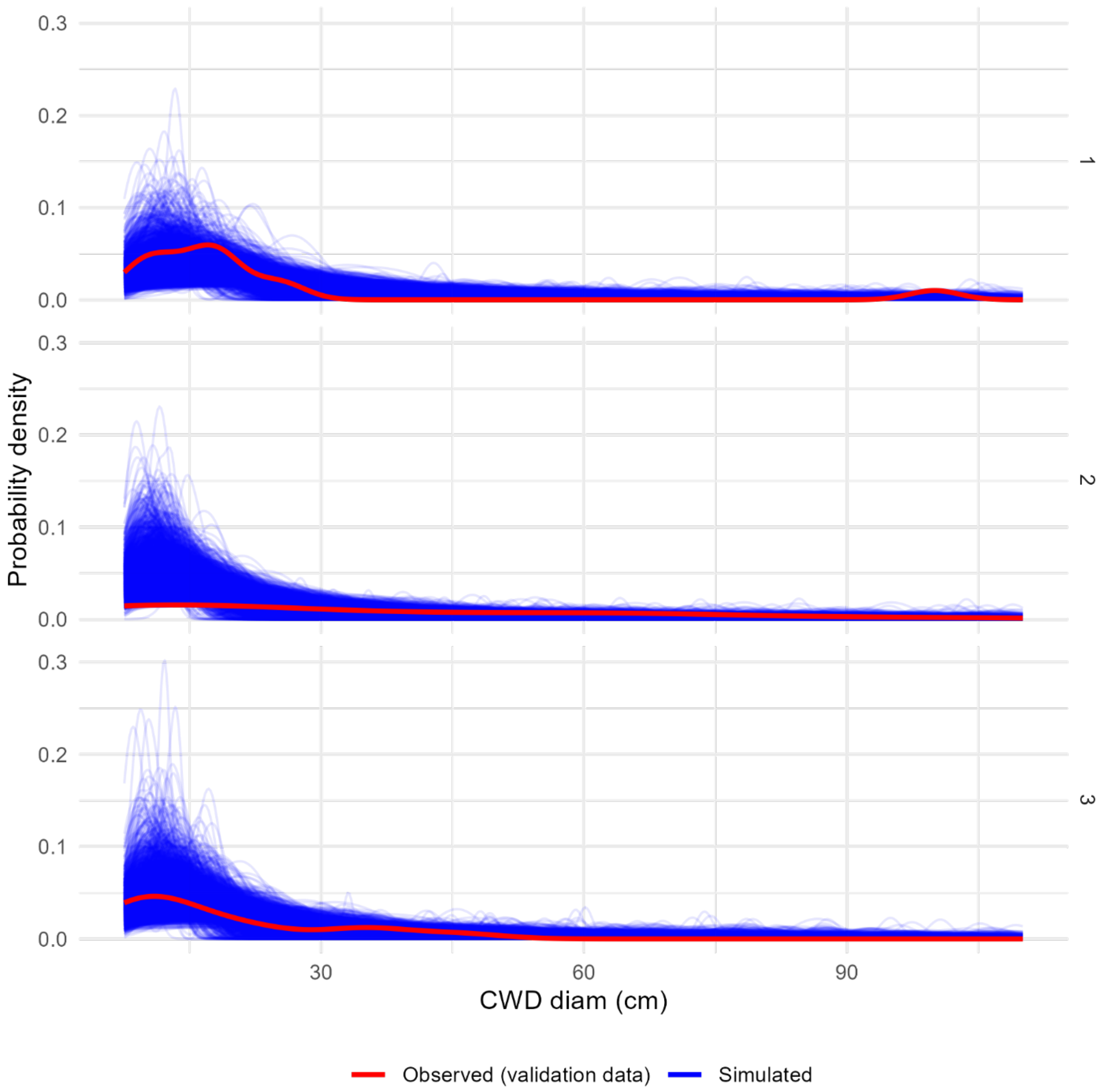

Supplementary Figure 38: Comparison of observed and simulated density distributions for the validation data and the coarse woody debris diameters model. Panels show the probability density functions of the observed validation data (red) and each of 4,000 simulated datasets generated using posterior parameter values and random effect realizations (blue) for each of the three sub-models corresponding to low, medium, or high levels of drought mortality. Observed cumulative density functions fall within the range of behaviors predicted by the model, though the dearth of observed diameters from approximately 5 to 25 cm for the medium drought mortality sub model is on the edge of model predicted behaviors.

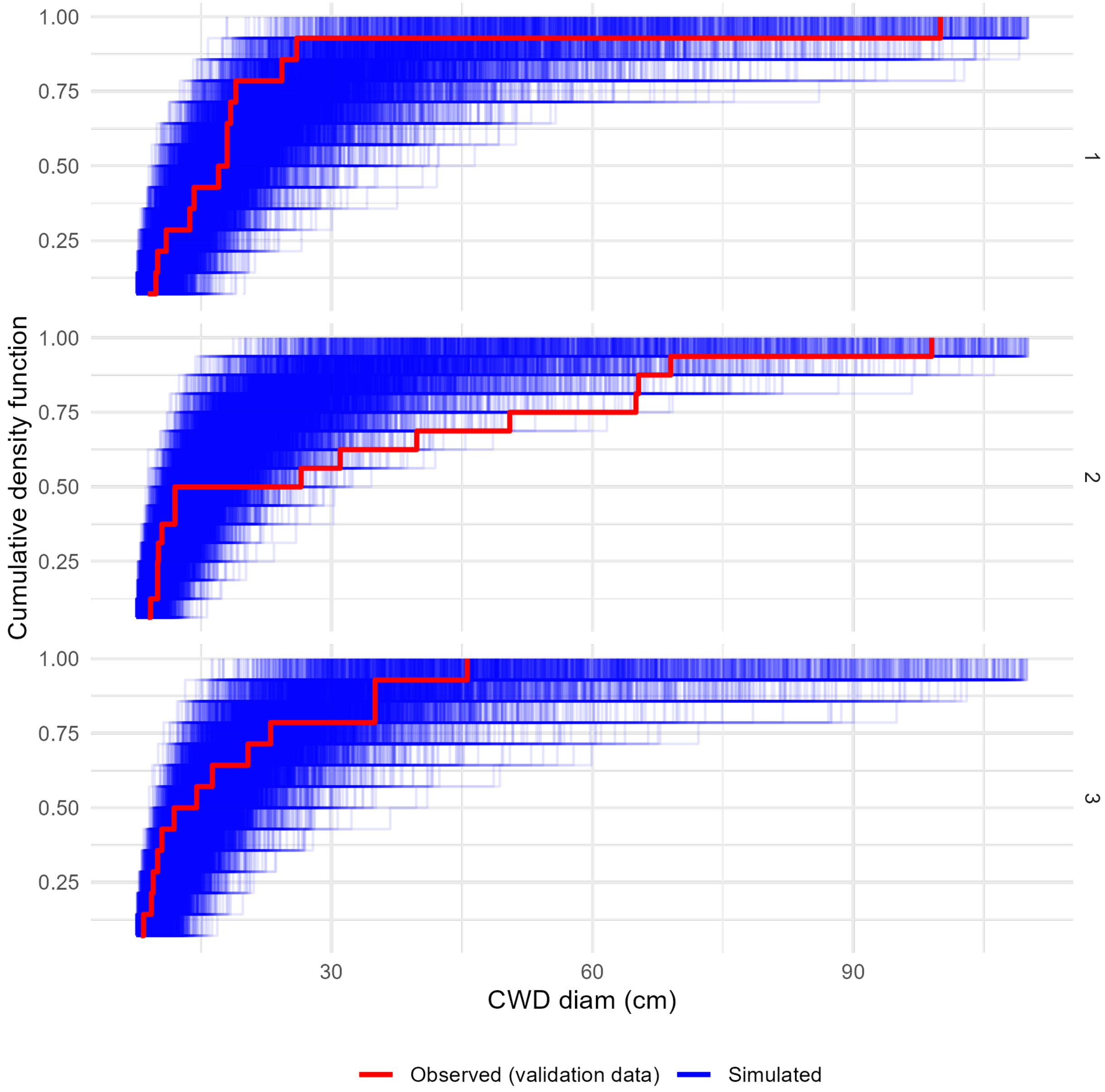

Supplementary Figure 39: Comparison of the observed and simulated cumulative density functions for the validation data and the coarse woody debris diameters model. Panels show the cumulative density functions of the observed validation data (red) and each of 4,000 simulated datasets generated using posterior parameter values and random effect realizations (blue) for each of the three sub-models corresponding to low, medium, or high levels of drought mortality. Observed cumulative density functions fall within the range of behaviors predicted by the model, though the dearth of observed diameters from approximately 5 to 25 cm for the medium drought mortality sub model is on the edge of model predicted behaviors.

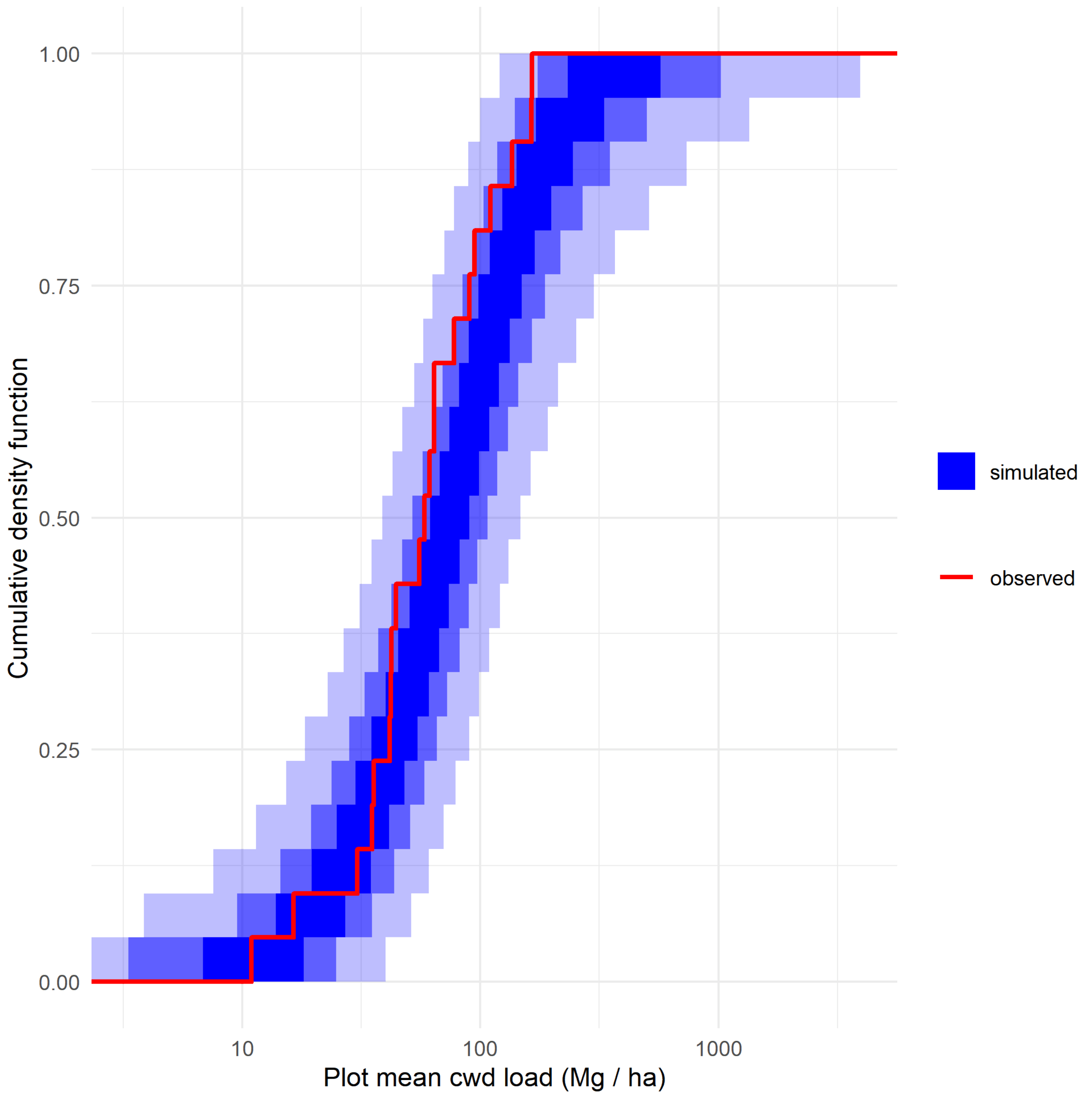

Supplementary Figure 40: Plot-level coarse woody debris simulations. For each of 4,000 posterior draws, 2,268 tallies of coarse woody debris on 1-meter subtransects were simulated using posterior parameter values from the coarse woody debris tallies model and drawing new random effect realizations for both fine-scale (Gaussian process) and coarse-scale (normally distributed plot intercepts) random effects. Then, for each simulated particle, a diameter was simulated using the coarse woody debris diameters model. The simulated particles on each subtransect were converted to biomass estimates on each subtransect and subtransects averaged at the plot level, giving 21 simulated plot-level fuel loads per posterior draw. The red cumulative density function is the cumulative density function of plot-level fuel loads calculated from the observed data. The blue bands show an envelope containing 50% (darkest), 90%, and 99% (lightest) of the cumulative density functions from the simulated draws. The observed data are within the range of behaviors predicted by the model, though the highest simulated loads are generally higher than the highest observed loads (red line is on the left edge of the envelope at the top of the figure).

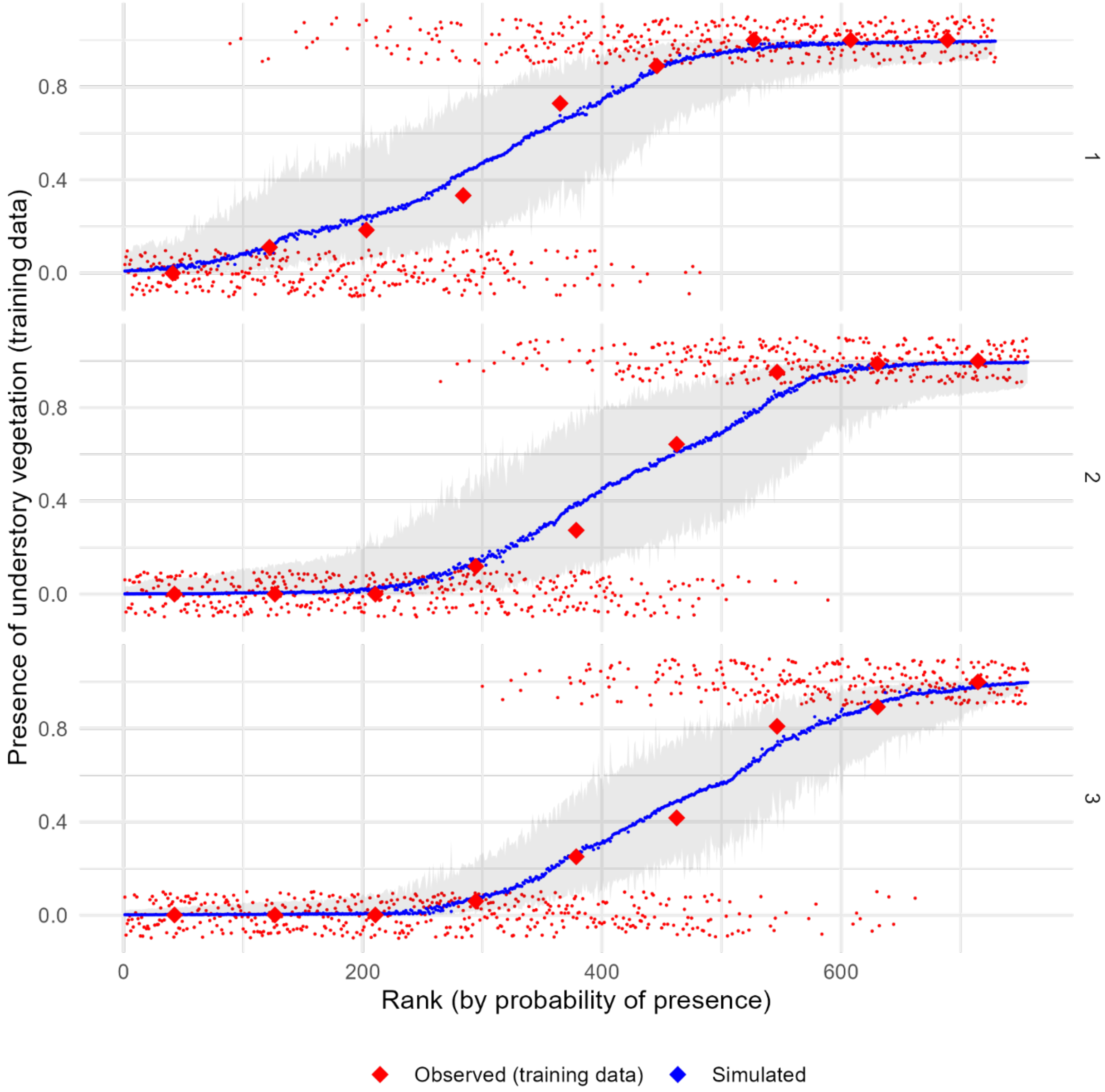

Supplementary Figure 41: Comparison of observed and simulated values from the training data and the vegetation presence model. For each of the 2,241 observations in the training dataset and each of the 4,000 posterior parameter samples, the probability of vegetation presence was calculated using the observed training data, posterior parameter values, and posterior random effect realizations. Each observation was assigned a rank based on the mean of its posterior presence probabilities. The red jittered points show the ranked probability of presence on the x-axis and the observed presence (1) or absence (0) for that observation. The red diamonds show the empirical proportion of presences for all observations in 10 bins (where the observations were binned by posterior predicted presence). The posterior mean (blue points) and a 95% credible interval (grey ribbon) presence probability for each individual observation are also shown. The model predictions generally agree well with the observed data, as indicated by the close correspondence between the mean observed behavior in the blue points and the predicted presence probabilities shown by the black points.

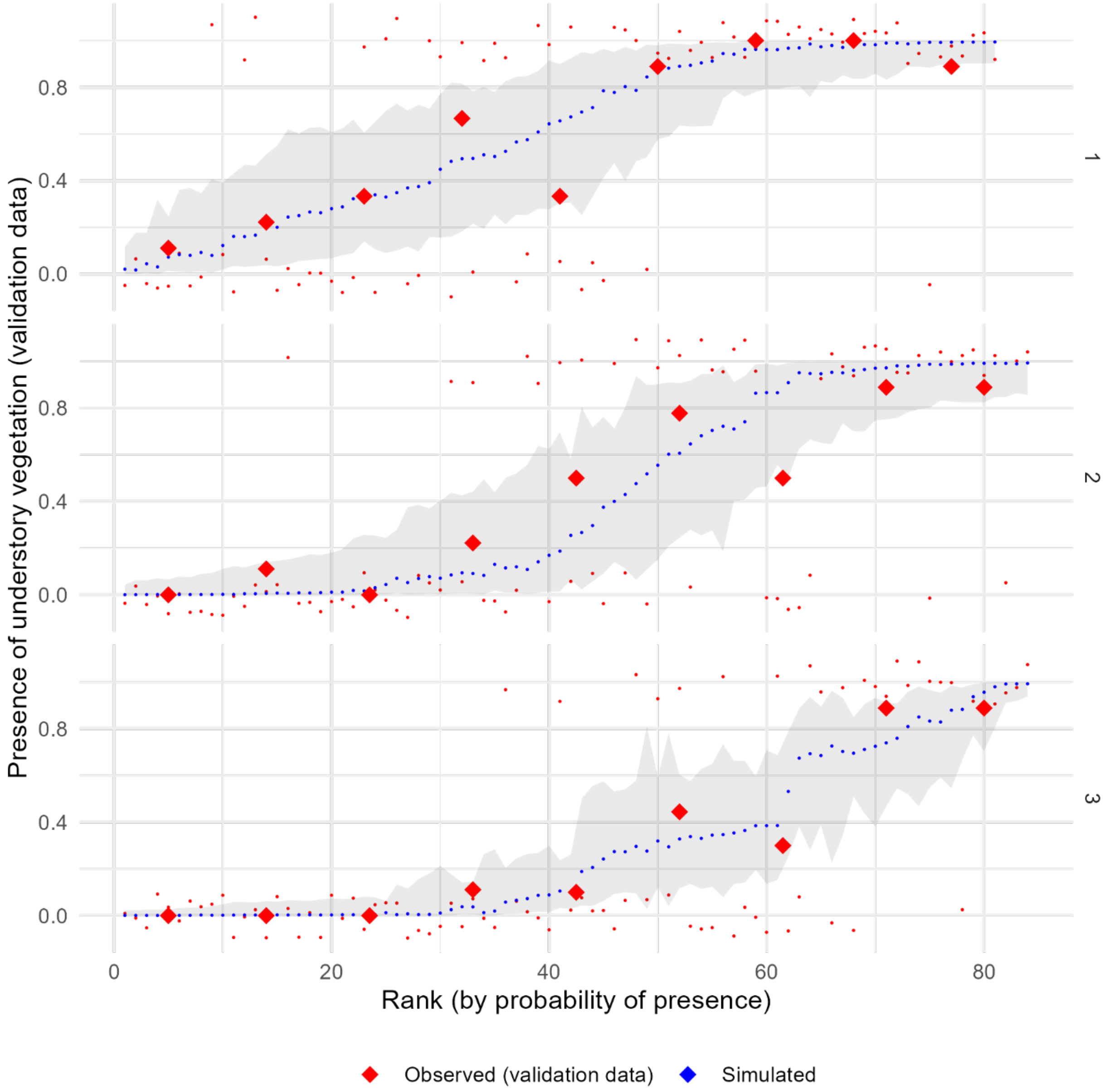

Supplementary Figure 42: Comparison of observed and simulated values for the validation data and the vegetation presences model. For each of the 249 observations in the validation dataset and each of the 4,000 posterior parameter samples, the probability of vegetation presence was calculated using the observed training data, posterior parameter values, and posterior random effect realizations. Each observation was assigned a rank based on the mean of its posterior presence probabilities. The red jittered points show the ranked probability of presence on the x-axis and the observed presence (1) or absence (0) for that observation. The red diamonds show the empirical proportion of presences for all observations in 10 bins (where the observations were binned by posterior predicted presence). The posterior mean (blue points) and a 95% credible interval (grey ribbon) presence probability for each individual observation are also shown. The model predictions generally agree well with the observed data, as indicated by the close correspondence between the mean observed proportions in the blue points and the predicted presence probabilities shown by the black points.

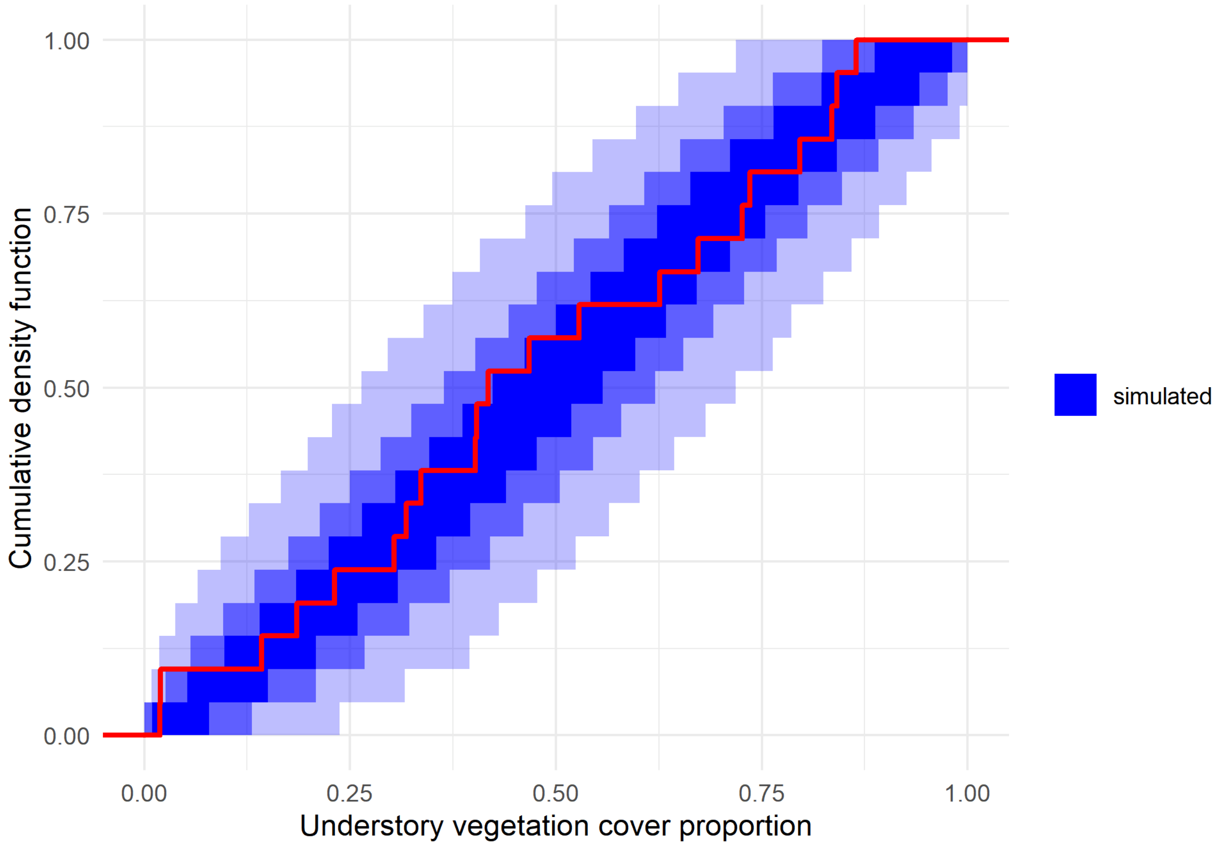

Supplementary Figure 43: Plot-level understory vegetation simulations. For each of 4,000 posterior draws, presence/absence of understory vegetation at 2,241 quadrature points was simulated using posterior parameter values from the understory vegetation model and drawing new random effect realizations for both fine-scale (Gaussian process) and coarse-scale (normally distributed plot intercepts) random effects. The simulated quadrature points were averaged at the plot level, giving 21 simulated plot-level cover proportions per posterior draw. The red cumulative density function is the cumulative density function of plot-level vegetation cover calculated from the observed data. The blue bands show an envelope containing 50% (darkest), 90%, and 99% (lightest) of the cumulative density functions from the simulated draws. The observed data are within the range of behaviors predicted by the model.

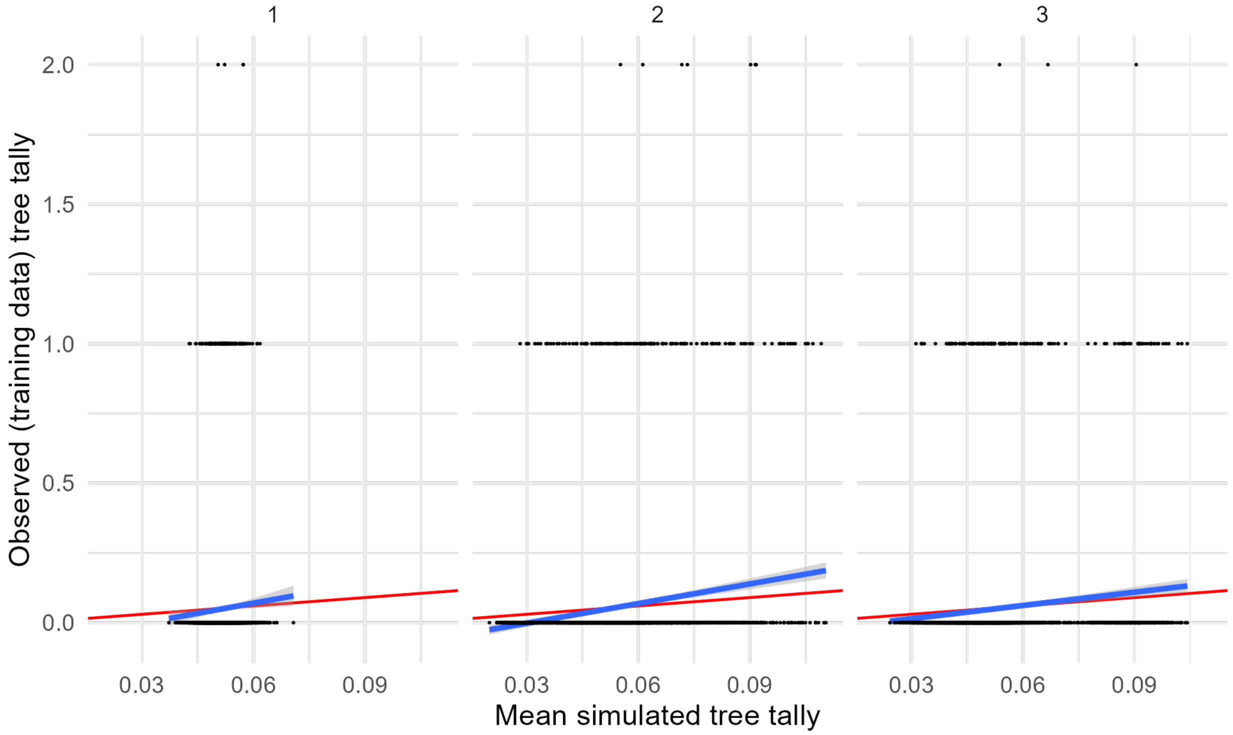

Supplementary Figure 44: Per-observation comparisons of mean predicted and observed values for the training data and the tree tallies model. For each of the 9.450 1 m^2 quadrats in the training data, a count of stems > 11.4 cm DBH was simulated from each of 4,000 posterior draws. The simulations were averaged together by quadrat, and a point is plotted for each quadrat with the x-axis being the mean simulated count of stems in that quadrat and the y-axis being the observed count of stems in that quadrat. A best-fit linear model between simulated and observed counts is plotted in blue, and a line with slope 1 and intercept 0 (representing perfect prediction) is plotted in red. The very low observed counts (95% of training quadrats had 0 trees, and only a handful had two) make interpretation of the relationship between predicted and observed values difficult. However, the linear relationship between predicted and observed is reasonably close to the perfect prediction line.

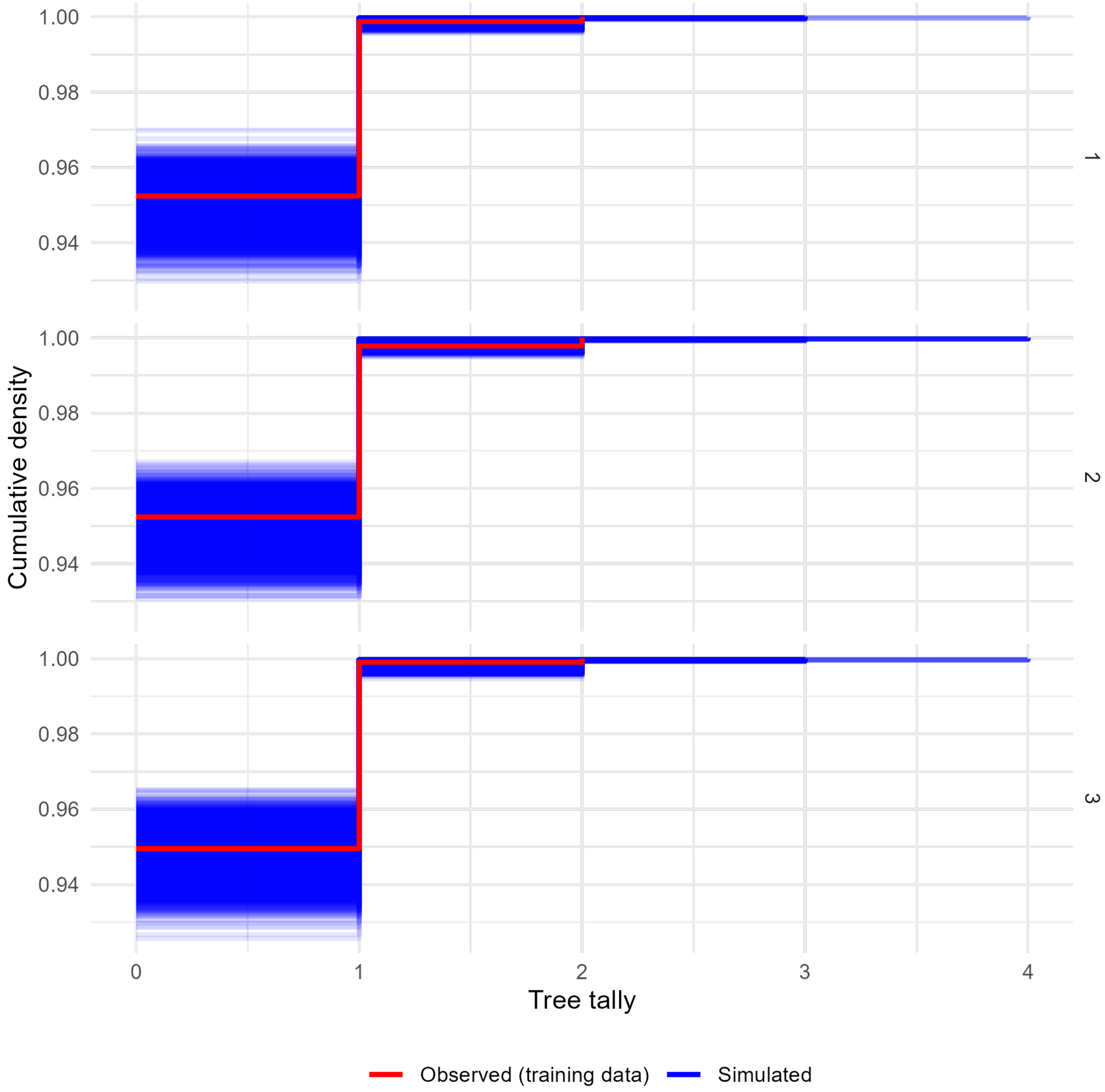

Supplementary Figure 45: Comparison of the observed and simulated cumulative density functions for the training data and the tree tallies model. Panels show the cumulative density functions of the observed training data (red) and each of 4,000 simulated datasets generated using posterior parameter values and random effect realizations (blue) for each of the three sub-models corresponding to low, medium, or high levels of drought mortality. Observed cumulative density functions fall within the range of behaviors predicted by the model, with the observed frequency of 0-count quadrats falling squarely in the range of simulated frequencies (left side of figure). However, the simulations include rare quadrats with 3 or even 4 trees in a single square meter, which never occurred in the training data.

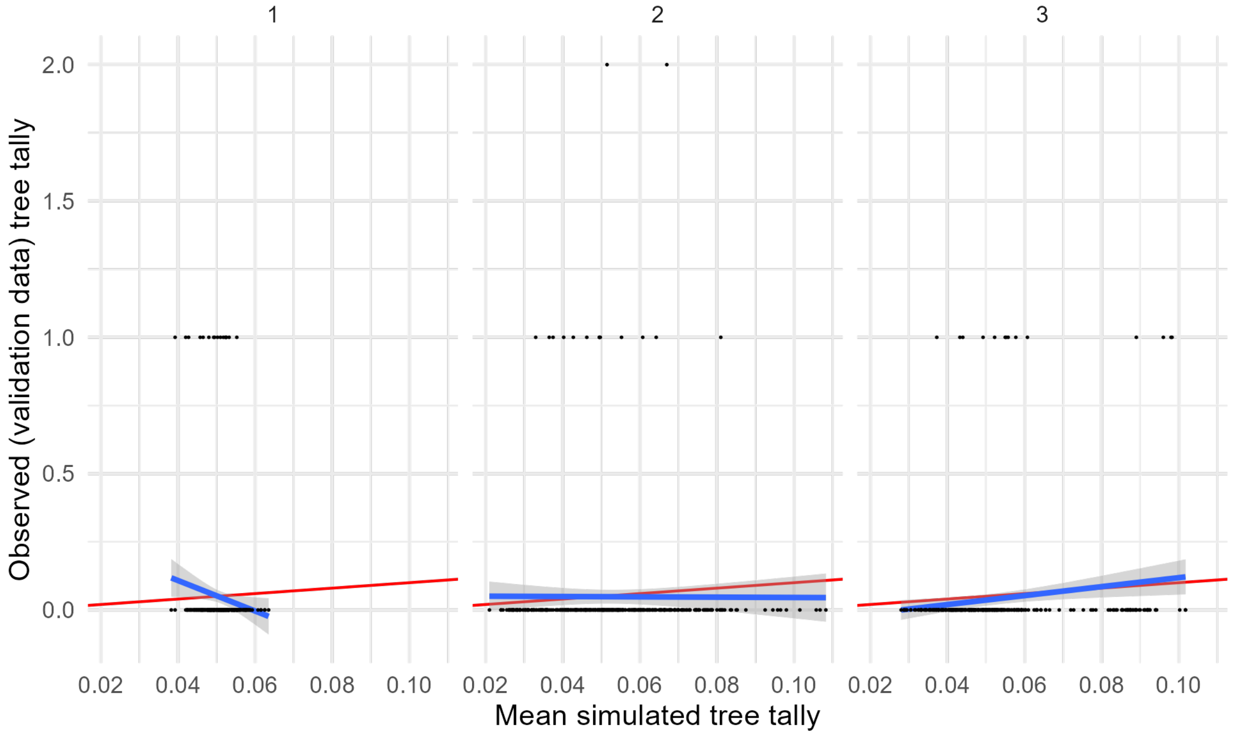

Supplementary Figure 46: Per-observation comparisons of mean predicted and observed values for the validation data and the tree tallies model. For each of the 1,050 1 m^2 quadrats in the validation data, a count of stems > 11.4 cm DBH was simulated from each of 4,000 posterior draws. The simulations were averaged together by quadrat, and a point is plotted for each quadrat with the x-axis being the mean simulated count of stems in that quadrat and the y-axis being the observed count of stems in that quadrat. A best-fit linear model between simulated and observed counts is plotted in blue, and a line with slope 1 and intercept 0 (representing perfect prediction) is plotted in red. The very low observed counts (95% of training quadrats had 0 trees, and only a handful had two) make interpretation of the relationship between predicted and observed values difficult. For sub-model 1 (low drought mortality), the model does a poor job and there is actually a negative linear relationship between the mean predicted counts and the observed counts. For sub-model 2 (medium drought mortality), the model again performs poorly and there is no clear relationship between the mean predicted counts and the observed counts. Only for sub-model 3 (high drought mortality) does the model perform reasonably well.

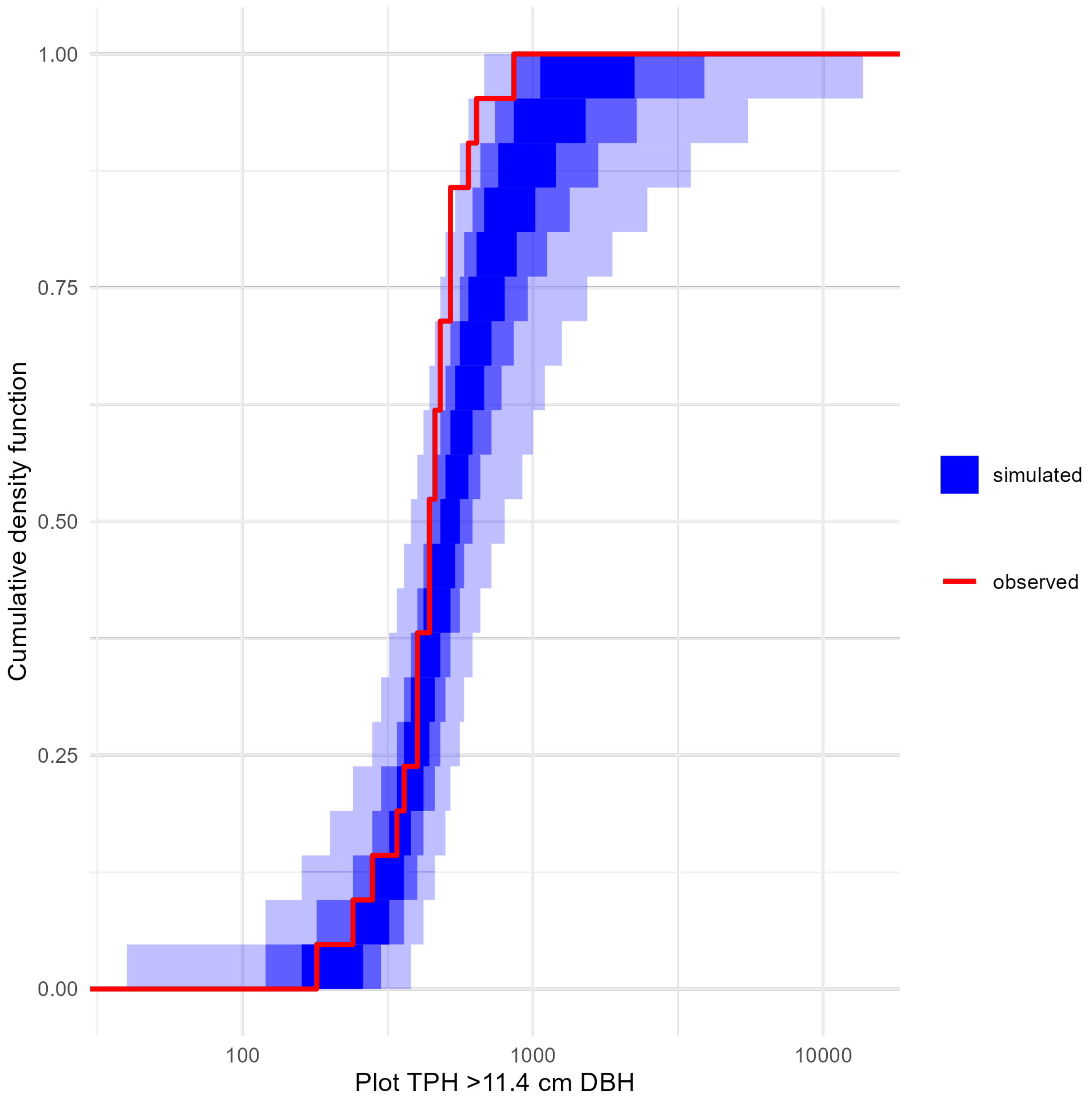

Supplementary Figure 47: Plot-level tree tally simulations. For each of 4,000 posterior draws, a count of trees on 9,450 1 m^2 quadrats was simulated using posterior parameter values from the tree counts model and drawing new random effect realizations for both fine-scale (Gaussian process) and coarse-scale (normally distributed plot intercepts) random effects. The number of simulated trees were then summed at the plot level, giving 21 simulated plot-level stem density realizations per posterior draw. The red cumulative density function is the cumulative density function of plot-level vegetation cover calculated from the observed data. The blue bands show an envelope containing 50% (darkest), 90%, and 99% (lightest) of the cumulative density functions from the simulated draws. The observed data are within the range of behaviors predicted by the model, but just barely. In particular, the model appears to overpredict the frequency of plots with more than 600 stems per hectare.

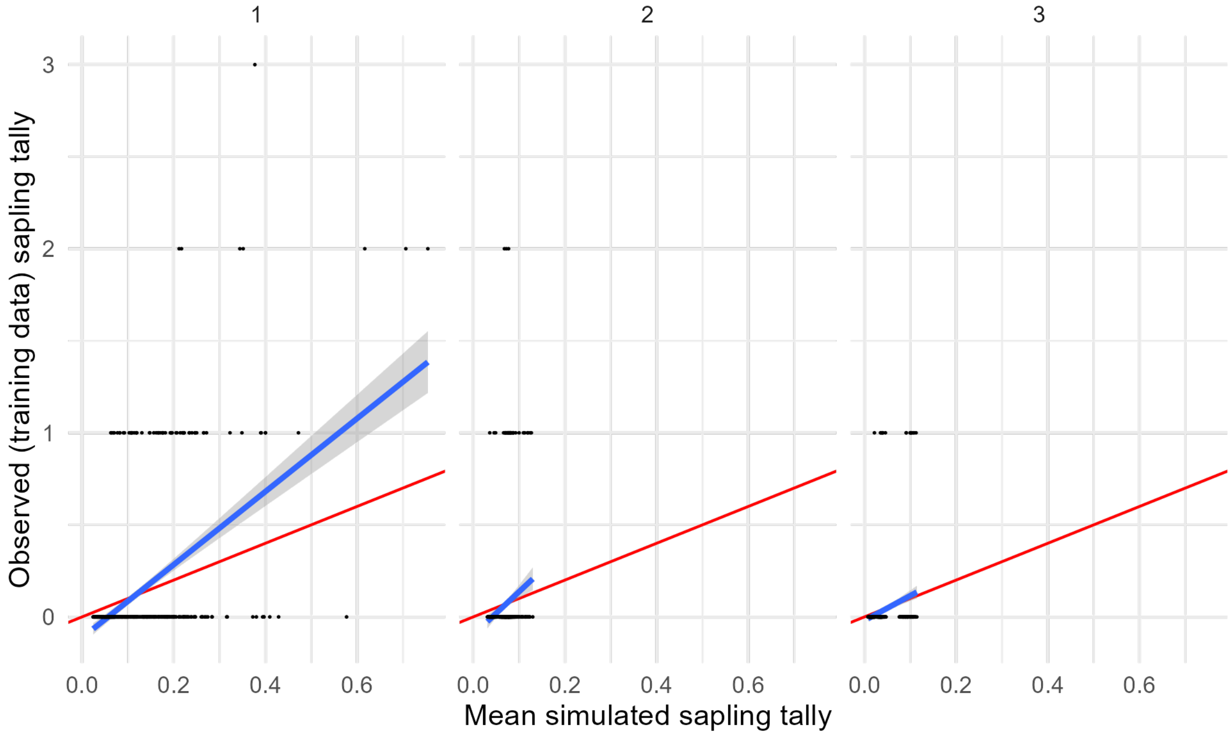

Supplementary Figure 48: Per-observation comparisons of mean predicted and observed values for the training data and the sapling tallies model. For each of the 2,190 1 m^2 quadrats in the training data, a count of stems < 11.4 cm DBH was simulated from each of 4,000 posterior draws. The simulations were averaged together by quadrat, and a point is plotted for each quadrat with the x-axis being the mean simulated count of stems in that quadrat and the y-axis being the observed count of stems in that quadrat. A best-fit linear model between simulated and observed counts is plotted in blue, and a line with slope 1 and intercept 0 (representing perfect prediction) is plotted in red. The very low observed counts make interpretation of the relationship between predicted and observed values difficult. However, there is at least a positive relationship between the mean predicted counts and the observed counts.

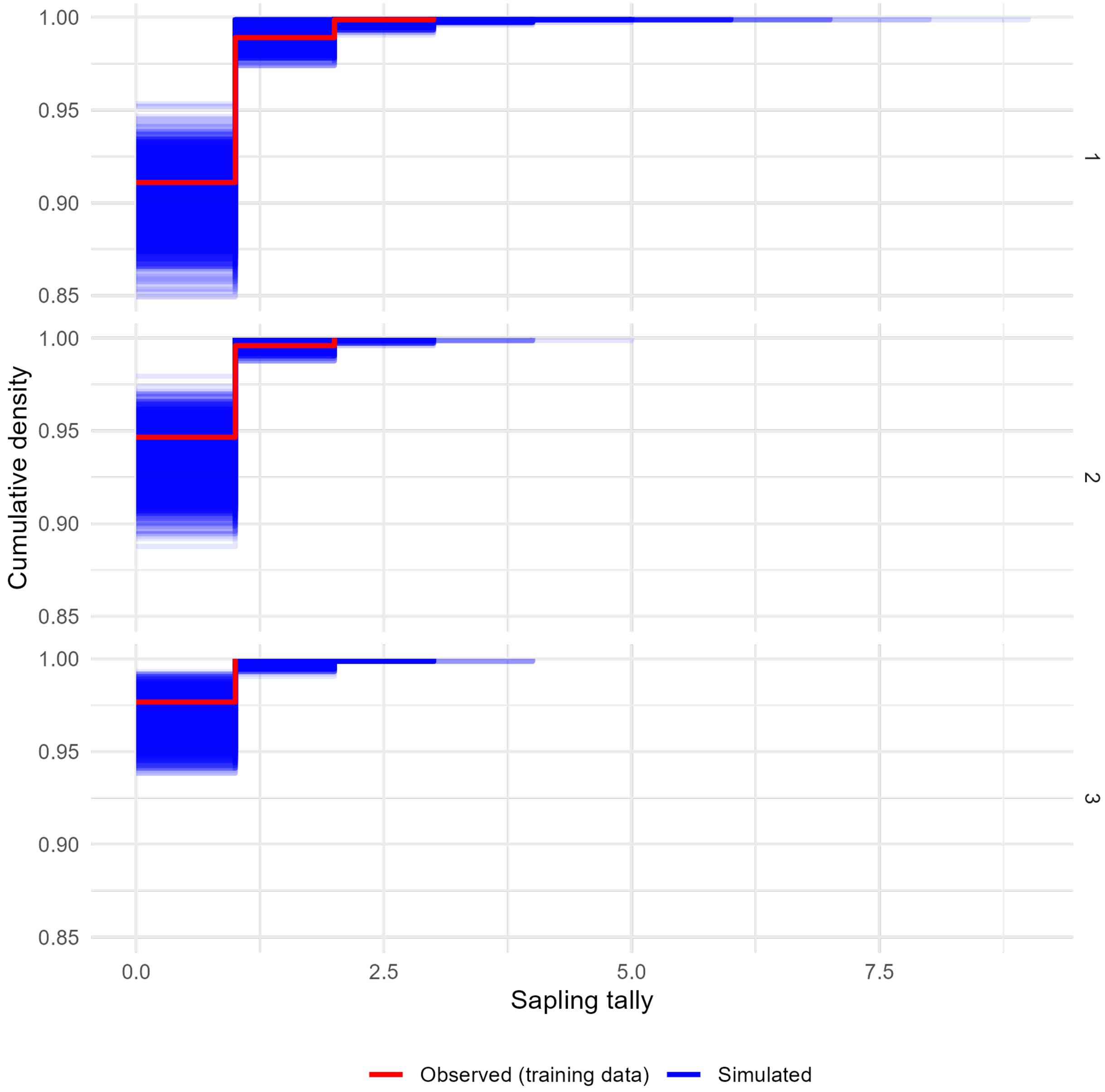

Supplementary Figure 49: Comparison of the observed and simulated cumulative density functions for the training data and the sapling tallies model. Panels show the cumulative density functions of the observed training data (red) and each of 4,000 simulated datasets generated using posterior parameter values and random effect realizations (blue) for each of the three sub-models corresponding to low, medium, or high levels of drought mortality. Observed cumulative density functions fall within the range of behaviors predicted by the model, with the observed frequency of 0-count quadrats falling squarely in the range of simulated frequencies (left side of figure). However, the simulations include rare quadrats with 4 or more saplings in a single square meter, which never occurred in the training data.

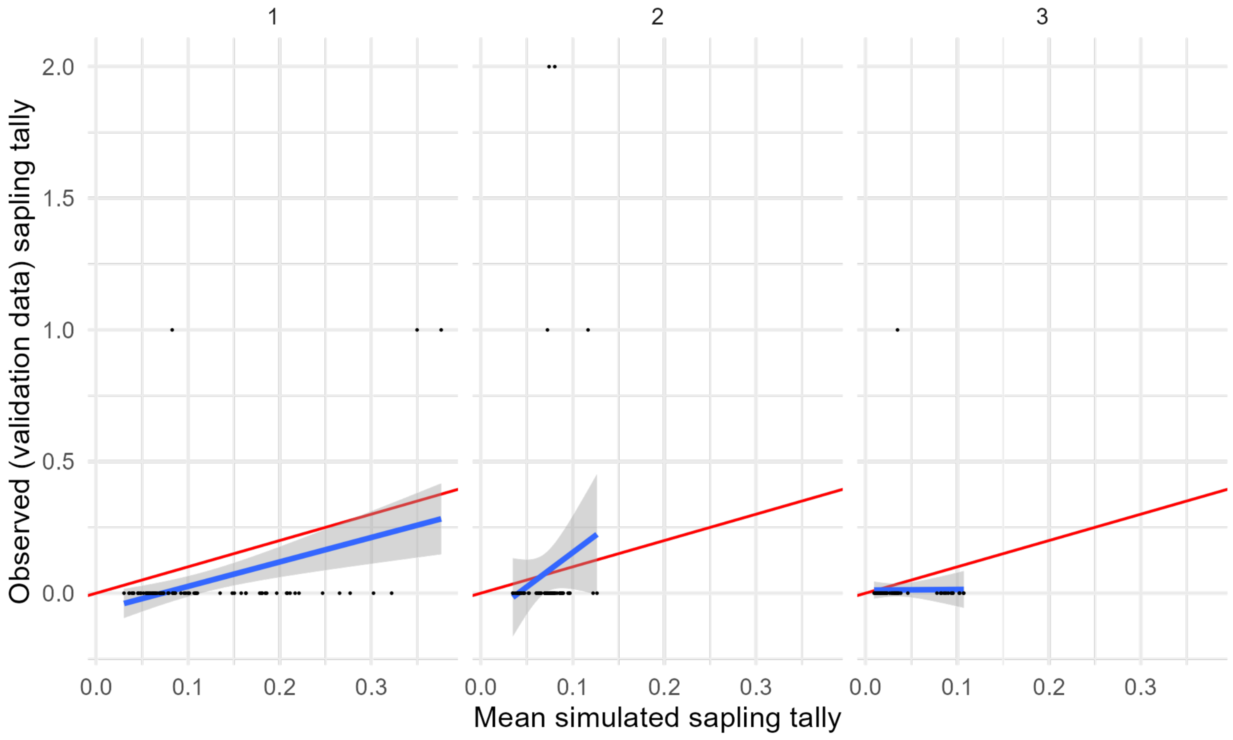

Supplementary Figure 50: Per-observation comparisons of mean predicted and observed values for the validation data and the sapling tallies model. For each of the 246 1 m^2 quadrats in the validation data, a count of stems < 11.4 cm DBH was simulated from each of 4,000 posterior draws. The simulations were averaged together by quadrat, and a point is plotted for each quadrat with the x-axis being the mean simulated count of stems in that quadrat and the y-axis being the observed count of stems in that quadrat. A best-fit linear model between simulated and observed counts is plotted in blue, and a line with slope 1 and intercept 0 (representing perfect prediction) is plotted in red. The very low observed counts make interpretation of the relationship between predicted and observed values difficult. For sub-model 3 (high drought mortality), the model does a poor job and there is actually a negative linear relationship between the mean predicted counts and the observed counts. For sub-model 1 (high drought mortality), the model consistently underpredicts the count of stems. Only for sub-model 2 (medium drought mortality) does the model perform reasonably well.

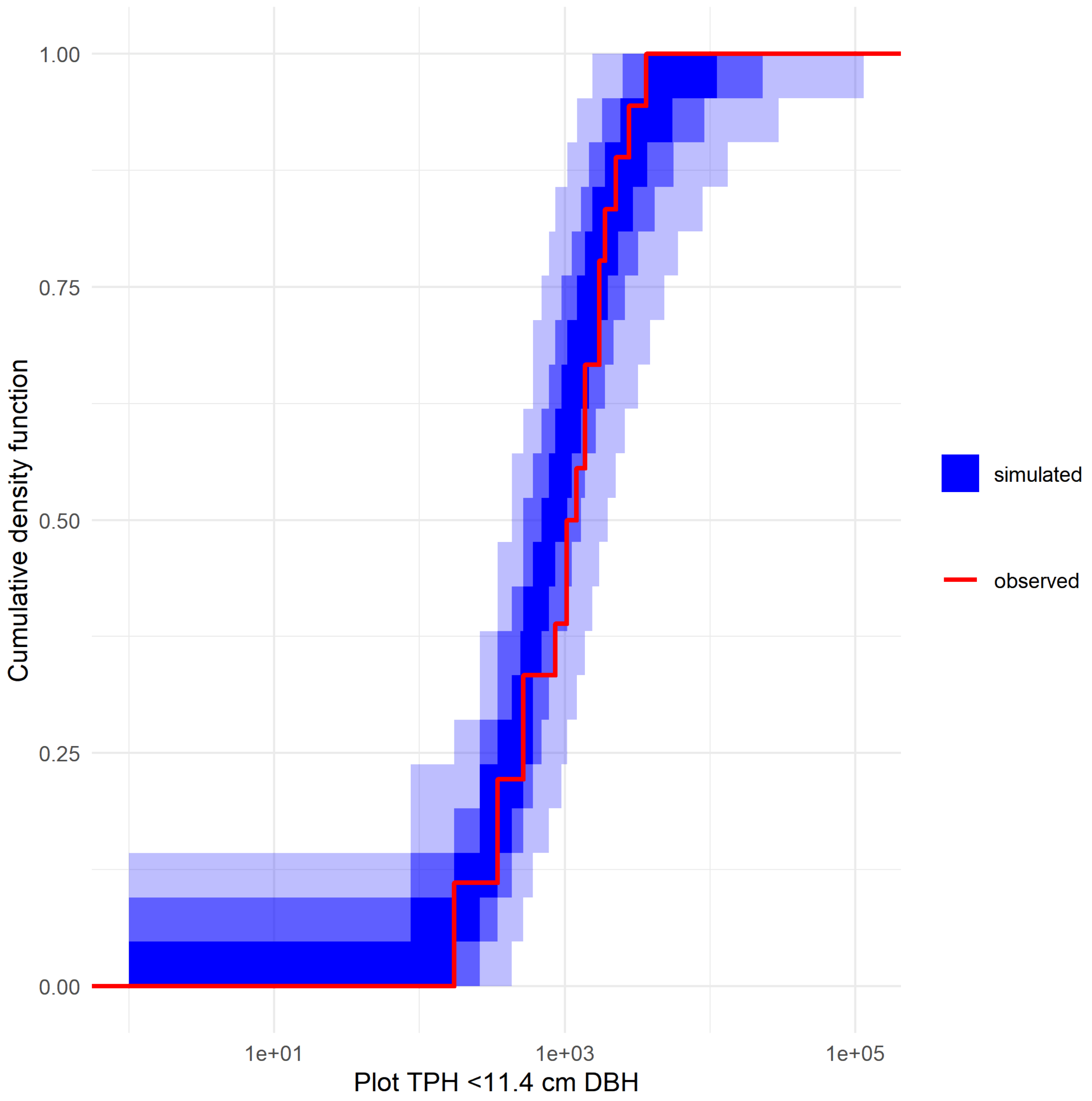

Supplementary Figure 51: Plot-level sapling count simulations. For each of 4,000 posterior draws, a count of stems on 2190 1 m^2 quadrats was simulated using posterior parameter values from the sapling counts model and drawing new random effect realizations for both fine-scale (Gaussian process) and coarse-scale (normally distributed plot intercepts) random effects. The number of simulated saplings were then summed at the plot level, giving 21 simulated plot-level stem density realizations per posterior draw. The red cumulative density function is the cumulative density function of plot-level vegetation cover calculated from the observed data. The blue bands show an envelope containing 50% (darkest), 90%, and 99% (lightest) of the cumulative density functions from the simulated draws. The observed data are within the range of behaviors predicted by the model.

13 Supplementary materials for “Beyond fuel reduction: Prescribed fire alters spatial pattern of wildland fuels”

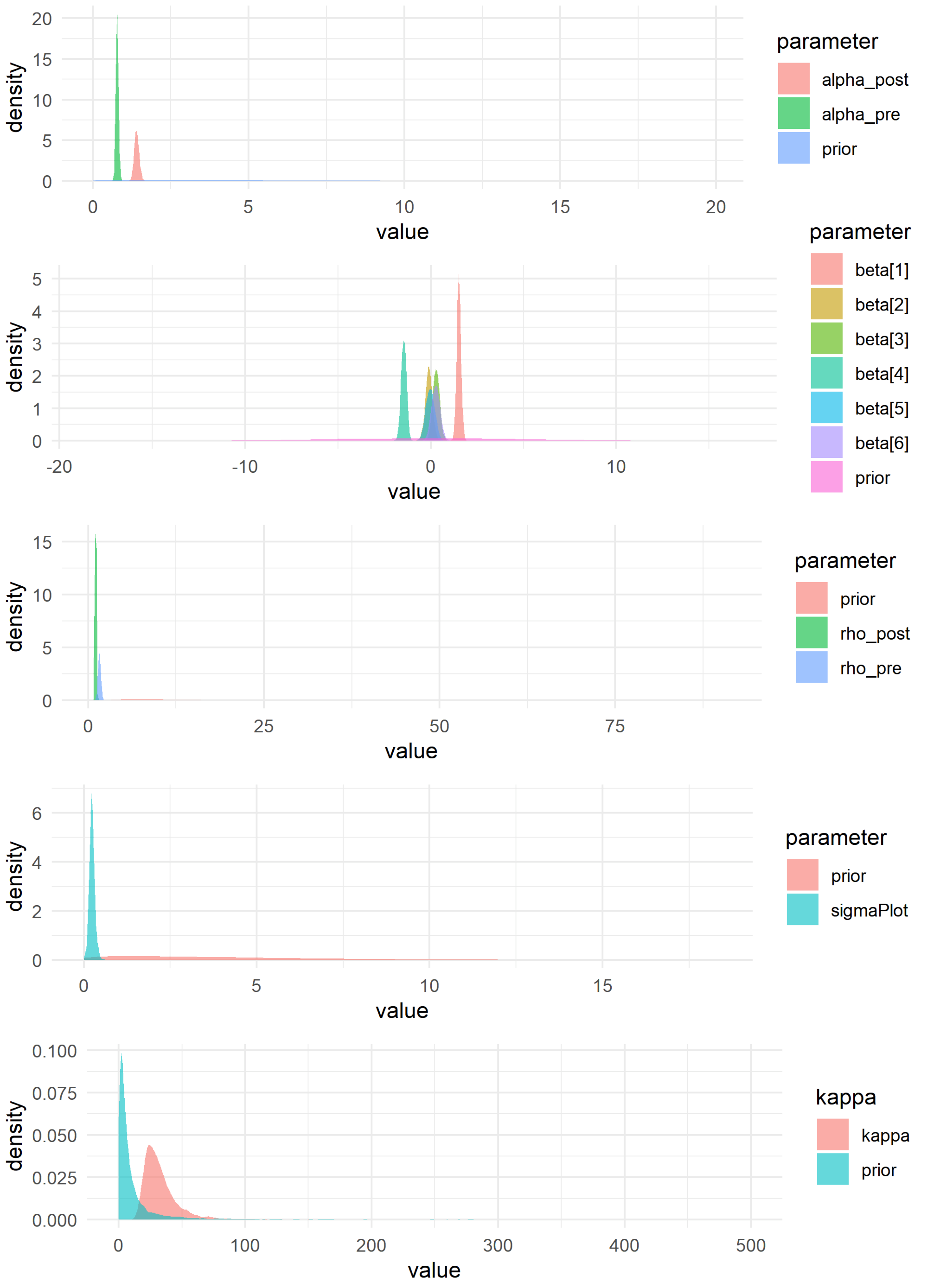

Supplementary Figure 52: Prior vs. posterior distributions for all parameters of the model for litter and duff depths. Clear differences between the prior and posterior distributions exist for all parameters, indicating that the posterior estimates were strongly informed by the data, rather than the priors.

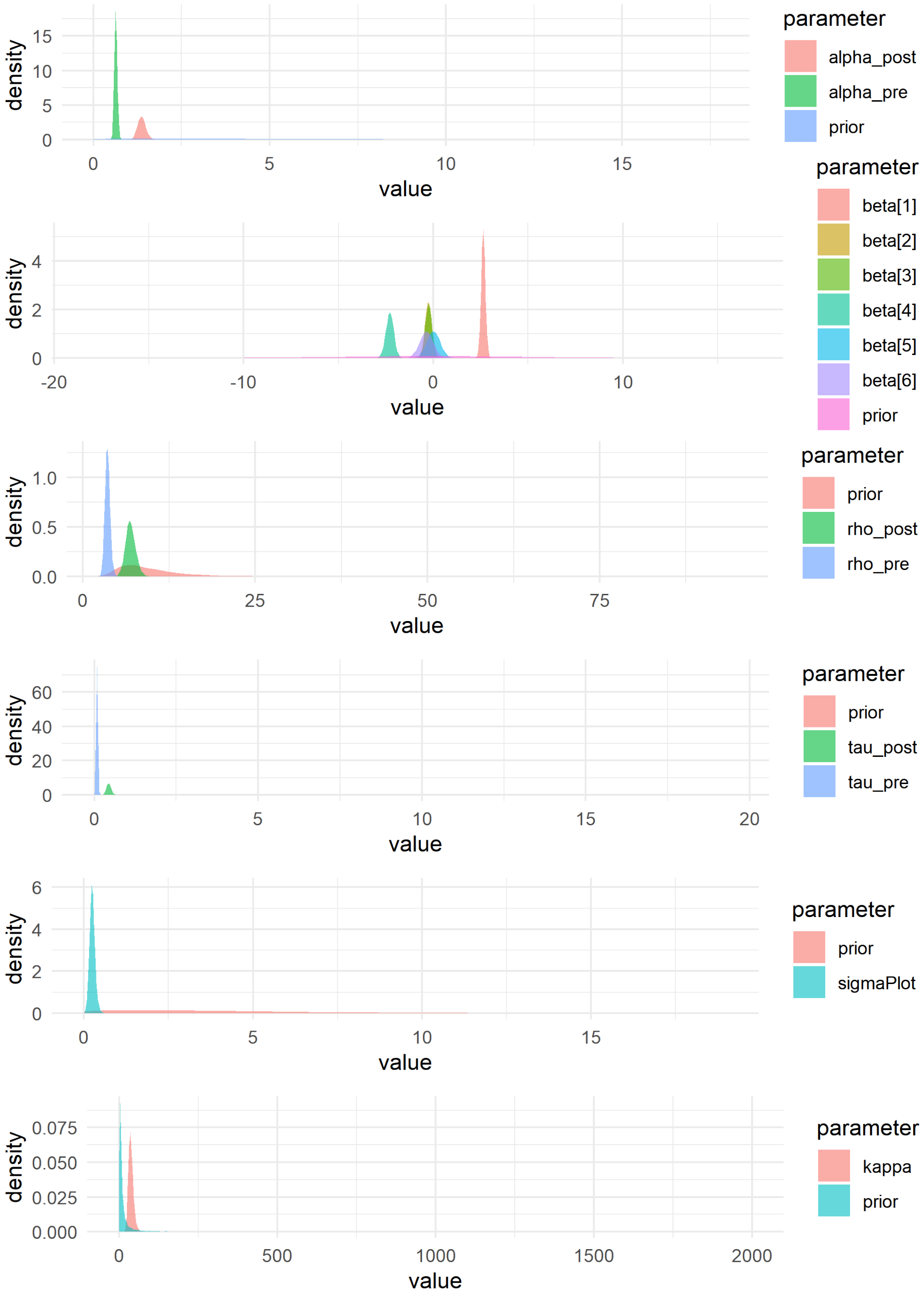

Supplementary Figure 53: Prior vs. posterior parameter distributions for all parameters in the model for 1-hour fine woody debris tallies. In all cases, there are clear differences between the prior and the posterior distributions, indicating that parameter estimates are strongly informed by the data, rather than the prior.

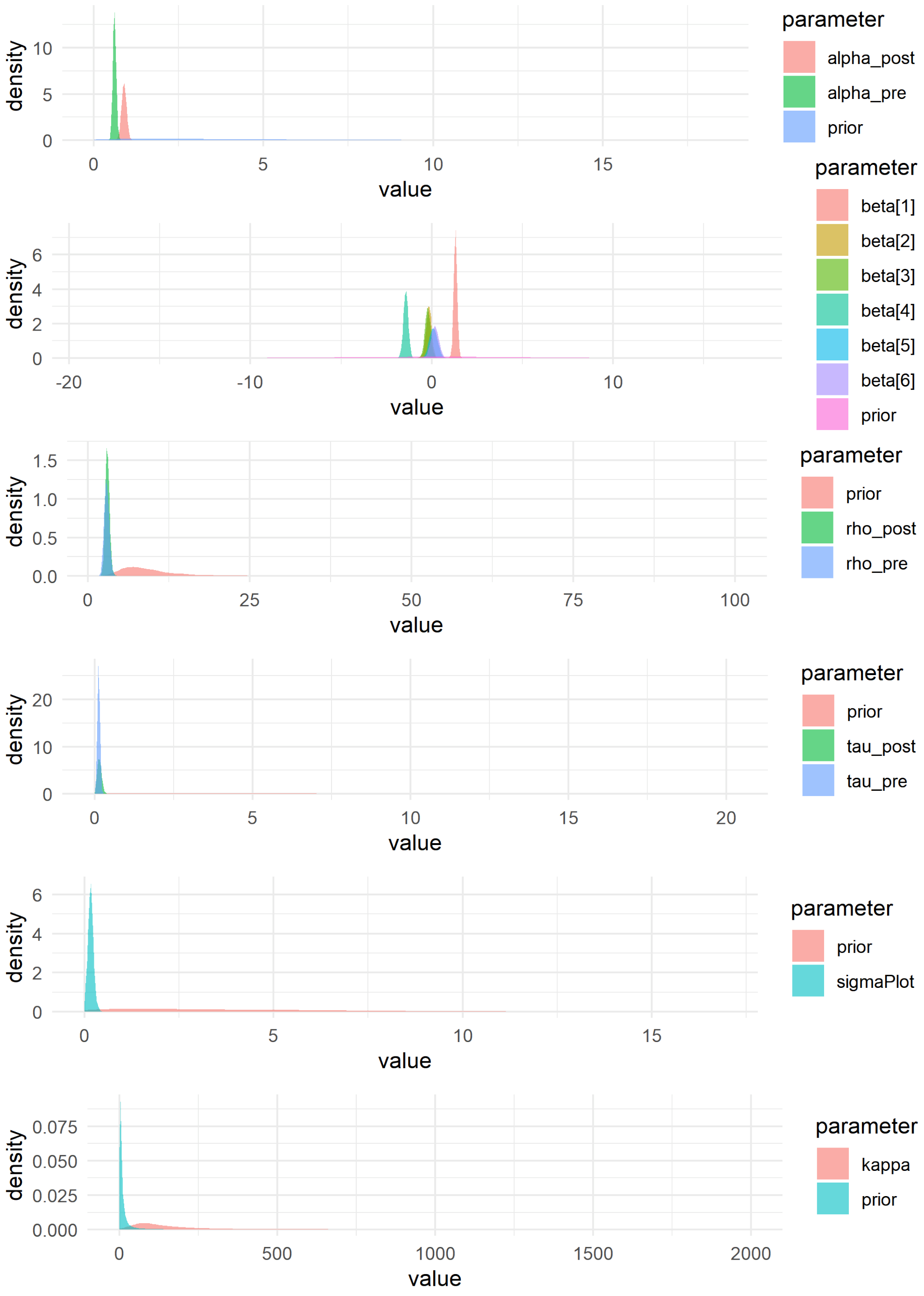

Supplementary Figure 54: Prior vs. posterior parameter distributions for all parameters in the model for 10-hour fine woody debris tallies. In all cases, there are clear differences between the prior and the posterior distributions, indicating that parameter estimates are strongly informed by the data, rather than the prior.

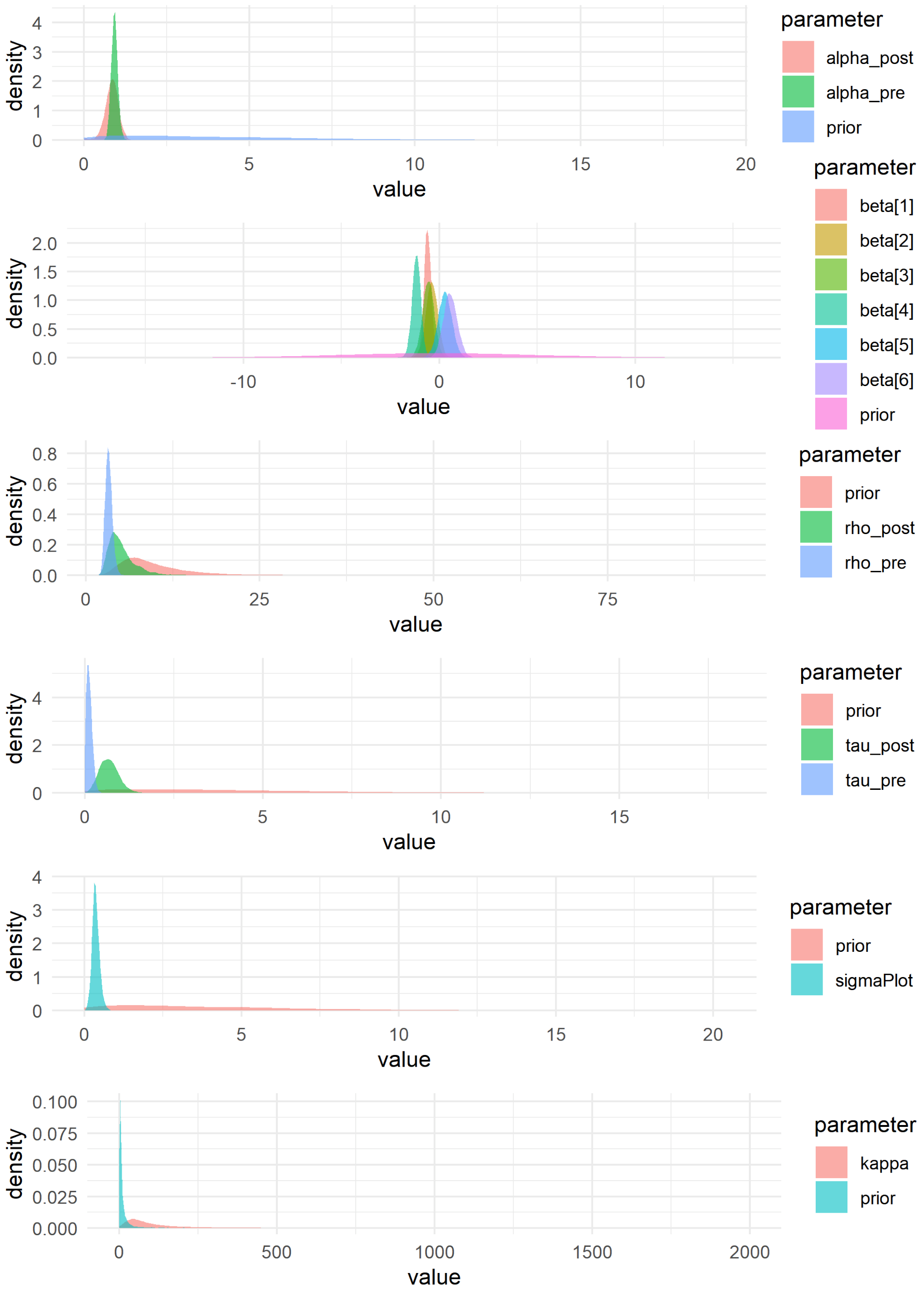

Supplementary Figure 55: Prior vs. posterior parameter distributions for all parameters in the model for 100-hour fine woody debris tallies. In most cases, there are clear differences between the prior and the posterior distributions, indicating that parameter estimates are strongly informed by the data, rather than the prior. However, the posterior distribution for ρ_{post} *substantially overlaps the prior, indicating that model estimates for that parameter were only moderately informed by the data, and may instead reflect prior assumptions.*

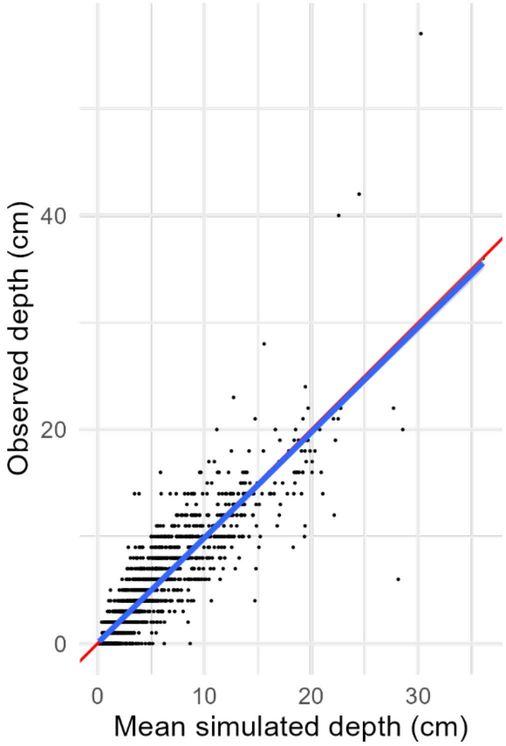

Supplementary Figure 56: Comparison between mean simulated litter and duff depth and observed depth for the training dataset. For each draw of the posterior, litter and duff depth was simulated for every sample in the training data. Each black point is an observed depth, plotted with its mean simulated value on the X-axis and its observed value on the Y-axis. A 1:1 line is plotted in red, and the actual linear relationship between (mean) simulated and observed counts in blue. Model predictions appear to be unbiased (slope between simulated and real data is very close to 1).

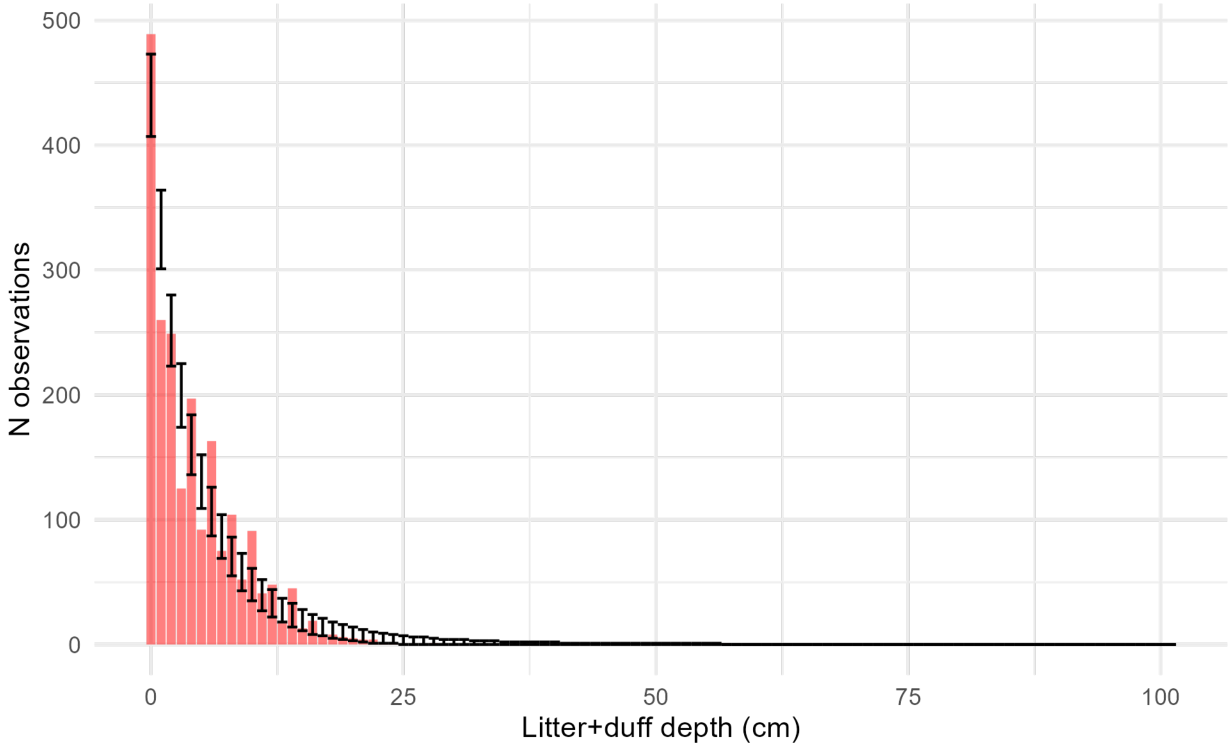

Supplementary Figure 57: Comparison of observed and simulated distribution of litter and duff depths for the training dataset. For each draw of the posterior, litter and duff depth was simulated for every sample in the training data. The observed frequencies are plotted as a histogram in red, with the observed value on the X-axis and the count of observations having that depth value on the Y-axis. The 2.5th and 97.5th percentiles of the count of samples for each depth value across all posterior draws are shown as the error bars. The model simulations broadly match the training data, though there is an unmodeled preference in the training data for even-numbered values of depth (even depth values appear more frequently than odd ones).

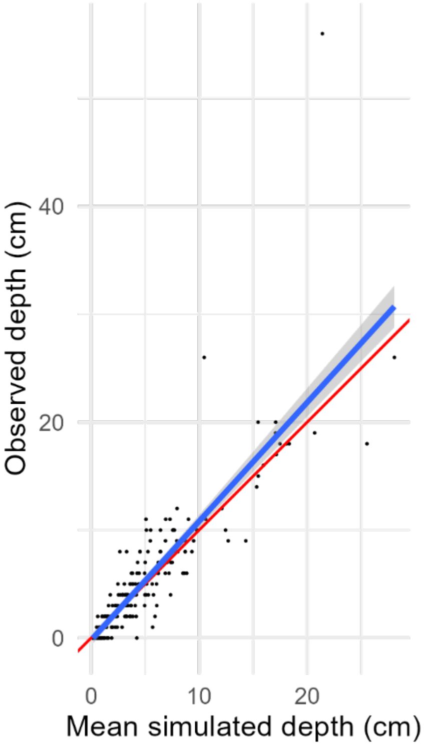

Supplementary Figure 58: Comparison between mean simulated litter and duff depth and observed depth for the validation dataset. For each draw of the posterior, litter and duff depth was simulated for every sample in the validation data. Each black point is an observed depth, plotted with its mean simulated value on the X-axis and its observed value on the Y-axis . A 1:1 line is plotted in red, and the actual linear relationship between (mean) simulated and observed counts in blue. Model predictions appear to be unbiased (slope between simulated and real data is very close to 1).

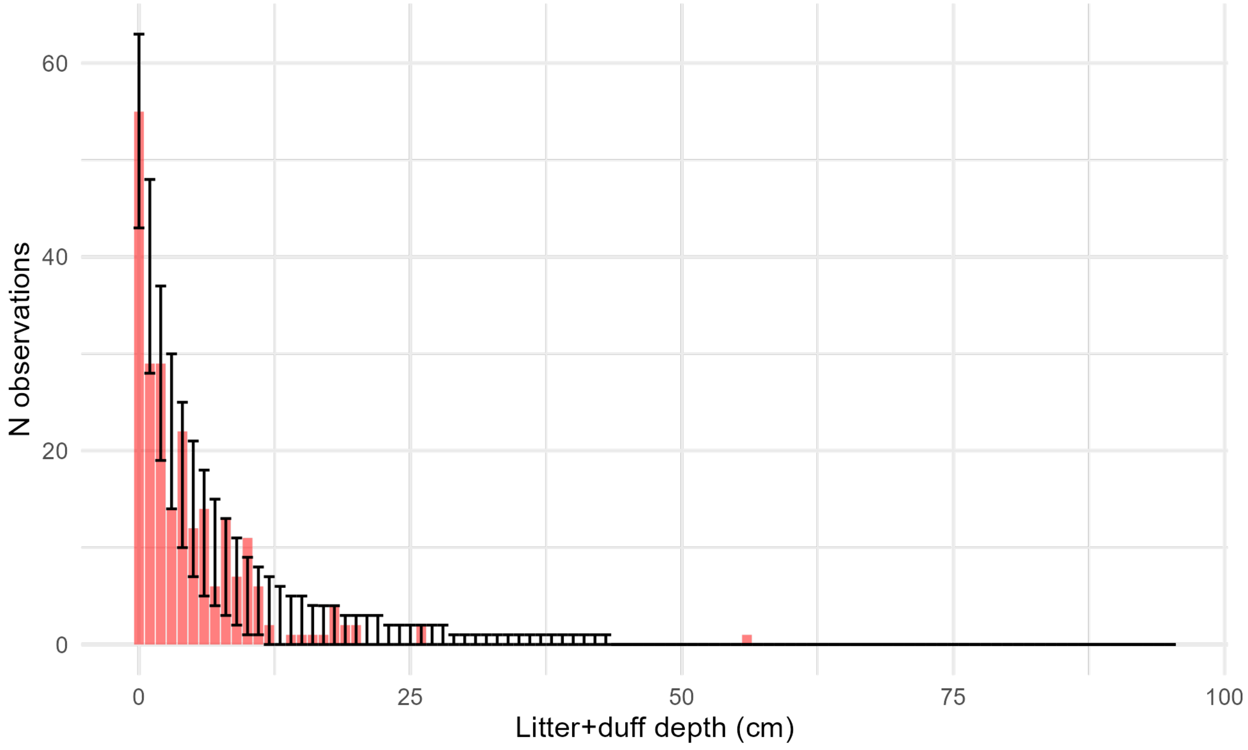

Supplementary Figure 59: Comparison of observed and simulated distribution of litter and duff depths for the validation dataset. For each draw of the posterior, litter and duff depth was simulated for every sample in the validation data. The observed frequencies are plotted as a histogram in red, with the observed value on the X-axis and the count of observations having that depth value on the Y-axis. The 2.5th and 97.5th percentiles of the count of samples for each depth value across all posterior draws are shown as the error bars. The model simulations broadly match the training data, though again there is an unmodeled preference in the training data for even values of depth (even depth values appear more frequently than odd ones).

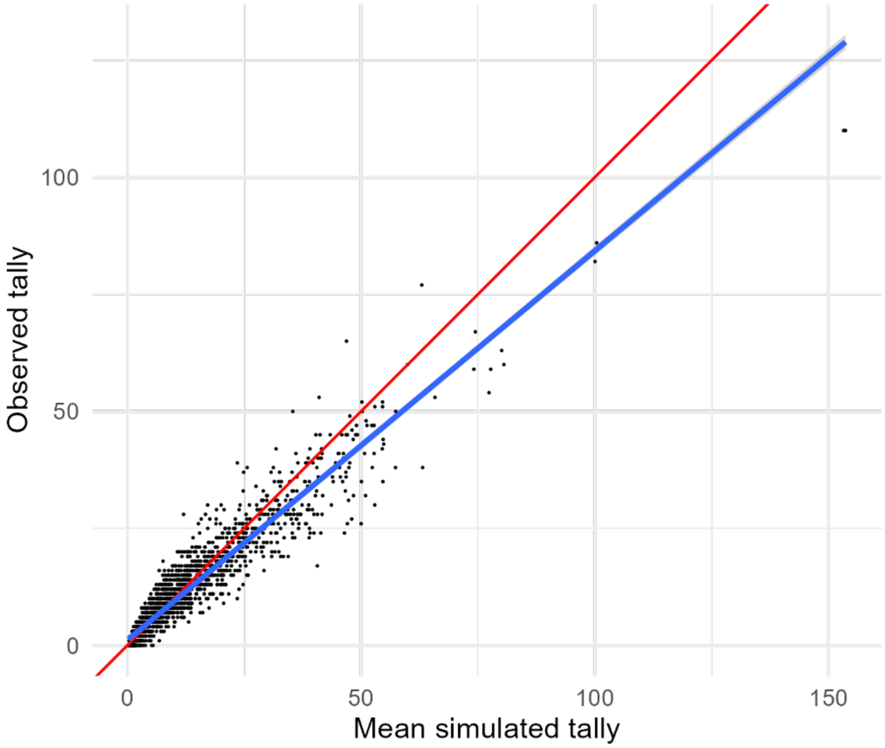

Supplementary Figure 60: Comparison between mean simulated 1-hour FWD tallies and observed tallies for the training dataset. For each draw of the posterior, 1-hour FWD tally was simulated for every sample in the training data. Each black point is an observed sample, plotted with its mean posterior predicted value on the X-axis and its observed value on the Y-axis. A 1:1 line is plotted in red, and the actual linear relationship between (mean) simulated and observed counts in blue. Again, there appears to be a mild bias towards overprediction for larger counts, with the observed values generally falling below the mean predicted value for predicted counts greater than ~25.

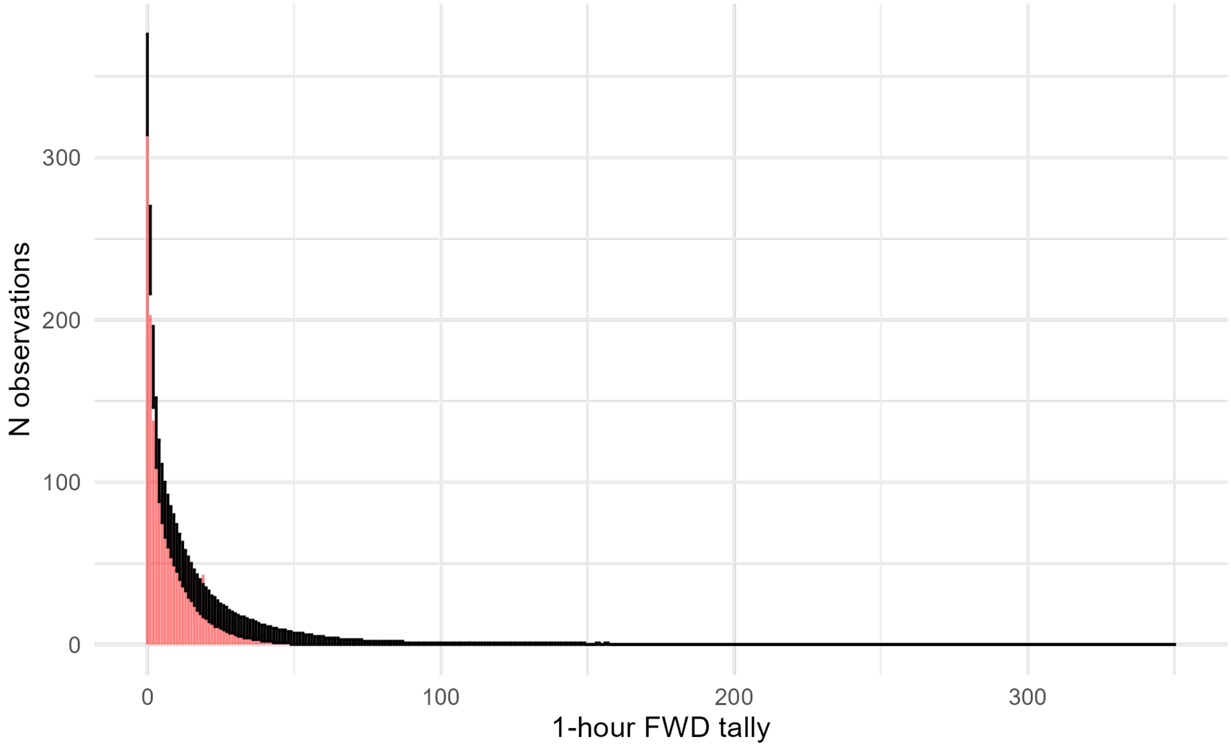

Supplementary Figure 61: Comparison of observed and simulated distribution of 1-hour FWD tallies for the training dataset. For each draw of the posterior, 1-hour FWD tally was simulated for every sample in the training data. The observed frequencies are plotted as a histogram in red, with the observed value on the X-axis and the count of observations having that tally value on the Y-axis. The 2.5th and 97.5th percentiles of the count of samples for each tally value across all posterior draws are shown as the error bars. The observed data generally fall within the range of behaviors predicted by the model, but there are fewer observations with a value of 1 or 2 tallies than the model predicts.

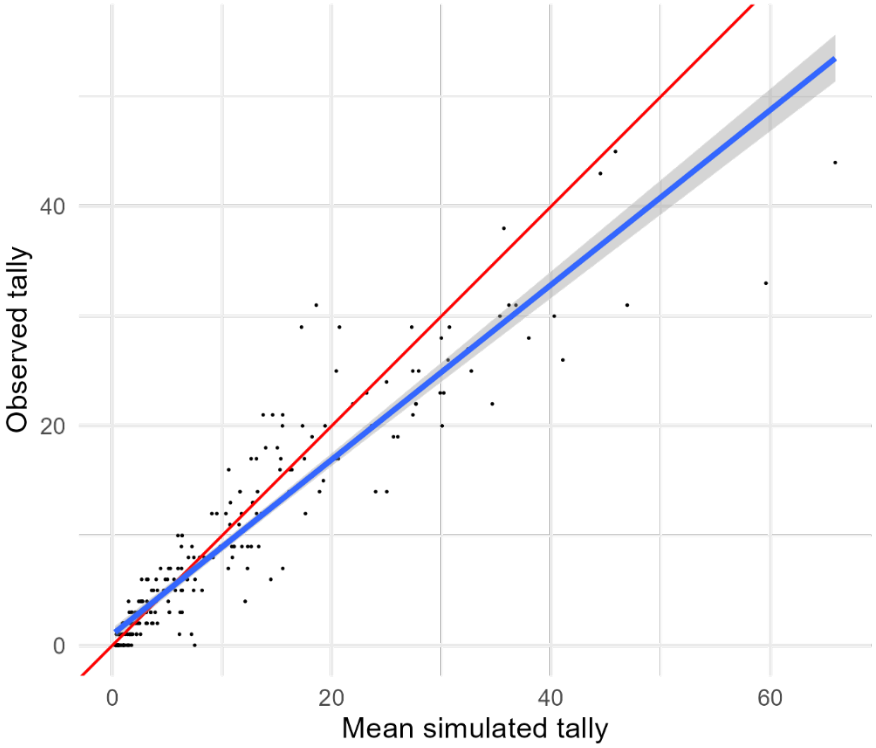

Supplementary Figure 62: Comparison between mean simulated 1-hour FWD tallies and observed tallies for the validation dataset. For each draw of the posterior, 1-hour FWD tally was simulated for every sample in the validation data. Each black point is an observed sample, plotted with its mean posterior predicted value on the X-axis and its observed value on the Y-axis. A 1:1 line is plotted in red, and the actual linear relationship between (mean) simulated and observed counts in blue. The simulated values show a mild bias towards overprediction of the observed counts above ~7, and a mild bias towards underprediction of observed counts below ~7.

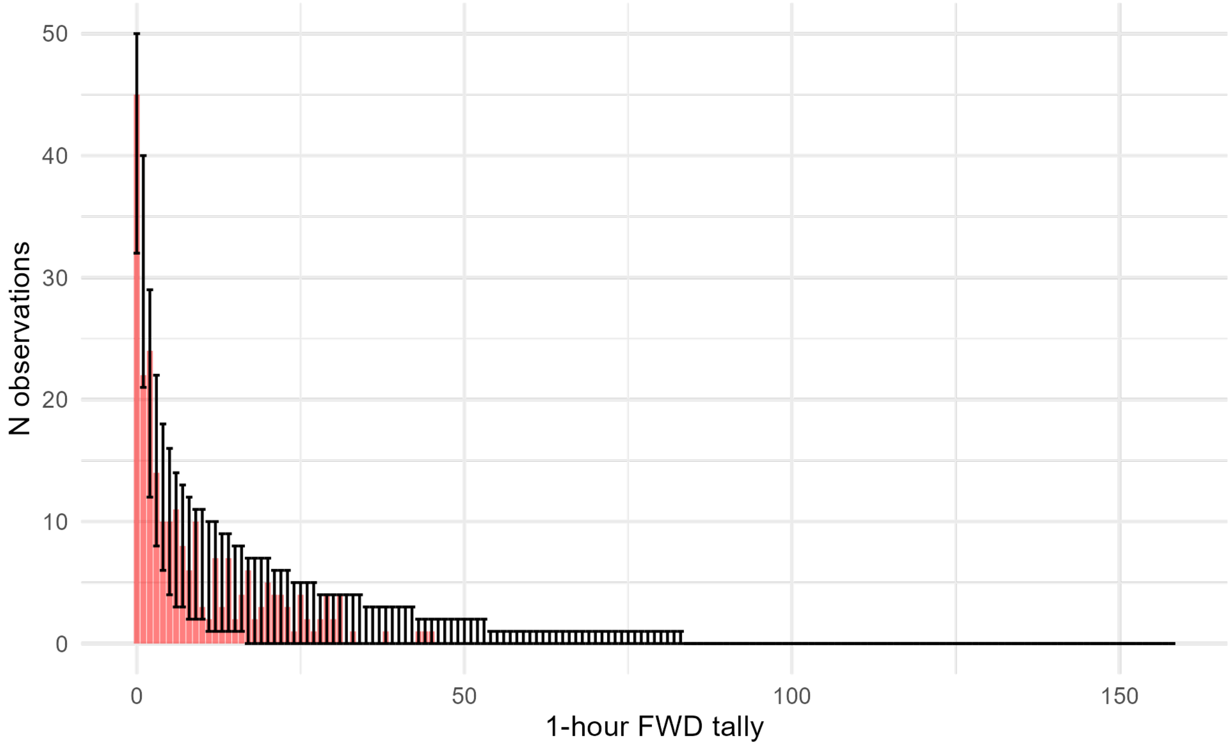

Supplementary Figure 63: Comparison of observed and simulated distribution of 1-hour FWD tallies for the validation dataset. For each draw of the posterior, 1-hour FWD tally was simulated for every sample in the validation data. The observed frequencies are plotted as a histogram in red, with the observed value on the X-axis and the count of observations having that tally value on the Y-axis. The 2.5th and 97.5th percentiles of the count of samples for each tally value across all posterior draws are shown as the error bars. The observed data fall within the range of behaviors predicted by the model.

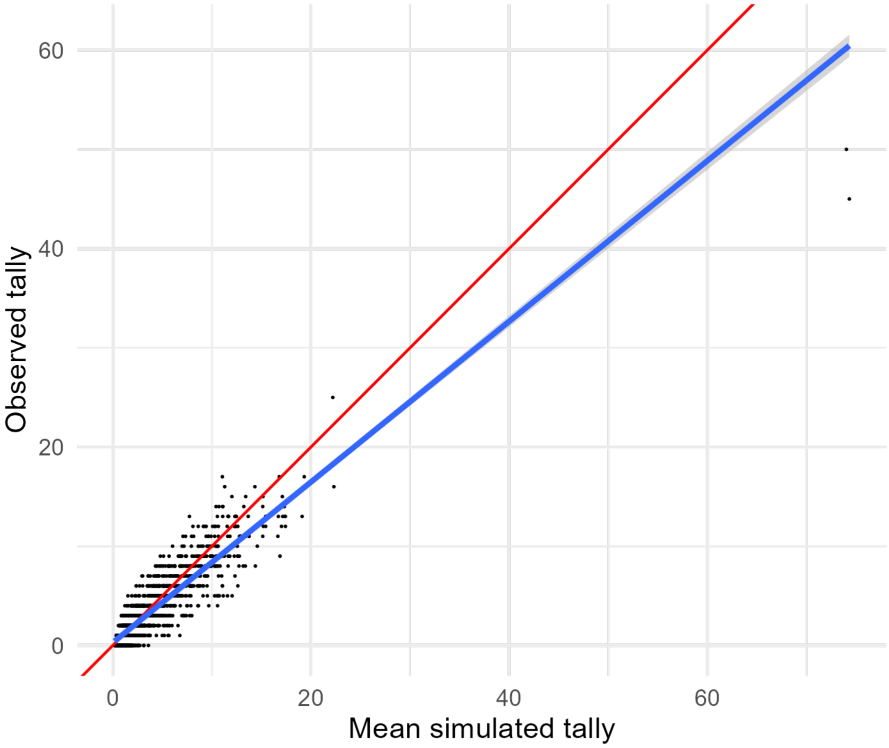

Supplementary Figure 64: Comparison between mean simulated 10-hour FWD tallies and observed tallies for the training dataset. For each draw of the posterior, 10-hour FWD tally was simulated for every sample in the training data. Each black point is an observed sample, plotted with its mean posterior predicted value on the X-axis and its observed value on the Y-axis. A 1:1 line is plotted in red, and the actual linear relationship between (mean) simulated and observed counts in blue. Again, there appears to be a mild bias towards overprediction for larger counts, with the observed values generally falling below the mean predicted value for predicted counts greater than ~25.

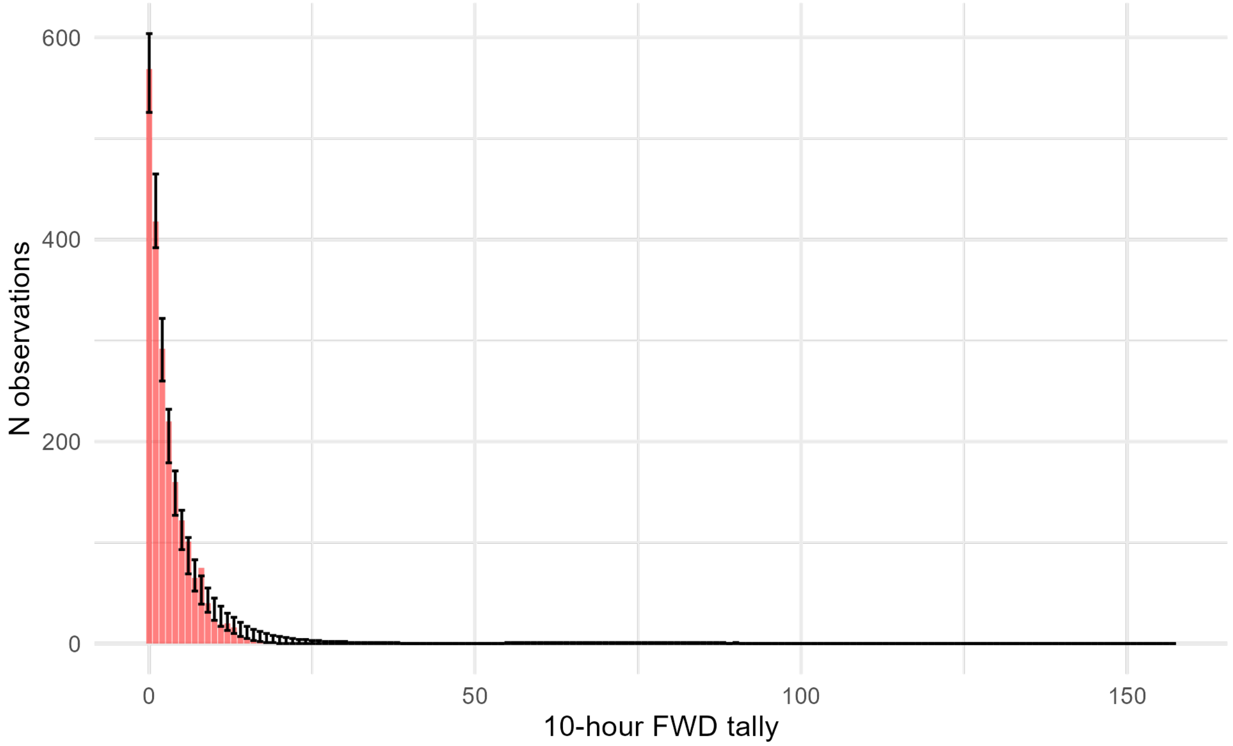

Supplementary Figure 65: Comparison of observed and simulated distribution of 10-hour FWD tallies for the training dataset. For each draw of the posterior, 10-hour FWD tally was simulated for every sample in the training data. The observed frequencies are plotted as a histogram in red, with the observed value on the X-axis and the count of observations having that tally value on the Y-axis. The 2.5th and 97.5th percentiles of the count of samples for each tally value across all posterior draws are shown as the error bars. The observed data fall within the range of behaviors predicted by the model.

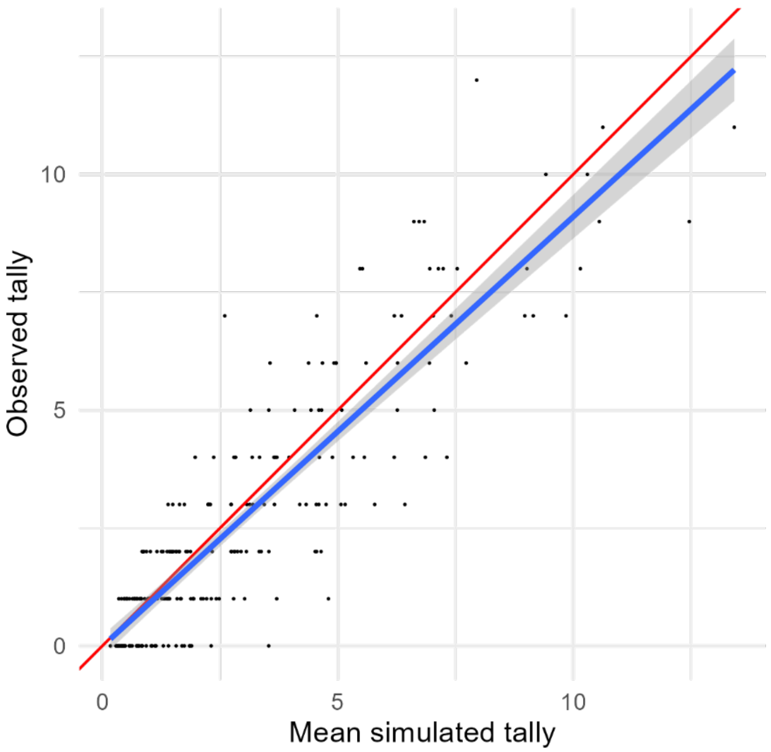

Supplementary Figure 66: Comparison between mean simulated 10-hour FWD tallies and observed tallies for the validation dataset. For each draw of the posterior, 10-hour FWD tally was simulated for every sample in the validation data. Each black point is an observed sample, plotted with its mean posterior predicted value on the X-axis and its observed value on the Y-axis. A 1:1 line is plotted in red, and the actual linear relationship between (mean) simulated and observed counts in blue. The simulated values show a mild bias towards overprediction of the observed counts above ~5.

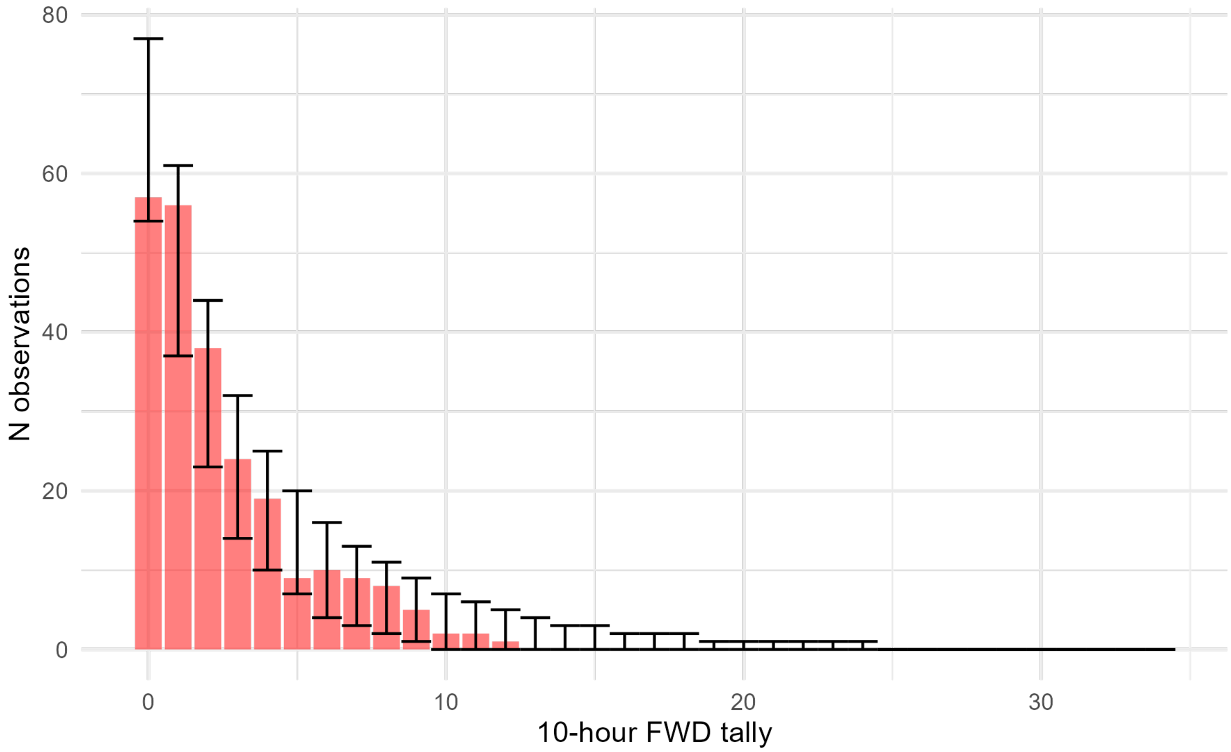

Supplementary Figure 67: Comparison of observed and simulated distribution of 10-hour FWD tallies for the validation dataset. For each draw of the posterior, 10-hour FWD tally was simulated for every sample in the validation data. The observed frequencies are plotted as a histogram in red, with the observed value on the X-axis and the count of observations having that tally value on the Y-axis. The 2.5th and 97.5th percentiles of the count of samples for each tally value across all posterior draws are shown as the error bars. The observed data fall within the range of behaviors predicted by the model.

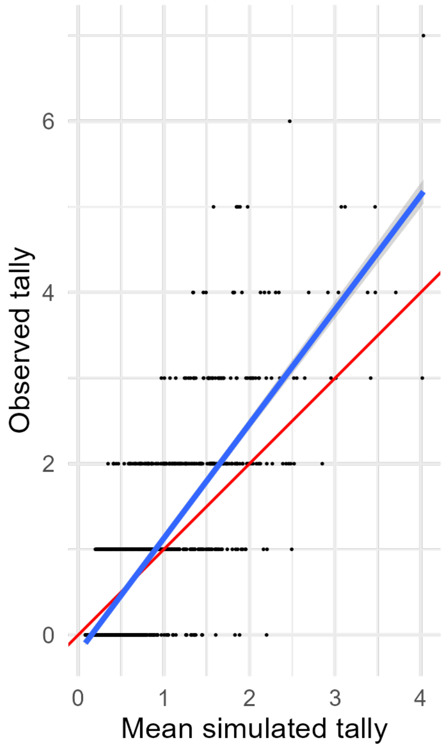

Supplementary Figure 68: Comparison between mean simulated 100-hour FWD tallies and observed tallies for the training dataset. For each draw of the posterior, 100-hour FWD tally was simulated for every sample in the training data. Each black point is an observed sample, plotted with its mean posterior predicted value on the X-axis and its observed value on the Y-axis. A 1:1 line is plotted in red, and the actual linear relationship between (mean) simulated and observed counts in blue. Again, there appears to be a mild bias towards underprediction, with the observed values generally falling above the mean predicted value for predicted values greater than approximately 0.5.

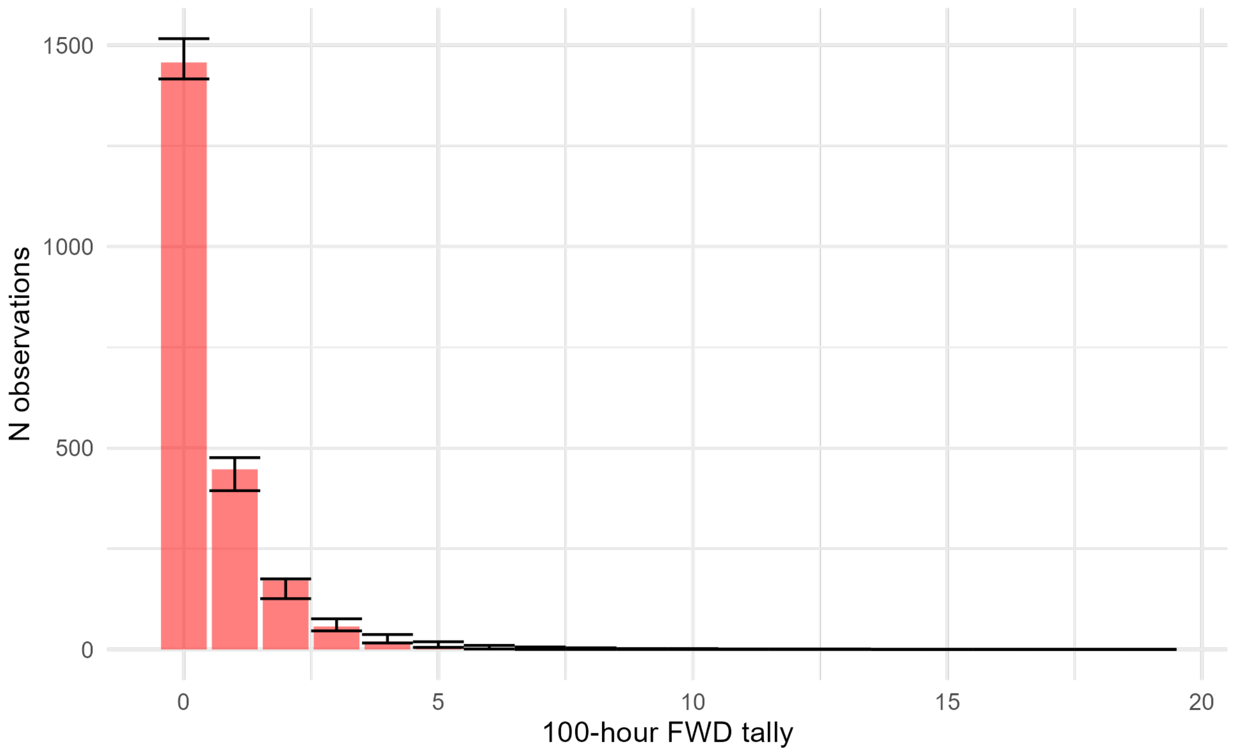

Supplementary Figure 69: Comparison of observed and simulated distribution of 100-hour FWD tallies for the training dataset. For each draw of the posterior, 100-hour FWD tally was simulated for every sample in the training data. The observed frequencies are plotted as a histogram in red, with the observed value on the X-axis and the count of observations having that tally value on the Y-axis. The 2.5th and 97.5th percentiles of the count of samples for each tally value across all posterior draws are shown as the error bars. The observed data fall within the range of behaviors predicted by the model.

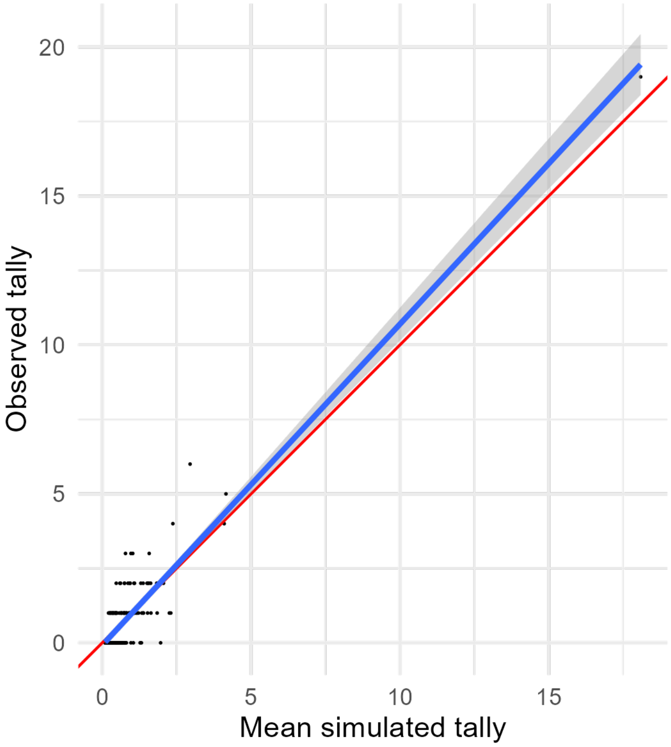

Supplementary Figure 70 Comparison between mean simulated 100-hour FWD tallies and observed tallies for the validation dataset. For each draw of the posterior, 10-hour FWD tally was simulated for every sample in the validation data. Each black point is an observed sample, plotted with its mean posterior predicted value on the X-axis and its observed value on the Y-axis. A 1:1 line is plotted in red, and the actual linear relationship between (mean) simulated and observed counts in blue. The simulated values show a mild bias towards underprediction of the observed counts.

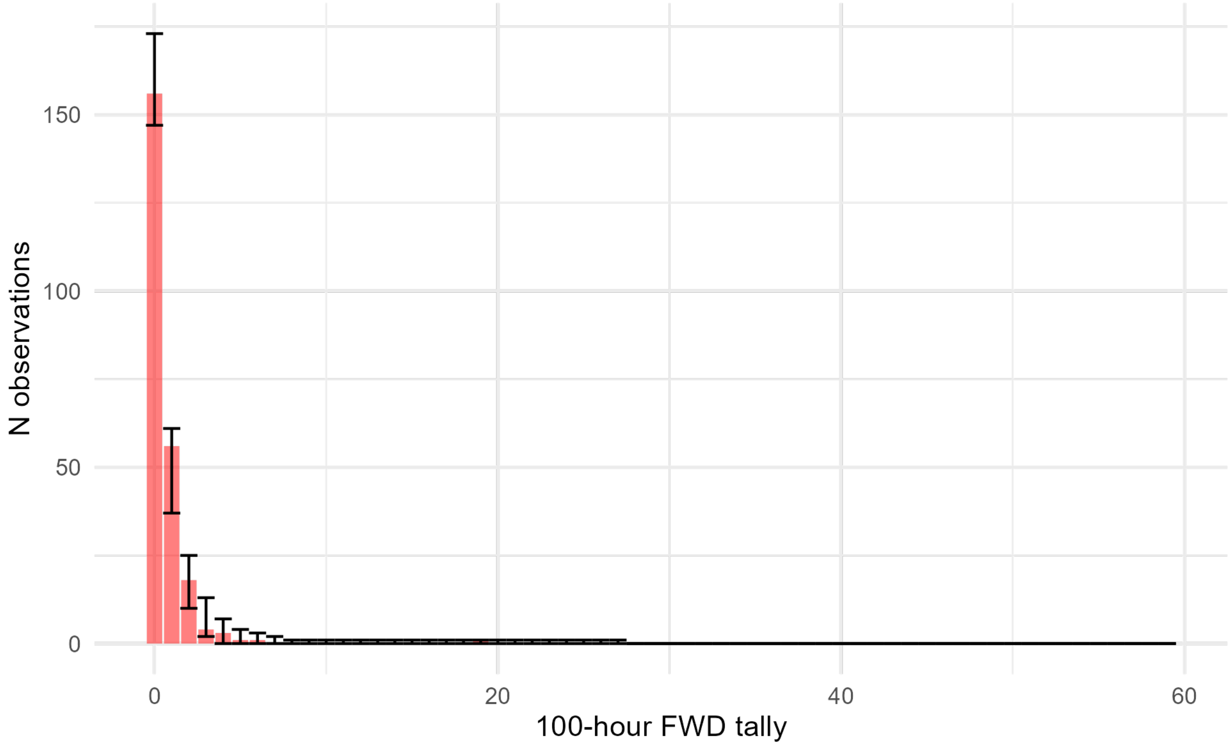

Supplementary Figure 71: Comparison of observed and simulated distribution of 100-hour FWD tallies for the validation dataset. For each draw of the posterior, 100-hour FWD tally was simulated for every sample in the validation data. The observed frequencies are plotted as a histogram in red, with the observed value on the X-axis and the count of observations having that tally value on the Y-axis. The 2.5th and 97.5th percentiles of the count of samples for each tally value across all posterior draws are shown as the error bars. The observed data fall within the range of behaviors predicted by the model.

14 SUPPLEMENTARY MATERIALS FOR "DEMOGRAPHIC STATUS, TRAJECTORY, AND STRESSORS OF *PINUS LAMBERTIANA* IN THE WESTERN US"

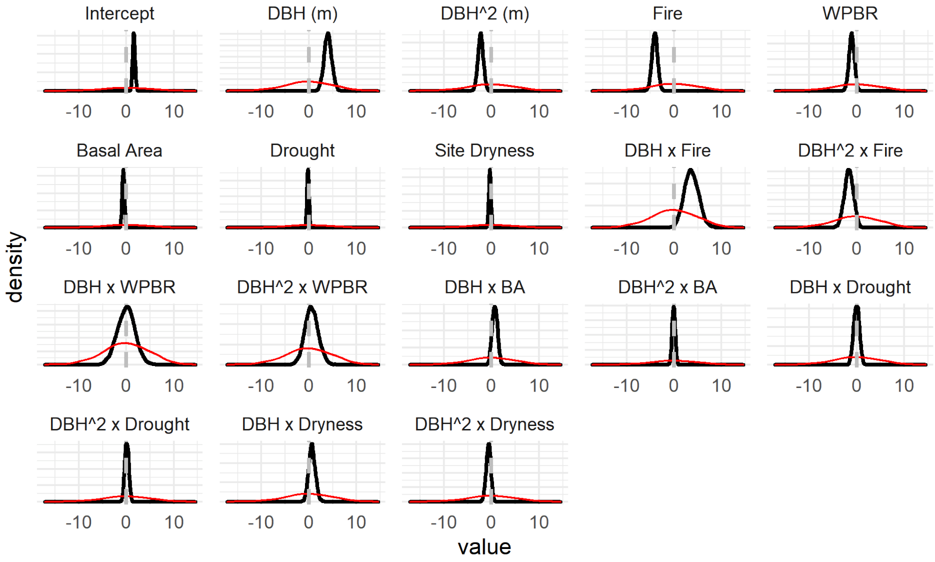

Supplementary Figure 72: Posterior distributions (black) and prior distributions (red) for $\beta_{(s)}$, the fixed effect coefficients for survival. The magnitude of the discrepancy between the two indicates the extent to which the posterior distribution was informed by the data, rather than the prior.

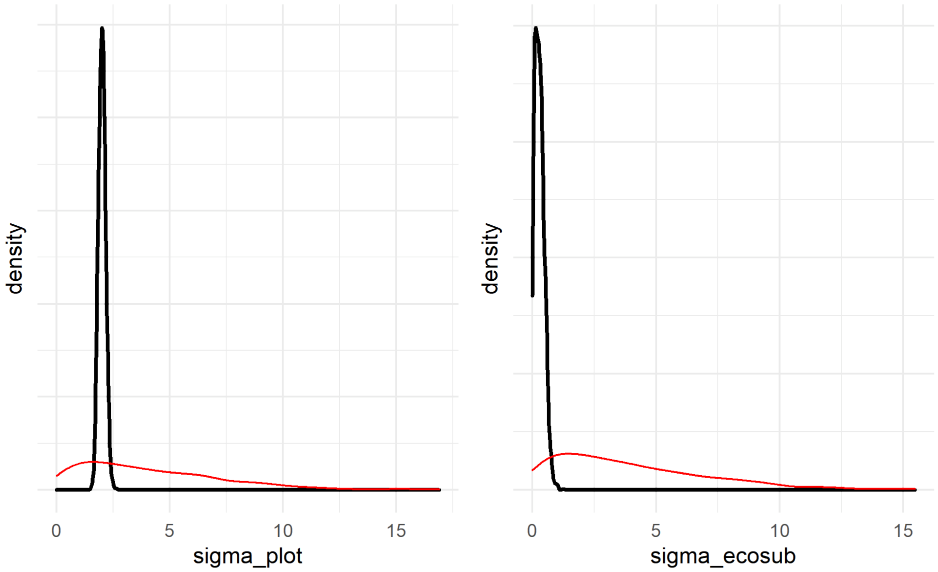

Supplementary Figure 73: Posterior distributions (black) against prior distributions (red) for the standard deviations of the plot and ecoregion random effects in the survival model.

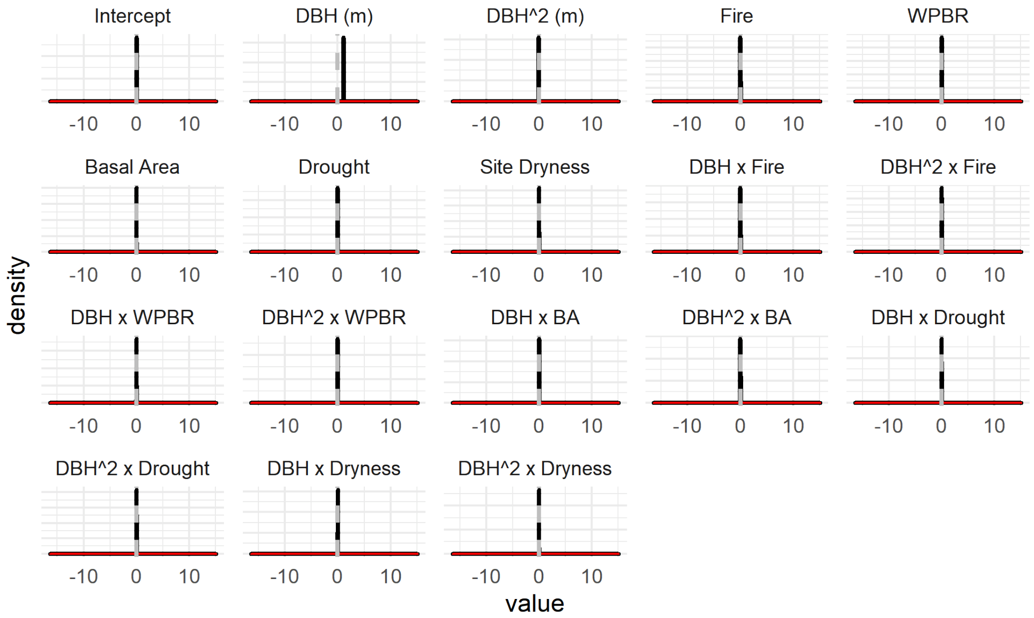

Supplementary Figure 74: Posterior distributions (black) against prior distributions (red) for fixed effect coefficients in the growth model.

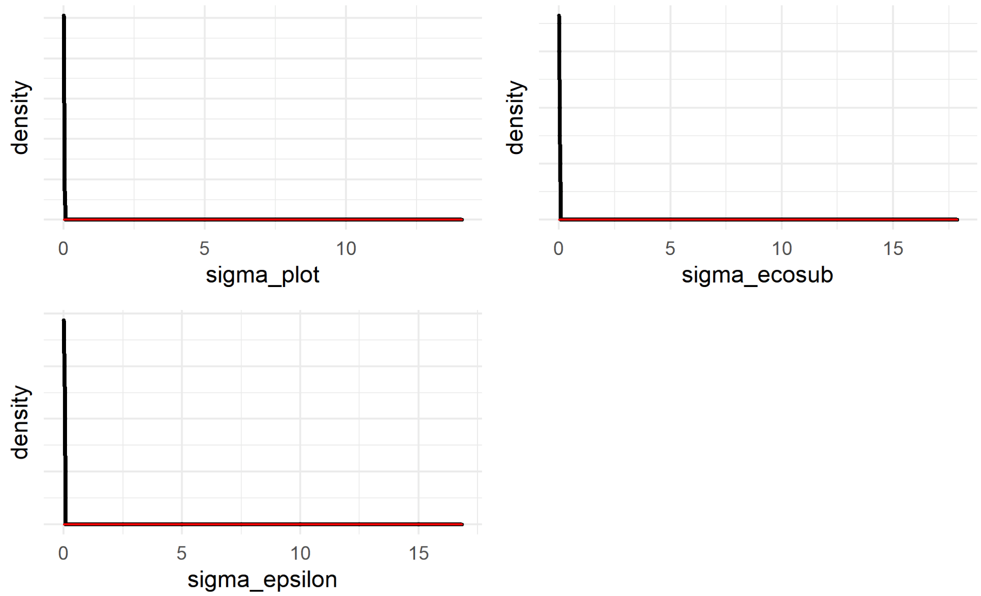

Supplementary Figure 75: Posterior distributions (black, along Y axis) against prior distributions (red, along X axis) for the standard deviations of the plot random effect, the ecoregion random effect, and the residuals in the growth model.

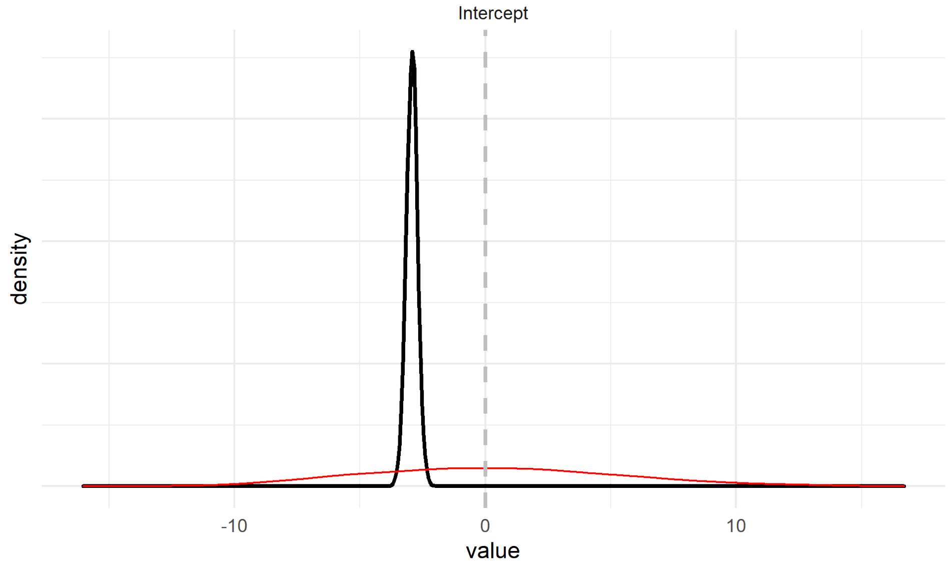

Supplementary Figure 76: Posterior distributions (black) against prior distributions (red) for the fixed effect coefficients affecting fecundity in the recruitment model.

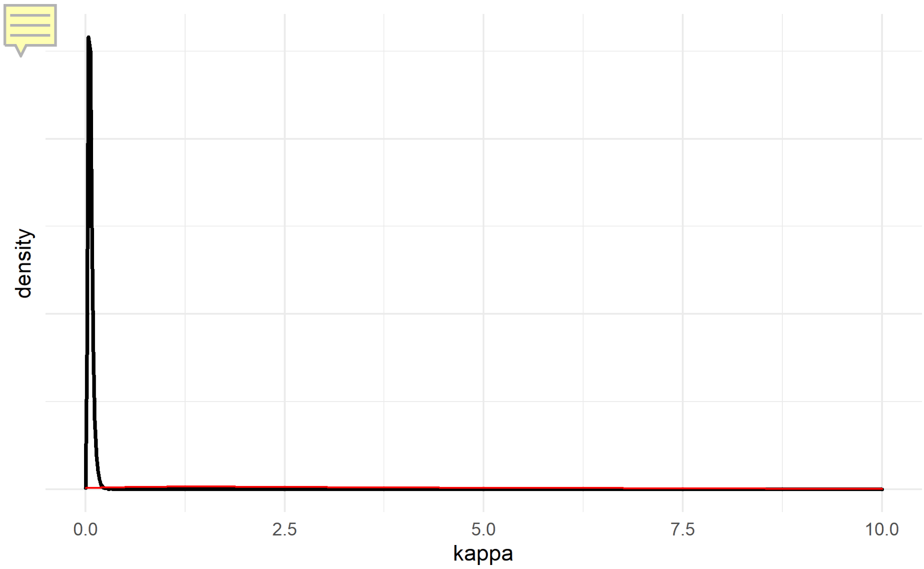

Supplementary Figure 77: Posterior distribution (black, along Y axis) against prior distribution (red, along X axis) for the dispersion term of the negative binomial response in the recruitment model.

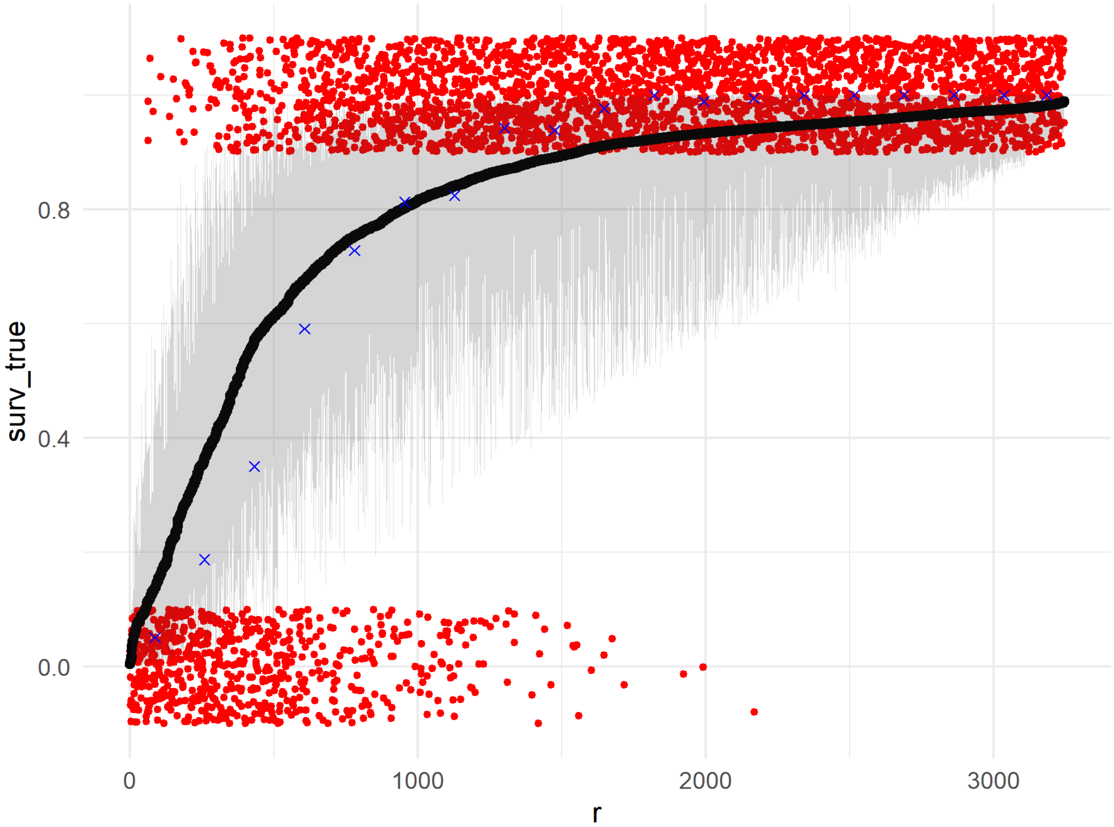

Supplementary Figure 78: Results of posterior retrodictive simulations for survival of individual trees. Posterior samples of the parameters were used to predict the survival probability of each individual tree using ***Error! Reference source not found.*** *and the training data used to fit the model. Individual trees (red points) are ranked along the X-axis by their mean predicted survival probability, and their actual survival (0 or 1) is plotted along the Y-axis (including a jitter for readability). Blue points indicate the actual proportion of individuals in each rank bin which survived. Black points indicate the mean predicted survival for each individual, with a gray ribbon showing a 95%*

credible interval for survival probability for each individual. The model does a good job ranking trees by their actual survival probability, as shown by the red points. However, the model is slightly under-certain about survival probability, relative to reality: It slightly overpredicts survival for the least-likely-to-survive trees, and slightly underpredicts survival for the most-likely-to-survive trees.

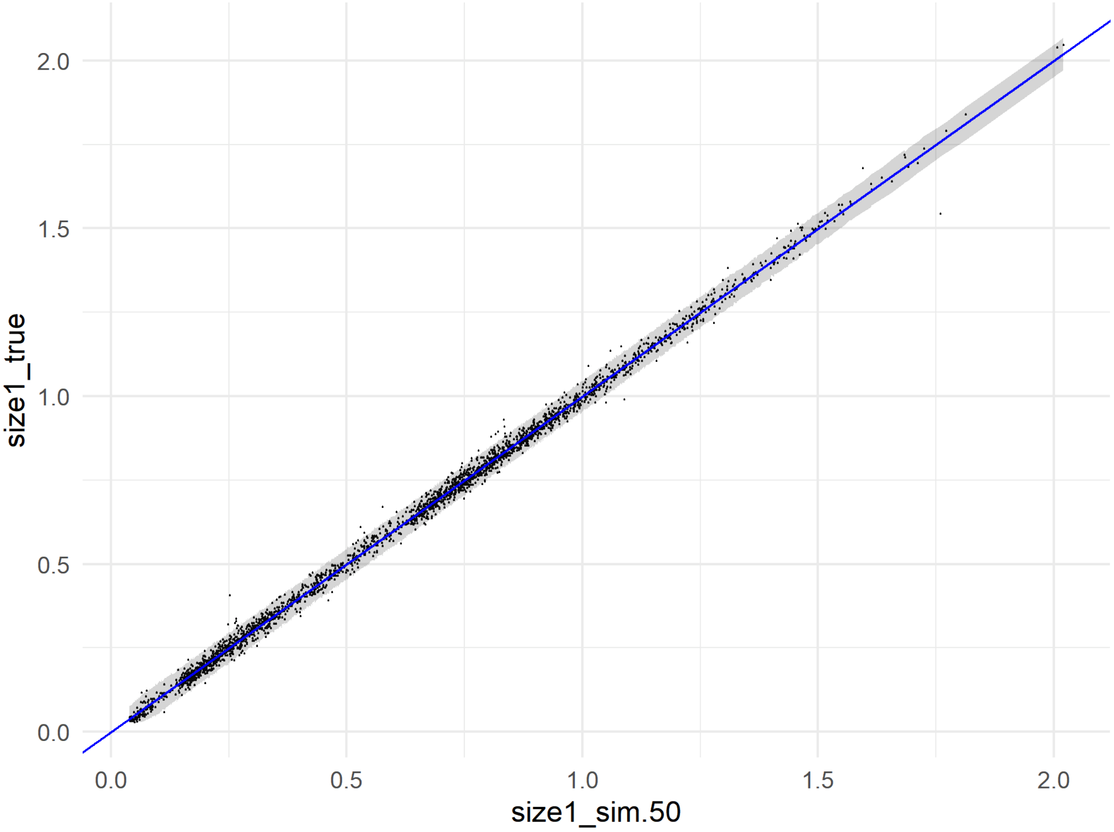

Supplementary Figure 79: Posterior retrodictions for the growth model, using posterior parameter values and the training data. Individual trees (black points) are plotted with their median predicted size at remeasurement along the X-axis, and their true size at remeasurement along the y axis. The blue line has slope 1 and intercept 0, i.e., perfect prediction. The gray ribbon gives a 95% credible interval for size at remeasurement as predicted by the model and contains nearly all of the true sizes.

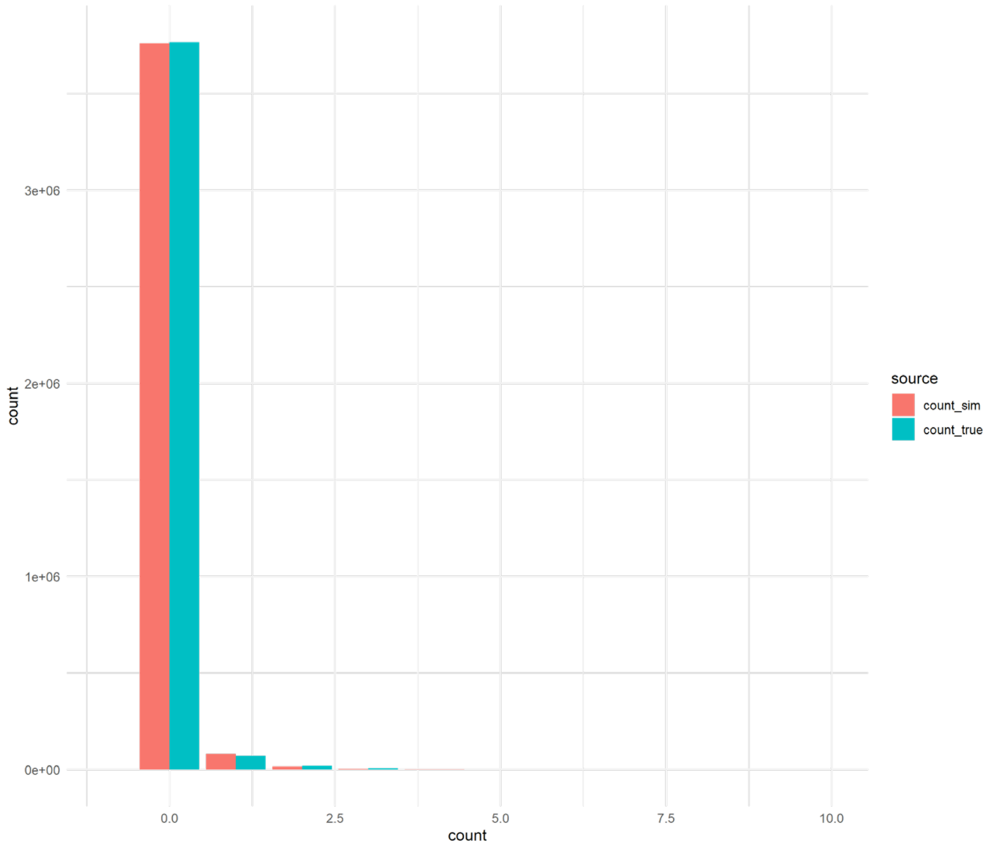

Supplementary Figure 80: Posterior retrodictions for the recruitment model. Histograms of simulated (one simulation per posterior draw) and observed per-plot counts of new recruits are plotted. The frequency distribution of simulated counts (red) closely matches the observed distribution (blue).

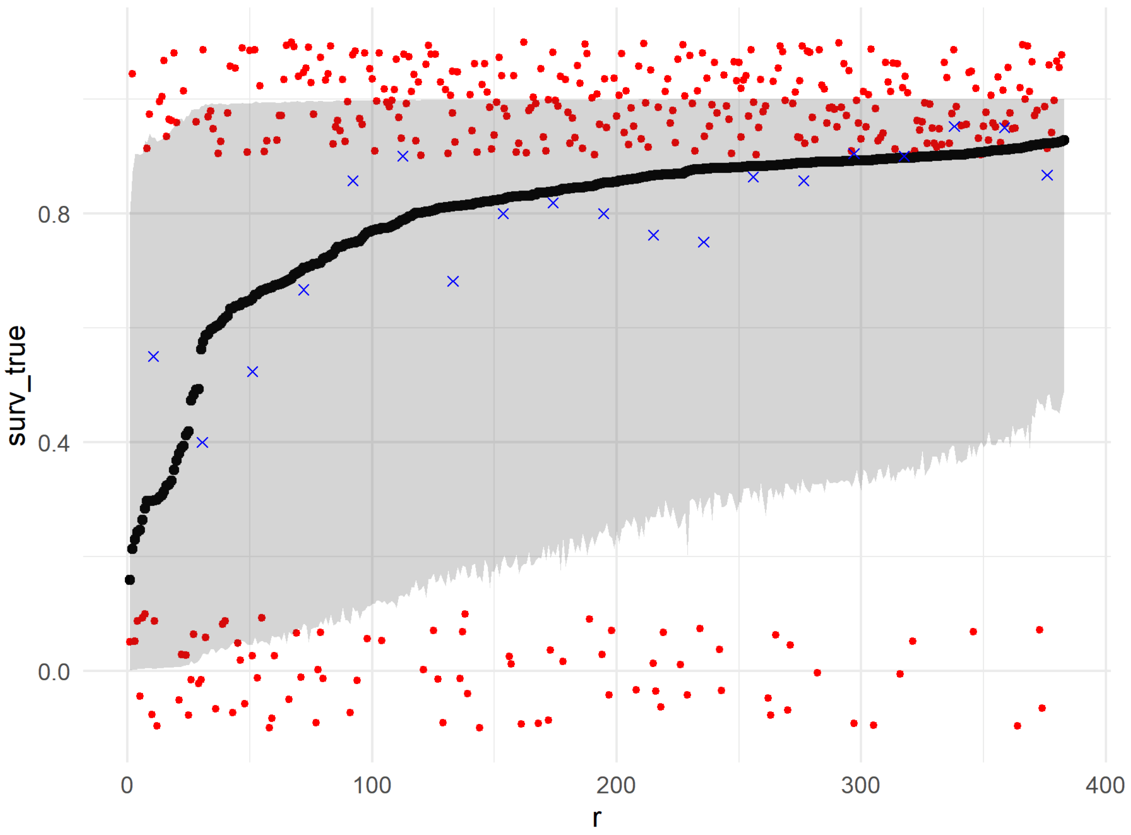

Supplementary Figure 81: Results of posterior predictive simulations for survival of individual trees. Posterior samples of the parameters were used to predict the survival probability of each individual tree using ***Error! Reference source not found.*** *and the validation data. Individual trees (red points) are ranked along the X-axis by their mean predicted survival probability, and their actual survival (0 or 1) is plotted along the Y-axis (including a jitter for readability). Blue points indicate the actual proportion of individuals in each rank bin which survived. Black points indicate the mean predicted survival for each individual, with a gray ribbon showing a 95% credible interval for survival probability for each individual.*

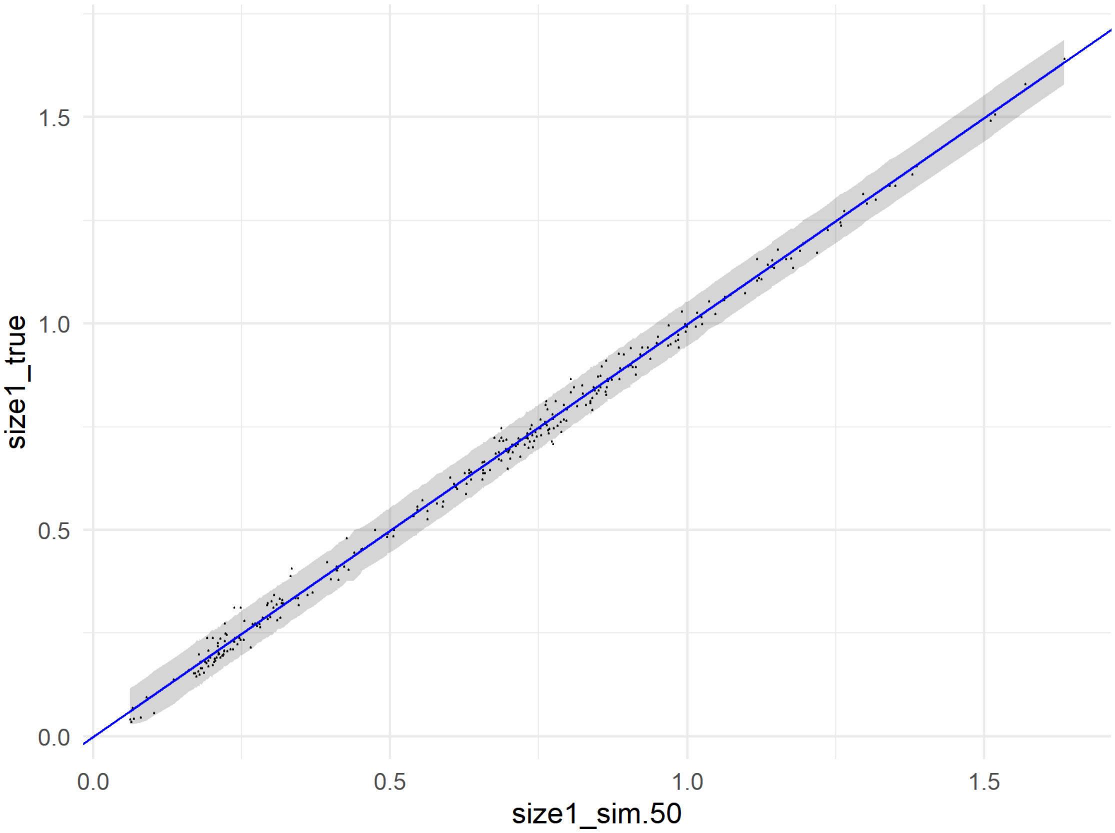

Supplementary Figure 82: Posterior predictions for the growth model, using posterior parameter values and the validation data. Individual trees (black points) are plotted with their median predicted size at remeasurement along the X-axis, and their true size at remeasurement along the y axis. The blue line has slope 1 and intercept 0, i.e., perfect prediction. The gray ribbon gives a 95% credible interval for size at remeasurement as predicted by the model and contains nearly all of the true sizes.

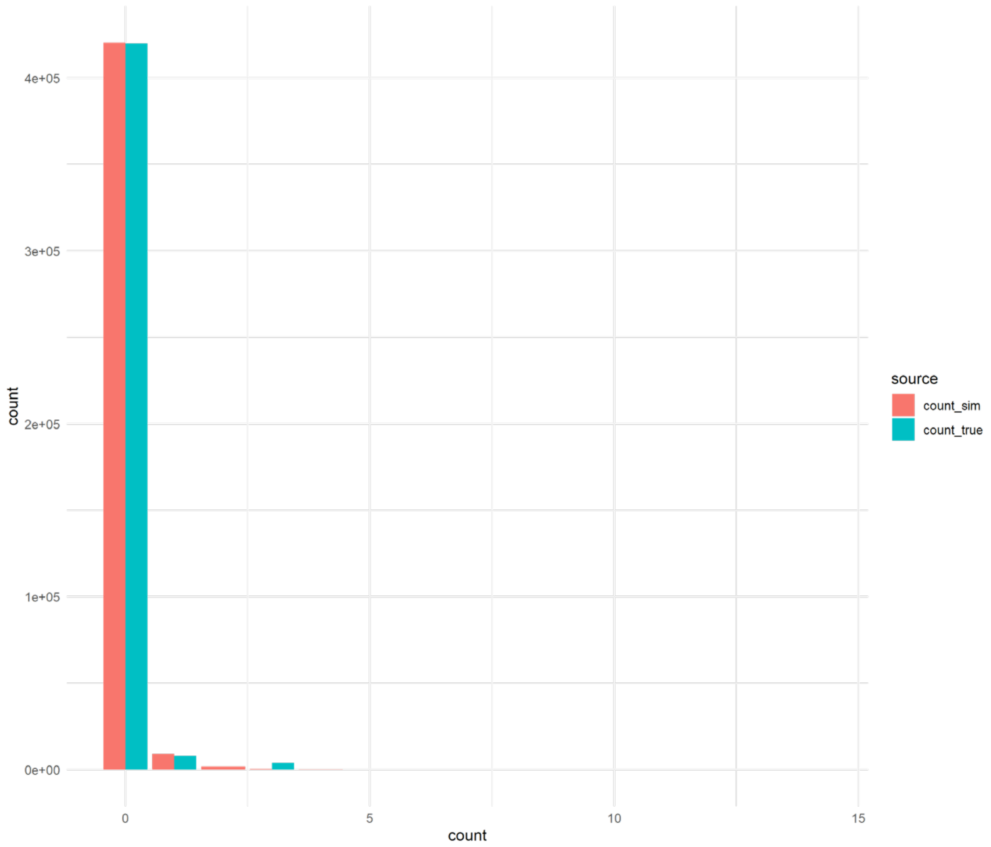

Supplementary Figure 83: Posterior predictions for the recruitment model, using the out-of-sample validation data. Histograms of simulated (one simulation per posterior draw) and observed per-plot counts of new recruits are plotted. The frequency distribution of simulated counts (red) closely matches the observed distribution (blue).

Scenario	**Lambda (median)**	**Lambda (5th percentile)**	**Lambda (95th percentile)**
Undisturbed	0.980	0.953	1.005
Fire	0.643	0.521	0.788
WPBR	0.948	0.857	0.994
Low BA	1.002	0.974	1.029
High BA	0.946	0.912	0.977
Low Drought	0.991	0.963	1.017
High Drought	0.967	0.933	0.998
Wet Site	1.000	0.974	1.025
Dry Site	0.953	0.918	0.986

Supplementary Table 1: Summary of posterior distributions of population asymptotic growth rate (λ) under a variety of idealized scenarios. In each scenario, the relevant stressor is either present (for fire and WPBR), elevated (BA, drought, and site dryness), or depressed (BA, drought, and site dryness), while other stressors are held at absent (fire and WPBR) or their mean value (BA, drought, and site dryness). λ was estimated for each posterior sample by constructing a transition matrix using the posterior sample parameters and the vital rate as described in the methods and taking the dominant eigenvalue of the transition matrix.